Joana de Sousa Dias Prata

DYNAMIC BEHAVIOUR OF LINEAR AND POINT THERMAL BRIDGES OF BUILDINGS - NUMERICAL AND EXPERIMENTAL SIMULATIONS

PhD Thesis in Sustainable Energy Systems
supervised by Professor António José Barreto Tadeu and Professor Nuno Albino Vieira Simões
submitted to the Department of Mechanical Engineering of the
Faculty of Sciences and Technology of the University of Coimbra

November 2017

· U C ·

UNIVERSIDADE DE COIMBRA

· U C ·

UNIVERSIDADE DE COIMBRA

DYNAMIC BEHAVIOUR OF LINEAR AND POINT THERMAL BRIDGES OF BUILDINGS – NUMERICAL AND EXPERIMENTAL SIMULATIONS

by

Joana de Sousa Dias Prata

Thesis submitted to the Department of Mechanical Engineering, FCTUC
in partial fulfilment of the requirements for the degree of
Doctor of Philosophy in Sustainable Energy Systems

Supervisors
Professor António José Barreto Tadeu
Professor Nuno Albino Vieira Simões

November 2017

MIT Portugal
ITeCons
FCT
Fundação para a Ciência e a Tecnologia
MINISTÉRIO DA CIÊNCIA, TECNOLOGIA E ENSINO SUPERIOR
POPH
UNIÃO EUROPEIA
Fundo Social Europeu

ABSTRACT

Linear and point thermal bridges (LTBs and PTBs) increase the heat loss of a building envelope in winter conditions due to a concentration of heat fluxes, which depends on the properties of the material(s) and the geometrical characteristics of the thermal bridge. Furthermore, in these two-dimensional (2D) and three-dimensional (3D) junctions, the surface temperatures are normally significantly lower, which increases the risk of surface condensation and the occurrence of building pathologies. Therefore, it is of the utmost importance to evaluate LTBs and PTBs at the design stage of the building and assess their contribution to the energy performance of buildings.

The steady-state analysis of the energy performance of buildings normally takes into account the LTBs, but the PTBs' contribution tends to be neglected. Whole building dynamic simulation studies, however, usually only assume the one-dimensional (1D) heat transfer through the building envelope and fail to consider the multidimensional heat flows through the linear and point thermal bridges. However, it is very important to predict the thermal behaviour of LTBs and PTBs dynamically, since the influence of the thermal inertia of materials can be considered and high performance solutions can be chosen to reduce the thermal bridging effect. This will prevent the development of pathologies associated with thermal bridges and increase the overall energy performance of the building.

Most studies on dynamic thermal bridging analysis use simplified techniques that do not give accurate information about the dynamic behaviour of linear and point thermal bridges. Therefore, more realistic models are required that can provide more accurate results and a better knowledge of the dynamic thermal bridges' behaviour.

The main goal set for this research was to analyse the dynamic effect of geometrical linear and point thermal bridges of buildings, such as 2D and 3D building corners, using the boundary element method (BEM) formulated in the frequency domain. For this, multidimensional numerical modelling tools were specially built to study the transient heat diffusion through LTBs and PTBs, using 2D and 3D BEM formulations. These tools enabled the computation of the temperature distribution and heat fluxes through the linear and point thermal bridges, over time. The numerical models were first verified against analytical schemes, known for regular geometries, and then were experimental validated using hot box measurements, simulating the dynamic thermal behaviour of a 2D and a 3D corner of a wooden building.

Several numerical simulations of the transient heat transfer through 2D and 3D building corners were performed to illustrate the applicability of the proposed BEM models and to evaluate the thermal bridging effect over time. The influence of the constructive solutions and the external temperature variation on the dynamic thermal behaviour of LTB and PTB was also analysed. The importance of modelling linear and point thermal bridges dynamically was demonstrated.

It was concluded that a static analysis underestimates the linear thermal transmittances and overestimates the wall's surface temperature in the vicinity of the LTB. Moreover, the additional heat flow through the PTBs analysed was found to be significantly lower than the heat flow through the adjacent building elements and through the LTB junctions. However, the evaluation of the dynamic point thermal bridging effect in building envelope details can be very important when it comes to overcoming moisture condensation problems, since lower surface temperatures are registered in the vicinity of the PTBs under dynamic conditions. The dynamic behaviour of the linear and point thermal bridges clearly depends on the thermal properties of the materials and the position of the insulation layer.

RESUMO

As pontes térmicas lineares e pontuais (PTL e PTP) são caracterizadas por uma concentração dos fluxos de calor, que depende das suas características geométricas e das propriedades térmicas dos materiais. Esta concentração de fluxos é responsável pelo aumento das perdas de calor através da envolvente do edifício, durante a estação de aquecimento. Para além disso, nestas ligações bidimensionais (2D) e tridimensionais (3D), as temperaturas na superfície são normalmente significativamente mais baixas, aumentando o risco de condensações superficiais e a ocorrência de patologias no edifício. Por este motivo, é de extrema importância avaliar as PTL e PTP na fase de projeto dos edifícios, bem como determinar a sua contribuição no desempenho energético dos mesmos.

A análise estática do desempenho energético de edifícios considera normalmente a existência de PTL, contudo a contribuição das PTP tende a ser desprezada. Por outro lado, os estudos de simulação dinâmica de edifícios, por norma, assumem apenas a transferência de calor unidimensional (1D) através da envolvente e não consideram os fluxos de calor multidimensionais que ocorrem através das PTL e PTP. No entanto, é muito importante prever o comportamento térmico dinâmico destas ligações, de modo a considerar a influência da inércia térmica dos materiais e assim ser possível escolher soluções construtivas de elevado desempenho que permitam reduzir o efeito da ponte térmica. Este tipo de análise permitirá prevenir o desenvolvimento de patologias associadas às pontes térmicas e aumentar o desempenho energético global do edifício.

A maior parte dos estudos de análise dinâmica de PTL e PTP usam metodologias simplificadas e não fornecem informações precisas sobre o comportamento térmico dinâmico das mesmas. Logo, são necessários modelos mais realistas, que permitam obter resultados mais precisos e um maior conhecimento sobre o comportamento térmico dinâmico das pontes térmicas.

O principal objetivo deste trabalho de investigação foi analisar o efeito dinâmico de pontes térmicas geométricas, lineares e pontuais, tais como os cantos 2D e 3D da envolvente de edifícios, através do Método dos Elementos de Fronteira (BEM) formulado no domínio da frequência. Para isso, foram desenvolvidas ferramentas de modelação numérica multidimensionais para o estudo da difusão de calor, em regime transiente, usando formulações 2D e 3D do BEM. Estas ferramentas permitiram calcular a distribuição de temperaturas e os fluxos de calor ao longo do tempo nas pontes térmicas lineares e pontuais. Os modelos numéricos foram primeiro verificados através de soluções analíticas, conhecidas para geometrias regulares. Posteriormente, estes modelos foram validados experimentalmente, através de medições realizadas numa *hot box* que simulam o comportamento térmico dinâmico de cantos 2D e 3D de um edifício em madeira.

Foram realizadas várias simulações numéricas da transferência de calor transiente em cantos 2D e 3D de edifícios para ilustrar a aplicabilidade dos modelos BEM propostos e para avaliar o efeito das pontes térmicas ao longo do tempo. Foi ainda analisada a influência das soluções construtivas e da variação da temperatura exterior no comportamento térmico dinâmico das PTL e das PTP. A importância da modelação das pontes térmicas, em regime dinâmico, foi demonstrada.

Este estudo permitiu concluir que uma análise estática subestima as transmissões térmicas lineares e sobrestima as temperaturas superficiais na PTL. Além disso, verificou-se que o fluxo de calor adicional através das PTP analisadas é significativamente menor do que o fluxo de calor que ocorre nos elementos construtivos adjacentes e nas PTL. No entanto, a avaliação do efeito dinâmico da PTP em pormenores construtivos da envolvente do edifício pode ser muito importante quando se trata de superar problemas de humidade, uma vez que, em condições dinâmicas, as temperaturas superficiais registadas nas PTP são mais baixas. O comportamento térmico dinâmico das pontes térmicas lineares e pontuais depende claramente das propriedades térmicas dos materiais e da localização da camada de isolamento.

AKNOWLEDGEMENTS

The research work presented in this thesis was funded by the Foundation for Science and Technology of the Portuguese Ministry of Education and Sciences (grant SFRH/BD/91688/2012), for which I am extremely grateful. I would also like to thank the Energy for Sustainability Initiative of the University of Coimbra (EfS) for supporting the dissemination of this work over the past few years. This work has also been developed under the projects: POCI-01-0247-FEDER-003408 - “Slimframe”, approved through the Incentive Scheme R&TD Co-promotion Projects and co-funded by the European Regional Development Fund (FEDER) through Compete2020 and POCI-01-0247-FEDER-003344/LISBOA-01-0247-FEDER-003344 - “ClimTestE+”, approved through the Incentive Scheme R&TD Co-promotion Projects and co-funded by FEDER through Compete2020 and Lisboa2020.

The development of this research work would not have been possible without the contribution of my supervisors and colleagues and without the support of my family and friends.

I would like to thank my supervisors, Professor António Tadeu and Professor Nuno Simões, for the patient guidance, encouragement and support they provided during the execution of this work. I would also like to thank all of my colleagues from the Institute for Research and Technological Development in Construction, Energy, Environment and Sustainability (ITeCons), in particular Inês Simões for her contribution in numerical modelling, Saúl Martins, António Nascimento, Filipe Pedro and Aurélio Gonçalves for their valuable collaboration in the laboratory work, and Catarina Serra for her precious help and friendship.

I must express my deepest gratitude to Hugo and my son Guilherme for everything they represent in my life: to Hugo for the dedication and patience demonstrated throughout this course and for his unconditional support during the most difficult moments; to my son Guilherme for giving new meaning to this work and an extra motivation.

I cannot fail to thank my father and grandparents for always believing and encouraging me, and also Leonor and Gabriel for being like a family to me.

Finally, I want to dedicate this thesis to the memory of my Mother, for the sacrifices she made so that I could complete all my projects and become the person I am today, and for still inspiring me every day.

TABLE OF CONTENTS

CHAPTER 1

INTRODUCTION

1 INTRODUCTION

1.1 Context and motivation

In the European Union (EU), buildings are responsible for 40% of energy consumption and 36% of CO_2 emissions. According to Directive 2010/31/EU, Member States should be drawing up national plans not only to improve the energy efficiency of existing buildings but also to increase the number of new buildings with very high energy performance (nearly zero-energy buildings), to reduce the impact of the building sector on long-term energy consumption and to achieve the energy targets set for 2020. Therefore, correctly characterizing the building envelope to enable high-quality constructive details to be chosen will be even more important.

The thermal behaviour of the building envelope depends on the characteristics of each building element (wall, roof, floor, door and window) and on the two-dimensional (2D) and three-dimensional (3D) junctions between these elements, known as linear thermal bridges (LTBs) and point thermal bridges (PTBs), respectively. These junctions are also known as geometrical thermal bridges since they result from the geometry of the building envelope. They are characterized by a concentration of a multi-dimensional heat flow, associated with additional heat loss in winter conditions which leads to lower internal surface temperatures. The convective effect is lower in these junctions, which increases the relative humidity and, therefore, the risk of moisture condensation that promotes the growth of mould and other pathologies.

In the EU, the contribution of LTBs to the energy performance of buildings is usually taken into account by using linear thermal transmittance (ψ) values calculated under steady-state conditions. PTBs, however, are not generally included into the energy performance calculation. Even the whole building dynamic simulation programs normally assume one-dimensional (1D) heat transfer through the building envelope and do not take into account the 2D and 3D dynamic heat flows that occur through the LTBs and PTBs, respectively. Moreover, thermal bridges have a dynamic behaviour and these simplified analyses may lead to serious errors in the thermal bridging effect evaluation, resulting in the selection of inappropriate constructive details and energy retrofits.

Thermal bridges decrease the overall thermal resistance of the building envelope and also affect its dynamic characteristics. Studies have therefore been conducted in the last few years to ascertain the importance of predicting the thermal behaviour of thermal bridges dynamically, assuming a variation of temperature over time and thus considering the influence of the thermal inertia of the construction materials. However, due to the complexity of multidimensional transient heat transfer formulations, most of these studies propose simplified approaches to including thermal bridging analysis in the building dynamic energy simulations. These simplified approaches not only do not give accurate information about the mould growth risk in the thermal bridge but they may actually considerably underestimate the annual cooling and heating loads compared with the 2D and 3D dynamic analysis using numerical modelling methods.

The models used for the numerical analysis of multi-dimensional transient heat transfer problems are normally mesh-based methods, such as the finite difference method (FDM), the finite element method (FEM) and the finite volume method (FVM). These methods involve the discretization of the entire problem domain into regular grids or meshes. Therefore, for irregular geometries the mesh generation process can be very time-consuming and considerable computational effort may be required. An alternative to those methods is the boundary element method (BEM), which is possibly one of the most suitable tools for modelling homogeneous systems with finite, semi-infinite or infinite domains, since it automatically satisfies the far field conditions of the problem.

As a result, the BEM enables a compact description of the regions and, even though only the boundaries of the inclusions are discretized, fully populated systems of equations are achieved, contrary to the sparse systems given by the FDM and FEM techniques. Thus, the size of the equation system to be solved is efficiently reduced, which considerably reduces the numerical data and the computation time required to solve the problem efficiently.

Most of the numerical models are formulated in the time domain, where the time increment determines the quality of the response. This requires very extensive calculations for long-term diffusion phenomena. An alternative approach is to solve the problem in the frequency domain. In this case, the response can be computed assuming a limited number of frequencies, since high frequencies can be neglected because the heat responses decay rapidly. This allows a significant reduction in the computation time.

The dynamic numerical simulation of LTBs and PTBs depends on many factors and requires the adoption of simplifying assumptions, which can lead to erroneous interpretation of the physical process. Therefore, the validation of the numerical models is essential to assess the confidence level of the simulations. The use of experimental data for that purpose can be very important since it allows the analysis of the real dynamic behaviour of the thermal bridges and the evaluation of the influence of the simplifications assumed in the numerical models.

This research work intends to develop alternative 2D and 3D numerical models based on the BEM, formulated in the frequency domain, to accurately evaluate the dynamic effect of linear and point thermal bridges in buildings. These models will be validated using experimental data. Case studies will be analysed to illustrate the applicability of the BEM models and also to evaluate the importance of assessing the linear and point thermal bridging effect dynamically.

1.2 Objectives

The aim of this research work is to evaluate the dynamic effect of linear and point thermal bridges in buildings, using the boundary element method (BEM), formulated in the frequency domain. To achieve this aim, the following specific objectives were established:

- Development of multi-dimensional numerical modelling tools to study the transient heat diffusion through linear and point thermal bridges in building corners, using 2D and 3D

BEM formulations in the frequency domain; development and verification of analytical solutions for the integration of the singular integrals that appear in the 3D BEM formulations. The developed tools must be able to compute the temperature distribution and the heat fluxes through the thermal bridges, over time, considering real climate data for the outdoor temperature variation. Time solutions will be obtained by applying inverse Fourier transformations.

- Development of analytical models for the verification of the 2D and 3D BEM algorithms and for the evaluation of the linear thermal bridges contribution in building details. For this, 2D and 3D analytical solutions known for stratified mediums and cylindrical inclusions, respectively, will be used.

- Development of experimental programs to validate the 2D and 3D BEM models. Particular care was taken to choose specimen materials and geometry that would limit the number of variables that affect the dynamic behaviour of the experimental system.

- Presentation of numerical applications to evaluate the 2D and 3D dynamic thermal bridging effect and quantify the effective importance of LTBs and PTBs in terms of heat flow and surface temperatures (under steady-state and dynamic conditions).

1.3 Thesis structure

This thesis can be divided into six main chapters that contain the development, experimental validation and numerical application of 2D and 3D BEM models for the simulation of the dynamic heat transfer by conduction through linear and point thermal bridges in buildings. Each chapter is a ‘stand-alone’ unit, with its own introduction, conclusions and references.

Chapter 2 presents a 2D BEM formulation in the frequency domain to simulate the dynamic behaviour of LTBs. The BEM algorithm is verified against a 1D analytical solution known for stratified media. The applicability of the BEM model is illustrated by using the two algorithms together to compute the dynamic heat flow rate through an LTB in a concrete wall corner, considering a sinusoidal external temperature variation. Time solutions are obtained by applying inverse Fourier transformations.

In Chapter 3 the 2D BEM formulation is validated using dynamic heat transfer measurements of a 2D wooden building corner. The tests are performed in the laboratory using a calibrated hot box apparatus. The temperatures imposed on the external and the internal environmental sides are controlled by a climatic chamber and a heating system, respectively. The surface temperatures are recorded using a set of thermocouples connected to a data logger system. The heat flow through the wooden corner is measured using heat flux sensors. The dynamic linear thermal bridging effect is then evaluated by comparing the heat responses near the corner with those at the adjacent plane walls. The experimental results are then compared with the results obtained with the proposed BEM model.

In Chapter 4, the 2D BEM formulation presented in Chapter 2 is used to simulate the transient heat diffusion through a wall corner, to evaluate the dynamic behaviour of the LTB. Several simulations are performed, for two different materials (concrete and wood), and with the insulation layer having different placements and thicknesses. Time solutions are obtained afterwards by means of inverse Fourier transformations, thus enabling the simulation of different external temperature variations. A sensitivity analysis is performed to assess the influence of the constructive solution and the external temperature variation on the dynamic thermal behaviour of the LTB. Climate data from four European cities are used in the simulations.

Chapter 5 presents the 3D BEM formulations in the frequency domain for the simulation of the heat diffusion through a PTB. An analytical formulation for the integration of singular integrals that appear while modelling 3D BEM problems is proposed. The 3D BEM solutions, incorporating the analytical formulation, are verified against analytical solutions derived for cylindrical circular inclusions. The applicability of the BEM formulation is first illustrated for cylindrical inclusions subjected to an external point heat source. Then, a PTB in a 3D concrete building corner, subjected to a sinusoidal external temperature variation over time, is simulated and the temperature distribution over time in two different planes of the building corner domain is computed. Time solutions are obtained by applying inverse Fourier transformations.

In Chapter 6 the 3D BEM formulation is validated by means of the experimental program described in Chapter 3. For this purpose, the heat transfer through a 3D wooden building corner (representing a junction between two walls and a roof) is measured under dynamic conditions. The dynamic point thermal bridging effect is evaluated by comparing the heat responses near the 3D corner with those recorded at the 2D junctions (LTBs) and at the adjacent plane walls and roof. The experimental results are then compared with the results given by the proposed 3D BEM model.

Chapter 7 of this thesis describes the application of the 3D BEM formulation proposed in Chapter 5 to simulate the heat diffusion through a 3D building corner. The dynamic thermal bridging effect in its vicinity is also evaluated. The temperature distribution and the dynamic point thermal transmittance are computed assuming a sinusoidal variation of the external temperature over time. The influence of the placement of an insulating material on the thermal behaviour of the point thermal bridge is also analysed.

The final chapter (Chapter 8) contains the main conclusions and the potential research work that may provide continuity to this thesis.

CHAPTER 2

2D BEM FORMULATION, IN FREQUENCY DOMAIN, TO STUDY THE TRANSIENT HEAT DIFFUSION THROUGH LINEAR THERMAL BRIDGES OF BUILDINGS

2 2D BEM FORMULATION, IN FREQUENCY DOMAIN, TO STUDY THE TRANSIENT HEAT DIFFUSION THROUGH LINEAR THERMAL BRIDGES OF BUILDINGS

2.1 Introduction

A linear thermal bridge (LTB) is characterised by a concentration of two-dimensional (2D) heat fluxes, associated with additional heat loss in winter conditions ([1],[2]). It leads to lower surface temperatures, which encourage the development of mould and other pathologies caused by condensation ([3],[4]). Linear thermal bridges (LTBs) must therefore be taken into account in simulations to prevent pathologies and to improve building energy efficiency, at the design stage of the building.

In the European Union (EU), the heat balance through LTBs in residential buildings is dealt with through simplified procedures, assuming a steady-state condition ([5],[6]).

In turn, building dynamic simulation software normally assumes one-dimensional (1D) heat transfer and does not take into account the two-dimensional (2D) dynamic heat flows that occur through the LTBs of building envelopes. These simplified analyses can lead to serious errors in the energy load estimations of a building [7]. Different approaches that allow for the LTBs in the dynamic energy simulations of buildings have been assumed. The Portuguese energy system code predicts that energy consumption for heating is increased by 5% if LTBs are present [8]. However, this simplified approach does not consider the real impact of LTBs, which strongly depends on constructive details such as the position and the thickness of the insulating materials, and any correction made to the thermal bridge detailing. Another approach, typically used with structural thermal bridges but sometimes with LTBs as well, is the equivalent U-value method [9]. In this method, the thermal resistance of the building elements is changed, normally by adjusting the thickness of the insulation layer, to consider the additional 2D heat flux that occurs through the LTBs without changing the thermal properties of the materials and assuming 1D heat transfer through the building envelope. This simplified approach allows the existence of thermal bridges to be considered but does not properly simulate the dynamic thermal bridging effect.

Some authors have reported the importance of predicting the thermal behaviour of thermal bridges dynamically, assuming a temperature variation over time, thereby considering the influence of the thermal inertia of materials ([10],[11]). Mao and Johannesson [12] developed a tool based on a frequency response method [13] to study 2D heat-flow problems, using the finite elements method (FEM). This method was used to analyse the dynamic behaviour of different types of thermal bridge, according to ISO 13786:2006 [14]. The results of their research showed that the amplitude and the phase lag of the building details may be changed due to the presence of thermal bridges.

In order to analyse the effective contribution of thermal bridges to the global energy performance of buildings, some researchers have been working on simplified numerical approaches to introduce thermal bridging analysis into whole building dynamic simulation software. The "thermally equivalent wall" idea was first presented by Kossecka and Kosny [15]. In this method, the response factors for a complex wall with thermal bridges are reproduced using those for a multilayer wall with the same dynamic properties. The equivalent wall may be used instead of the complex wall in the dynamic energy simulation of buildings. More recently, Martin *et al.* [16] have developed a methodology based on the equivalent wall concept to calculate equivalent walls with the same dynamic thermal behavior as an LTB. The equivalent wall has the same internal heat flow and surface temperatures as the LTB, but the heat transfer physical problem is one dimensional (1D), which allows the solution to be implemented in building dynamic simulation programs. Aguillar *et al.* [17] have implemented the equivalent wall method in the study of two highly-inertial LTBs: a junction between a vertical wall and an intermediate floor slab and a junction between a vertical wall and a ground floor slab. The authors concluded that the equivalent wall method achieves a reliable transient response of LTB physical problems. However, this 1D simplified approaches may generate serious errors in mould growth estimations [18] and may considerably underestimate the annual cooling and heating loads when compared with the dynamic 2D/3D modelling methods as has been shown by Ge and Baba [9]. Also, Ascione *et al.* [19] have concluded that 1D dynamic simplified models lead to an inaccurate evaluation of thermal bridges and, consequently, inappropriate energy retrofits.

Some researchers have worked on multidimensional heat transfer models to be implemented in dynamic building simulation programs. Gao *et al.* [11] used a state model reduction technique to lessen the complexity of a 3D heat transfer model. They used this low-order model to study the dynamic behaviour of thermal bridges in a simplified form and presented the results in 3D dynamic simulation software - TRNSYS [20]. Gao's work shows that, in the case studied, the thermal bridges led to an increase of 9 to 19 % in total heat loss through the building envelope. Déqué *et al.* [10] proposed an algorithm based on the integration of a simplified dynamic treatment of thermal bridges in CLIM 2000 software [21], showing that accurately modelling thermal bridges is better than conventional approaches that use tabulated values. They concluded that a better estimation of heat loss through thermal bridges, particularly in T and L shaped structures, can represent an increase of 5% in the total heat loss of a building. Ascione *et al.* [22] proposed a new simplified state space method for implementing 2D heat transfer in dynamic energy simulation software. This numerical model was experimentally validated by the author [23] using in situ measurements of the surface temperatures and the heat fluxes in a building corner.

The importance of accurately estimating the dynamic effect of thermal bridges using numerical approaches complying with EN ISO 10211:2007, by means of a progressive thickening of the computational mesh, is advocated by some authors [23]. Mesh-based methods such as the finite difference method (FDM) ([24],[25]), the finite element method (FEM) [26] and the finite volume method (FVM) [27] have been successfully used for the numerical analysis of 2D transient heat diffusion problems, such as LTB of buildings. However, if the model to be analysed is more complex, the mesh generation process characteristic of these methods can become very time-consuming and a considerable computational effort may be required. An alternative to those methods is the boundary element method (BEM) ([28],[29],[30]) which is possibly one of the most suitable approaches for the analysis of heat diffusion problems, since the far field boundary conditions are automatically satisfied and only the discontinuities or interfaces of the materials require discretization. The BEM generates fully populated systems of equations, contrary to the sparse systems given by the mesh-based methods. However, it reduces the size of the system of equations that needs to be solved. The BEM uses fundamental solutions, or Green's functions, to continuously relate the field variables in a homogeneous medium to point sources placed within it. The fundamental solution most often used corresponds to an infinite homogeneous domain, since it is known in closed-form and has a relatively simple structure. One disadvantage of the BEM is that it can only be applied to more general geometries and media when the corresponding fundamental solution is known (to avoid having to discretize the boundary interfaces), and this is not always possible.

In this section, a 2D dynamic BEM model, formulated in the frequency domain, is proposed to simulate the dynamic thermal behaviour of LTBs of buildings. The BEM model is verified by comparing the results for a multilayer system wall with analytical solutions. The analytical formulation, obtained as Green’s functions, is established by imposing temperature and heat flux continuity at the interfaces of the various layers. Both algorithms are experimentally validated for the simulation of 1D multilayer systems. Finally, the applicability of the proposed BEM model is illustrated for a 2D concrete wall corner subjected to a sinusoidal external temperature variation over time. Time solutions are obtained by applying inverse Fourier transformations.

2.2 Problem definition

Consider a corner of a building, representing an LTB, as illustrated in Figure 2.1. The surface of the outer-facing wall is subjected to a temperature variation, while the indoor temperature is assumed to be constant. At a certain distance from the corner the heat flux becomes perpendicular to the wall. So, null fluxes can be prescribed along the wall for those cut-off sections.

The next section describes the formulation to compute the dynamic heat transfer by conduction through the building corner, using a 2D BEM model in the frequency domain. Then an analytical solution to compute the response in the plane walls, when the problem is 1D, is presented. These two algorithms can be used together to compute the heat flux through the LTB, as will be demonstrated in section 2.5 of this chapter.

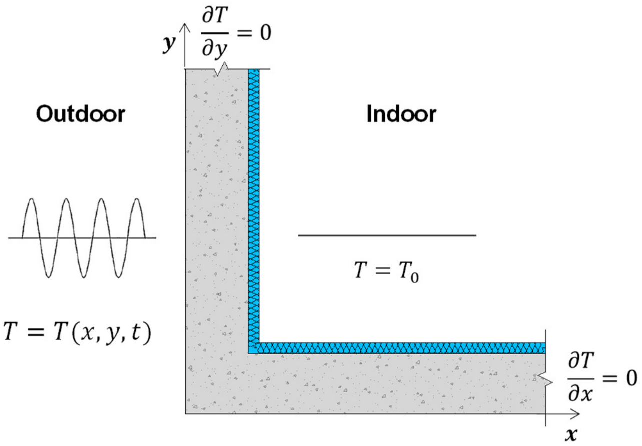

Figure 2.1: Building corner scheme used to evaluate the dynamic behaviour of a thermal bridge.

2.3 Problem formulation

This section describes how the heat transfer by conduction under unsteady-state conditions can be computed numerically in a frequency domain. It first presents a BEM formulation to solve the 2D problem. Then an analytical solution, formulated in the frequency domain, that allows computing 1D heat flows is presented. Time solutions can be obtained by applying inverse Fourier transformations as will be described at the end of this section.

2.3.1 2D BEM formulation in frequency domain

Consider an unbounded medium (Medium 1) with an embedded inclusion (Medium 2), bounded by a surface S, $\{S_1, S_2, S_3\} \in S$, as illustrated in Figure 2.2.

Null heat fluxes $\left(\frac{\partial T}{\partial n} = 0\right)$ and prescribed temperatures $T = T_0$ are imposed respectively along the boundary sections S_1 and S_2, while continuity of temperatures and heat fluxes are assumed along the rest of the boundary, S_3.

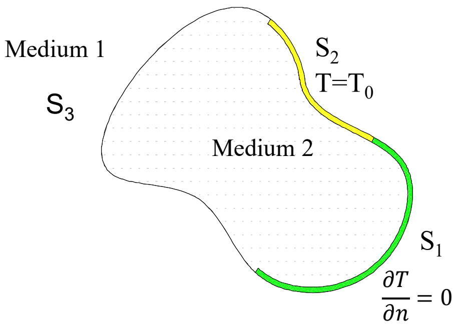

Figure 2.2: Problem definition.

The 2D transient heat transfer by conduction is governed by the equation

$$\left(\frac{\partial^2}{\partial x^2}+\frac{\partial^2}{\partial y^2}\right)T=\frac{1}{K}\frac{\partial T}{\partial t}, \tag{2.1}$$

in which t is time, $T(x,y,t)$ is temperature, $K=\lambda/(\rho c)$ is the thermal diffusivity, λ is the thermal conductivity, ρ is the density and c is the specific heat. This formulation assumes that the material's properties are not dependent on the temperature and moisture content.

To solve this equation, we move from the time domain to the frequency domain by applying a Fourier transformation in the time domain to equation (2.1) to obtain

$$\left(\frac{\partial^2}{\partial x^2}+\frac{\partial^2}{\partial y^2}+\left(\sqrt{-\frac{\mathrm{i}\omega}{K}}\right)^2\right)\hat{T}(x,y,\omega)=0, \tag{2.2}$$

where $\hat{T}(x,y,\omega)=\int_0^\infty T(x,y,t)e^{-\mathrm{i}\omega t}\,dt$, $\mathrm{i}=\sqrt{-1}$ and ω is the frequency.

The boundary integral equation, formulated in the frequency domain, can be constructed by applying the reciprocity theorem [31], leading to

a) along the exterior domain of inclusion (Medium 1):

$$\begin{aligned} b\hat{T}^{(1)}(x_0,y_0,\omega)=&\int_{S_3} q^{(1)}(x,y,\eta_n,\omega)G^{(1)}(x,y,x_0,y_0,\omega)\,ds\\ &-\int_{S_3} H^{(1)}(x,y,\eta_n,x_0,y_0,\omega)\hat{T}^{(1)}(x,y,\omega)\,ds \end{aligned}, \tag{2.3}$$

b) along the interior domain of inclusion (Medium 2):

$$b\hat{T}^{(2)}(x_0,y_0,\omega)=\int_{S_2+S_3} q^{(2)}(x,y,\eta_n,\omega)G^{(2)}(x,y,x_0,y_0,\omega)\,ds$$
$$-\int_{S_1+S_3} H^{(2)}(x,y,\eta_n,x_0,y_0,\omega)\hat{T}^{(2)}(x,y,\omega)\,ds-\int_{S_2} H^{(2)}(x,y,\eta_n,x_0,y_0,\omega)\hat{T}_0(x,y,\omega)\,ds, \tag{2.4}$$

In these equations, the superscripts (1) and (2) refer to the exterior and interior domains, η_n is the unit outward normal along the boundary, G and H are respectively the fundamental solutions (Green's functions) for the temperature $(\hat{T})$ and heat flux (q), at (x,y) due to a virtual point heat load at (x_0,y_0). The factor b is a constant defined by the shape of the boundary, taking the value 1/2 if the shape is smooth and $(x_0,y_0)\in S_1$ or $(x_0,y_0)\in S_3$.

The required Green's functions for temperature and heat flux in Cartesian coordinates are given by

$$G(x,y,x_0,y_0,\omega)=\frac{-\mathrm{i}}{4\lambda}H_0(k\,r), \tag{2.5}$$

$$H(x,y,\eta_n,x_0,y_0,\omega)=\frac{\mathrm{i}}{4\lambda}kH_1(k\,r)\frac{\partial r}{\partial \eta_n}, \tag{2.6}$$

In which $r=\sqrt{(x-x_0)^2+(y-y_0)^2}$, $k=\sqrt{-\mathrm{i}\omega/K}$ and $H_n(\;)$ are Hankel functions of the second kind and order n.

The final system of equations is assembled so as to ensure the continuity of temperatures and heat fluxes along S_3. This requires the discretization of the interface S into N straight boundary elements, with one nodal point at the middle of each element (N_1, N_2 and N_3 boundary elements along S_1, S_2 and S_3, respectively). The final integral equations are manipulated and combined so as to impose the continuity of temperatures and heat fluxes along S_3, null heat fluxes along S_1 and prescribed temperatures along S_2, to establish a system of $[(N_1+N_2+2N_3)\times(N_1+N_2+2N_3)]$ equations. The unknown nodal temperatures and heat fluxes are obtained by solving this system of equations so that the heat field in the domain can be defined.

The integrations in equations (2.3) and (2.4) are evaluated by means of a Gaussian quadrature scheme, using 8 points, when the element to be integrated is not the loaded element. For the loaded element, the existing singular integrands in the source terms of the Green's functions are calculated in closed form (see Tadeu *et al.* [32],[33]), as follows,

$$\int_0^{L/2} H_0(k\,r)dr = \frac{L}{2} H_0\left(k\frac{L}{2}\right) + \pi\frac{L}{4}\left[H_1\left(k\frac{L}{2}\right)S_0\left(k\frac{L}{2}\right) - H_0\left(k\frac{L}{2}\right)S_1\left(k\frac{L}{2}\right)\right], \tag{2.7}$$

$$\int_0^{L/2} H_1(k\,r)\frac{\partial r}{\partial \eta_n}dr = 0\ , \tag{2.8}$$

where $S_{ns}(\ldots)$ are Struve functions of order ns and L the boundary element length. The integrals $\int_0^{L/2} H_1(k\,r)\frac{\partial r}{\partial \eta_n}dr$ are zero because $\frac{\partial r}{\partial \eta_n} = 0$ along the loaded element.

2.3.2 1D analytical solutions for stratified mediums

Consider a system consisting of a set of m plane layers of infinite extent, as shown in Figure 2.3.

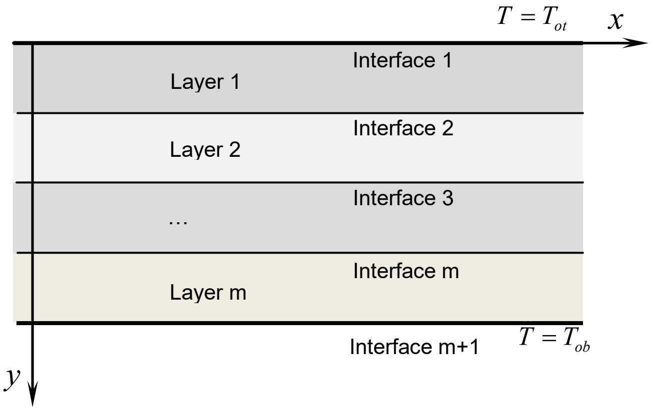

Figure 2.3: Multilayer system.

The temperatures T_{0t} and T_{0b} are imposed at the top and bottom external surfaces. The thermal material properties and thickness of the various layers may differ.

The solution is defined in the frequency domain as the superposition of plane heat sources. Thus, the temperatures T_{0t} and T_{0b} were first defined by applying a direct discrete fast Fourier transform to the imposed temperature variations in the time domain. As it is assumed that T_{0t} and T_{0b} do not vary along x , the problem becomes one-dimensional. The definition of the solution involves establishing surface terms at each interface. The total heat field is found by adding the sets of surface terms arising within each layer and at each interface that are required to satisfy the boundary conditions at the interfaces, i.e. continuity of temperatures and normal fluxes between layers (see [34]).

For the layer j , the heat surface terms on the upper and lower interfaces can be expressed as

$$\hat{T}_{j1}(y,\omega)=\frac{-\mathrm{i}}{2\lambda_j}\frac{e^{-\mathrm{i}k_j\left|y-\sum_{l=1}^{j-1}h_l\right|}}{k_j}A_j^t, \tag{2.9}$$

$$\hat{T}_{j2}(y,\omega)=\frac{-\mathrm{i}}{2\lambda_j}\frac{e^{-ik_j\left|y-\sum_{l=1}^{j}h_l\right|}}{k_j}A_j^b, \tag{2.10}$$

where $k_j=\sqrt{-\frac{\mathrm{i}\omega}{K_j}}$, λ_j is the thermal conductivity, ρ_j is the density, c_j is the specific heat of the material in the layer j and h_l is the thickness of the layer l.

A system of $2m$ equations is derived, ensuring the continuity of temperatures and heat fluxes:

$$\begin{bmatrix} \frac{1}{k_1\lambda_1} & \frac{\mathrm{e}^{-\mathrm{i}k_1h_1}}{k_1\lambda_1} & \ldots & 0 & 0 \\ \mathrm{e}^{-\mathrm{i}k_1h_1} & -1 & \ldots & 0 & 0 \\ \frac{\mathrm{e}^{-\mathrm{i}k_1h_1}}{k_1\lambda_1} & \frac{1}{k_1\lambda_1} & \ldots & 0 & 0 \\ \ldots & \ldots & \ldots & \ldots & \ldots \\ 0 & 0 & \ldots & -1 & \mathrm{e}^{-\mathrm{i}k_mh_m} \\ 0 & 0 & \ldots & -\frac{1}{k_1\lambda_m} & -\frac{\mathrm{e}^{\mathrm{i}k_mh_m}}{k_m\lambda_m} \\ 0 & 0 & \ldots & \frac{\mathrm{e}^{-\mathrm{i}k_mh_m}}{k_m\lambda_m} & \frac{1}{k_m\lambda_m} \end{bmatrix} \begin{bmatrix} A_1^t \\ A_1^b \\ \ldots \\ A_m^t \\ A_m^b \end{bmatrix} = \begin{bmatrix} T_{0t} \\ 0 \\ 0 \\ \ldots \\ 0 \\ 0 \\ T_{0b} \end{bmatrix}, \tag{2.11}$$

The resolution of this system gives the amplitude of the surface terms at each interface, leading to the following temperature fields at layer j :

$$\tilde{T}(y,\omega) = E_{0j} \left(\frac{e^{-\mathrm{i}k_j \left| y - \sum_{l=1}^{j-1} h_l \right|}}{k_j} A_{0j}^{t} + \frac{e^{-\mathrm{i}k_j \left| y - \sum_{l=1}^{j} h_l \right|}}{k_j} A_{0j}^{b} \right) \text{, if } \sum_{l=1}^{j-1} h_l < y < \sum_{l=1}^{j} h_l \tag{2.12}$$

2.3.3 Time domain

An inverse Fourier transform is applied in frequency domain to determine the heat responses in the spatial-temporal domain and a special procedure is followed to prevent the occurrence of aliasing. This procedure involves the use of complex frequencies that have a small imaginary part, $\omega_c = \omega - i\eta$ (where $\eta = 0.7\Delta\omega$ and $\Delta\omega$ is the frequency step). Care is needed to ensure that the constant η is not unduly large as this can seriously impair the numerical accuracy, or result in underflows and overflows when evaluating the exponential windows. The temperature amplitude can develop at various rates, while the frequency domain for which the BEM solution is to be calculated is determined by the time Fourier transform applied to the incident heat field:

$$\hat{T}_0(x,y,\omega) = \int_0^{\infty} T_0(x,y,t) e^{-\mathrm{i}\omega t}\, dt\,, \tag{2.13}$$

Responses ranging from 0.0 Hz to very high frequencies must be computed, but since the heat responses decay more rapidly the higher the frequency it is possible to set a limit on the upper frequency.

The final equation is given by

$$T(x,y,t) = \frac{1}{2\pi} \int_0^{\infty} \hat{T}_0(x,y,\omega) \hat{T}(x,y,\omega) e^{\mathrm{i}\omega t}\, d\omega\,, \tag{2.14}$$

which is computed as a discrete inverse fast Fourier transform.

2.4 Verification of the 2D BEM formulation

The BEM algorithm and the analytical solutions were both validated experimentally. A multilayer testing system was built from four square layers ($500.0 \times 500.0 \text{ mm}^2$) of different materials: moulded expanded polystyrene (EPS) 18.84 mm thick, medium-density fibreboard (MDF) 19.65 mm thick, cork (CN) 20.60 mm thick and EPS 19.86 mm thick. The thermal conductivity, the mass density and the specific heat of each material were characterized experimentally. The thermal conductivity was evaluated by the Guarded Hot-Plate Method (ISO 8302:1991 [35]) using a Lambda-Meßtechnik GmbH Dresden apparatus, single-specimen Lambda-meter EP-500 model, following the test procedure defined in EN 12667:2001 [36]. The mass density was determined using the procedure described in EN 1602:1996 [37]. The specific heat was obtained using a Netzsch apparatus, model DSC200F3, following the ratio method. Table 2.1 gives the averages of the thermal properties for the three materials used in the experiments.

Table 2.1: Materials' thermal properties.

Material	Thermal conductivity $\lambda\ \left(\text{W.m}^{-1}.^{\text{o}}\text{C}^{-1}\right)$	Density $\rho\ \left(\text{kg.m}^{-3}\right)$	Specific heat $c\ \left(\text{J.kg}^{-1}.^{\text{o}}\text{C}^{-1}\right)$
Cork board	0.046	130.00	1638.00
Molded expanded polystyrene (EPS)	0.041	14.30	1430.00
Medium-density fibreboard (MDF)	0.120	712.00	1550.00
Concrete	1.40	2300.00	880.00
External surface layer 3mm thick	0.075	1.29	1000.00
Internal surface layer 3mm thick	0.0231	1.29	1000.00

For the experimental measurements, the multilayer system was subject to an unsteady heat flow rate imposed at the external multilayer surfaces using the single-specimen Lambda-meter EP-500. Temperatures were recorded using a thermocouple set connected to a data logger system. The specimens tested were first pre-conditioned in a Fitoclima 300EC10 climatic chamber from Aralab, in a controlled environment with a set-point temperature of (23 ± 2) °C and (50 ± 5) % relative humidity, until constant mass was reached. The tests were carried out in a controlled laboratory environment with the same set points of temperature and relative humidity as those of the climatic chamber. Figure 2.4 gives a scheme of the measurements and the apparatus layout.

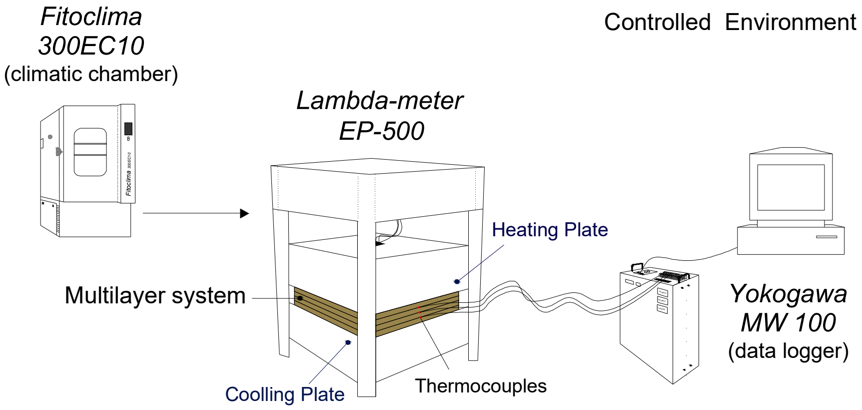

Figure 2.4: Scheme of the experimental layout

The single-specimen Lambda-meter EP-500 was first programmed to reach a mean temperature of 23 °C in the test specimen, establishing a 15 °C temperature difference between the heating and the cooling units. So, during the test, the temperature of the top multilayer surface (in contact with the heating plate unit) rose, while the temperature of the bottom multilayer surface (in contact with the lower plate) fell. The energy input was maintained until a permanent heat flow rate was reached, meaning that there is no temperature variation at the multilayer interfaces. The system then stopped heating and cooling until the initial temperatures were reached again.

The temperature variation at each interface layer was measured using T-type (copper) thermocouples made of wire with a diameter of 0.2 mm. Three thermocouples were placed at each system interface, including the top and bottom surfaces, respectively in contact with the heating and cooling plates (see Figure 2.3). The data were recorded using a Yokogawa MW 100 data logger, with a time interval of 10 seconds.

The temperatures T_{0t} and T_{0b} , required to run the proposed algorithms, were first defined by applying a direct discrete fast Fourier transform in the time domain to the temperatures recorded by the thermocouples on the external surfaces of the system and subtracting the initial temperature. Analysis of the experimental responses led to an analysis period of 16 h being established. This was enough to find the energy equilibrium of the multilayer system with the environment (temperatures at the interfaces almost restored to the initial test temperatures). The upper frequency of the analysis was defined such that its contribution to the global response is negligible.

The analytical computations were performed in the frequency domain for frequencies ranging from 0.0 Hz to $2048.0/(16\times3600)$ Hz, with a frequency increment of $1.0/(16\times3600)$ Hz, which determined a full analysis window of 16 h. In the BEM model, each horizontal interface, 500 mm long, is modelled with 100 constant boundary elements, while 10 boundary elements are used to discretize each lateral boundary where null fluxes are prescribed.

The temperature in the time domain was found by applying a discrete inverse fast Fourier transform in the frequency domain, as described above. The final temperatures were obtained by adding the initial test temperatures to these responses.

The results of the experimental measurements are presented below (Figure 2.5) and compared with those computed analytically and numerically (using the BEM).

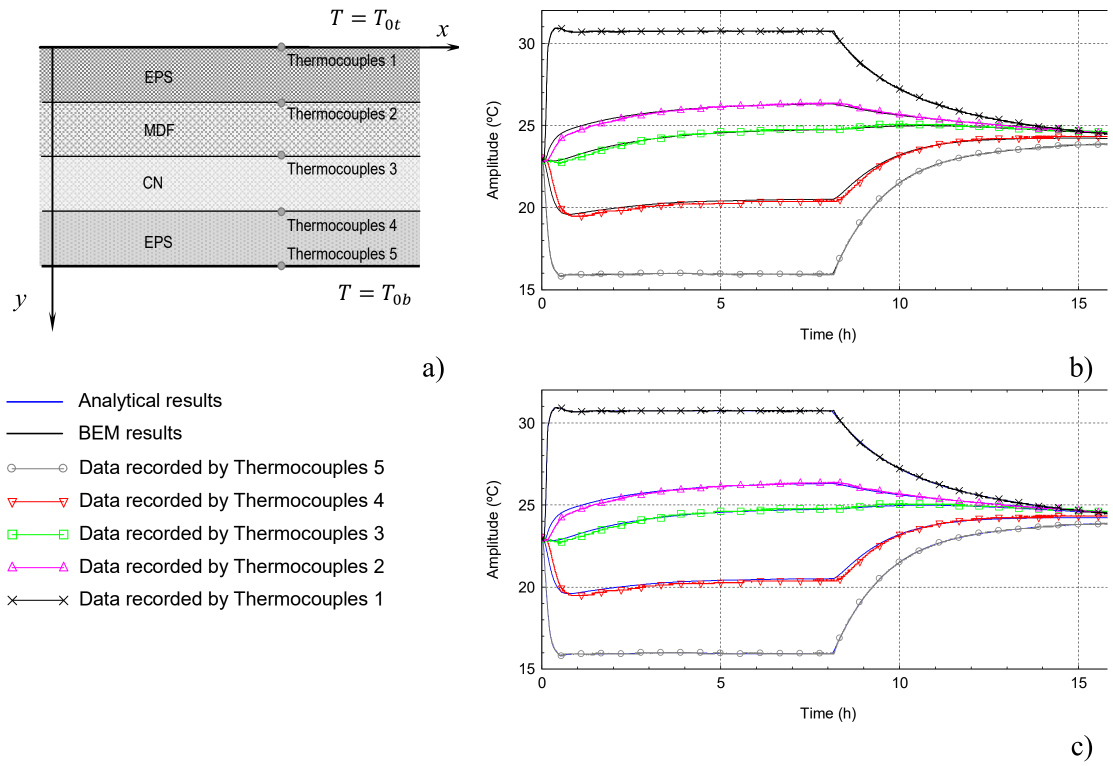

Figure 2.5: Multilayer algorithm validations: a) multilayered system; b) BEM versus experimental results; c) analytical versus experimental results.

In the figures, the solid lines are the analytical and BEM responses and the experimental results are represented by the lines with marked points. The experimental results plotted at each interface correspond to the arithmetic mean of three thermocouple temperatures. Comparison of the results shows that the analytical and the BEM solutions agree with the experimental ones.

In addition, the accuracy of the BEM solution has been studied by computing the response for a different number of boundary elements. Figure 2.6 gives the errors obtained at the receivers placed in the middle of the interface between the NC and the EPS layers (where thermocouple 4 was positioned) when the system is excited with a frequency of 2.6725×10^{-3} rad/s. For this frequency $T_{0t} = (-90.7495 - \mathrm{i}\ 27.6114)$ °C and $T_{0b} = (64.2377 + \mathrm{i}\ 11.1006)$ °C. Figure 2.6 shows the absolute value (magnitude) of the real and imaginary parts of the difference between the BEM response and the analytical result $(17.6039 - \mathrm{i}\ 10.2668)$ °C. To better illustrate the results the errors are plotted on a log scale. The results confirm that the results very quickly approach the analytical solution as the number of boundary elements increases. For a number of boundary elements greater than 300, the error is close to 10^{-7} °C, which illustrates the good accuracy of the responses.

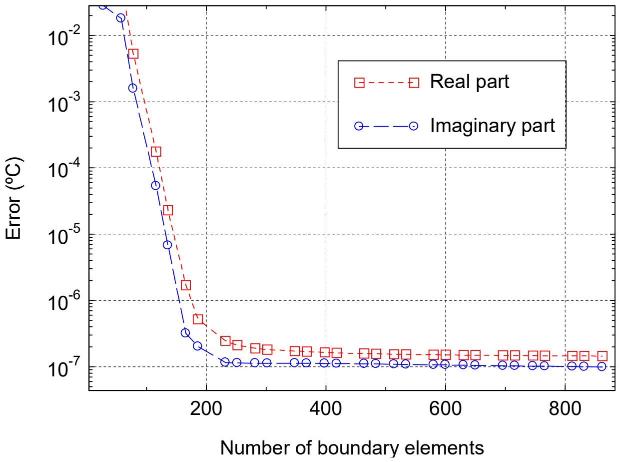

Figure 2.6: Variation of the BEM error with the number of boundary elements.

2.5 Numerical application

In order to illustrate the applicability of the proposed BEM model, the heat transfer across a 2D building corner, corresponding to a geometrical LTB, was simulated. To account for convection and radiation phenomena the surfaces' thermal resistance was modelled as thin air layers on the inner and outer surfaces [38]. Figure 2.7 illustrates the physical model of the problem.

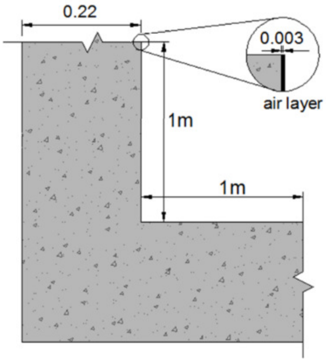

Figure 2.7: Wall geometry used in the numerical applications – concrete wall without thermal insulation (dimensions in m).

The corner is modelled as adjacent lateral walls long enough to ensure that the heat transfer at the cut-off sections is not affected by the presence of the LTB associated with the walls junction. This procedure allows 1D heat fluxes at those extremities. So, null heat fluxes can be prescribed along those cut-off sections, in their normal directions. In this case study, the length of the wall was taken to be 1.0 m, as recommended in ISO 10211:2007 [1]. The material's thermal properties are those of the concrete and are listed in Table 2.1.

The wall system was assumed to have a uniform temperature of 20 °C throughout the domain at $t = 0.0\ \text{s}$. At $t = 0.0\ \text{s}$ it was subjected to an exterior temperature change, as illustrated in Figure 2.8.

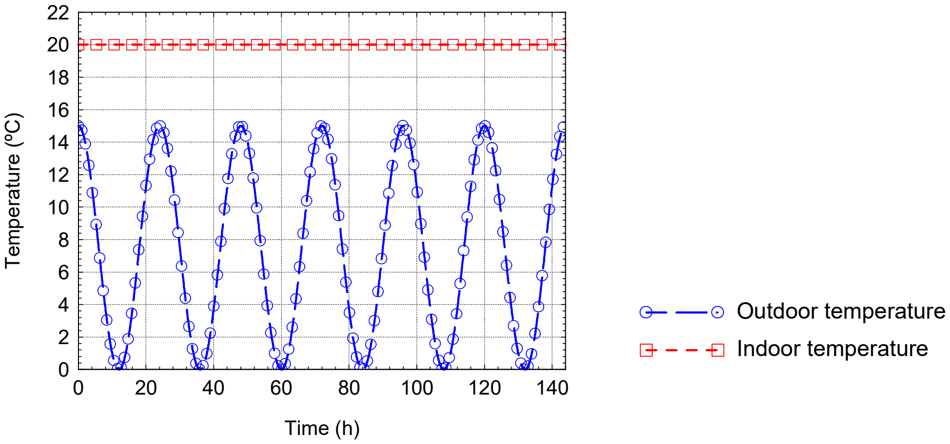

Figure 2.8: Imposed temperatures over time: sinusoidal change in the outdoor environment temperature (6 cycles of 24h); constant indoor temperature.

The temperature time dependence was assumed to be sinusoidal, with a period of 24 hours, and with amplitude oscillations of 15 °C. The indoor temperature was kept at 20 °C. The analysis simulates 6 cycles in order to allow the system response to start behaving almost in a 24 hour cycle.

The frequency domain of computation ranged from 0.0 Hz to $4096/(144\times 3600)$ Hz, with a frequency increment of $1.0/(144\times 3600)$ Hz, which determined a total time window of 144 h for the analysis.

The wall's longitudinal material interfaces were discretized by 100 constant boundary elements, while 60 constant boundary elements were used to model the lateral cut-off sections. The temperature distribution is obtained at a very fine two-dimensional grid of receivers equally spaced along the x and y directions.

A set of snapshots of the time domain simulations is presented to illustrate the resulting heat diffusion across the LTB. Figure 2.9 shows the temperature field distribution at different time instants (a) $t \approx 6.0$ h, b) $t \approx 12.0$ h, c) $t \approx 18.0$ h, d) $t \approx 24.0$ h and e) $t \approx 30.0$ h).

A colour scale is used in the plots, with the dark red and blue shades corresponding respectively to the higher and the lower temperatures.

It can be seen that the surface temperatures near the corner tend to be lower when compared with the surface temperatures in the walls. At $t \approx 18.0$ h (Figure 2.9 c)), the thermal phase lag in the LTB is clearly evidenced, since the exterior temperature had already increased from 0 ºC to 7.5 ºC and the temperature in middle of the corner domain was still decreasing. It is interesting to note that in the last snapshot, which was taken at $t \approx 30.0$ h (Figure 2.9 e)), the exterior temperature change had already started a new cycle. It had again reached 7.5 ºC. The temperature distribution differed from that registered at the same phase $t \approx 6.0$ h. This was because at $t = 0.0$ h the wall system registered a uniform temperature of 20 ºC.

As the time passed, the system tended to behave periodically and exhibits similar temperature and flux distribution for equivalent phases.

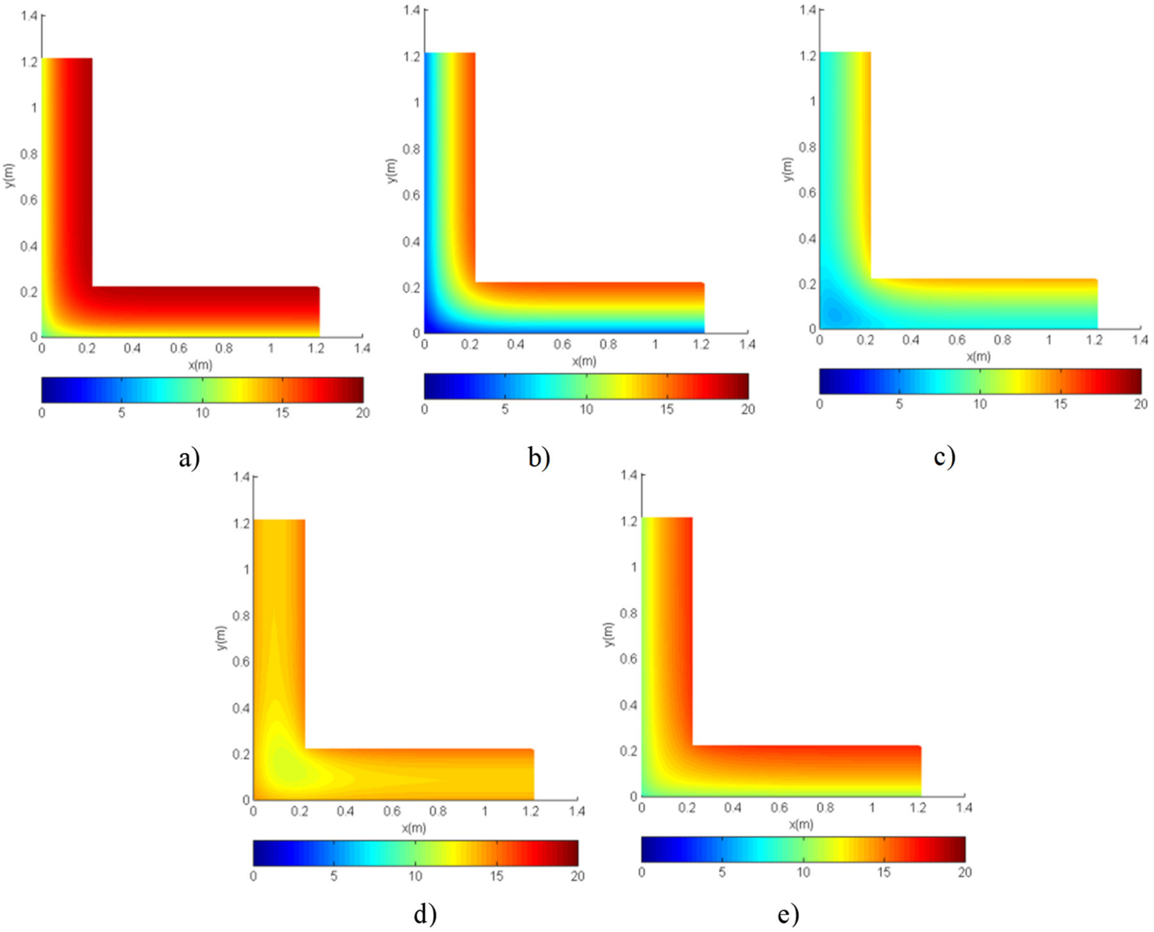

a) b) c)

d) e)

Figure 2.9: Temperature distribution (in °C) across the 2D concrete building corner. Time responses at a) $t \approx 6.0$ h ; b) $t \approx 12.0$ h ; c) $t \approx 18.0$ h ; d) $t \approx 24.0$ h ; and e) $t \approx 30.0$ h .

The linear thermal transmittance was computed using the heat fluxes registered at the interior surface. As the problem is dynamic, the position of the line over which the global heat flux is computed is determinant, since it leads to distinct values because of the thermal delay effects. In this work, the inner surface was selected because this is where moisture condensation and pathologies often occur, and because it is this wall surface that is relevant to evaluating the heat flow. The global heat flow rate (ϕ_{total}), in $\mathrm{W/m}$, was computed for the total system. The heat flow rate through the two walls (ϕ_{walls}), in $\mathrm{W/m}$, was calculated by imposing 1D heat transfer on the lateral walls, using the analytical model proposed in section 2.3.2.

Figure 2.10 a) presents the difference of these interior global heat fluxes $\phi_{total} - \phi_{walls}$. Figure 2.10 b) presents the dynamic linear thermal transmittance computed by dividing these values by the amplitude difference (ΔT) between the internal and the external environments, at the corresponding time $\frac{\phi_{total} - \phi_{walls}}{\Delta T}$. It can be seen that, as the time passed, the heat flux curves have a cyclic behaviour. The absolute heat flux amplitude in the LTB is about 1.6 W/m and 0.5 W/(m.ºC), ranged between 1.9 W/m and 3.5 W/m and between 0.10 W/(m.ºC) and 0.60 W/(m.ºC), respectively.

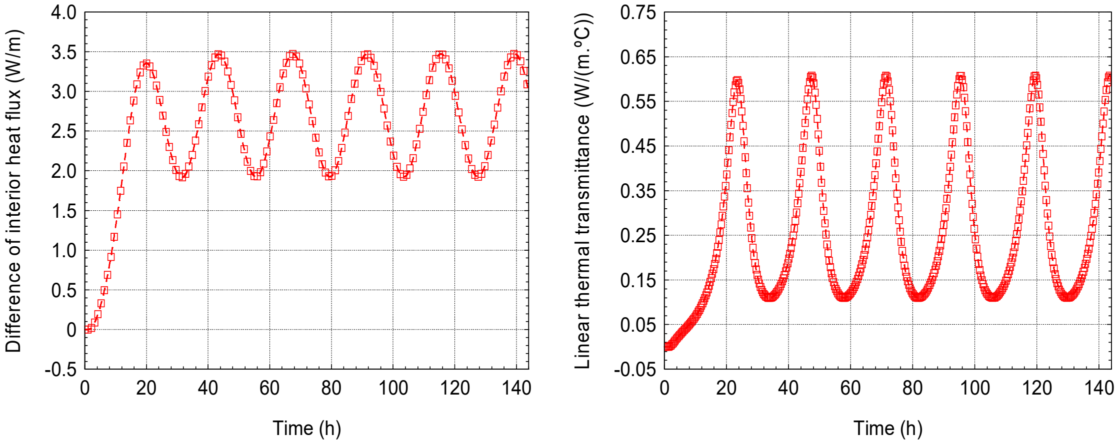

Figure 2.10: Dynamic behaviour of the LTB: a) difference of interior global heat fluxes $\phi_{total} - \phi_{walls}$;

b) Dynamic linear thermal transmittance $\frac{\phi_{total} - \phi_{walls}}{\Delta T}$.

2.6 Conclusions

This chapter has described a 2D Boundary Element Method (BEM) formulation, in the frequency domain, for the computation of the dynamic behaviour of Linear Thermal Bridges (LTBs) of buildings, allowing the simulation of transient states for which the external and internal temperatures may vary over time. The BEM formulation was verified against analytical solutions known for stratified mediums, by comparing the results obtained for a multilayer system wall. The two algorithms were validated experimentally. The experimental results showed a very good agreement with the numerical and analytical calculations.

In order to demonstrate the applicability of the proposed methodology, a numerical application was performed to simulate the transient heat diffusion through a 2D building corner subjected to a sinusoidal external temperature variation over time. The 2D BEM model and the 1D analytical solution, both formulated in the frequency domain, were used together to compute the heat fluxes through the LTB, over time. Time solutions were then obtained by applying inverse Fourier transformations. The two algorithms were found to be suitable for computing the linear thermal transmittances under dynamic conditions.

References

[1] International Organization for Standardization, ISO 10211: Thermal bridges in building construction - Heat flows and surface temperatures - Detailed calculations, 2007.

[2] T. Theodosiou, A. Papadopoulos, The impact of thermal bridges on the energy demand of buildings with double brick wall constructions, Energy and Buildings 40 (2008) 2083-2089.

[3] M.H. Corvacho, Pontes térmicas, análise do fenómeno e proposta de soluções, PhD thesis, Faculdade de Engenharia da Universidade do Porto, Portugal, 1996.

[4] M. Krarti, Heat Loss and moisture condensation for wall corners of buildings, International Journal of Heat and Mass Transfer, 41(4-5) (1998) 681-689.

[5] H. Erhorn, H. Erhorn-Klutting, M. Citterio, M. Cocco, D. Orshoven, A. Tilmans, P. Schild, P. Bloem, K.E. Thomsen, J. Rose, An effective handling of thermal bridges in the EPBD context, final report of the IEE ASIEPI work on thermal bridges, March 2010.

[6] International Organization for Standardization, ISO 13790, Energy performance of buildings - Calculation of energy use for space heating and cooling, 2008.

[7] J. Kosny, E. Kossecka, Multi-dimensional heat transfer through complex building envelope assemblies in hourly energy simulation programs, Energy and Buildings 34 (2002) 445-454.

[8] Portuguese Law no. 58/2013, 20th August 2013 – directive 349-D/2013, 2 December 2013.

[9] H. Ge, F. Baba, Dynamic effect of thermal bridges on the energy performance of a low-rise residential buildings, Energy and Buildings 105 (2015) 106-118.

[10] F. Déqué, F. Ollivier, JJ. Roux, Effect of 2D modelling of thermal bridges on the energy performance of buildings: numerical application on the Matisse apartment, Energy and Buildings 33(6) (2001) 583-7.

[11] Y. Gao, J.J. Roux, L.H. Zhao, Y. Jiang, Dynamical building simulation: A low order model for thermal bridges losses, Energy and Buildings 40 (2008) 2236-2243.

[12] G. Mao, G. Johannesson, "Dynamic calculation of thermal bridges". Energy and Buildings 26 (1997) 233-240.

[13] A.C. Andersson, G. Johannesson, Application of frequency responses for fast analysis of two-dimensional heat-flow problems, Coden LUTVDDG/(TVBH-7072)/1-8, Lund, Sweden, 1983.

[14] International Organization for Standardization, ISO 13786: Thermal performance of building components - Dynamic thermal characteristics -Calculation methods, 2006.

[15] E. Kossecka, J. Kosny, Equivalent wall as a dynamic model of a complex thermal structure, Journal of Thermal Insulation and Building Envelopes 20 (1997) 249-268.

[16] K. Martin, C. Escudero, A. Erkoreka, I. Flores, J.M. Sala, Equivalent wall method for dynamic characterisation of thermal bridges, Energy and Buildings 55 (2012) 704–714.

[17] F. Aguilar, J.P. Solano, P.G. Vicente, Transient modeling of high-inertial thermal bridges in buildings using the equivalent thermal wall method, Applied Thermal Engineering 67 (1-2) (2014) 370-377.

[18] G.H. Santos, N. Mendes, P.C. Philippi, A building corner model for hygrothermal performance and mould growth risk analyses, International Journal of Heat and Mass Transfer 52 (21-22) (2009) 4862–4872.

[19] F. Ascione, N. Bianco, F. D. Rossi, G. Turni, G. P. Vanoli, Different methods for the modelling of thermal bridges into energy simulation programs: Comparisons of accuracy for flat heterogeneous roofs in Italian climates, Applied Energy (2012) 1-14.

[20] TRNSYS - A transient System Simulation Program, Madison, Solar Energy Laboratory University of Wisconsin, Madison, WSA, 1990.

[21] D. Bonneau, FX. D. Rongere, Covalet, B. Gautier, Clim 2000: modular software for energy simulation in buildings, in: Proceedings of the IBPSA Third International

Conference on Building Simulation'93, University of Adelaide, Australia, August, pp. 85-91, 1993.

[22] F. Ascione, N. Bianco, R.F.D. Masi, F. Rossi, G.P. Vanoli, Simplified state space representation for evaluating thermal bridges in building: Modelling, application and validation of a methodology, Applied Thermal Engineering 61 (2013) 344-354.

[23] F. Ascione, N. Bianco, G. M. Mauro, M. Musto, G. Turni, G. P. Vanoli, Experimental validation of a numerical code by thin film heat flux sensors for the resolution of thermal bridges in dynamic conditions, Applied Energy 124 (2014) 213-222.

[24] M.N. Ozisik, Finite Difference Methods in Heat Transfer. CRC Press Inc, USA, 1994.

[25] Gh. Juncu, Unsteady conjugate forced convection heat/mass transfer from a finite flat plate, International Journal of Thermal Sciences 47 (2008) 972–984.

[26] K.J. Bathe, Numerical methods in finite element analysis. Prentice-Hall, New Jersey, 1976.

[27] Z. Cai, J. Mandel, S. McCormick, The finite volume element method for diffusion equations on general triangulations, SIAM Journal on Numerical Analysis 28 (1991) 392-403.

[28] C.A. Brebbia, J.C. Telles, L.C. Wrobel, Boundary elements techniques: theory and applications in engineering. Springer-Verlag, Berlin-New York, 1984.

[29] Y. Ochiai, Steady heat conduction analysis in orthotropic bodies by triple-reciprocity BEM, Computer Modeling in Engineering and Sciences 2 (4) (2001) 435-446.

[30] A.I. Abreu, A. Canelas, W.J. Mansur, A CQM-based BEM for transient heat conduction problems in homogenous materials and FGMs, Applied Mathematical Modelling 37 (2013) 776-792.

[31] L.C. Wrobel, CA. Brebbia, A formulation of the boundary element method for axisymmetric transient heat conduction, International Journal of Heat and Mass Transfer 24 (1981) 843-850.

[32] A. Tadeu, P. Santos, E. Kausel, Closed-form integration of singular terms for constant, linear and quadratic boundary elements - Part I: SH wave propagation, EABE - Engineering Analysis with Boundary Elements 23-(8) (1999) 671-681.

[33] A. Tadeu, P. Santos, E. Kausel, Closed-form integration of singular terms for constant, linear and quadratic boundary elements - Part II: SV-P wave propagation, EABE - Engineering Analysis with Boundary Elements 23-(9) (1999) 757-768.

[34] A. Tadeu, N. Simões, Three-dimensional fundamental solutions for transient heat transfer by conduction in an unbounded Medium, half-space, slab and layered media, Engineering Analysis with Boundary Elements 30-(5) (2006) 338–349.

[35] International Organization for Standardization, ISO 8302: Thermal insulation – Determination of steady-state thermal resistance and related properties – Guarded hot plate apparatus, 1991.

[36] European Standards, EN 12667: Thermal performance of building materials and products. Determination of thermal resistance by means of guarded hot plate and heat flow meter methods. Products of high and medium thermal resistance, 2001.

[37] European Standards. EN 1602: Thermal insulating materials, Thermal insulation, Construction materials, Density measurement, Bulk density, Test specimens, Testing conditions, Buildings, 1996.

[38] International Organization for Standardization, ISO 6946: Building components and building elements - Thermal resistance and thermal transmittance - Calculation method, 2007.

CHAPTER 3

EXPERIMENTAL VALIDATION OF THE FREQUENCY DOMAIN BEM MODEL FOR THE 2D DYNAMIC SIMULATION OF LINEAR THERMAL BRIDGES OF BUILDINGS

3 EXPERIMENTAL VALIDATION OF THE FREQUENCY DOMAIN BEM MODEL FOR THE 2D DYNAMIC SIMULATION OF LINEAR THERMAL BRIDGES OF BUILDINGS

3.1 Introduction

The improvement of building energy simulations depends on the development of new models to evaluate the thermal behaviour of linear thermal bridges (LTBs). Those models must have the capacity to predict the thermal performance of materials that are subjected to temperature variations over time. The validation of those models using experimental measurements is of major interest. Furthermore, the linear thermal bridge (LTB) effect depends on factors such as geometry, the material properties, the environment temperature variations ([1],[2]) as well as the convective and radiative heat transfer effect near the surface ([3],[4]). Normally, the complexity of considering all these factors in the dynamic numerical simulation of an LTB requires the adoption of simplifying assumptions, such as assuming that some of these factors do not vary with the temperature. This is why it is extremely important to have experimental results that can be used in the validation phase of the numerical simulation tools. These results can be obtained using in situ or laboratory measurements of the real dynamic behaviour of the LTB.

The in situ quantitative evaluation of the thermal behaviour of building elements and their assemblies is normally performed with heat flux and temperature sensors ([5]-[8]). Cuce *et al.* [9] used such sensors to evaluate the impact of internal aerogel retrofitting on the thermal bridging effect of a residential building envelope. Ascione *et al.* [10] used experimental in situ data to evaluate the thermal behaviour of a building corner. The results were used to validate a dynamic simplified methodology proposed by the authors, based on the conduction transfer function methods. Corvacho [11] performed measurements of the dynamic thermal behaviour of different types of LTB, using two test cells with well-known constructive details. The experimental results were used to evaluate the dynamic hygrothermal behaviour of each LTB and also to validate a numerical modelling tool.

Laboratory tests might be more advantageous than in situ measurements, since it is possible to control and measure some of the factors that can significantly influence the thermal performance of the building elements and LTB. Another great advantage of performing tests in laboratory is that repeatability tests can be carried out under the same measurement conditions to determine the precision of the equipment, and thus to assess the confidence level of the tests. It is also possible to repeat the same test conditions in other specimens in order to obtain comparable results.

The hot box method [12] is one of the most suitable method to evaluate the thermal behaviour of building components. It is normally used to experimentally determine the thermal transmittance of building components (such as walls and windows) under steady-state conditions ([13],[14]). However, some experimental simulations of plane thermal bridges have been carried out in laboratory settings using hot box testing facilities under dynamic conditions. Martin *et al.* [15] presented a dynamic testing method that uses a guarded hot box to determine the response factors of a wall. The method was validated with a two-dimensional (2D) finite volumes model. The results show a good agreement between the two methods. The guarded hot box was also used by Martin *et al.* [16] to analyse the thermal behaviour of a pillar thermal bridge. A series of dynamic tests were performed to obtain amplitude values and the phase lag of the internal heat flux. Mao [17] performed laboratory measurements on the dynamic thermal performance of an insulated concrete sandwich structure with wooden studs. The experimental results were compared to the results obtained using a ∏-link RC network method. The steady-state deviation for the total thermal resistance was about 2 % over a measuring period of ten days.

In the European Union, hot box tests may be built in accordance with ISO 8990:1994 [12], and the test procedures are given by different European standards ([18]-[22]). According to ISO 8990:1994, these tests can follow two alternative methods: the calibrated hot box method and the guarded hot box method. In the calibrated hot box, the two chambers are constructed with high thermal resistance walls made using an insulation material to minimize the heat loss by conduction to the exterior. To quantify the box wall heat loss as well as the flanking heat loss, several calibration tests are performed for a wide range of environmental temperatures, using calibration panels with a known thermal resistance range. In the guarded hot box, a metering box that envelops a great part of the specimen on the hot side is surrounded by a guard box with controlled environment. The temperature and air movement inside and outside of the metering box must be controlled to prevent unexpected heat loss through the metering box walls. The main difference between this method and the calibrated hot box method is that no calibration is required. The measured area of the specimen is smaller than in the calibrated hot box, making this latter apparatus better for the analysis of non-regular specimens, such as a building corner.

In this research work, a calibrated hot box is therefore used to evaluate the dynamic thermal performance of a building corner, representing a geometrical LTB. The hot box measurements are then used to validate the 2D BEM model developed under this research work [23] and presented in Chapter 2). The building corner specimen is made by two cross laminated timber (CLT) panels, to minimize the thermal bridging effects caused by structural heterogeneities. Preliminary tests are first performed to calibrate and verify the precision of the measuring equipment and the capabilities and reliability of the apparatus. Then, the wooden corner specimen is placed between the two hot box chambers. The temperature set point of the hot chamber is constant and the temperature of the cold chamber varies. The heat flux across the LTB and the surface temperature variation are registered by heat flux sensors and thermocouples, respectively. The heat responses near the corner are compared with the ones at the adjacent plane walls (centre of the wood panels). Finally, the experimental measurements are compared with the numerical results obtained with the 2D BEM formulation.

3.2 Description of the calibrated hot box apparatus and measurement devices

The present section presents the experimental campaign proposed to evaluate the dynamic thermal performance of a wooden corner joint. The calibrated hot box apparatus and the measuring equipment specifications are described.

The calibrated hot box apparatus was designed as specified in ISO 8990:1994 [12]. In this method, the specimen is placed in a suitable surround panel (EPS panel) between two chambers, one hot and the other cold, in order to promote the heat transfer through the specimen. Both chambers have thermally insulated walls about 15 cm thick to prevent heat loss between the internal and the external environments. The walls are coated with stainless steel inside and PVC outside. Two thermally insulated doors allow access to the inside of each chamber. Figure 3.1 gives a scheme of the calibrated hot box apparatus layout.

The chambers have an opening at the end, for the hot chamber to be coupled to a heating system and the cold chamber to a climatic chamber (Fitoclima 1000 by Aralab), which will provide the desired test temperature inside the boxes. The climatic chamber can work for a wide range of temperatures [-80; 180] °C. A set of fans inside the cold chamber control the air flow velocity during the tests.

The hot box apparatus is inside a room with controlled laboratory environment (set point of 20 ºC).

Measuring equipment specifications

The internal surface temperatures of the specimen are recorded using a thermocouple (T type) set, made of wire, with a diameter less than 0.25 mm, connected to a data logger system (Agilent 34980A). The uncertainty of each T-type thermocouple is ± 0.16 ºC, and they are suited for measurements in the −200 to 350 °C range. The thermocouples and the data acquisition system were accurately calibrated before the laboratory tests (see section 3.4). The temperature responses measured by the thermocouples during the tests are recorded at a time interval of 1 minute.

The heat flow through the specimen is measured by three ultrathin flat plate heat flux sensors and the HFP01 heat flux sensors [24] of a high-accuracy thermal resistance measuring system (TRSYS01) [25] from Hukseflux.

The ultrathin flat plate heat flux sensors consist of thermoelectric panels laminated between flexible heterogeneous plastic layers.

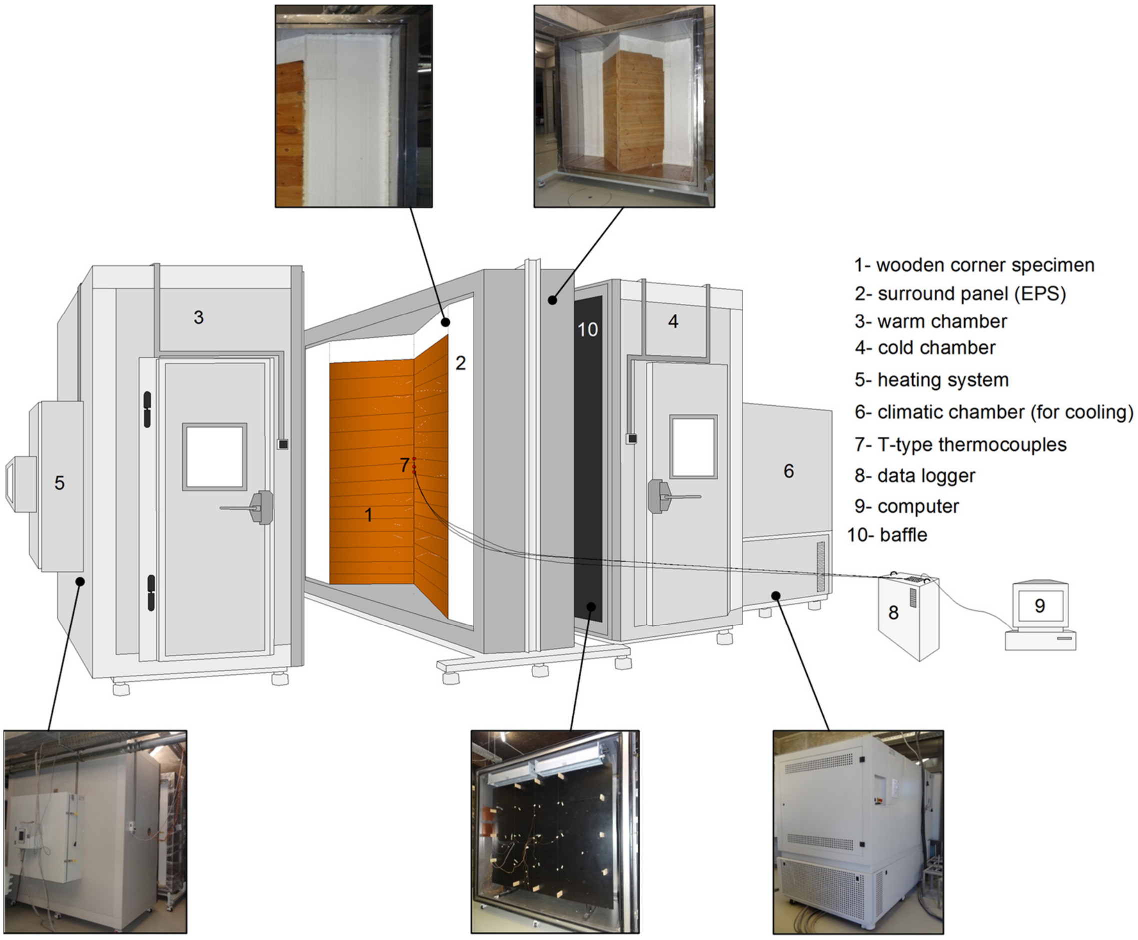

Figure 3.1: Calibrated hot box: apparatus components.

The TRSYS01 is a measurement system that analyses the thermal resistance and thermal transmittance of building elements by in situ measurement. The system includes two thermocouple pairs and two HFP01 heat flux plates. The sensor in HFP01 is a thermopile, which measures the differential temperature across the ceramic-plastic composite body of HFP01. HFP01 generates a small output voltage proportional to the local heat flux. The heat flux is then calculated by dividing the voltage by the sensitivity of the instrument. The accuracy of the sensors is ± 5 %. The TRSYS01 data are recorded by a GL820 Midi DataLogger at a time interval of 10 min. The two pairs of thermocouples from the TRSYS01 system are also used in the experimental tests to register the surface temperature on both sides of the specimen. The accuracy of each TRSYS01 thermocouple is ± 0.1 ºC and they are suitable for measurements in the -30 to 70 °C range.

3.3 Description of the specimen and the laboratory procedure

The specimen is composed of two cross laminated timber (CLT) panels (Figure 3.2) bonded together to simulate the dynamic thermal behaviour of a wooden building corner, representing an LTB (wall to wall junction). The CLT panels consist of several layers of structural lumber boards stacked crosswise and glued together. They are used to build walls, floors and roofs. The CLT panels used in this research were composed of seven layers. The total thickness of each panel is 0.18 m, the width is 1 m and the length is 2.15 m.

Figure 3.2: Cross Laminated Timber (CLT) panel [26].

The thermal conductivity, the mass density and the specific heat of the CLT material were experimentally determined. The thermal conductivity was evaluated by the guarded hot plate method (ISO 8302:1991 [27]) using a single-specimen Lambda-meter, EP-500 model, from Lambda-Meβtechnik GmbH Dresden, following the test procedure defined in EN 12667:2001 [28]. The mass density was determined using the procedure described in EN 1602:1997 [29]. The specific heat was obtained using a Netzsch (DSC200F3) apparatus, following the ratio method. These tests were carried out at ITeCons - Institute for Research and Technological Development in Construction, Energy, Environment and Sustainability. For each test procedure, five tests were performed using different specimens.

Table 3.1 gives the average value and standard deviation obtained for each CLT thermal property.

Table 3.1: CLT panels' thermal properties.

Material	Thermal conductivity $\lambda\ (\mathrm{W.m^{-1}.^{o}C^{-1}})$		Density $\rho\ (\mathrm{kg.m^{-3}})$		Specific heat $c\ (\mathrm{J.kg^{-1}.^{o}C^{-1}})$	
CLT	average	standard deviation	average	standard deviation	average	standard deviation
	0.13	0.003	574.69	35.63	1406.60	114.43

Figure 3.3 illustrates the wooden corner representing an LTB (wall to wall junction). The cold chamber of the hot box represents the external environment and the warm chamber represents the indoor environment. The external surface of the walls was subjected to a temperature variation $(T = T(x, y, t))$, while the indoor temperature was assumed to be constant $(T = T_0)$.

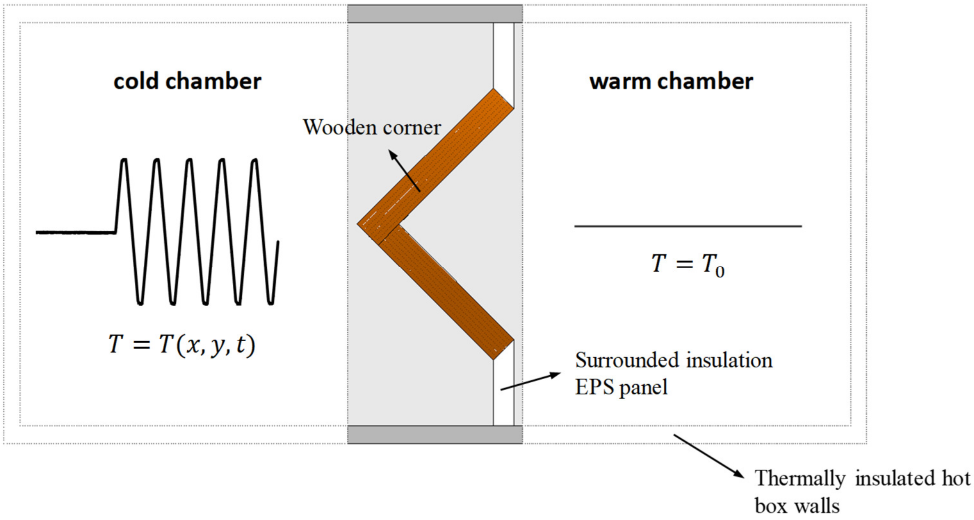

Figure 3.3:Wooden building corner scheme and boundary conditions of the problem – schematic plan view.

In the early stage of the tests, over a period between $t = 0.0$ h and $t = 48.0$ h, the set point temperature inside the hot and the cold chambers were kept constant (20 °C and 0 °C, respectively) to reach steady state up to the first time step of the dynamic simulations at $t = 48.0$ h. At $t = 48.0$ h the temperature inside the cold chamber started to vary. The temperature time dependence followed a sinusoidal evolution, with a period of 24 hours, and with amplitude oscillations of 20 °C, ranging between -10 °C and 10 °C, as illustrated in Figure 3.4. The temperature set point inside the warm chamber was kept at 20 °C. However, since the heating system used in the warm chamber does not allow cooling, the temperature inside the chamber ranged between 19.5 °C and 20.5 °C, without ever stabilizing at 20 °C. The real temperature registered inside the warm chamber is given in Figure 3.4. The experimental simulation comprised 5 cycles.

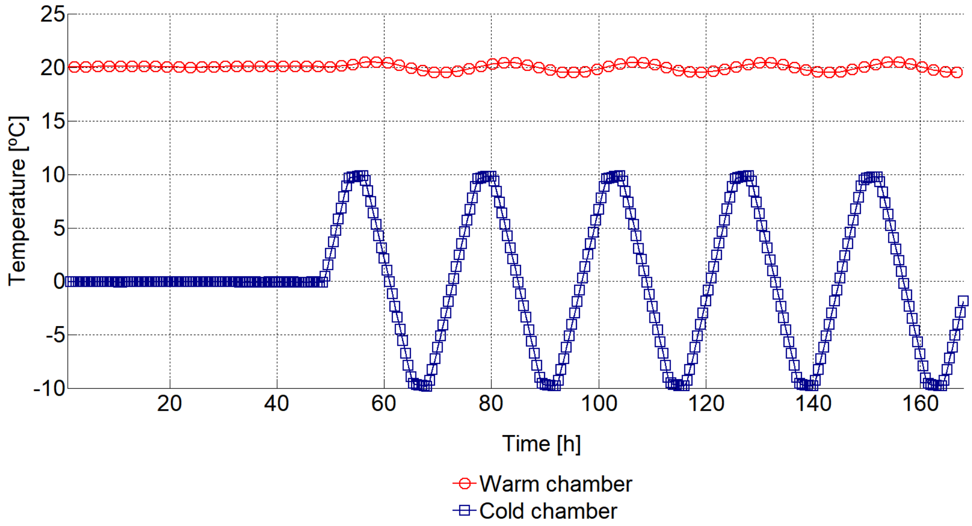

Figure 3.4: Imposed temperature over time: sinusoidal change in the cold chamber temperatures (5 cycles of 24 h); imposed temperature inside the warm chamber.

A set of 44 thermocouples were placed in a line up to about 0.6 m from the corner. The thermocouples were fixed to the surface using adhesive tape with an outer surface of high emissivity (> 0.8), without influencing the measurement of the surface temperatures.

The heat flux through the wall (centre of the panel) was measured on both sides of the specimen by the three ultrathin flat plate heat flux sensors. The heat flux through the LTB (near the corner) was measured on both sides of the specimen by the two HFP01 heat flux sensors of TRSY01 system. The internal surface temperatures at the LTB and at the centre of the panel, on the warm side of the specimen, was registered using the line of T-type thermocouples and one pair of TRSYS01 thermocouples (TC12 and TC11, respectively). The other pair of TRSYS01 thermocouples (TC21 and TC22) was used to measure the surface temperatures at the LTB and at the centre of the panel on the cold side of the wooden corner.

Figure 3.5 gives a scheme of the sensors layout.

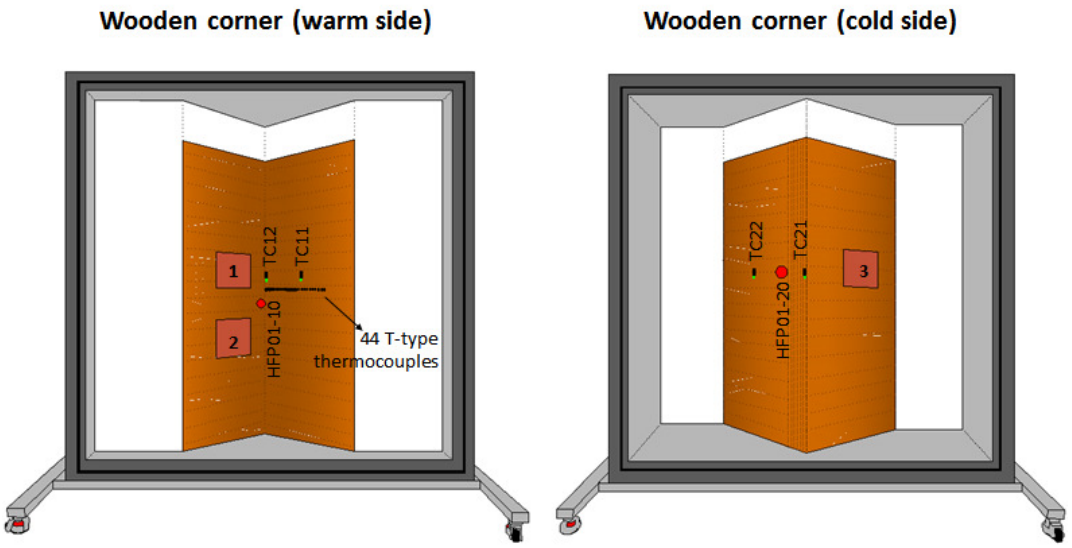

Figure 3.5: Scheme of the sensors layout (1, 2 and 3 -ultrathin plate heat flux sensors; HFP01-10 and HFP01-20 – TRSY01 heat flux sensors; TC11, TC12, TC21 and TC22 – TRSY01 thermocouples).

3.4 Verification of the measurement sensors

Before the experimental test of the wooden building corner some preliminary tests were carried out to determine the errors associated with the experimental measurements and to evaluate the measuring equipment in terms of reliability and reproducibility. The results of the equipment calibration and verification of the sensors are now presented.

T-type thermocouples calibration

The T-type thermocouples were calibrated by immersion at 150 mm depth in a liquid bath temperature calibrator. The temperature value measured by each sensor was compared with a reference value measured by a standard platinum resistance temperature detector (provided by a calibration laboratory in physical metrology). The difference between the two measurements gives the error of each sensor. The measurements were performed under 3 different environment conditions (20 ºC, 10 ºC and 0 ºC). The calibration was done in a controlled room environment under a temperature of 20 ± 2 ºC and 50 ± 5 % relative humidity.

The results of this calibration procedure are presented in Table A1 in Appendix A. The uncertainty of the sensors' calibration is ± 0.16 ºC. Linear regressions were performed to determine the calibration function for each thermocouple. These functions allowed the measurement deviation of each sensor to be corrected at each instant of the laboratory tests. The maximum error registered was 0.4 ºC.

Verification of the TRSY01 system

The TRSY01 measuring system was checked using the Guarded Hot Plate Method [27]. A Lambda-Meßtechnik GmbH Dresden, single-specimen Lambda-meter EP-500 model was used. The test procedure followed was that defined in EN 12667:2001 [28].

Figure 3.6 gives two photographs of the apparatus layout.

Figure 3.6: TRSY01 system check using a single specimen Lambda-meter EP-500 (Guarded Hot Plate Method) – apparatus layout.

The test specimen used was composed of two polyethylene foam boards measuring 500x500 mm^2, and thickness between 51.2 and 51.7 mm. It was first pre-conditioned in a Fitoclima 300EC10 climatic chamber (Aralab), in a controlled environment with a set-point temperature of 23 ± 2 ºC and 50 ± 5 % relative humidity, until constant mass was reached. The tests were carried out in a controlled laboratory environment with same set-point temperature and relative humidity conditions as those of the climatic chamber.

The heat flux HFP01-10 sensor and the pair of thermocouples TC11 and TC12 from the TRSY01 system were placed in the centre of the interface between the two foam boards, as shown in Figure 3.6. This setup was then placed between the two plates of the single-specimen Lambda-meter EP-500 (a heating plate above and a cooling plate below). The system was subjected to the heat flow rate imposed at the external surfaces due to the temperature gradient caused by the two plates. The energy input was maintained until a permanent heat flow and a constant mean temperature at the interface between the two foam boards were reached.

The single-specimen Lambda-meter EP-500 was first programmed to reach a mean temperature of 10 ºC at the interface between the two foam boards, establishing a 15 ºC difference between the heating and the cooling plates. The test was also performed for the mean temperatures of 25 ºC and 40 ºC at the same interface, as can be seen in Figure 3.7 b) and d).

The heat flux registered by the HFP01-10 sensor and the temperatures registered by the TC11 and TC12 thermocouples for the three measurements are given in Figure 3.7 a) and b), respectively. The same test was performed using the second sensor HFP01-20 and the second pair of thermocouples TC21 and TC22. The results are given in Figure 3.7 c) and d). The heat flux registers a slight increase with the increment of the mean temperature. During the transition of the temperature conditions there is a heat flux drop, automatically controlled by the apparatus. However, the steady-state heat flow is restored in a couple of hours.

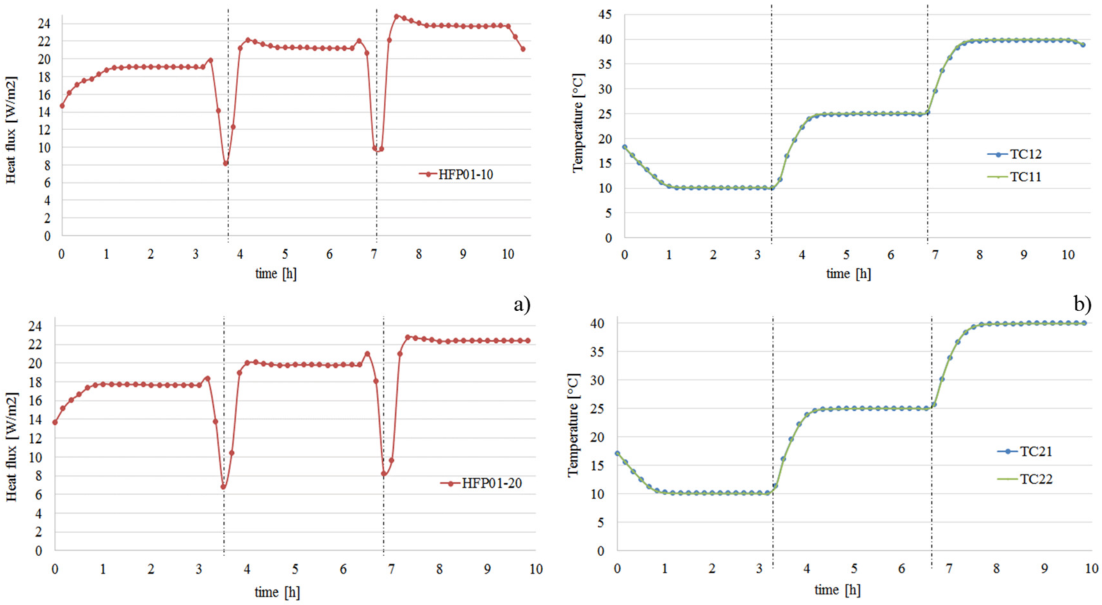

a)

b)

c)

d)

Figure 3.7: TRSY01 system verification - Test 1: a) Heat flux measured by HFP01-10 over time; b) Temperatures registered by TC11 and TC12 over time; c) Heat flux measured by HFP01-20 over time; d) Temperatures registered by TC21 and TC22 over time.

The heat flux and the temperatures registered by the TRSY01 system sensors were compared with those given by the single-specimen Lambda-meter EP-500 during the tests. This comparison is made only after steady state has been reached. The effective thermal conductivity values of the specimen, obtained when thermal equilibrium is achieved, were used to compute the heat flow through the specimen under steady-state conditions. For that purpose, the Fourier Law equation was applied $\left(q = \lambda\left(\Delta T/e\right)\right)$, where q is the heat flow rate, λ is the thermal conductivity of the specimen, ΔT is the temperature gradient between the two external surfaces of the specimen and e is the thickness of the specimen). The difference between the two measurements gives the error of each TRSY01 system sensor. Two more tests were performed to evaluate the precision of the TRSY01 equipment, assuming exactly the same conditions of measurement. The results for the three tests are presented in Tables A2-A5 in Appendix A. The results show a good agreement between the two experimental measurements, with maximum errors of 5.41 % for the HFP01-10 sensor, 3.11 % for the HFP01-20 sensor, 2.25 % for TC11 and TC12 sensors and 1.90 % for TC21 and TC22 sensors. For each sensor, the results of the repeatability tests under the same conditions are very close, showing the good precision of the TRSY01 sensors and, therefore, ascribing a good trust level to the equipment.

Verification of the TRSY01 system in the hot box test procedure

The confidence level of the hot box tests procedure was ascertained by performing calibration measurements using two glazed calibration panels of different thicknesses, from the National Physics Laboratory (NPL). The two panels consist of an expanded polystyrene (EPS) layer, coated by a 4 mm glazing panel on each side. The thermal conductance of each panel, measured by the NPL, is given in Table 3.2. The calibration panels were placed between the two hot box chambers and the measurements were performed under the conditions given in Figure 3.4. The internal and external surface temperatures and the heat fluxes over time were registered by the thermocouples and the heat flux sensors from the TRSYS01 system, respectively. These calibration measurements also enabled to check the TRSY01 system when the measuring surface is exposed to radiation and convection phenomena.

Table 3.2: Calibration panels' properties according to NPL report.

	Panel 1	Panel 2
Total thickness [mm]	20	58
Thickness of EPS [mm]	12	50
Density of EPS [kg/m^3]	31.6	30.7
Thermal conductance (mean temperature =10 ºC) [W/(m^2.ºC)]	2.512 ± 0.12	0.645 ± 0.018

Figures 3.8 and 3.9 give the variation of the surface temperature and the heat flux over time, respectively, registered on both sides of panels 1 and 2 under the conditions given in Figure 3.4.

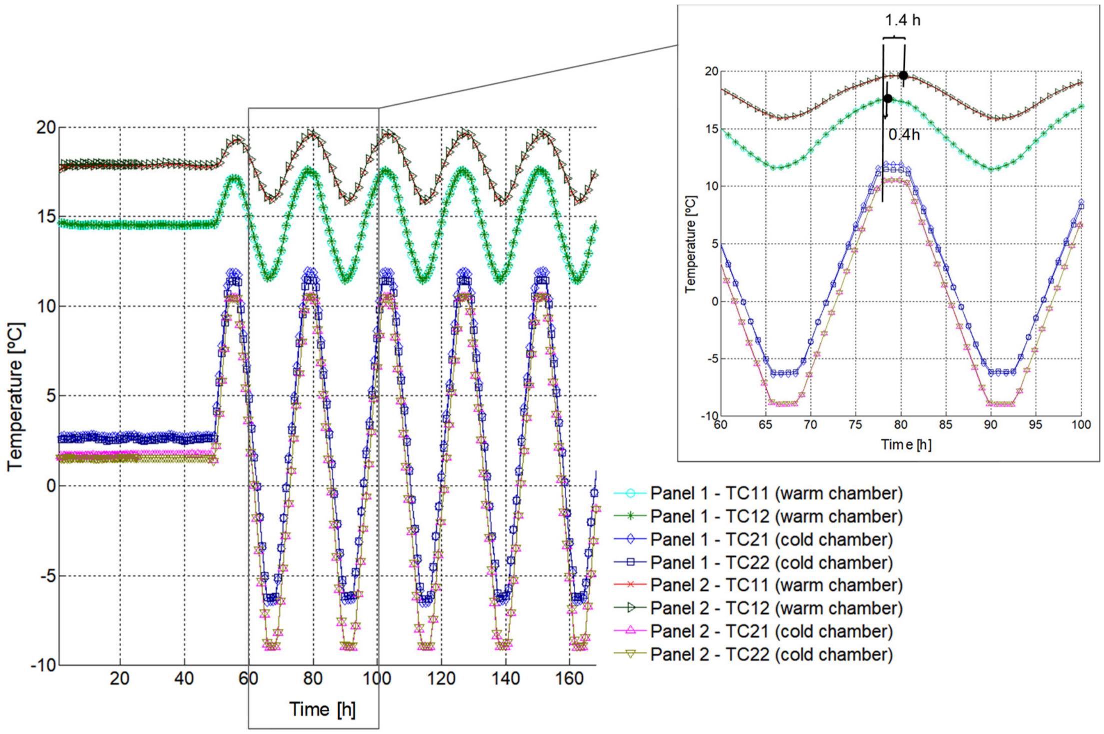

Figure 3.8: Variation of the surface temperature over time, registered by the two pairs of TRSYSO1 system thermocouples located on the warm and the cold side of the two calibration panels. Thermal phase lag in each panel, determined for the second period of the dynamic simulation.

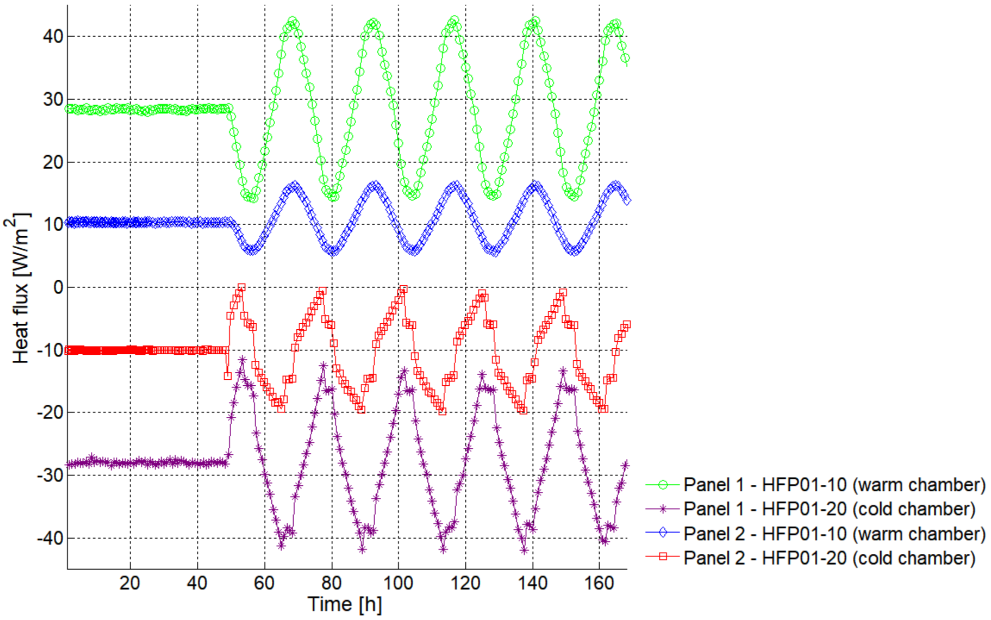

Figure 3.9: Variation of the surface heat flux over time, registered by the two heat flux sensors from the TRSYS01 system, placed on the warm and on the cold side of the two calibration panels.

The internal and external surface temperatures, registered when steady-state conditions are achieved ($t = 48$ h), are 14.5 ºC and 2.7 ºC, respectively, for panel 1 and 17.9 ºC and 1.6 ºC, respectively, for panel 2 (Figure 3.8). The heat flux through panel 1 and panel 2 registered under steady-state conditions is about 28.3 W/m^2 and 10 W/m^2, respectively (Figure 3.9). These results allowed the application of Fourier's law to calculate the thermal conductance of each panel, resulting in 2.40 W/(m^{2}ºC) for panel 1 and 0.63 W/(m^{2}ºC) for panel 2. Comparing with the NPL measurements (see Table 3.2), we find the thermal conductance deviation for panel 1 is about 4 % and for panel 2 about 3 %. This shows a good confidence level and the reliability of the testing apparatus.

After the TRSY01 system check with the hot box test apparatus, the calibration panels were used to define and evaluate the dynamic conditions that were intended to apply to the wooden corner measurements. These additional tests confirmed the dynamic responses of the equipment and the reliability of the sensors under unsteady conditions. The temperatures and heat fluxes registered between $t = 48$ h and $t = 168$ h in the two panels under dynamic conditions are given in Figures 3.8 and 3.9. Figure 3.8 shows that the thermal amplitude is significantly higher in panel 1 with lower thermal resistance. The thermal phase lag is slightly larger in panel 2. The heat flux amplitudes are significantly higher in panel 1 and the amplitude difference between the internal and the external heat fluxes are greater in panel 2, as can be seen in Figure 3.9.

3.5 Laboratory measurements

This section presents the results of the tests described in sections 3.2 and 3.3. The thermal behaviour of the wooden corner is evaluated under steady-state and dynamic conditions. In both cases, the dynamic thermal bridging effect is evaluated by comparing the heat responses near the corner with the ones at the centre of the wood panels (walls).

Figure 3.10 presents the temperature responses measured by the line of 44 T-type thermocouples, arranged on the warm surface of the wood panel, under steady-state conditions ($t = 48$ h). The temperatures inside the hot chamber and the cold chamber are 20 ºC and 0 ºC, respectively. It can be seen that the lowest surface temperature ($T_{sur,\min} = 15.4$ ºC) is registered near the corner, where the thermal bridging effect is more pronounced. At a distance of 0.2 m from the corner, the effect of the thermal bridge is no longer perceptible and the surface temperature tends to be constant ($T_{sur} = 18$ ºC).

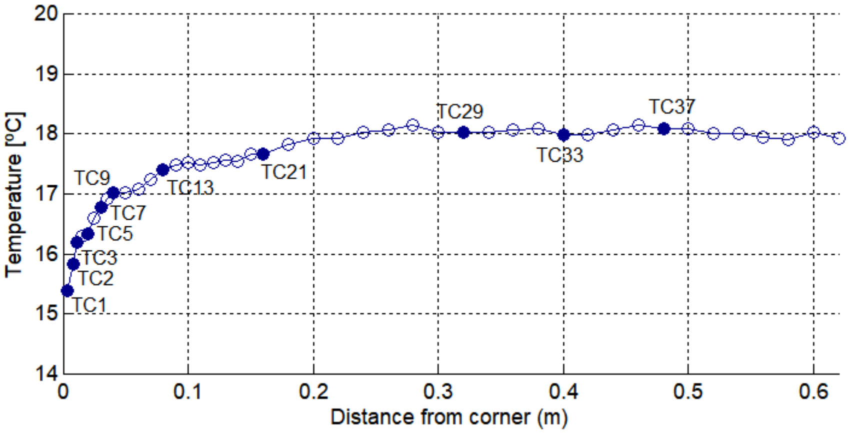

Figure 3.10: Internal surface temperature registered by the T-type thermocouples placed on the warm side of the wooden corner, under steady-state conditions.

A set of eleven thermocouples identified in Figure 3.10 (filled markers) were used to illustrate the thermal behaviour of the LTB, under the dynamic conditions given in Figure 3.4 (between $t = 48$ h and $t = 168$ h). Of these eleven thermocouples, number 1 is the nearest to the corner (0.003 m) and number 37 is farthest from the corner (0.48 m). Figure 3.11 gives the variation of the surface temperature over time, registered by these thermocouples.

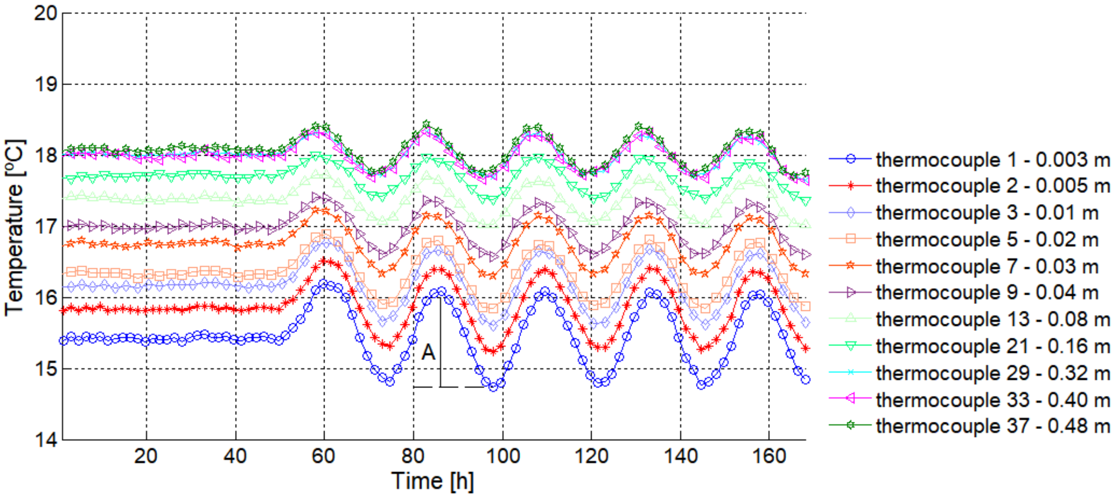

Figure 3.11: Variation of the surface temperature over time, registered by eleven T-type thermocouples placed on the hot side of the wooden corner. Key gives the distance of each thermocouple to the corner.

The results show that the surface temperature curves have a cyclic behaviour, however, we may notice a slight dampening in the first two periods of the curve, particularly closer to the corner. The thermal phase lag is slightly larger in the LTB. The thermal amplitude (A) in the close vicinity of the corner is about twice that registered at receivers placed at distances greater than 0.10 m from the corner, due to the thermal bridging effect. This is seen in Figure 3.12, which gives the thermal amplitude (A) variation at the thermocouples for the second period of 24 hours.

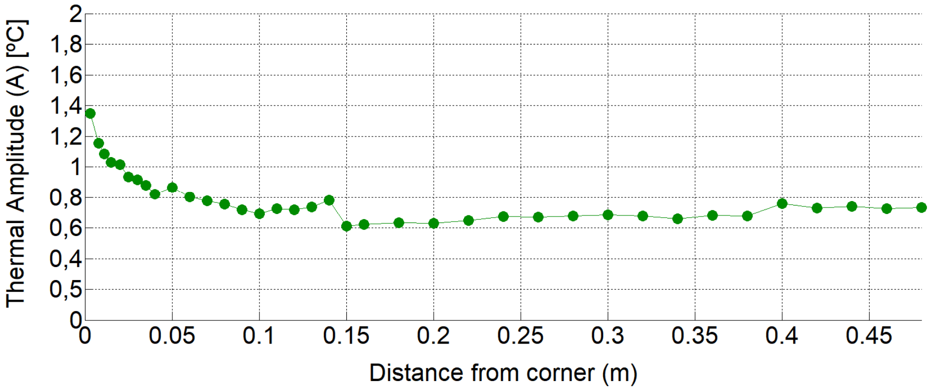

Figure 3.12: Thermal amplitude variation at the T-type thermocouples for a certain period of the temperature curves.

Figure 3.13 gives the variation of the surface temperature over time, registered by the four thermocouples of the TRSYS01 system, placed on both sides of the wooden corner as shown in Figure 3.5.

It can be observed that on the cold side the surface temperatures at the corner registered by thermocouple TC21 are similar to the temperatures imposed on the cold chamber environment (see Figure 3.4). Therefore, they are not being affected by the concentration of the heat flow from the hot side of the LTB and the surface resistance on the wooden corner. Under steady-state conditions, the external surface temperature registered at the centre of the wood panel by thermocouple TC22 is 1.7 ºC, higher than the external surface temperature registered at the corner by thermocouple TC21, which is 0.2 ºC. Under dynamic conditions, the minimum surface temperature registered by thermocouple TC22 is about 3 °C higher than the minimum surface temperature registered at the corner by thermocouple TC21. However, the maximum temperatures recorded on both surfaces by TC21 and TC22 over time are similar ($T_{sur} = 10$ ºC). These differences may be explained in terms of the variation of the surface thermal resistance value in the specimen with the temperature inside the cold chamber. It can also be seen that, on the warm side, the surface temperatures and the thermal amplitudes registered by the TRSYS01 thermocouples (TC11 and TC12) are similar to those registered by the T-type thermocouples (TC2 and TC37), taking into account the same distance from the corner (see Figure 3.11).

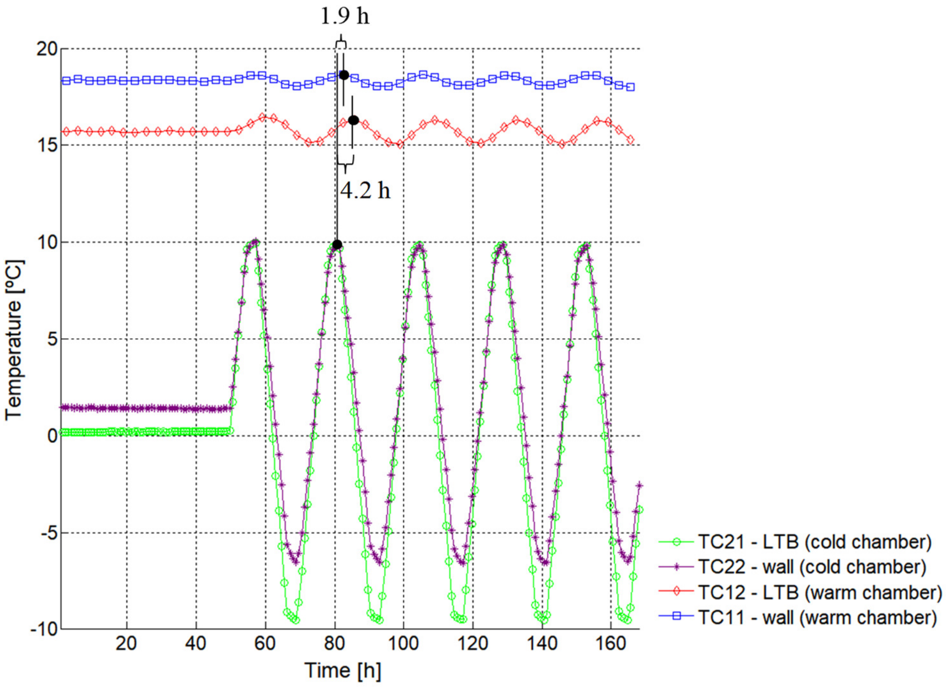

Figure 3.13: Variation of the surface temperature over time, registered by the TRSYS01 thermocouples placed on both sides of the wooden corner.

The figure also presents the thermal phase lag in the LTB and in the wall, determined for the second period of the dynamic simulation. It can be seen that the thermal phase lag is larger in the LTB, since the temperature response to the external temperature variation is slower (4.2 h). The average thermal phase lag in the LTB and the wall is 4.1 h and 1.8 h, respectively. The results are presented in Table 3.3.

Table 3.3:Thermal phase lag in the LTB and the wall, based on the dynamic experimental results.

Cycle	1	2	3	4	5	AVERAGE
Thermal Phase Lag – Wall (h)	1.6	1.9	1.7	1.9	1.7	1.8
Thermal Phase Lag – LTB (h)	4.2	4.2	4.2	4.1	3.9	4.1

Figure 3.14 gives the variation of the heat flux over time, registered by the heat flux plate HFP01-10 and by the two flat plate heat flux sensors (1 and 2) placed on the warm side of the wooden corner, as shown in Figure 3.5.

The heat fluxes registered in the centre of the wood panel by the flat plate heat flux sensors 1 and 2 are significantly lower than the heat fluxes registered in the LTB (near the corner), by HFP01-10. The heat flux amplitude is significantly higher near the LTB, as was found in the temperature curves. Under steady-state conditions, the heat flux through the LTB is 17.2 W/m^2 and the heat flux through the wall is 12.3 W/m^2. Under dynamic conditions, the heat flux amplitude is about 4.6 W/m^2 through the wall and 7.6 W/m^2 in the LTB, ranging between 9.8 W/m^2 and 14.4 W/m^2 and between 13.2 W/m^2 and 20.8 W/m^2, respectively.

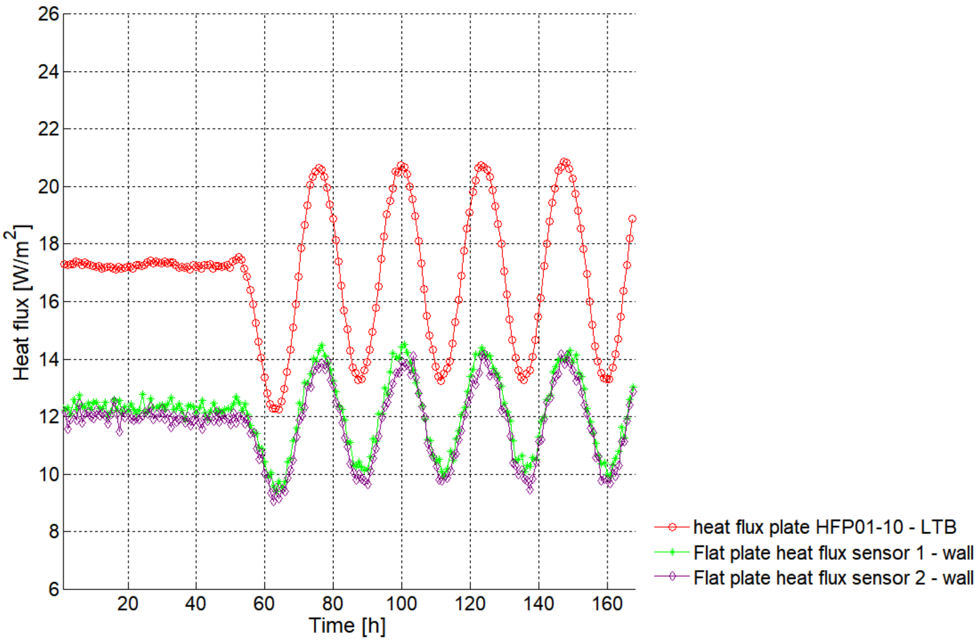

Figure 3.14: Variation of the heat flux over time, registered by the two heat flux plates HFP01 and by the two flat plate heat flux sensors placed on the hot side of the wooden corner.

Figure 3.15 gives the variation of the heat flux over time, registered by the heat flux plate HFP01-20 and by the Flat plate heat flux sensor 3, placed on the cold side of the wooden corner, according to the scheme presented in Figure 3.5.

The heat flux absolute values registered in the centre of the wood panel by flat plate sensor 3 are higher than the heat flux absolute values registered in the LTB by the HFP01-20 sensors. Under steady-state conditions, the heat flux through the LTB is -7 W/m^2 and the heat flux through the wall is about -12 W/m^2. Under dynamic conditions, the heat flux amplitude is about 45 W/m^2 through the wall and 43 W/m^2 through the LTB, ranging between -35 W/m^2 and 10 W/m^2 and between -28 W/m^2 and 15 W/m^2, respectively.

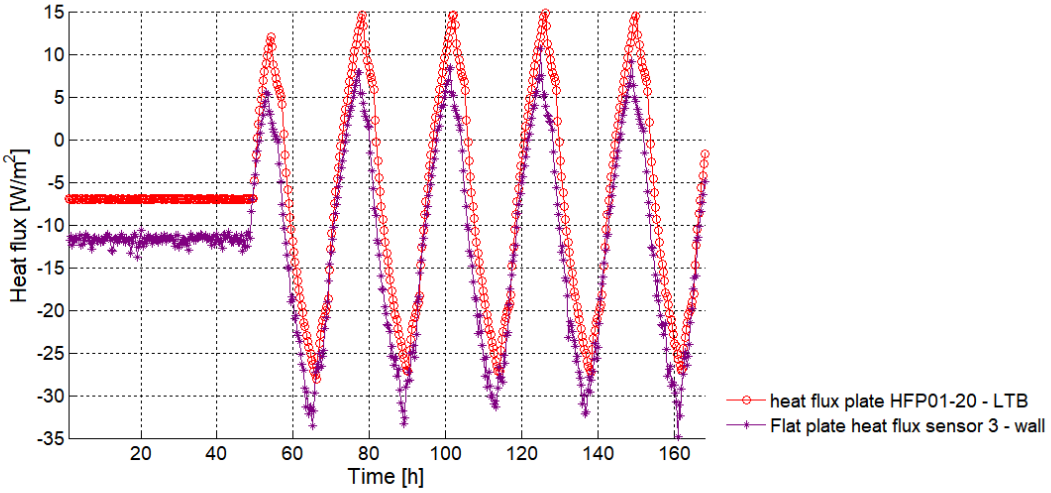

Figure 3.15: Variation of the heat flux over time, registered by the TRSYS01 thermocouples placed on the cold side of the wooden corner.

3.6 Experimental vs numerical results

This section presents the experimental validation of the 2D BEM model presented in Chapter 2, for the simulation of the transient heat diffusion through LTBs. For that purpose, the BEM formulation was used to simulate the dynamic heat conduction through the wooden corner. The heat transfer measurements of the wooden building corner, under steady-state and dynamic conditions, obtained using the calibrated hot box are compared with the numerical results of the BEM simulations.

Figure 3.16 illustrates the 2D physical model of the problem. Medium 2 is the wood used for the corner, while Medium 1 and Medium 3 represent two thin air layers that, respectively, account for the convection and radiation phenomena on the outer and inner surfaces of the corner.

Medium 1 is bounded by surfaces S_1, S_2, S_3 and S_4, Medium 2 is bounded by surfaces S_3, S_5, S_6 and S_7 and Medium 3 is bounded by surfaces S_6, S_8, S_9 and S_{10}.

Temperatures $T = T(x, y, t)$ and $T = T_0$ are prescribed along the exterior boundary of the fictitious thin air layers (sections S_1 and S_9, respectively). Continuity of heat fluxes and temperatures are imposed along boundary sections S_3 and S_6.

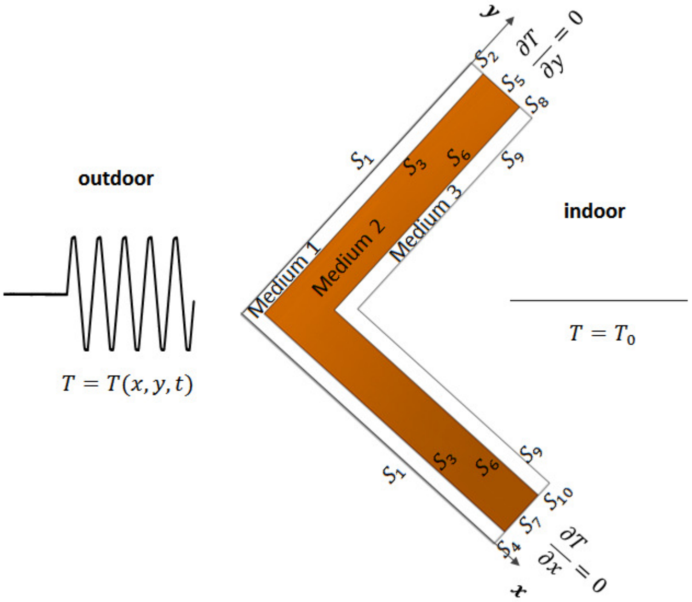

Figure 3.16: 2D wooden building corner scheme and boundary conditions of the problem.

The corner was modelled as adjacent lateral walls long enough to ensure that the heat transfer at the cut-off sections would not be affected by the presence of the thermal bridge formed at the junction of the walls, following ISO 10211:2007 [1]. Thus, null heat fluxes $(\partial T/\partial n = 0)$ are prescribed along the cut-off sections S_2, S_4, S_5, S_7, S_8 and S_{10}.

The thermal properties of the CLT panels were experimentally determined and are listed in Table 3.1 (see section 3.3).

The heat transfer through the wooden corner was simulated numerically under the same dynamic conditions used for the experimental simulations (see Figure 3.4, section 3.3). At $t = 0.0$ h the systems were assumed to have a uniform temperature of 20 ºC throughout the full domain. The frequency domain of computation ranged from 0.0 Hz to $4096/(168 \times 3600)$ Hz, with a frequency increment of $1.0/(168 \times 3600)$ Hz, which determined a total time window of 168.0 h for the analysis.

The BEM formulation only requires the discretisation of the interface media. The walls' longitudinal material interfaces were discretized using 200 constant boundary elements, while 60 constant boundary elements were used to model the lateral interfaces at the cut-off sections. The temperature and heat flux were obtained for different receivers placed at the same coordinates of the thermocouples and the heat flux sensors used in the experimental measurements.

The surfaces' thermal resistances R_{si} and R_{se} were modelled as a thin air layer on the inner and outer surfaces, respectively, to take into account convection and radiation phenomena. The R_{si} and R_{se} values considered in the numerical simulation were determined using the steady-state experimental measurements, following the equations:

$$R_{si} = \frac{1}{h_i} = \frac{1}{\dfrac{q_{si}}{\left(T_i - T_{si}\right)}}, \tag{3.1}$$

$$R_{se} = \frac{1}{h_e} = \frac{1}{\dfrac{q_{se}}{\left(T_e - T_{se}\right)}}, \tag{3.2}$$

Where h_i and h_e are the internal and the external surface heat transfer coefficients, in W/(m^2.ºC), T_{si} and T_{se} are the internal and the external surface temperatures in ºC, measured by the temperature sensors, T_i and T_e are the temperatures of the internal and the external environment in ºC, and q_{si} and q_{se} are the heat flow rates measured by the heat flow sensors placed, respectively, on the internal and the external surfaces of the wooden corner.

At the junctions between two surfaces, such as building corners, the radiation/convection effect is reduced, leading to higher surface thermal resistances. Therefore, preliminary tests were performed under steady-state conditions to evaluate the variation of the surface thermal resistance in the wall, starting from the corner. The results made it possible to estimate a mean value for the R_{si} up to 0.18 m from the corner. The estimated surfaces thermal resistances, R_{si} and R_{se}, are presented in Table 3.4.

Table 3.4: Surface thermal resistances used in the numerical simulations.

	R_{si} [m^2.ºC/W]	R_{se} [m^2.ºC/W]
Wall (plane surface)	0.16	0.14
LTB (up to 0.18 m from the corner)	0.18	0.14

The following figures give the surface temperatures and the heat fluxes obtained with the BEM, under steady-state and dynamic conditions, for different points of the internal and the external surfaces of the wooden corner. The numerical results are compared with the experimental results.

Steady-state conditions:

Figure 3.17 presents the surface temperatures measured by the line of 44 T-type thermocouples as well as the surface temperatures obtained with the BEM model at the same points on the wooden corner and under the same steady-state conditions (20 ºC inside the hot chamber and 0 ºC inside the cold chamber). The error bar related to the experimental results represents the uncertainty of each thermocouple $(\pm\ 0.16\ ℃)$. The results show a good agreement between experimental and numerical steady-state analysis.

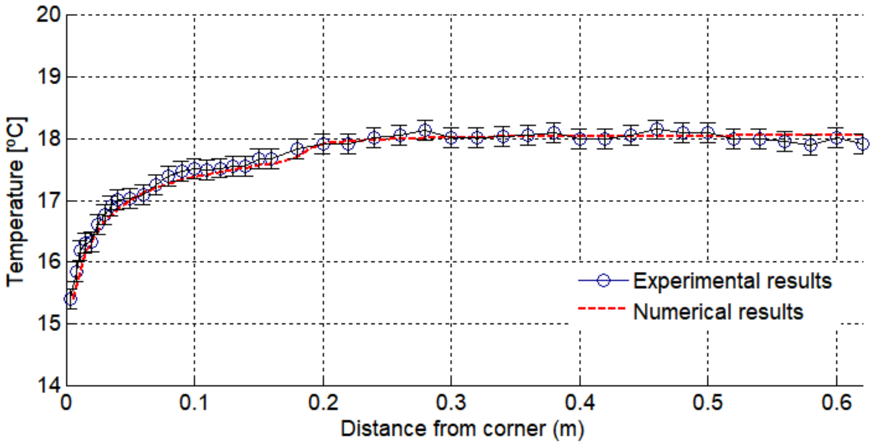

Figure 3.17: Variation of the internal surface temperature with the distance from the corner, under steady-state conditions: numerical and experimental results.

Steady-state conditions and unsteady-state conditions:

Figure 3.18 presents the variation of the internal surface temperature over time, registered by three T-type thermocouples under the dynamic conditions given in Figure 3.4. Thermocouple number 1 is the nearest to the corner (0.003 m), thermocouple number 3 is 0.01 m from the corner and number 37 is 0.48 m from the corner. The figure also gives the responses of the BEM simulation at three receivers placed at the same points as the thermocouples. In the initial part of the time window it can be seen that the numerical results need a period of time to reach the steady-state. This is because the initial conditions prescribed at $t = 0.0$ h were at a uniform temperature of 20 ºC in the full domain. After the steady-state was reached and in the dynamic conditions the results show a good agreement between the numerical responses and experimental measurements.

Note that, other measuring points of the physical model could have been used in this analysis since the numerical responses obtained for the remaining points were also found to be in agreement with the experimental results.

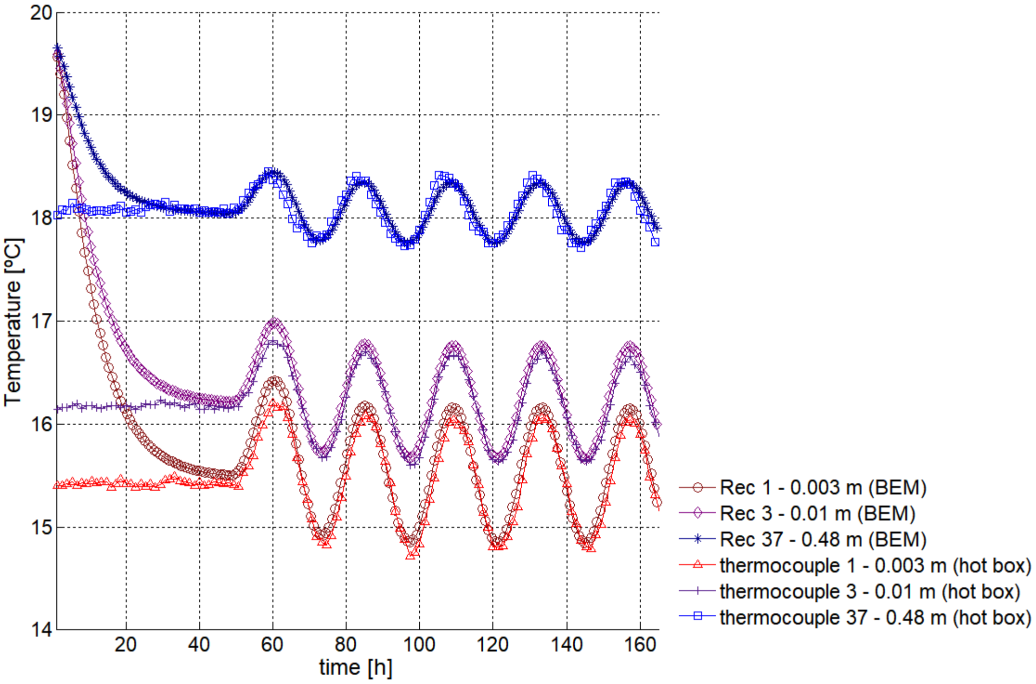

Figure 3.18: Variation of the internal surface temperature over time: experimental and numerical results. The key gives the distance of each thermocouple/receptor from the corner.

Figure 3.19 gives the variation of the surface temperature over time on the cold side of the wooden corner, obtained near the corner (LTB) and in the centre of the wooden panel (wall) by the numerical simulation and with the experimental measurements. It can be seen that the results are very close over the full time window.

Figure 3.20 gives the variation of the heat flux over time, on the warm side of the wooden corner, obtained near the corner (LTB) and in the centre of the wooden panel (wall) by the numerical simulation and with the experimental measurements. It can be seen that the heat flux in the centre of the wooden panel measured experimentally is very close to the heat flux curve obtained with the numerical simulation. However, near the corner, the heat flux amplitude obtained with BEM is slightly lower than that found experimentally.

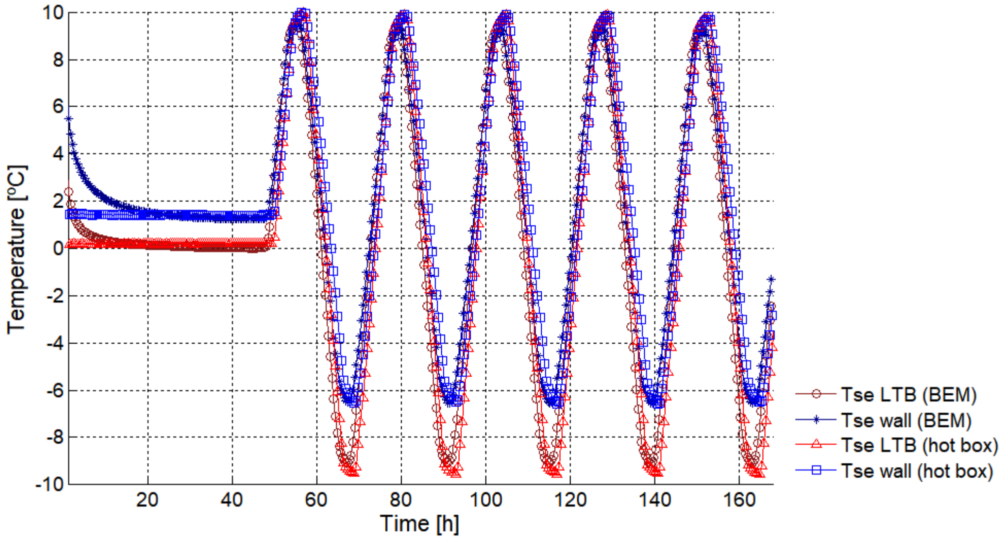

Figure 3.19: Variation of the external surface temperature over time: experimental and numerical results.

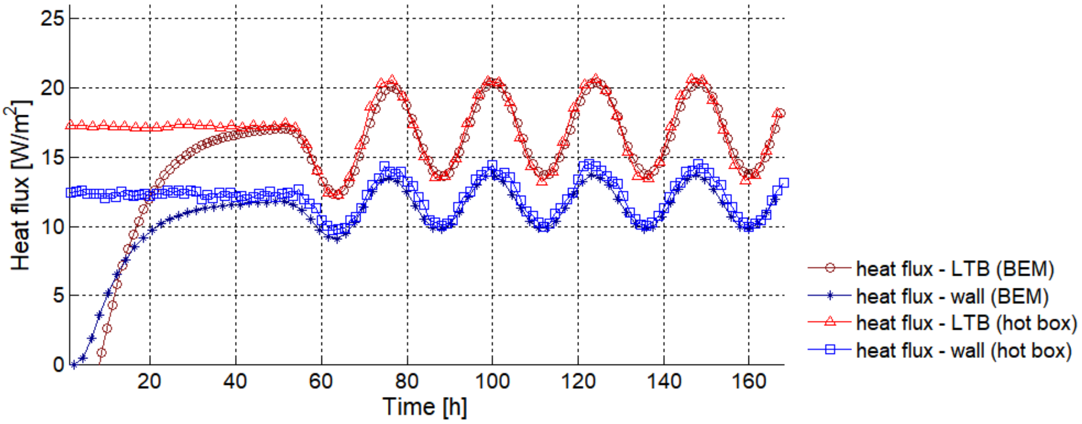

Figure 3.20: Variation of the internal heat flux over time: experimental and numerical results.

Figure 3.21 presents the variation of the heat flux over time on the cold side of the wooden corner, obtained by the numerical and experimental simulations.

It can be seen that the dynamic heat flux near the corner measured experimentally is similar to the dynamic heat flux obtained with the numerical simulation. The heat flux amplitude in the centre of the wooden panel obtained with BEM is slightly higher than the one obtained experimentally.

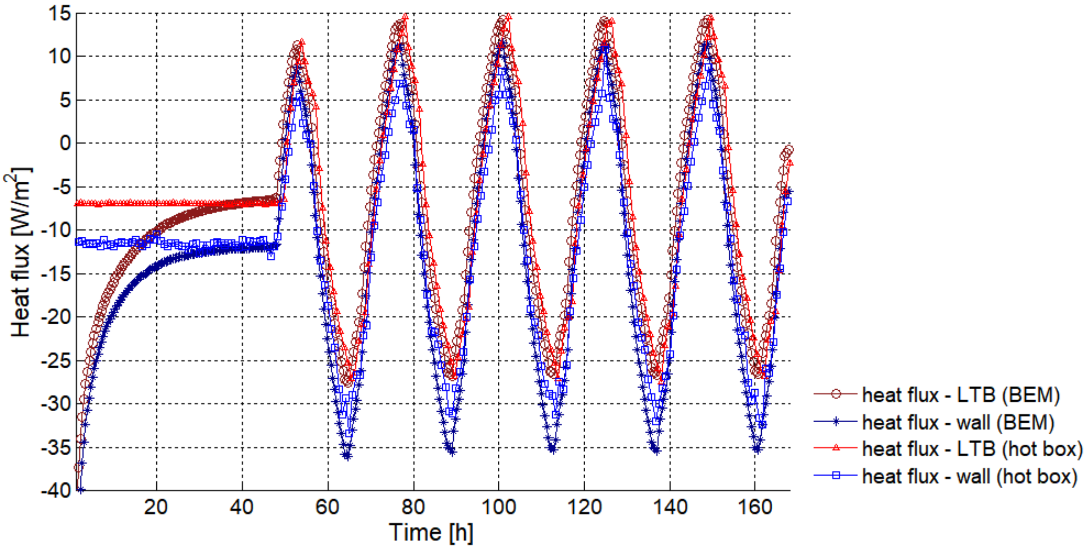

Figure 3.21: Variation of the external heat flux over time: experimental and numerical results.

3.7 Conclusions

This chapter conducted a test program to evaluate the dynamic thermal behaviour of a wooden building corner, representing an LTB. The tests were performed with a calibrated hot box. A set of preliminary tests showed that the testing apparatus and measuring devices could be trusted and were reliable. The change of the surface temperatures and the heat fluxes over time was then registered at different distances from the corner in order to evaluate the dynamic thermal bridging effect. The results clearly showed that the thermal phase lag and the thermal amplitude are higher near the corner.

A numerical simulation of the wooden corner was then performed, using the BEM model proposed in Chapter 2 and considering the same dynamic boundary conditions of the experimental campaign. The surface temperatures and the heat fluxes obtained with the BEM for different points of the internal and external surfaces of the wooden corner were compared with the experimental results. The experimental and numerical results showed good agreement, which validates the proposed BEM model.

Appendix A

Table A1 gives the results of the T-type thermocouples calibration procedure, described in section 3.4.

Table A1: T-type thermocouples (TC) calibration results

TC	Reference value [ºC]	Measured value [ºC]	Error	Uncertainty	TC	Reference value [ºC]	Measured value[ºC]	Error	Uncertainty
1	20.018	19.8	-0.2	±0.16	23	20.018	19.6	-0.4	±0.16
	10.014	9.9	-0.1	±0.16		10.014	9.7	-0.3	±0.16
	0.033	0.0	0.0	±0.16		0.033	-0.2	-0.2	±0.16
2	20.018	19.8	-0.2	±0.16	24	20.018	19.6	-0.4	±0.16
	10.014	9.9	-0.1	±0.16		10.014	9.7	-0.3	±0.16
	0.033	0.0	0.0	±0.16		0.033	-0.2	-0.2	±0.16
3	20.018	19.7	-0.3	±0.16	25	20.018	19.8	-0.2	±0.16
	10.014	9.8	-0.2	±0.16		10.014	10.1	0.1	±0.16
	0.033	-0.2	-0.2	±0.16		0.033	-0.2	-0.2	±0.16
4	20.018	19.7	-0.3	±0.16	26	20.018	19.8	-0.2	±0.16
	10.014	9.8	-0.2	±0.16		10.014	9.9	-0.1	±0.16
	0.033	-0.1	-0.1	±0.16		0.033	0.3	0.3	±0.16
5	20.018	19.9	-0.1	±0.16	27	20.018	19.7	-0.3	±0.16
	10.014	10.0	0.0	±0.16		10.014	10.0	0.0	±0.16
	0.033	0.0	0.0	±0.16		0.033	0.0	0.0	±0.16
6	20.018	19.9	-0.1	±0.16	28	20.018	19.7	-0.3	±0.16
	10.014	9.9	-0.1	±0.16		10.014	9.9	-0.1	±0.16
	0.033	0.0	0.0	±0.16		0.033	0.1	0.1	±0.16
7	20.018	19.8	-0.2	±0.16	29	20.018	19.7	-0.3	±0.16
	10.014	9.9	-0.1	±0.16		10.014	10.0	0.0	±0.16
	0.033	-0.1	-0.1	±0.16		0.033	0.1	0.1	±0.16
8	20.018	19.8	-0.2	±0.16	30	20.018	19.8	-0.2	±0.16
	10.014	9.8	-0.2	±0.16		10.014	9.9	-0.1	±0.16
	0.033	-0.2	-0.2	±0.16		0.033	0.1	0.1	±0.16
9	20.018	19.9	-0.1	±0.16	31	20.018	19.8	-0.2	±0.16
	10.014	10.0	0.0	±0.16		10.014	9.9	-0.1	±0.16
	0.033	0.0	0.0	±0.16		0.033	0.3	0.3	±0.16
10	20.018	20.0	0.0	±0.16	32	20.018	19.8	-0.2	±0.16
	10.014	10.1	0.1	±0.16		10.014	10.1	0.1	±0.16
	0.033	0.2	0.2	±0.16		0.033	0.3	0.3	±0.16
11	20.018	19.9	-0.1	±0.16	33	20.018	19.8	-0.2	±0.16
	10.014	9.9	-0.1	±0.16		10.014	10.1	0.1	±0.16
	0.033	0.2	0.2	±0.16		0.033	0.4	0.4	±0.16
12	20.018	19.9	-0.1	±0.16	34	20.018	19.8	-0.2	±0.16
	10.014	9.9	-0.1	±0.16		10.014	10.2	0.2	±0.16
	0.033	-0.1	-0.1	±0.16		0.033	0.2	0.2	±0.16
13	20.018	19.9	-0.1	±0.16	35	20.018	19.9	-0.1	±0.16
	10.014	10.0	0.0	±0.16		10.014	10.0	0.0	±0.16
	0.033	-0,1	-0.1	±0.16		0.033	0.4	0.4	±0.16
14	20.018	19.9	-0.1	±0.16	36	20.018	19.9	-0.1	±0.16
	10.014	10.0	0.0	±0.16		10.014	10.1	0.1	±0.16
	0.033	0.0	0.0	±0.16		0.033	0.1	0.1	±0.16
15	20.018	20.0	0.0	±0.16	37	20.018	19.9	-0.1	±0.16
	10.014	10.1	0.1	±0.16		10.014	10.3	0.3	±0.16
	0.033	0.0	0.0	±0.16		0.033	0.3	0.3	±0.16
16	20.018	20.0	0.0	±0.16	38	20.018	19.9	-0.1	±0.16

TC	Reference value [ºC]	Measured value [ºC]	Error	Uncertainty	TC	Reference value [ºC]	Measured value[ºC]	Error	Uncertainty
	10.014	10.0	0.0	±0.16		10.014	10.2	0.2	±0.16
	0.033	0.2	0.2	±0.16		0.033	0.1	0.1	±0.16
17	20.018	20.0	0.0	±0.16	39	20.018	19.9	-0.1	±0.16
	10.014	10.0	0.0	±0.16		10.014	10.0	0.0	±0.16
	0.033	0.0	0.0	±0.16		0.033	0.0	0.0	±0.16
18	20.018	20.0	0.0	±0.16	40	20.018	19.9	-0.1	±0.16
	10.014	10.2	0.2	±0.16		10.014	10.0	0.0	±0.16
	0.033	0.0	0.0	±0.16		0.033	0.4	0.4	±0.16
19	20.018	20.0	0.0	±0.16	41	20.018	19.9	-0.1	±0.16
	10.014	10.2	0.2	±0.16		10.014	10.2	0.2	±0.16
	0.033	0.3	0.3	±0.16		0.033	0.8	0.8	±0.16
20	20.018	19.6	-0.4	±0.16	42	20.018	20.0	0.0	±0.16
	10.014	9.9	-0.1	±0.16		10.014	10.4	0.4	±0.16
	0.033	0.3	0.3	±0.16		0.033	0.0	0.0	±0.16
21	20.018	19.7	-0.3	±0.16	43	20.018	19.7	-0.3	±0.16
	10.014	10.0	0.0	±0.16		10.014	10.0	0.0	±0.16
	0.033	0.0	0.0	±0.16		0.033	-0.2	-0.2	±0.16
22	20.018	19.6	-0.4	±0.16	44	20.018	19.6	-0.4	±0.16
	10.014	9.8	-0.2	±0.16		10.014	9.8	-0.2	±0.16
	0.033	-0.2	-0.2	±0.16		0.033	-0.2	-0.2	±0.16

Tables A2-A5 present the results of the TRSY01 system check, described in Section 2.3. These results compare the heat fluxes measured by the HFP01 sensors and the heat fluxes determined using the single specimen Lambda-meter EP-500, for three laboratory tests performed under the same measurement conditions.

Table A2: TRSY01 system verification – Comparison between the heat flux measured by the HFP01-10 sensor and the heat flux determined using the single specimen Lambda-meter EP-500, for three laboratory tests performed under the same measurement conditions.

	Test temperature [°C]	Thermal conductivity [mW/(m. °C)]	Heat flux [W/m^2]		Absolute Error [%]
			Lambda-meter EP-500	TRSYS01 HFP01-10	
Test 1	10	63.14	18.51	19.02	2.76
	25	69.59	20.38	21.38	4.91
	40	77.00	22.56	23.67	4.92
Test 2	10	63.25	18.55	19.1	2.96
	25	69.68	20.42	21.34	4.51
	40	77.04	22.57	23.75	5.23
Test 3	10	63.34	18.52	19.1	3.13
	25	69.67	20.40	21.31	4.46
	40	77.01	22.56	23.78	5.41

Table A3: TRSY01 system verification – Comparison between the heat flux measured by the HFP01-20 sensor and the heat flux determined using the single specimen Lambda-meter EP-500, for three laboratory tests performed under the same measurement conditions.

	Test temperature [°C]	Thermal conductivity [mW/(m. °C)]	Heat flux [W/m2]		Absolute Error [%]
			Lambda-meter EP-500	TRSYS01 HFP01-20	
Test 1	10	62.89	18.32	17.75	3.11
	25	69.66	20.27	19.92	1.73
	40	77.19	22.48	22.2	1.25
Test 2	10	63.27	18.40	17.96	2.39
	25	69.77	20.31	20.11	0.98
	40	77.16	22.47	22.31	0.71
Test 3	10	63.30	18.45	18.01	2.38
	25	69.75	20.32	20.06	1.28
	40	77.26	22.51	22.32	0.84

Table A4: TRSY01 system verification – Comparison between the temperature measured by the TC11 and TC12 sensors and the temperature registered by the single specimen Lambda-meter EP-500, for three laboratory tests performed under the same measurement conditions.

	Test temperature [°C]	Temperature [°C]		Absolute Error [%]
		Lambda-meter EP-500	TRSYS01 TC11/TC12	
Test 1	10	10.00	10.22	2.25
	25	25.00	25.09	0.35
	40	40.00	39.87	0.33
Test 2	10	9.99	10.21	2.16
	25	25.00	25.08	0.32
	40	40.00	39.89	0.28
Test 3	10	10.01	10.23	2.17
	25	25.01	25.11	0.42
	40	40.00	39.92	0.20

Table A5: TRSY01 system verification – Comparison between the temperature measured by the TC21 and TC22 sensors and the temperature registered by the single specimen Lambda-meter EP-500, for three laboratory tests performed under the same measurement conditions.

	Test temperature [°C]	Temperature [°C]		Absolute Error [%]
		Lambda-meter EP-500	TRSYS01 TC21/TC22	
Test 1	10	10.00	10.14	1.40
	25	25.01	25.03	0.08
	40	40.00	39.88	0.30
Test 2	10	10.01	10.18	1.70
	25	25.01	25.07	0.24
	40	40.00	39.93	0.18
Test 3	10	9.99	10.18	1.90
	25	25.00	25.08	0.32
	40	40.00	39.90	0.25

References

[1] European Standard, EN ISO 14683: Thermal bridges in building construction - Linear thermal transmittance - Simplified methods and default values, 2007.

[2] J. Prata, A. Tadeu, N. Simões, Influence of material properties and boundary conditions on the dynamic thermal behaviour of a building corner, in Proceedings of Eco-Architecture V: Sienna, Italy, September 24-26, 2014.

[3] G. Mao, Thermal bridges: From research to applications. Tekn. Lic. thesis, Arbetsrapport 1995:1, KTH, Avd. för Byggnadsteknik, Stockholm, Sweden.

[4] T. Kalema and T. Haapala, Effect of interior heat transfer coefficients on thermal dynamics and energy consumption, Energy and Buildings 22 (1995) 101-113.

[5] R.G. Martinez, A.U. Arrien, I.A. Egaña, Calibration procedures for multidimensional heat transfer models based on on-site experimental data, Energy Procedia 78 (2015) 3222-3227.

[6] L. Zalewski, S. Lassue, D. Rousse, K. Boukhalfa, Experimental and numerical characterization of thermal bridges in prefabricated building walls, Energy Conversion and Management 51 (2010) 2869-2877.

[7] C. Peng, Z. Wu, In situ measuring and evaluating the thermal resistance of building construction, Energy and Buildings 40 (11) (2008) 2076-2082.

[8] G. Desogus, S. Mura, R. Ricciu, Comparing different approaches to in situ measurement of building components thermal resistance, Energy and Buildings 43 (2011) 2613-2620.

[9] E. Cuce, P.M. Cuce, The impact of internal aerogel retrofitting on the thermal bridges of residential buildings: An experimental and statistical research, Energy and Buildings 116 (2016) 449-454.

[10] F. Ascione, N. Branco, R.F. Masi, G.M. Mauro, M. Musto, G.P. Vanoli, Experimental validation of a numerical code by thin film heat flux sensors for the resolution of thermal bridges in dynamic conditions, Applied Energy 124 (2014) 213-222.

[11] M.H. Corvacho, Pontes térmicas, análise do fenómeno e proposta de soluções, PhD thesis, Faculdade de Engenharia da Universidade do Porto, Portugal, 1996 (in portuguese).

[12] International Organization for Standardization, ISO 8990: Thermal insulation - Determination of steady-state thermal transmission properties - Calibrated and guarded hot box, 1994.

[13] F. Asdrubali, G. Baldinelli, Thermal transmittance measurements with the hot box method: Calibration, experimental procedures, and uncertainty analysis of three different approaches, Energy and Buildings 43 (2011) 1618-1626.

[14] Y. Fang, P.C. Eames, B. Norton, T.J. Hyde, Experimental validation of a numerical model for heat transfer in vaccum glazing, Solar Energy 80 (2006) 564-577.

[15] K. Martín, I. Flores, C. Escudero, A. Apaolaza, J.M. Sala, Methodology for the calculation of response factors through experimental tests and validation with simulation, Energy and Buildings 42 (2010) 461-467.

[16] K. Martin, C. Escudero, I. Gómez, J. M. Sala, Analysis of a thermal bridge in a guarded hot box testing facility, Energy and Buildings 50 (2012) 139-149.

[17] G. Mao, Laboratory measurements and modelling of the dynamic thermal performance of a thermal bridge, Nordic Journal of Building Physics, 11 (1997-1998).

[18] European Standard, EN 12567-1: Thermal performance of windows and doors - Determination of thermal transmittance by the hot-box method - Part 1: Complete windows and doors, 2010.

[19] European Standard, EN 12412-2: Thermal performance of windows, doors and shutters. Determination of thermal transmittance by hot box method. Parte 2 – Frames, 2003.

[20] European Standard, EN 1946-4: Thermal performance of building products and components; Specific criteria for the assessment of laboratories measuring heat transfer properties; Part 4: Measurements by hot box methods, 2000.

[21] European Standard, EN 1745: Masonry and masonry products; Methods for determining thermal properties, 2012.

[22] European Standard, EN 1934: Thermal performance of buildings. Determination of thermal resistance by hot box method using heat flow meter. Masonry, 1998.

[23] A. Tadeu, I. Simões, N. Simões, J. Prata, Simulation of dynamic linear thermal bridges using a boundary element method model in the frequency domain, Energy and Buildings 43 (2011) 3685-3695.

[24] Hukseflux Thermal Sensors, User Manual HFP01/ HFP03, manual version 0612, June 2016.

[25] Hukseflux Thermal Sensors, User Manual TRSYS01 - High-accuracy building thermal resistance measuring system with two measurement locations, TRSYS01 manual v1620, 2016.

[26] APA - The engineered wood association. (c2016). Cross-Laminated Timber (CLT) - Retrieved 5 Abril, 2016, from http://www.apawood.org/cross-laminated-timber.

[27] International Organization for Standardization, ISO 8302: Thermal insulation - Determination of steady-state thermal resistance and related properties - Guarded hot plate apparatus, 1991.

[28] European Standard, EN 12667: Thermal performance of building materials and products. Determination of thermal resistance by means of guarded hot plate and heat flow meter methods. Products of high and medium thermal resistance, 2001.

[29] European Standard, EN 1602: Thermal insulating products for building applications. Determination of the apparent density, 1997.

CHAPTER 4

DYNAMIC BEHAVIOUR OF LINEAR THERMAL BRIDGES IN 2D BUILDING CORNERS

4 DYNAMIC BEHAVIOUR OF LINEAR THERMAL BRIDGES IN 2D BUILDING CORNERS

4.1 Introduction

During the last decade, a set of policies and measures was drafted by the European Union (EU), including the improvement of the energy performance of buildings by applying minimum requirements to the thermal and energy performance of new and existing buildings that undergo major renovation ([1],[2]). With these measures the improvement of the building envelope, particularly around the junctions of different building elements, corresponding to linear thermal bridges (LTBs), have gradually becoming even more important ([3],[4]).

Numerous works have been published on the characterization of stationary thermal behaviour of thermal bridges to assess their contribution to the overall energy performance of a building. The Intelligent Energy Europe project ASIEPI has developed a final report of their work on thermal bridges which includes international and national information from up to 17 EU Member States on thermal bridging [5]. The study shows that the total impact of thermal bridges on the heating energy needs is usually considerable and it can be as high as 30% as has been shown by Theodosiou and Papadopoulos [6]. However, the correct characterization of LTBs, in order to choose high-quality details, can reduce this impact considerably. Evola *et al*. [7] have shown that, in mild Mediterranean climate, the correction of thermal bridges can reduce the primary energy needs for heating up to 25%. Despite the high costs associated, interesting energy and environmental benefits may be achieved.

Heat losses through thermal bridges often lead to surface condensations, responsible for building pathologies. Ascione *et al*. [8] underlined the importance of modelling thermal bridges accurately, by using numerical approaches, in order to provide appropriate energy-retrofits and therefore to avoid these pathologies. Krarti [9] has studied the hygrothermal behaviour of an insulated building corner, using for that purpose a two-dimensional (2D) steady-state analytical formulation (The Interzone Temperature Profile Estimation (ITPE) technique). The results show that even reducing heat losses through thermal bridges by increasing the insulation thermal resistance, the risk of pathologies, due to the occurrence of surface condensation, increases near the walls junction.

Due to the complexity of multidimensional dynamic simulations, most studies on the thermal behaviour of constructive elements and thermal bridging analysis use steady-state approaches. For the same reason, most dynamic simulation programs for the thermal performance of buildings assume one-dimensional (1D) heat transfer and do not take into account the 2D dynamic heat flows that occur through the thermal bridges of building envelopes [10]. However, it might be very important to predict the dynamic thermal behaviour of LTBs at the buildings design stage, assuming temperature variation over time and so considering the influence of the thermal diffusivity of materials, responsible for the thermal phase lag ([11],[12]).

Mao and Johannesson [13] have analysed the dynamic behaviour of different types of LTBs, according to ISO 13786:2006 [14]. The results show that LTBs affect the dynamic characteristics of the building details such as the thermal amplitude and the thermal phase lag. Santos *et al*. [15] used the finite volume method and the MTDMA (multitridiagonal-matrix algorithm) to analyse the dynamic hygrothermal behaviour of a building corner by calculating the spatial distribution of temperature, partial vapour pressure and moist air pressure and determining the heat fluxes over time as well as the risk of mould developing due to surface condensation. The results show that near the corner, where the effect of convection and radiation is lower, the risk of these pathologies occurring is higher.

Other studies report the importance of predicting the dynamic thermal behaviour of LTBs and propose simplified numerical approaches to be implemented in dynamic simulation software in order to consider thermal bridging effects ([16],[17]). However, despite advances in thermal bridging analysis, there are still very limited studies demonstrating the dynamic thermal bridging effect in constructive details and how it depends on the materials' properties and on the boundary conditions of the problems.

In this chapter, the dynamic effect of a Linear Thermal Bridge (LTB) in a 2D building corner is analysed. The problem is solved using the numerical methodology presented in Chapter 2. The 2D boundary element model (BEM), formulated in the frequency domain, experimentally validated in Chapter 3, is used to simulate transient heat diffusion through the building corner. Three cases are analysed: walls without thermal insulation; walls with an external thermal insulation layer; walls with an internal insulation layer. Two different materials of the support walls (concrete and wood) are considered in the simulations. The simulations are first performed considering a sinusoidal variation of the external temperature over time. The dynamic heat fluxes though the LTB are compared with the linear thermal transmittances determined under steady-state conditions. The same case studies are then analysed, considering different thicknesses of the insulation layer (between 3 and 12 cm) and real climate data from four European cities. To better understand the importance of the dynamic behaviour of LTB, the heat loss across the LTB over time is compared with the heat loss through a plane wall, computed analytically and for the same boundary conditions. The influence of the constructive solutions and the external temperature variation on the dynamic thermal behaviour of the LTB is evaluated. The results under dynamic conditions are compared with the results obtained assuming steady-state conditions.

4.2 Problem definition

Figure 4.1 illustrates the LTB at the corner of a building (wall to wall junction). The external surface of the walls is subjected to a temperature variation $\left(T = T\left(x, y, t\right)\right)$, while the indoor temperature is assumed to be constant $T = T_0$. At a certain distance from the corner the heat flux becomes perpendicular to the wall (1D heat flux). Therefore, null heat fluxes can be prescribed along the cut-off sections.

The 2D dynamic heat transfer by conduction through the building corner can be computed using the proposed BEM formulation, presented in Chapter 2. The analytical solution, presented in the same chapter, can be used to compute the response at the two plane walls, where the problem is 1D. The two algorithms can be used together to compute the heat flow rate through the LTB over time.

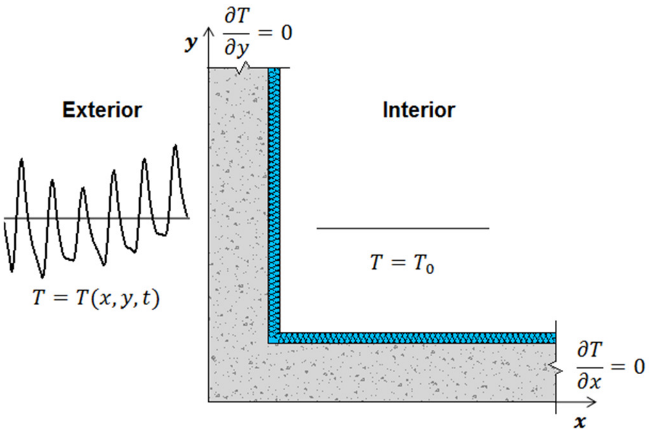

Figure 4.1: Building corner scheme and boundary conditions used to evaluate the dynamic behaviour of an LTB.

4.3 Case studies

The methodology proposed in Chapter 2 was used to simulate the heat transfer by conduction through a geometrical LTB, corresponding to a wall to wall junction in a 2D building corner. Three cases were simulated, as illustrated in Figure 4.2: the wall without thermal insulation (Case 1); the wall with an external thermal insulation layer (Case 2); the wall with an internal thermal insulation layer (Case 3). Two materials were considered for the wall: concrete (Figure 4.2 a)) and wood (Figure 4.2 b)). The surfaces' thermal resistances are modelled as thin air layers on the inner and outer surfaces to take into account convection and radiation phenomena. Thermal resistance for the inner surface was assumed to be 0.13 m^2.ºC/W and for the outer surface it was 0.04 m^2.ºC/W according to ISO 6946:2007 [18].

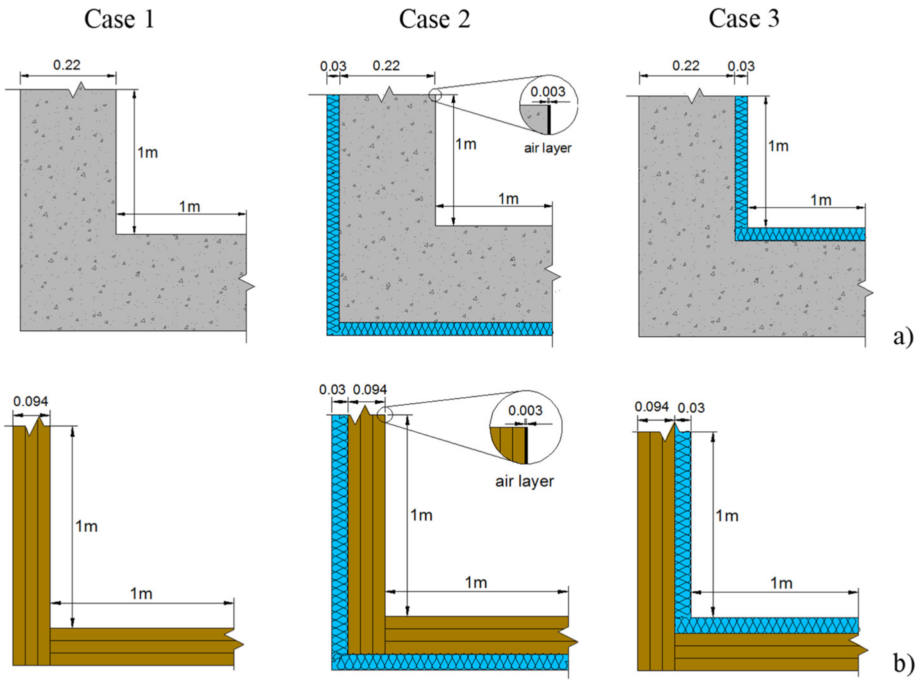

Figure 4.2: Building corner geometry used in the numerical applications: Case 1 – the wall without any insulation; Case 2 – the wall with a thermal insulation layer on the outside surface; Case 3 - the wall with a thermal insulation layer on the inside surface (dimensions in m). a) Concrete corner; b) Wooden corner.

The thermal conductivity, the mass density and the specific heat of each material were characterized experimentally. The thermal conductivity was evaluated by the Guarded Hot-Plate Method (ISO 8302:1991 [20]) using a Lambda-Meßtechnik GmbH Dresden apparatus, single-specimen Lambda-meter EP-500 model, following the test procedure defined in EN 12667:2001 [21]. The mass density was determined using the procedure described in EN 1602:1996 [22]. The specific heat was obtained using a Netzsch apparatus, model DSC200F3, following the ratio method. The thermal properties of the materials are listed in Table 4.1

Table 4.1: Materials' thermal properties.

Material	Thermal conductivity $\lambda\left(\mathrm{W.m^{-1}.{}^{o}C^{-1}}\right)$	Density $\rho\left(\mathrm{kg.m^{-3}}\right)$	Specific heat $c\left(\mathrm{J.kg^{-1}.{}^{o}C^{-1}}\right)$
Thermal insulation (Natural cork)	0.046	130.00	1638.00
Wood	0.13	574.70	1406.60
Concrete	1.40	2300.00	880.00
External surface layer 3mm thick	0.075	1.29	1000.00
Internal surface layer 3mm thick	0.0231	1.29	1000.00

The corner is modelled as adjacent lateral walls long enough to ensure that the heat transfer at the cut-off sections is not affected by the presence of the LTB formed at the junction of the walls. Thus, null heat fluxes can be prescribed along those cut-off sections, in their normal direction. In the examples (Figure 4.2), the length of the wall followed ISO 10211:2007 [19], enabling a length of 1 m to be applied.

The heat flow rates through the different configurations of LTB can be determined. First, the heat flow rate, per metre length, ϕ_l, is computed for the global system, $\phi_{l,total}$ (in W/m), using the BEM model proposed in Chapter 2. $\phi_{l,total}$ includes the heat flow rate, per metre length, associated with the LTB ($\phi_{l,LTB}$) and the heat flow rate, per metre length, crossing the lateral walls ($\phi_{l,walls}$), $\phi_{l,total} = \phi_{l,LTB} + \phi_{l,walls}$. The heat flow rate $\phi_{l,walls}$ can be calculated by imposing 1D heat transfer on the lateral walls, using the analytical model proposed in the Chapter 2. The $\phi_{l,LTB}$ is then obtained by computing the difference between the interior global heat flow rates $\phi_{l,LTB} = \phi_{l,total} - \phi_{l,walls}$.

The computations of the $\phi_{l,total}$ and $\phi_{l,walls}$ are performed by integrating the heat fluxes along the inner wall surface. When the problem is solved under steady-state conditions, any other integration line through the system, connecting both cut-off sections would give the same result (e.g. along the outer wall surface). When the problem is dynamic, the position of the line over which the global heat flux is computed is determinant, since it leads to distinct values because of the thermal delay effects. In this work, the inner surface was selected because this is where moisture condensation and pathologies often occur, and because it is this wall surface that is relevant to evaluating the heat flow.

Finally, the linear thermal transmittance, over time, is computed by dividing the $\phi_{l,LTB}$ by the amplitude difference of the imposed indoor and outdoor temperatures (θ_1 and θ_2, respectively) at the corresponding time, $\phi_{l,LTB} / (\theta_1 - \theta_2)$, in W/(m°C).

The wall's longitudinal material interfaces were discretized, when modelled by the BEM, by 100 constant boundary elements, while 60 constant boundary elements were used to model the lateral cut-off sections. The temperature distribution was obtained at a very fine 2D grid of receivers equally spaced $0.01\,\text{m}$ along the x and y directions.

4.3.1 Steady-state conditions

To illustrate the importance of computing LTBs dynamically, the problem was first solved assuming a steady-state condition, by imposing time independent indoor and outdoor temperatures. The steady-state computations were performed using the proposed BEM and analytical model, imposing a null frequency with a small imaginary part, $\omega_c = -i\eta$ ($\eta = 0.7\Delta\omega$, with $\Delta\omega$ being nearly zero, $\Delta\omega = 1.0 \times 10^{-40}$ Hz).

Figure 4.3 shows the temperature distribution obtained, for each case study, when the exterior and interior temperatures were 15 ºC and 20 ºC, respectively.

Table 4.2 gives the static linear thermal transmittance, ψ, in W/(m.ºC) computed for each case study, following the methodology described above.

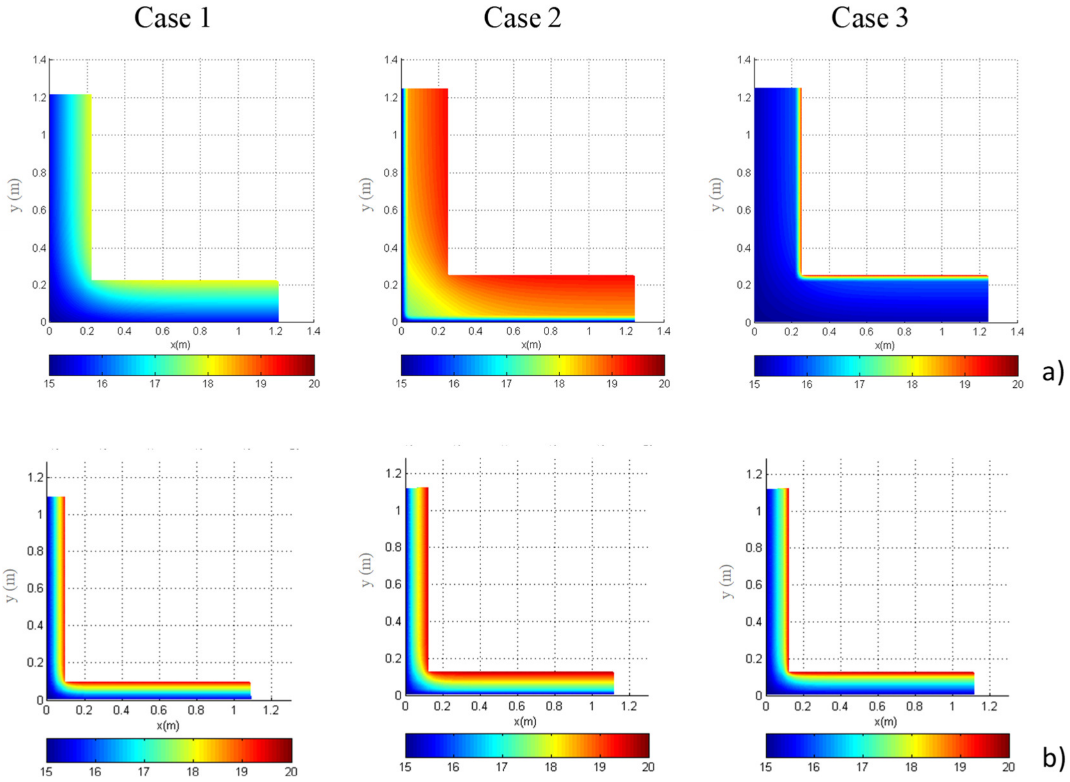

Figure 4.3: Temperature distribution (in ◦C) across the wall representing the corner of a building under steady-state conditions: Outdoor – 15 °C; Indoor – 20 °C - a) concrete building corner; b) wooden building corner.

Table 4.2: Linear thermal transmittance, ψ, computed for each case study

	Concrete building corner	Wooden building corner
	$\psi\ \left(\mathrm{W.m^{-1}.{}^{o}C^{-1}}\right)$	$\psi\ \left(\mathrm{W.m^{-1}.{}^{o}C^{-1}}\right)$
Case 1	0.236	0.033
Case 2	0.282	0.042
Case 3	0.040	0.026

As expected, lower surface temperatures were found in Case 1 while Case 3 recorded the lowest temperatures inside the wall. This is more evident in the concrete corner, where the thermal resistance of the walls is lower. For both constructive solutions (concrete and wood), Case 2 showed the largest thermal bridge contribution in terms of its heat flux pattern. This behaviour, together with the high thermal resistance exhibited by the lateral wall, yielded to a larger value of ψ. The concrete corner presents ψ values considerably higher than the wooden corner.

4.3.2 Unsteady-state conditions

In this section, the thermal bridging effect in the 2D building corner case studies is analysed under dynamic conditions. The simulations were first performed considering a sinusoidal variation of the external temperature over time. Then, the influence of the constructive solutions and the external temperature variation on the dynamic thermal behaviour of the LTB is evaluate. For that purpose, the same cases were simulated considering different thicknesses of the insulation layer (between 3 and 12 cm) and real climate data from four European cities.

4.3.2.1 Sinusoidal temperature variation

Figure 4.4 illustrates the imposed internal and external temperature variation over time. The different wall systems were assumed to have a constant initial temperature of 20 ºC. Non-uniform initial conditions could be imposed throughout the domain, but this would make the BEM model mathematically more elaborate. At $t = 0.0$ h, they were all subjected to an exterior temperature change. The temperature time dependence was assumed to be sinusoidal, with a period of 24 h, and with amplitude oscillations of 15 °C. The indoor temperature was kept at 20 °C. Since the full domain has an initial uniform temperature of 20 °C, 6 cycles were considered in the simulations to guarantee that, at the end of the time window, the system has similar repetitive responses in each 24 h cycle.

The frequency domain of computation ranged from 0.0 Hz to 4096/(144×3600) Hz, with a frequency increment of 1/(144×3600) Hz, which determined a total time window of 144 h for the analysis. The BEM model was implemented using the same boundary discretization as described in Section 4.3.

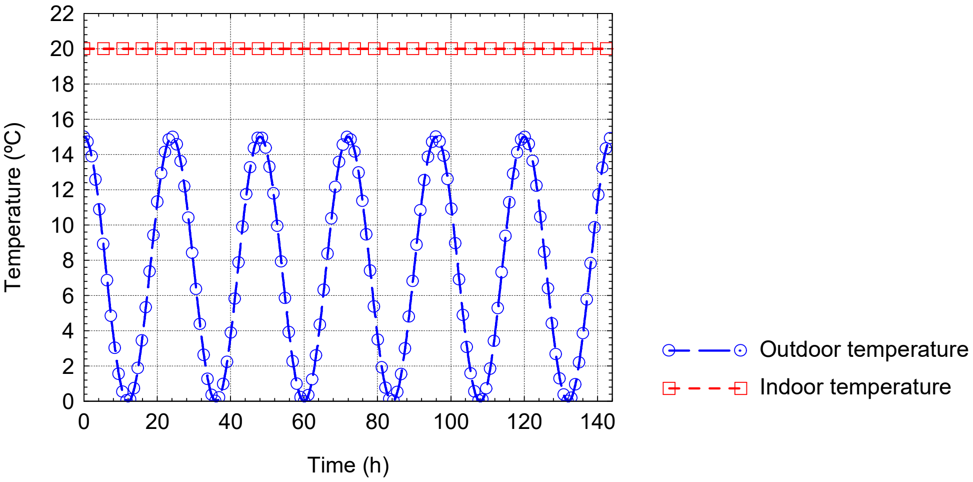

Figure 4.4: Imposed temperature over time: sinusoidal change in the outdoor environment temperature (6 cycles of 24h); constant indoor temperature.

The temperature distribution was computed in the same grid of receivers used to compute the static response (see Section 4.3). A set of snapshots of the time domain simulations is presented to illustrate the resulting heat diffusion across the LTBs in the concrete building corner, where the thermal bridging effect is more pronounced. Figure 4.5 shows the temperature field distribution at different time instants. A colour scale is used in the plots, with the red and blue shades corresponding respectively to higher and lower temperature amplitudes.

In the first plot, at $t \approx 6.0$ h (Figure 4.5 a)), after the exterior temperature had already dropped from 15 °C to 7.5 °C, the temperature decrease in the wall can be seen, particularly in Case 1 and Case 3. In Case 2 the presence of the exterior thermal insulation determined a delay in heat propagation. Here, the highest temperatures were recorded inside the concrete wall.

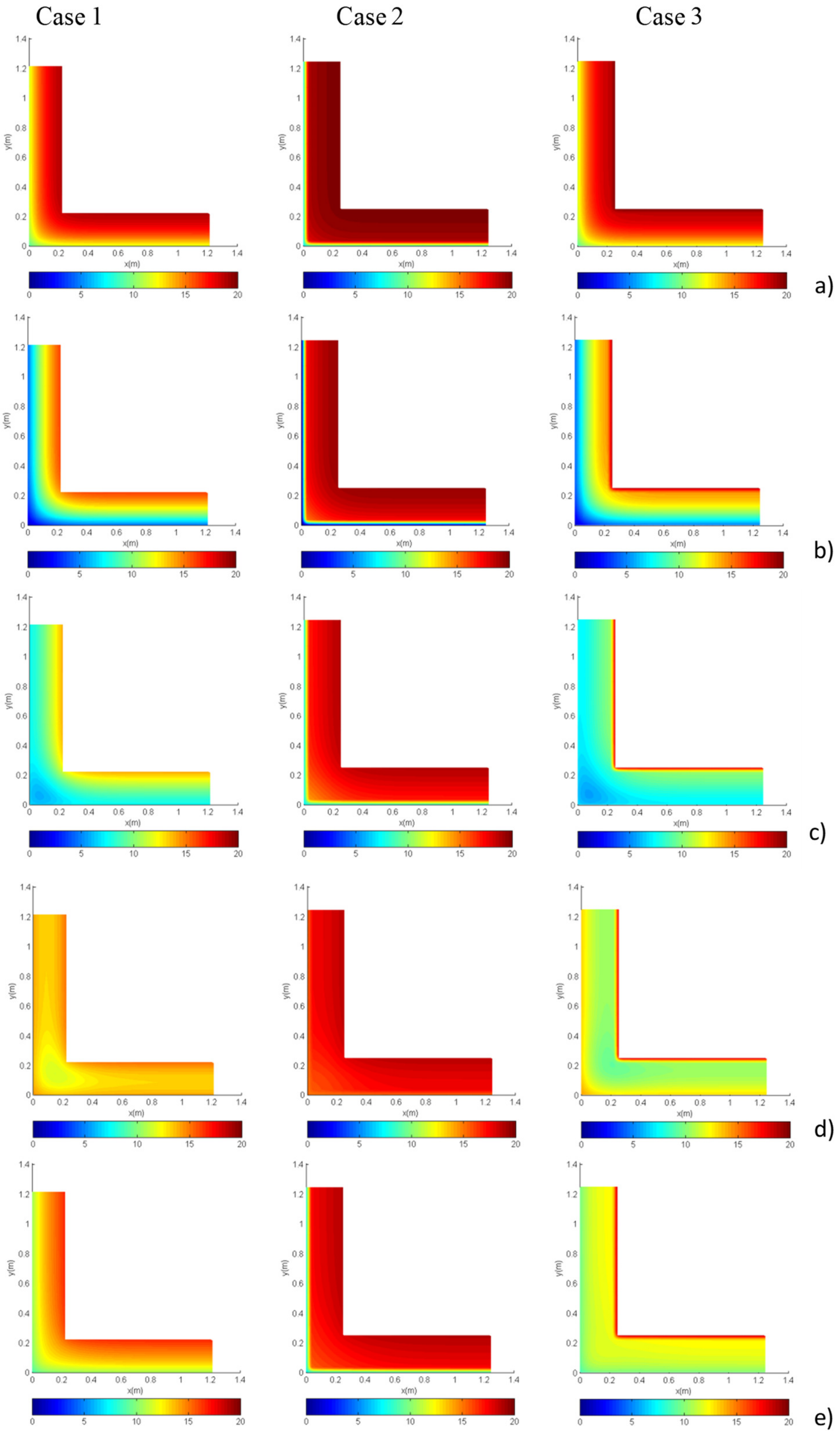

Figure 4.5: Temperature distribution (in ◦C) across the wall representing the corner of a building. Time responses at a) $t \approx 6.0$ h ; b) $t \approx 12.0$ h ; c) $t \approx 18.0$ h ; d) $t \approx 24.0$ h ; e) $t \approx 30.0$ h .

At $t \approx 12.0\,\mathrm{h}$ (Figure 4.5 b)), the exterior temperature had fallen to 0 °C. The heat transfer behaviour, in terms of fluxes direction, described at $t \approx 6.0$ h is similar. The temperature distribution in Cases 1 and 3 is quite different from that registered by Case 2. Differences between Cases 1 and 3 can now be seen: the contribution of the interior insulating layer can be perceived in Case 3.

As time passed, the exterior temperature rose and at $t \approx 18.0\,\mathrm{h}$ it again stood at 7.5 °C (Figure 4.5 c)). Although the exterior temperature had already increased from 0 °C to 7.5 °C, the temperature was still decreasing in some regions of the domain, close to the interior surface, showing the existence of a thermal phase lag. At this instant, the presence of the thermal insulating layer in Case 3 is clearly visible, as the temperatures on the interior surface bear out.

At $t \approx 24.0\,\mathrm{h}$ (Figure 4.5 d)), the exterior temperature had increased to 15 °C. The temperature increase at the receivers placed closed to the exterior is very clear. At this instant, in Case 1 and, particularly, in Case 3, the temperature is lower inside the wall than close to the surface. So, we may conclude that the heat flows from both walls' surfaces to their interior.

In the last snapshot, taken at $t \approx 30.0$ h (Figure 4.5 e)), the exterior temperature change had already started a new cycle. It had again reached 7.5 °C. The thermal phase lag is evidenced in cases 1 and 3, with lower temperature in the interior domain than in the inner and outer walls surfaces. The temperature distribution differed from that registered at the same phase $t \approx 6.0\,\mathrm{h}$, since at $t = 0.0\,\mathrm{h}$ the wall systems registered a uniform temperature of 20 °C. However, as the time passed, the systems tended to behave periodically and exhibit similar temperature and flux distribution for equivalent phases.

Figure 4.6 a) and Figure 4.6 b) present the variation of the heat flow rate through the LTB, $\phi_{l,LTB}$ and the variation of the dynamic linear thermal transmittance, $\phi_{l,LTB}/(\theta_1 - \theta_2)$, over time, respectively, determined according to the methodology described in Section 4.3. Figure 4.6 b) also includes the ψ values computed above for steady-state conditions, represented by straight lines.

For all the three cases, the heat flow rates in the LTB, over time, are significantly lower in the wooden corner detail. This difference is, however, less expressive when the insulation is placed on the inner surface of the wall (Case 3). This case presents the lowest heat flow rates, over time, for the two details (concrete and wood).

For the concrete building corner, Figure 4.6 a) and Figure 4.6 b), show that the responses of the Cases 1 and 3 are the firsts to start behaving cyclic, almost in a 24 h cycle. By contrast, the Case 2 system requires more time to reach the cyclic behaviour. Figure 4.6 a) shows that, after Case 2 starts behaving cyclic, the heat flow amplitude over time is similar in Case 2 and Case 3. However, the maximum absolute heat flow values reached in Case 2 are similar to the ones reached in Case 1. It can also be seen that these variations in heat flow over time are significantly smaller than those exhibited by Case 1.

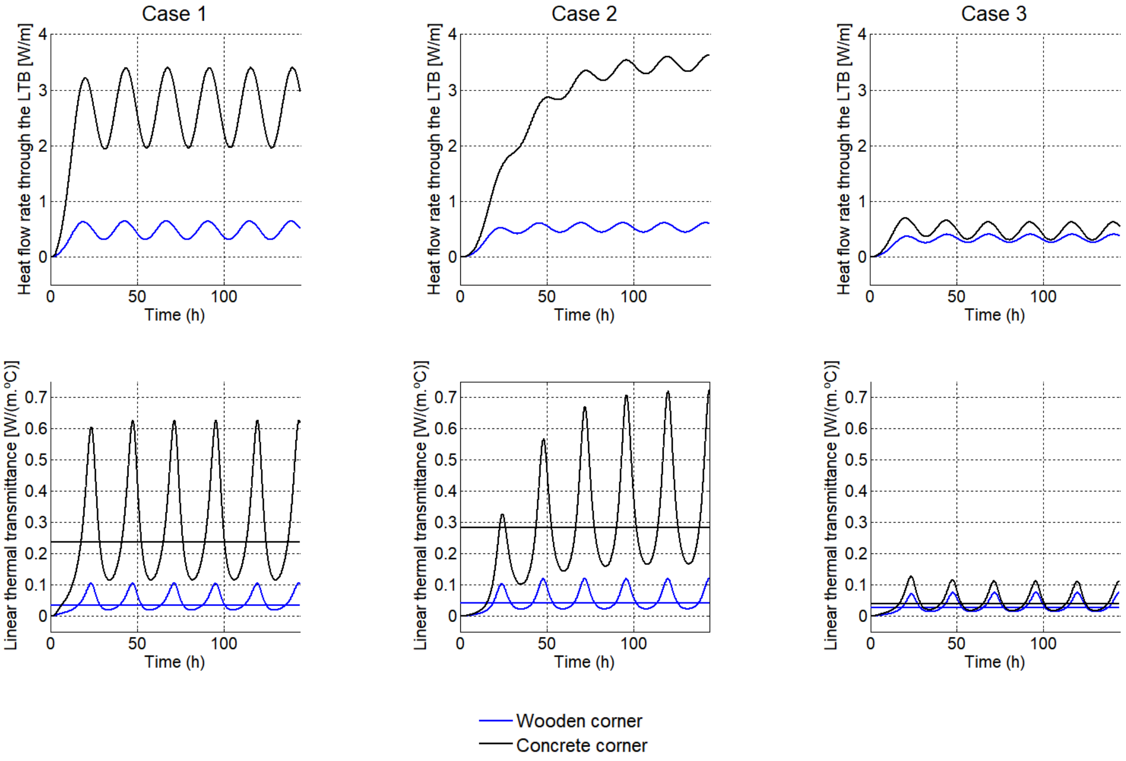

Figure 4.6: Dynamic behaviour of the LTB: a) difference of interior global heat flow rates $\phi_{l,total} - \phi_{l,walls}$; b) dynamic linear thermal transmittance $\left(\phi_{l,total} - \phi_{l,walls}\right)/\left(\theta_1 - \theta_2\right)$.

For the wooden building corner, Figure 4.6 a) shows that the heat flow amplitudes in Cases 2 and 3 are similar. In Case 1 the heat flow amplitude is significantly higher. On the other hand, Figure 4.6 b) shows that the dynamic linear thermal transmittance amplitude in Case 3 is considerably lower than in the other 2 cases.

Figure 4.6 b) shows that the dynamic linear thermal transmittances reach considerably higher values than those obtained in steady-state conditions: 2.8 times higher in Case 3; 2.5 times higher in Case 2; 2.6 times higher in Case 1, for the concrete corner. For the wooden corner detail, the dynamic linear thermal transmittances are 3 times higher in Case 1; 2.9 times higher in Case 2 and 2.7 times higher in Case 3, when compared with steady-state analyses.

For all the case studies, the dynamic heat loss through the LTBs reaches higher values over a cycle than those considered in steady-state conditions. Therefore, surface temperatures at the inner face of the wall will be lower than those estimated in a static analysis. Thus, following the dynamic analysis, a higher risk of surface condensation is expected than for the results provided by a static simulation, that is, assuming a steady-state.

4.3.2.2 Real climate data

The dynamic thermal behaviour of the LTB was analysed for the first 6 days of the year, considering climate data from four European cities (Figure 4.7): Évora (Portugal), Bragança (Portugal), Amsterdam (Netherlands) and Helsinki (Finland). The average annual heating degree days for each of the cities are: 1150 (Évora), 2015 (Bragança), 2940 (Amsterdam) and 4394 (Helsinki).

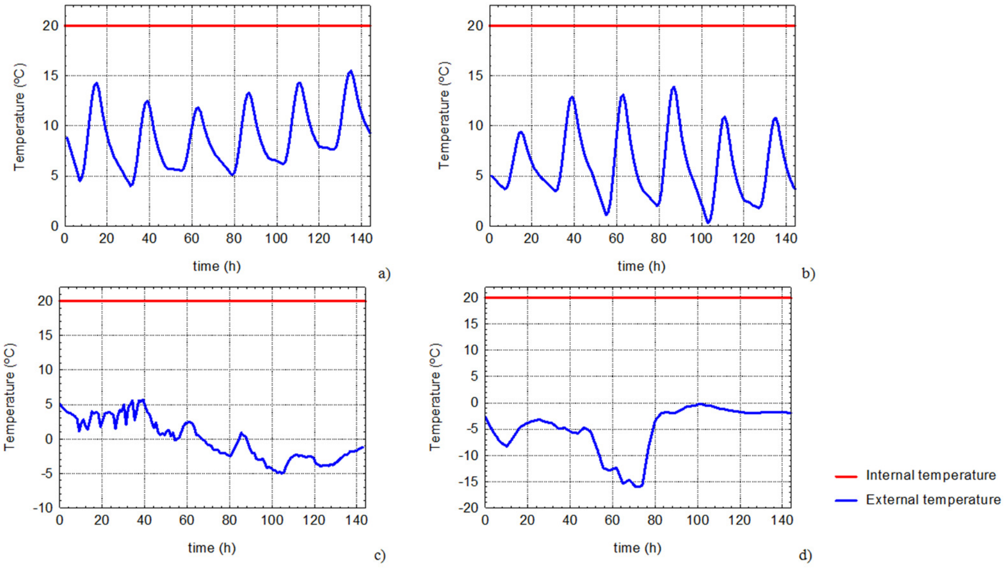

Figure 4.7: Temperature over time. Climate data related to the first 6 days of the year: a) Évora (Portugal); b) Bragança (Portugal); c) Amsterdam (Netherlands); d) Helsinki (Finland).

The methodology described in Section 4.3 was used to compute the heat flow rate across the LTB $\left(\phi_{l,LTB}\right)$ over time. The simulations were performed for each case study (Figure 4.2), using the climate data indicated in Figure 4.7. An initial period of 48 h before registering the results was considered at the simulations. Over this period, the initial values of the boundary conditions' function are kept constant and the same as those observed at $t = 0.0$ h to attain steady-state conditions up to the first-time step of the dynamic simulations, ($t = 0.0$ h).

The frequency domain for the computation ranged from 0.0 Hz to $4096/(192 \times 3600)$ Hz, with a frequency increment of $1/(192 \times 3600)$ Hz, which determined a total time window of 192 h for the analysis.

The simulations of Cases 2 and 3 were performed for different thicknesses for the thermal insulation layer (3 cm, 6 cm and 12 cm) and the responses were compared with those obtained in the simulations of Case 1 (no insulation). The results for the concrete corner and for the wooden corner are shown in Figure 4.8 and in Figure 4.9, respectively.

It can be seen that the heat flow across the LTB varies with the external boundary conditions. The variation of the heat flow amplitude is greatest in case 1 (no insulation). The heat flow in Case 3 is significantly lower. The variation of the heat flow amplitudes with the insulation thickness and with the climate data is greatest in Case 2. When the insulation layer is thicker the heat loss in Case 2 declines significantly. It can also be seen that the heat loss through the wooden corner is significantly lower than it is for the concrete corner.

The total heat loss that occurs through 1 m of LTB over the 6 days of simulation ($q_{1m\ LTB}$), in Wh, was then computed for each case study and compared with the total heat loss through a wall 1 m^2 in area ($q_{1m^2\ \mathrm{wall}}$), in Wh. The results are presented in Table 4.3 and in Table 4.4, for the concrete corner and for the wooden corner, respectively.

The total heat loss through the LTB was then divided by the total heat loss through the wall to obtain the ratio between the two losses, for each wall configuration and taking into account the four climate data sets (Figure 4.7). The results are shown in Figure 4.10.

According to the results presented in Figure 4.10, the ratio increases for greater insulation layer thickness and is higher when the insulation layer is applied to the outside of the wall. However, the ratio does not significantly depend on the external temperature variation, since the differences between the ratio values obtained for the different countries are very small.

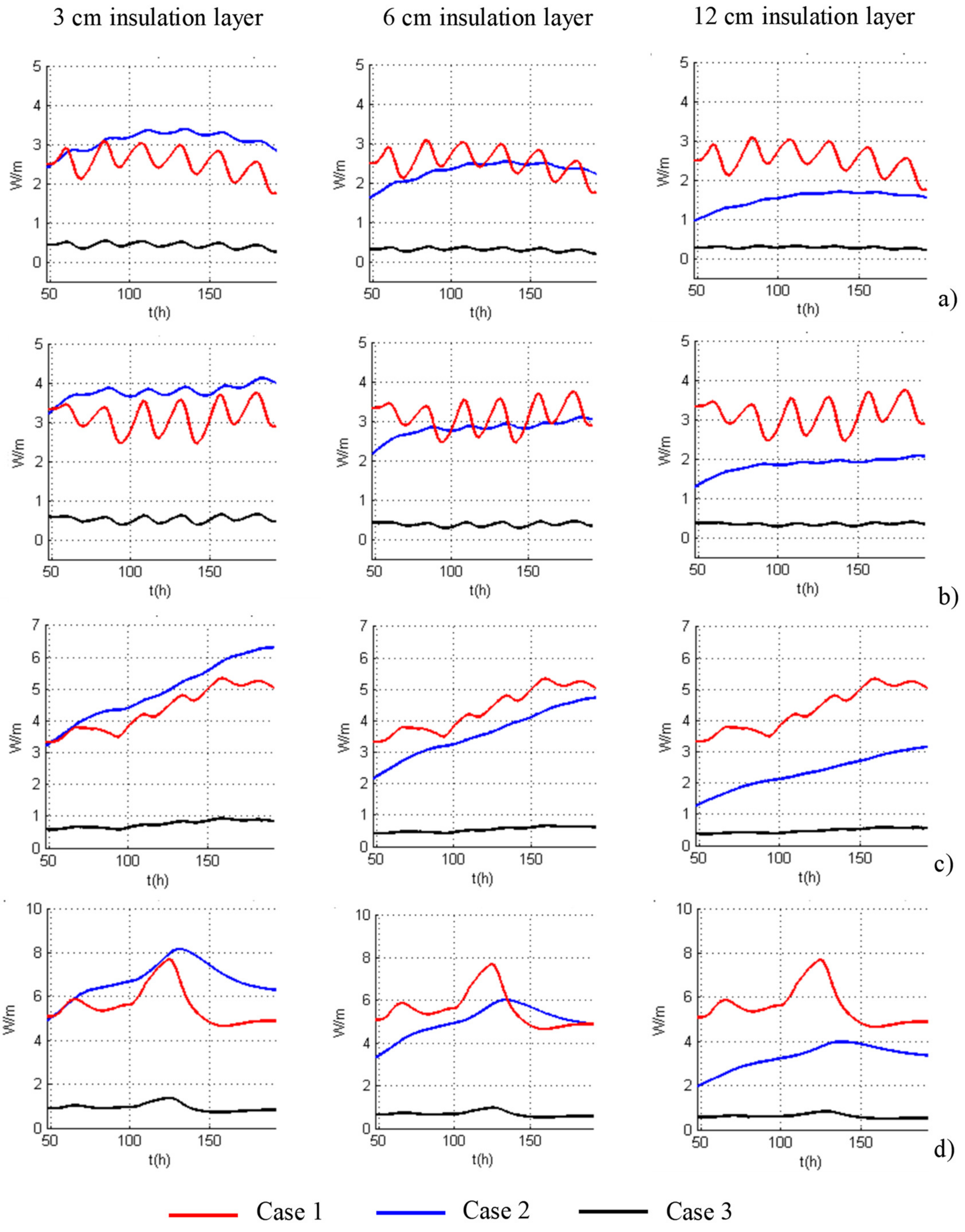

Figure 4.8: Variation of the heat flow rate through the LTB $\left(\phi_{l,LTB}\right)$, over time, in the concrete corner for each set of climate data, taking into account the placement and the thickness of the insulation layer – a) Évora (Portugal); b) Bragança (Portugal); c) Amsterdam (Netherlands); d) Helsinki (Finland).

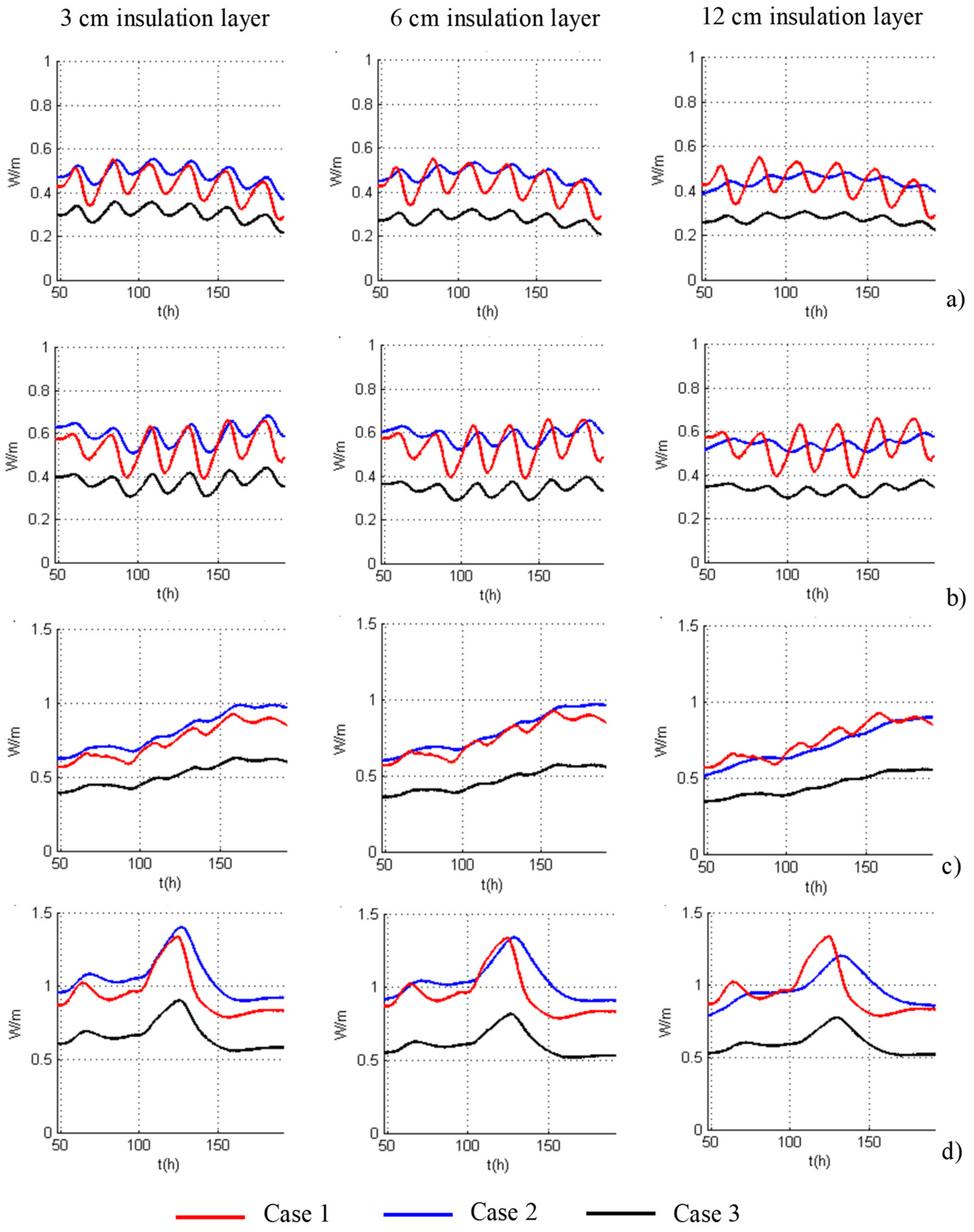

Figure 4.9: Variation of the heat flow rate through the LTB $(\phi_{l,LTB})$, over time, in the wooden corner for each set of climate data, taking into account the placement and the thickness of the insulation layer – a) Évora (Portugal); b) Bragança (Portugal); c) Amsterdam (Netherlands); d) Helsinki (Finland).

Table 4.3: Total heat loss through 1m of LTB $\left(q_{1m\ LTB}\right)$ and the total heat loss through a wall with 1m^2 $\left(q_{1m^2\ wall}\right)$ of area, during the 6 days of simulation - concrete corner.

Concrete corner cases								
Place	Total heat loss	Case 1 (no insulation)	Case 2 (external insulation)			Case 3 (internal insulation)		
			3cm	6cm	12cm	3cm	6cm	12cm
Évora	$q_{1m^2\ wall}$ [Wh]	5005.2	1674.3	1001.1	554.0	1679.3	1009.3	562.6
	$q_{1m\ LTB}$ [Wh]	367.0	448.5	333.2	219.8	61.6	44.6	40.3
Bragança	$q_{1m^2\ wall}$ [Wh]	6182.3	2051.7	1225.3	676.7	2066.3	1240.3	689.5
	$q_{1m\ LTB}$ [Wh]	452.7	546.9	406.2	267.9	76.3	54.7	49.5
Amsterdam	$q_{1m^2\ wall}$ [Wh]	8610.9	2559.7	1634.9	892.5	2837.3	1694.5	932.0
	$q_{1m\ LTB}$ [Wh]	627.1	709.1	519.2	337.5	107.5	76.7	67.7
Helsinki	$q_{1m^2\ wall}$ [Wh]	11000.0	3653.2	2181.9	1204.9	3675.5	2205.9	1225.7
	$q_{1m\ LTB}$ [Wh]	804.6	974.7	723.4	476.5	135.2	97.0	87.8

Table 4.4: Total heat loss through 1 m of LTB $\left(q_{1m\ LTB}\right)$ and the total heat loss through a wall 1 m^2 in area $\left(q_{1m^2\ wall}\right)$, over the 6 days of simulation - wooden corner.

Wooden corner cases								
Place	Total heat loss	Case 1 (no insulation)	Case 2 (external insulation)			Case 3 (internal insulation)		
			3cm	6cm	12cm	3cm	6cm	12cm
Évora	$q_{1m^2\ wall}$ [Wh]	1466.6	931.0	681.8	444.4	929.9	681.1	444.4
	$q_{1m\ LTB}$ [Wh]	62.5	70.0	69.2	64.1	43.8	40.3	39.5
Bragança	$q_{1m^2\ wall}$ [Wh]	1817.1	1148.4	838.9	544.5	1147.9	838.8	545.0
	$q_{1m\ LTB}$ [Wh]	77.3	85.9	84.6	78.2	53.9	49.5	48.4
Amsterdam	$q_{1m^2\ wall}$ [Wh]	2558.2	1592.0	1152.1	735.6	1595.6	1156.2	739.6
	$q_{1m\ LTB}$ [Wh]	107.8	117.0	113.6	102.9	74.2	67.6	65.0
Helsinki	$q_{1m^2\ wall}$ [Wh]	3238.5	2042.2	1491.2	967.9	2041.8	1491.0	968.4
	$q_{1m\ LTB}$ [Wh]	137.4	152.6	150.6	139.7	95.8	88.0	86.1

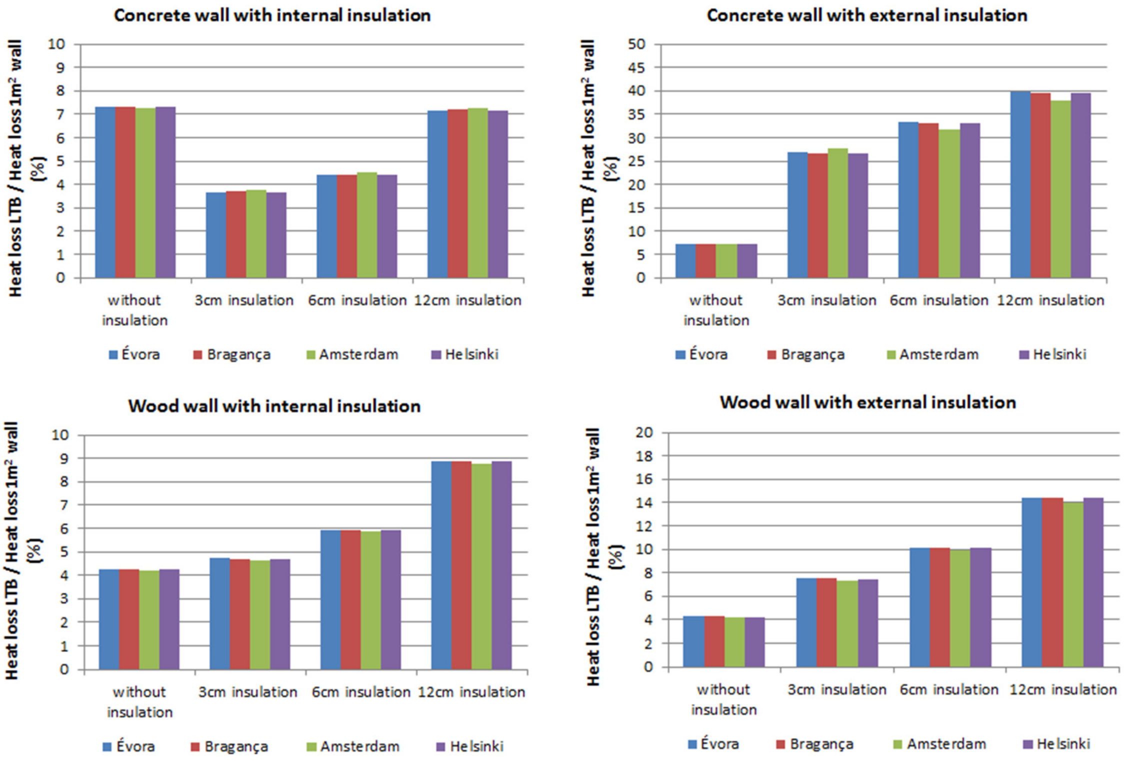

Figure 4.10: Ratio between the total heat loss though the LTB and the total heat loss though 1 m^2 of wall, taking into account the climate data from Évora, Bragança, Amsterdam and Helsinki.

A mean average ratio was then calculated for each wall configuration (Figure 4.2), taking into account the results for the different climate data shown in Figure 4.7. The average ratio given by the dynamic simulations for each wall configuration were then compared with the results obtained assuming steady-state conditions. The proposed 2D BEM model was used to compute the steady-state response, which occurs when the frequency is zero. The results are presented in Figure 4.11. The average ratio results of the dynamic numerical simulations for each wall configuration are similar to those obtained assuming steady-state conditions. Thus, the ratio between the total heat loss through the LTB and the total heat loss through 1 m^2 of wall surface does not depend on the external temperature variation. Therefore, it can be concluded that the effective percentage contribution of the LTB to the thermal performance of a building envelope in the dynamic simulation of buildings may have the same importance as in a steady-state analysis.

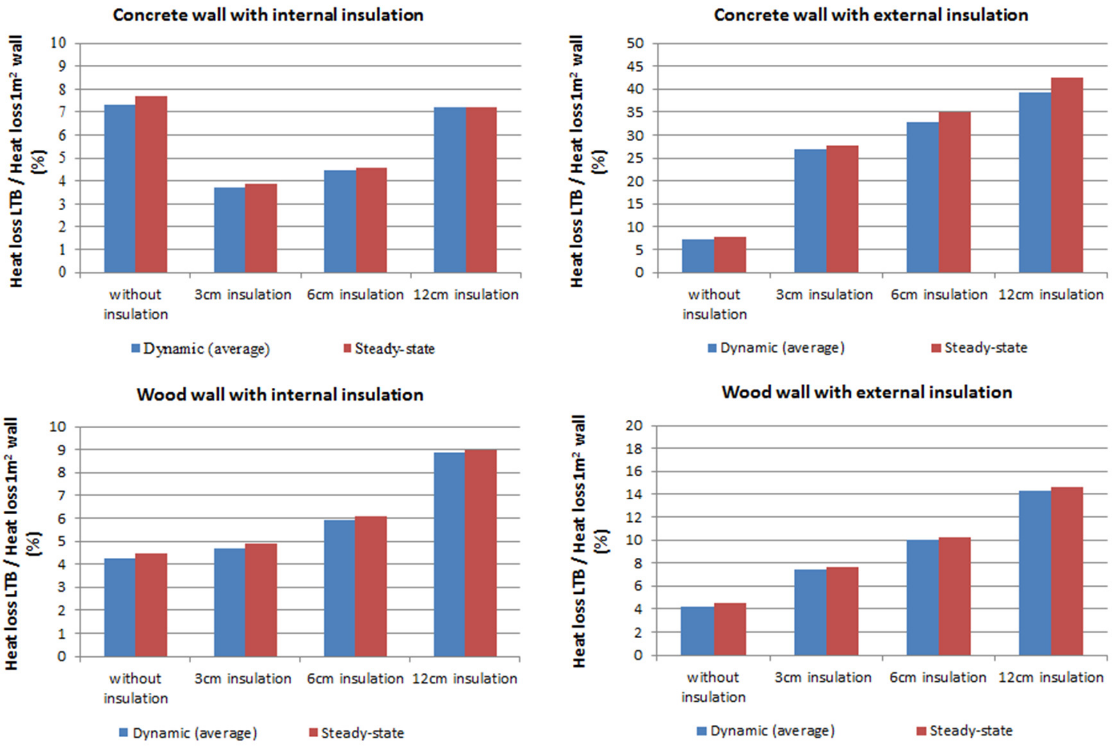

Figure 4.11: Mean average ratio between the total heat loss though the LTB and the total heat loss though 1 m^2 of wall: comparison between the dynamic and steady-state results.

4.4 Conclusions

In this chapter, the simulation of the transient heat diffusion through a linear thermal bridge (LTB), corresponding to a wall building corner, has been presented. Several simulations were analysed for two materials, concrete and wood, and with the insulation layer having different placements and thicknesses. For each simulation, the BEM model and the analytical solution, presented in Chapter 2, were used together to compute the heat flow rate through the LTB. The importance of modelling the LTBs dynamically was shown.

The computations showed that the variation of the heat flow rate in the LTB strongly depends on the building materials and on the constructive detail. Furthermore, the linear thermal transmittances obtained under dynamic conditions reach values significantly higher than the ψ values determined under steady-state conditions. Thus, a static analysis may overestimate the wall's surface temperatures in the vicinity of the LTB, leading to significant errors in the assessment of moisture condensation risk in these junctions.

It can be concluded that the analysis of the dynamic thermal bridging effect can be very important, in order to avoid surface condensation and the associated pathologies. Therefore, the choice of the constructive details of LTB, in the building design phase, should take into account, not only the thermal resistance of materials, but also their specific heat and density, which are responsible for their dynamic thermal effects, such as the thermal inertia and the thermal phase lag.

A sensitivity analysis was performed to analyse the influence of the constructive solutions and the external temperature variation on the dynamic thermal behaviour of the LTB. The results showed that the ratio between the total heat loss through 1 m of LTB and the total heat loss through 1 m^2 of wall surface varies with the thermal resistance of the constructive elements and with the placement of the insulation layer. However, it was observed that this ratio does not depend on the external temperature variation. Furthermore, the average ratio results of the dynamic numerical simulations are similar to those found for steady-state conditions. These results allow us to conclude that the effective percentage contribution of the LTB to the thermal performance of buildings envelope in the dynamic simulation of buildings may have the same importance as in a steady-state analysis. Therefore, linear thermal bridges shall not be neglected during the dynamic energy simulation of buildings.

References

[1] Directive no. 2002/91/EC of the European Parliament and of the Council of 16 December on the energy performance of buildings, Official Journal of the European Union, Brussels, 4 January 2003, pp. 65–71.

[2] Directive no. 2010/31/UE of the European Parliament and of the Council of 19 May on the energy performance of buildings, Official Journal of the European Union, Brussels, 18 June 2010, pp. 153/13 -153/35.

[3] F. Déqué, F. Ollivier, J.J. Roux, Effect of 2D modelling of thermal bridges on the energy performance of buildings: numerical application on the Matisse apartment. Energy and Buildings 33-(6) (2001) 583–7.

[4] P. Levin, G. Mao, The importance of thermal bridges for new Swedish multi-family buildings. Proc. 3rd Syrup. Building Physics in the Nordic Countries, Fredriksdal, Denmark, 1993, pp. 99-107.

[5] H. Erhorn, H. Erhorn-Klutting, M. Citterio, M. Cocco, D. Orshoven, A. Tilmans, P. Schild, P. Bloem, K.E. Thomsen, J. Rose, An effective handling of thermal bridges in the EPBD context, final report of the IEE ASIEPI work on thermal bridges, March 2010.

[6] T. Theodosiou, A. Papadopoulos, The impact of thermal bridges on the energy demand of buildings with double brick wall constructions. Energy and Buildings 40 (2008) 2083-2089.

[7] G. Evola, G. Margani, L. Marletta, Energy and cost evaluation of thermal bridge correction in Mediterranean climate, Energy and Buildings 43 (2011) 2385-2393.

[8] F. Ascione, N. Bianco, F. D. Rossi, G. Turni, G. P. Vanoli, Different methods for the modelling of thermal bridges into energy simulation programs: Comparisons of accuracy for flat heterogeneous roofs in Italian climates, Applied Energy (2012) 1-14.

[9] M. Krarti, Heat Loss and moisture condensation for wall corners of buildings, Int. Heat Mass Transfer 41(4-5) (1998) 681-689.

[10] K. Martin, A. Erkoreka, I. Flores, M. Odriozola, J.M. Sala, Problems in the calculation of the thermal bridges in dynamic conditions, Energy and Buildings 43 (2011) 529-535.

[11] G. Mao, G. Johannesson, Dynamic calculation of thermal bridges, Energy and Buildings 26 (1997) 233-240.

[12] I. Simões, N. Simões, A. Tadeu, Thermal Delay Simulation in Multilayer Systems using Analytical Solutions. *Energy and Buildings* (2012), doi: 10.1016/j.enbuild.2012.03.005.

[13] A.C. Andersson, G. Johannesson, Application of frequency responses for fast analysis of two-dimensional heat-flow problems, Coden LUTVDDG/(TVBH-7072)/1-8, Lund, Sweden, 1983.

[14] International Organization for Standardization, ISO 13786, Thermal performance of building components - Dynamic thermal characteristics -Calculation methods, 2006.

[15] G.H. Santos, N. Mendes, P.C. Philippi, A building corner model for hygrothermal performance and mould growth risk analyses, International Journal of Heat Transfer and Mass Transfer 52 (2009) 4862-4872.

[16] Y. Gao, J.J. Roux, L.H. Zhao, Y. Jiang, Dynamical building simulation: A low order model for thermal bridges losses, Energy and Buildings 40 (2008) 2236-2243.

[17] K. Martin, C. Escudero, A. Erkoreka, I. Flores, J.M. Sala, Equivalent wall method for dynamic characterisation of thermal bridges, Energy and Buildings 55 (2012) 704–714.

[18] International Organization for Standardization, ISO 6946: Building components and building elements - Thermal resistance and thermal transmittance - Calculation method, 2007.

[19] International Organization for Standardization, ISO 10211, Thermal bridges in building construction - Heat flows and surface temperatures - Detailed calculations, 2007.

[20] International Organization for Standardization, ISO 8302: Thermal insulation – Determination of steady-state thermal resistance and related properties – Guarded hot plate apparatus, 1991.

[21] European Standards, EN 12667: Thermal performance of building materials and products. Determination of thermal resistance by means of guarded hot plate and heat flow meter methods. Products of high and medium thermal resistance, 2001.

[22] European Standards. EN 1602: Thermal insulating materials, Thermal insulation, Construction materials, Density measurement, Bulk density, Test specimens, Testing conditions, Buildings, 1996.

CHAPTER 5

BEM FORMULATION, IN FREQUENCY DOMAIN, TO STUDY THE TRANSIENT HEAT DIFFUSION THROUGH 3D THERMAL BRIDGES OF BUILDINGS

5 BEM FORMULATION, IN FREQUENCY DOMAIN, TO STUDY THE TRANSIENT HEAT DIFFUSION THROUGH 3D THERMAL BRIDGES OF BUILDINGS

5.1 Introduction

The thermal bridging analysis has been increasingly important in the last few years. However, there are very limited studies demonstrating the dynamic behaviour of point thermal bridges (PTBs) of buildings [1]. Due to the complexity of three-dimensional (3D) dynamic simulations, most studies on thermal bridging effects use one-dimensional (1D) ([2],[3],[4]) or two-dimensional (2D) approaches ([5],[6],[7]) and when 3D numerical approaches are used, normally steady-state conditions are assumed ([8]-[10]).

The simulation of PTBs under unsteady-state conditions requires the development of accurately 3D dynamic numerical models. Different approaches can be used, depending whether the numerical method is based on domain-discretization such as finite elements (FEM) [12] and finite differences (FDM) ([13],[14]) or on boundary discretization such as the boundary element method (BEM) ([15],[16]). More recently, some researchers have been focused on the development of meshless methods to study physical phenomenon of heat transfer, requiring neither domain nor boundary discretization, such as the method of fundamental solutions (MFS) [17].

Of the available numerical methods, the BEM is possibly one of the most suitable tools for modelling systems composed by homogeneous layers, since it enables a compact description of the regions by discretizing only the boundaries and the interfaces between materials. As a result, the BEM gives fully populated systems of equations, contrary to the sparse systems given by the FDM and FEM techniques. Thus, the size of the equation system to be solved is efficiently reduced. One disadvantage of the BEM is that it can only be applied to more general geometries and media when the relevant fundamental solution is known. However, this may not always be possible. Furthermore, it is well known that, depending on the distance between the source point and the node being integrated, the boundary integrals may become singular or nearly singular, which increases the difficulty associated with the mathematical model, since the direct BEM degenerates and becomes inaccurate.

Despite the high computational cost entailed by 3D simulation phenomena, a number of BEM formulations have been proposed. Ma *et al.* [18] used a BEM formulation in the time domain to study transient heat conduction in 3D solids with fibre inclusions. Jabłoński [19] solved 3D Laplace and Poisson equations by proposing the analytical evaluation of the surface integrals appearing in BEM. Qin *et al.* [20] implemented changes to the conventional distance transformation technique to evaluate nearly singular integrands on 3D boundary elements, including planar and curved surface elements and very irregular elements of slender shape.

The correct integration of the singular integrals is one of the biggest challenges of the BEM. Various methods have been proposed by the BEM research community to overcome some difficulties posed by singularities, as described by Zhou *et al.* [21]. Alternatively, analytical and semi-analytical methods and approaches such as nonlinear transformation ([22],[23],[24]) or distance transformation techniques ([25],[26]) can be used.

Contrary to 2D problems, for which some closed form solutions for singular integrals may be found, they are not known for singular integrals for 3D heat diffusion problems. In fact, for 3D problems, singular integrals are mostly solved using numerical schemes based on Gaussian integration schemes. However, as the accuracy of the BEM is highly dependent on the precision of those integrals, some researchers have been looking for semi-analytical solutions or sophisticated approaches to solve specific problems [27]. Niu *et al.* [28] propose a semi-analytical algorithm for 3D elastic problems that require the evaluation of nearly strongly singular and hypersingular integrals on the triangular and quadrilateral elements. Applying a scheme of integration by parts, the nearly singular surface integrals are transformed to a set of line integrals along the boundary for which standard numerical quadrature can be used. Tadeu and António [29] have presented a set of analytical solutions for singular and hypersingular integrals for 3D acoustic problems.

Most of the numerical models used for the dynamic simulation of the heat transfer through constructive materials and systems are normally formulated in the time domain. However, for long-term diffusion phenomena, this method requires very extensive calculations, since the time increment determines the quality of the response. An alternative approach is to solve the problem in the frequency domain by computing the responses of the system to a sinusoidal heat wave of different frequencies. Since the heat responses decay rapidly, high frequencies can be neglected and the responses can be computed assuming a limited number of frequencies. Thus, the time cost by this method can be much less than time-domain numerical models, depending on the physical problem. Furthermore, unlike the time domain, where the response at each instant depends on the previous responses, in the frequency domain each frequency response can be computed separately reducing the complexity of the formulations involved.

This chapter first presents 3D BEM formulations in the frequency domain to simulate the transient heat diffusion inside 3D inclusions containing an inner 3D body/defect. An analytical expression for the integration of the singular integrals that appear in the 3D BEM formulations, when the element being integrated is the loaded one, is proposed. The analytical integration is compared with the numerical integration results by means of techniques based on standard Gaussian quadrature, which uses an enormous amount of sampling points, to validate the singular integrals presented. The BEM formulations incorporating the proposed analytical solutions is then verified against analytical solutions derived for two concentric cylindrical circular inclusions limited by two perpendicular sections, where null heat fluxes were imposed.

The applicability of the BEM formulations is illustrated for two different problems. The proposed model is first used to simulate the heat conduction through a concrete column with a cylindrical inclusion embedded within it, subjected to a 3D external heat point source. The effect of the inclusion properties and inclination on the temperature distribution inside the column and on its outer surface is analysed. The BEM model is then used to simulate the heat conduction through a geometrical point thermal bridge in a 3D building corner. The dynamic thermal bridging effect near the 3D corner is analysed using the proposed BEM model formulated in the frequency domain. A sinusoidal variation of the external temperature is simulated. However, the model allows the simulation of any variation of the external and internal temperatures over time. Time solutions are obtained using inverse Fourier transformations.

The variation of the temperature distribution over time in two different planes of the building corner domain is analysed.

5.2 3D BEM formulation in frequency domain

This section describes the 3D BEM formulations, in the frequency domain, to simulate the transient heat diffusion by conduction through an inclusion heated by an incident 3D heat point source. Different boundary conditions are assumed. The singular integrals that appear in 3D BEM formulations in the frequency domain, when the element being integrated is the loaded one, are evaluated analytically. Numerical integrations using existing techniques based on standard Gaussian integration schemes that incorporate an enormous amount of sampling points are used to verify the analytical integration of the singular integrals.

5.2.1 Null heat fluxes and null temperatures along the boundary

Consider an unbounded spatially uniform solid medium of density ρ , thermal conductivity λ and specific heat c , with a 3D embedded inclusion, bounded by a surface S (see Figure 5.1).

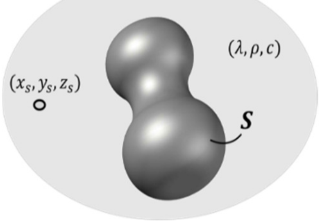

Figure 5.1: Three-dimensional geometry of the problem.

This system is subjected to a point heat source placed at $\left(x_s, y_s, z_s\right)$, expressed as:

$$\hat{f}(x,y,z,t) = \delta\left(x - x_s\right)\delta\left(y - y_s\right)\delta\left(z - z_s\right)\mathrm{e}^{\mathrm{i}\omega t}, \tag{5.1}$$

where $\delta\left(x - x_s\right)$, $\delta\left(y - y_s\right)$ and $\delta\left(z - z_s\right)$ are Dirac-delta functions, and ω is the frequency of the source. The response of this heat source can be expressed by

$$\hat{T}_{inc}\left(x,y,z,x_s,y_s,z_s,\omega\right) = \frac{e^{-i\sqrt{-\frac{i\omega}{K}}r_0}}{2\lambda r_0}, \tag{5.2}$$

in which K is the thermal diffusivity defined by $\dfrac{\lambda}{\rho\, c}$, ω is the oscillating frequency, $\mathrm{i} = \sqrt{-1}$ and $r_0 = \sqrt{\left(x - x_s\right)^2 + \left(y - y_s\right)^2 + \left(z - z_s\right)^2}$.

The transient heat transfer by conduction to calculate the heat ($\hat{T}$) at any point of the spatial 3D homogeneous solid domain is governed by the Helmholtz equation:

$$\left(\frac{\partial^2}{\partial x^2} + \frac{\partial^2}{\partial y^2} + \frac{\partial^2}{\partial z^2}\right)\hat{T}(\boldsymbol{x},\omega) + k^2\hat{T}(\boldsymbol{x},\omega) = 0, \tag{5.3}$$

where $\hat{T}(x,y,z,\omega) = \int_0^\infty T(x,y,z,t)e^{-i\omega t}dt$, $\boldsymbol{x} = (x,y,z)$ and $k = \sqrt{\dfrac{-\mathrm{i}\omega}{K}}$.

The boundary integral equation, formulated in the frequency domain, can be constructed by applying the reciprocity theorem [30], leading to:

$$\begin{aligned} b\hat{T}(\boldsymbol{x}_0,\omega) &= \int_S q(\boldsymbol{x},\mathbf{n}_{n1},\omega)G(\boldsymbol{x},\boldsymbol{x}_0,\omega)\,\mathrm{d}s \\ &\quad - \int_S H(\boldsymbol{x},\mathbf{n}_{n1},\boldsymbol{x}_0,\omega)T(\boldsymbol{x},\omega)\,\mathrm{d}s + \hat{T}_{\mathrm{inc}}(\boldsymbol{x}_0,\boldsymbol{x}_s,\omega) \end{aligned}, \tag{5.4}$$

Where G and H are respectively the fundamental solutions (Green's functions) for the temperature $\left(\hat{T}\right)$ and heat flux $\left(q\right)$, at a point $\boldsymbol{x} = \left(x,y,z\right)$ on the boundary S, due to a virtual point heat source at $\boldsymbol{x}_0 = \left(x_0, y_0, z_0\right)$; $\mathbf{n}_{n1}$ represents the unit outward normal along the boundary

S, at $\boldsymbol{x}=(x,y,z))$; b is a constant defined by the shape of the boundary, taking the value $1/2$ if $\boldsymbol{x}_0=(x_0,y_0,z_0)\in S$, and 1 otherwise.

The required Green's functions for temperature in an unbounded medium, in Cartesian coordinates, is given by:

$$G(\boldsymbol{x},\boldsymbol{x}_0,\omega)=\frac{\mathrm{e}^{-\mathrm{i}kr}}{4\lambda\pi r}, \tag{5.5}$$

with $r=\sqrt{(x-x_0)^2+(y-y_0)^2+(z-z_0)^2}$.

By deriving equation (5.5), we obtain the Green's functions for the heat flux:

$$H(\boldsymbol{x},\mathbf{n}_{n1},\boldsymbol{x}_0,\omega)=\frac{\mathrm{e}^{-\mathrm{i}kr}(-\mathrm{i}kr-1)}{4\lambda\pi r^2}\frac{\partial r}{\partial \mathbf{n}_{n1}}, \tag{5.6}$$

<u>Null heat fluxes along its boundary</u>

When null heat fluxes are prescribed along the boundary, Equation (5.4) is simplified resulting in:

$$b\hat{T}(\boldsymbol{x}_0,\omega)=-\int_S H(\boldsymbol{x},\mathbf{n}_{n1},\boldsymbol{x}_0,\omega)\hat{T}(\boldsymbol{x},\omega)\,\mathrm{d}s+\hat{T}_{\mathrm{inc}}(\boldsymbol{x}_0,\boldsymbol{x}_s,\omega), \tag{5.7}$$

<u>Null temperatures along its boundary</u>

Null temperatures on the surface of the inclusion are now prescribed, which leads to the following equation:

$$0=\int_S q(\boldsymbol{x},\mathbf{n}_{n1},\omega)G(\boldsymbol{x},\boldsymbol{x}_0,\omega)\,\mathrm{d}s+\hat{T}_{inc}(\boldsymbol{x}_0,\boldsymbol{x}_s,\omega), \tag{5.8}$$

5.2.2 Continuity of temperatures and heat fluxes along the boundary

Consider now a 3D body (Medium M1) bounded by a surface S_1, implanted in a 3D inclusion (Medium M2) with surface S_2, which is surrounded by an infinite spatially uniform solid medium (M3) (see Figure 5.2). The thermal diffusivity of each medium n (K_n) is defined by $\dfrac{\lambda_n}{(\rho_n\ c_n)}$.

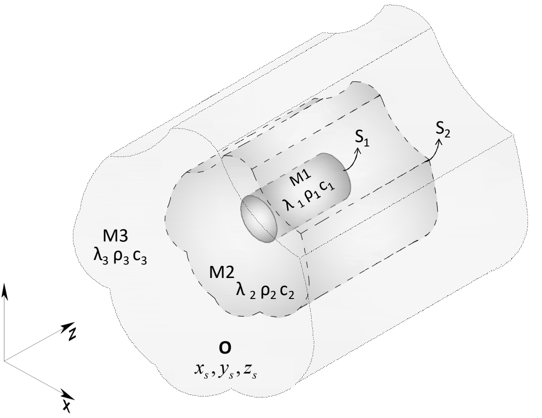

Figure 5.2: Three-dimensional geometry of a problem with three different media: surfaces S_1 and S_2 have continuity of temperatures and heat fluxes.

Assuming that this system is subjected to a point heat source placed at $\boldsymbol{x}_S = (x_S, y_S, z_S)$, the incident temperature field produced at $\boldsymbol{x} = (x, y, z)$ can be expressed by Equation (5.2), with $K = K_3$ and $\lambda = \lambda_3$.

The transient heat diffusion in the frequency domain is expressed by the Helmholtz equation:

$$\left(\frac{\partial^2}{\partial x^2} + \frac{\partial^2}{\partial y^2} + \frac{\partial^2}{\partial z^2}\right)\hat{T}^{(n)}(\boldsymbol{x},\omega) + (k_n)^2\,\hat{T}^{(n)}(\boldsymbol{x},\omega) = 0, \tag{5.9}$$

in which $\hat{T}^{(n)}(\boldsymbol{x},\omega)$ is the transient temperature in the frequency domain at a point $\boldsymbol{x} = (x, y, z)$ and $k_n = \sqrt{-\mathrm{i}\omega/K_n}$.

The BEM formulation in the frequency domain obtained by applying the reciprocity theorem [30] is given by the following boundary integral equations:

a) along the interior domain of the implanted body (Medium 1)

$$\begin{aligned} b\hat{T}^{(1)}(\boldsymbol{x}_0,\omega) &= \int_{S_1} q^{(1)}(\boldsymbol{x},\mathbf{n}_{n1},\omega)\,G^{(1)}(\boldsymbol{x},\boldsymbol{x}_0,\omega)\,\mathrm{d}s \\ &\quad - \int_{S_1} H^{(1)}(\boldsymbol{x},\mathbf{n}_{n1},\boldsymbol{x}_0,\omega)\,\hat{T}^{(1)}(\boldsymbol{x},\omega)\,\mathrm{d}s \end{aligned}, \tag{5.10}$$

b) along the interior domain of the inclusion (Medium 2)

$$\begin{aligned} b\hat{T}^{(2)}(\boldsymbol{x}_0,\omega) &= \int_{S_1} q^{(2)}(\boldsymbol{x},-\mathbf{n}_{n1},\omega)\, G^{(2)}(\boldsymbol{x},\boldsymbol{x}_0,\omega)\,\mathrm{d}s \\ &+ \int_{S_2} q^{(2)}(\boldsymbol{x},\mathbf{n}_{n2},\omega)\, G^{(2)}(\boldsymbol{x},\boldsymbol{x}_0,\omega)\,\mathrm{d}s \\ &- \int_{S_1} H^{(2)}(\boldsymbol{x},-\mathbf{n}_{n1},\boldsymbol{x}_0,\omega)\,\hat{T}^{(2)}(\boldsymbol{x},\omega)\,\mathrm{d}s \\ &- \int_{S_2} H^{(2)}(\boldsymbol{x},\mathbf{n}_{n2},\boldsymbol{x}_0,\omega)\,\hat{T}^{(2)}(\boldsymbol{x},\omega)\,\mathrm{d}s \end{aligned}, \qquad (5.11)$$

c) along the exterior domain of the inclusion (Medium 3)

$$\begin{aligned} b\hat{T}^{(3)}(\boldsymbol{x}_0,\omega) &= \int_{S_2} q^{(3)}(\boldsymbol{x},-\mathbf{n}_{n2},\omega)\, G^{(3)}(\boldsymbol{x},\boldsymbol{x}_0,\omega)\,\mathrm{d}s \\ &- \int_{S_2} H^{(3)}(\boldsymbol{x},-\mathbf{n}_{n2},\boldsymbol{x}_0,\omega)\,\hat{T}^{(3)}(\boldsymbol{x},\omega)\,\mathrm{d}s + \hat{T}_{\mathrm{inc}}(\boldsymbol{x}_0,\boldsymbol{x}_s,\omega) \end{aligned}, \qquad (5.12)$$

In these equations $G^{(n)}$ and $H^{(n)}$ are, respectively, the fundamental solutions (Green's functions) for the temperature $\left(\hat{T}^{(n)}\right)$ and heat flux $\left(q^{(n)}\right)$, at a point $\boldsymbol{x}=(x,y,z)$ on the boundary S_1 and S_2, due to a virtual point heat source at $\boldsymbol{x}_0=(x_0,y_0,z_0)$; $\mathbf{n}_{n1}$ and $\mathbf{n}_{n2}$ represent the unit outward normal along the boundaries S_1 and S_2, respectively, at $\boldsymbol{x}=(x,y,z)$; b is a constant defined by the shape of the boundary, taking the value $1/2$ if $\boldsymbol{x}_0=(x_0,y_0,z_0)\in S$, and 1 otherwise.

The required Green's functions for temperature and heat flux in an unbounded medium, in Cartesian coordinates, are given by:

$$G^{(n)}(\boldsymbol{x},\boldsymbol{x}_0,\omega)=\frac{\mathrm{e}^{-\mathrm{i}k_n r}}{4\lambda_n \pi r}, \qquad (5.13)$$

$$H^{(n)}\left(\boldsymbol{x},\mathbf{n}_{n1},\boldsymbol{x}_0,\omega\right)=\frac{\mathrm{e}^{-\mathrm{i}k_n r}\left(-\mathrm{i}k_n r-1\right)}{4\lambda_n \pi r^2}\frac{\partial r}{\partial \mathbf{n}_{n1}}, \qquad (n=1,2) \qquad (5.14)$$

$$H^{(n)}\left(\boldsymbol{x},\mathbf{n}_{n2},\boldsymbol{x}_0,\omega\right)=\frac{\mathrm{e}^{-\mathrm{i}k_n r}\left(-\mathrm{i}k_n r-1\right)}{4\lambda_n \pi r^2}\frac{\partial r}{\partial \mathbf{n}_{n2}}, \qquad (n=2,3) \qquad (5.15)$$

with $r=\sqrt{\left(x-x_0\right)^2+\left(y-y_0\right)^2+\left(z-z_0\right)^2}$.

5.2.3 Imposition of null heat fluxes and prescribed temperatures

The 3D inclusion (M1) illustrated in Figure 5.3 is bounded by a surface S_1, with thermal diffusivity K_1 and is surrounded by a uniform solid medium (M2), bounded by a surface S_2, $\left\{S_{2,1}, S_{2,2}\right\} \in S_2$, with thermal diffusivity K_2.

Continuity of temperatures and heat fluxes are assumed along surface S_1. Null heat flux $\left(\partial T / \partial n = 0\right)$ and prescribed temperatures $\left(T = T_0\right)$ are imposed along the boundary sections $S_{2,1}$ and $S_{2,2}$, respectively.

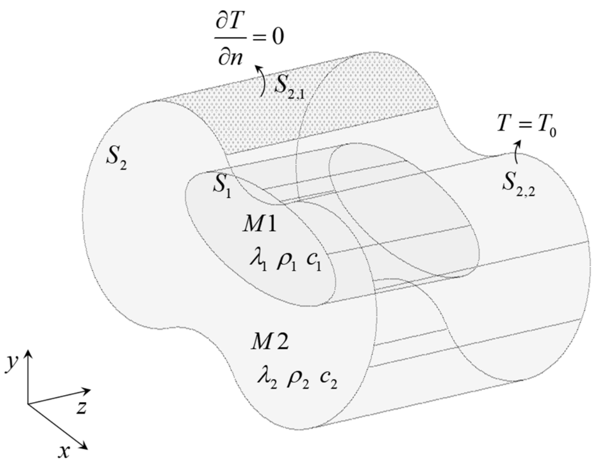

Figure 5.3: Problem definition. 3D inclusion geometry and boundary conditions of the problem.

The transient heat transfer by conduction employed to calculate the temperature $\hat{T}^{(n)}(\boldsymbol{x}, \omega)$ at any point of the 3D domain, in the frequency domain, is governed by the Helmholtz equation (equation 5.9, section 5.2.2).

The application of the reciprocity theorem [30] leads to the following boundary equations.

a) along the interior domain of medium 1:

$$b\,\hat{T}^{(1)}(\boldsymbol{x}_0, \omega) = \int_{S_1} q^{(1)}(\boldsymbol{x}, \mathbf{n}_{n1}, \omega)\, G^{(1)}(\boldsymbol{x}, \boldsymbol{x}_0, \omega)\, \mathrm{d}s - \int_{S_1} H^{(1)}(\boldsymbol{x}, \mathbf{n}_{n1}, \boldsymbol{x}_0, \omega)\, \hat{T}^{(1)}(\boldsymbol{x}, \omega)\, \mathrm{d}s \ , \qquad (5.16)$$

b) along the interior domain of medium 2:

$$\begin{aligned} b\hat{T}^{(2)}(\boldsymbol{x}_0,\omega) &= \int_{S_1} q^{(2)}(\boldsymbol{x},-\mathbf{n}_{n1},\omega)\,G^{(2)}(\boldsymbol{x},\boldsymbol{x}_0,\omega)\,\mathrm{d}s + \int_{S_{2,2}} q^{(2)}(\boldsymbol{x},\mathbf{n}_{n2},\omega)\,G^{(2)}(\boldsymbol{x},\boldsymbol{x}_0,\omega)\,\mathrm{d}s \\ &- \int_{S_1} H^{(2)}(\boldsymbol{x},-\mathbf{n}_{n1},\boldsymbol{x}_0,\omega)\,\hat{T}^{(2)}(\boldsymbol{x},\omega)\,\mathrm{d}s - \int_{S_{2,1}} H^{(2)}(\boldsymbol{x},\mathbf{n}_{n2},\boldsymbol{x}_0,\omega)\,\hat{T}^{(2)}(\boldsymbol{x},\omega)\,\mathrm{d}s \;, \\ &- \int_{S_{2,2}} H^{(2)}(\boldsymbol{x},\mathbf{n}_{n2},\boldsymbol{x}_0,\omega)\,\hat{T}_0(\boldsymbol{x},\omega)\,\mathrm{d}s \end{aligned} \qquad (5.17)$$

The Green's functions for temperature $\left(G^{(n)}(\boldsymbol{x},\boldsymbol{x}_0,\omega)\right)$ and heat flux $\left(H^{(n)}(\boldsymbol{x},\boldsymbol{x}_0,\mathbf{n}_n,\omega)\right)$ are given by equations (5.13)-(5.15).

5.2.4 Analytical integration of singular Integrals

The global solutions are found by solving the boundary integral equation, which requires the discretization of the interfaces S into N planar boundary elements. Constant elements are used. Thus, only one nodal point is used in the middle of each element.

The integrations in equations (5.4), (5.10), (5.11), (5.12), (5.16) and (5.17) are evaluated using a Gaussian quadrature scheme when the element to be integrated is not the loaded element. For the loaded element (the singular element), however, the integrands exhibit a singularity and the integration can be carried out in closed form, as will be demonstrated.

Consider the singular rectangular boundary element of width W (in the x direction) and length L (in the z direction) shown in Figure 5.4.

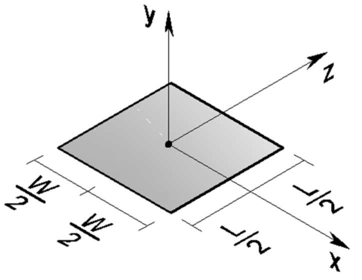

Figure 5.4: Scheme of a planar boundary element.

Since in this case r is perpendicular to the normal (e.g. $\boldsymbol{r}\,\mathbf{n}_n = 0$), the singular term $\int_{-L/2}^{L/2}\int_{-W/2}^{W/2} H(\boldsymbol{x},\mathbf{n}_n,\boldsymbol{x}_0,\omega)\,dx\,dz$ disappears. On the other hand, the integration of the Green's function $\int_{-L/2}^{L/2}\int_{-W/2}^{W/2} G(\boldsymbol{x},\boldsymbol{x}_0,\omega)\,dx\,dz$ leads to a singular term.

This integration is evaluated by first expressing $G(\boldsymbol{x},\boldsymbol{x}_0,\omega)$ as the sum of two-dimensional Green's functions with varying spatial wavenumbers. This is accomplished by first applying a spatial Fourier transformation along the z direction to the three-dimensional Green's function $G(\boldsymbol{x},\boldsymbol{x}_0,\omega)$. The application of a Fourier-transformation to Equations (5.5) and (5.13) in that direction leads to a line heat field, whose amplitude varies sinusoidally in the third dimension (z),

$$\widehat{G}(x,y,x_0,y_0,k_z,\omega) = \frac{-\mathrm{i}}{8\pi\lambda} H_0\left(k\overline{r}_0\right), \tag{5.18}$$

in which $H_n(\dots)$ are second kind Hankel functions of the order n, $k = \sqrt{-\frac{\mathrm{i}\omega}{K} - k_z^2}$, with $\operatorname{Im}(k) < 0$, $\overline{r}_0 = \sqrt{\left(x-x_0\right)^2 + \left(y-y_0\right)^2}$, where k_z is the wavenumber in the z direction.

Assuming the presence of an infinite set of equally-spaced sources in the z direction, the former Green's function can be recast as:

$$G(\boldsymbol{x},\boldsymbol{x}_0,\omega) = \frac{2\pi}{L_{vs}} \sum_{m=-\infty}^{\infty} \widehat{G}(x,y,x_0,y_0,k_z,\omega)\,\mathrm{e}^{-\mathrm{i}k_{zm}z}, \tag{5.19}$$

where L_{vs} is the spatial source interval, and $k_{zm} = \frac{\sqrt{2\pi}}{L_{vs}} m$, $m = 1,\dots,M$.

This equation converges very fast and can be approximated by a finite sum of terms (M). The distance L_{vs} needs to be large enough to avoid spatial contamination. Given that the frequency increment defines the time window for the analysis, $1/\Delta f$, the minimum distance needs to be at least $2.0\sqrt{K}\,\sqrt{1/\Delta f}$. The number of terms depends on this distance L_{vs}. However, a larger value of L_{vs} corresponds to a higher number of terms (M).

Note that the use of complex frequencies further reduces the influence of the neighbouring fictitious sources. The 3D Green's field can therefore be computed as the heat irradiated by a sum of harmonic (steady-state) line loads, whose amplitude varies sinusoidally in the z dimension.

This procedure allows the integration of $\int_{-L/2}^{L/2}\int_{-W/2}^{W/2} G(\boldsymbol{x},\boldsymbol{x}_0,\omega)\,dx\,dz$ to be obtained in a similar manner, thus

$$\int_{-L/2}^{L/2}\int_{-W/2}^{W/2} G(\boldsymbol{x},\boldsymbol{x}_0,\omega)\,dx\,dz = \frac{-\mathrm{i}}{4\lambda L_{vs}} \sum_{m=-M}^{M} \int_{-L/2}^{L/2} I_1(k\overline{r}_0)\,\mathrm{e}^{-\mathrm{i}k_{zm}z}\,dz, \tag{5.20}$$

with $\int_{-L/2}^{L/2} I_1(k\overline{r}_0)\,\mathrm{e}^{-\mathrm{i}k_{zm}z}\,dz = I_1(k\overline{r}_0)L$ if $m = 0$

$$\int_{-L/2}^{L/2} I_1(k\overline{r}_0)\,\mathrm{e}^{-\mathrm{i}k_{zm}z}\,dz = I_1(k\overline{r}_0)\frac{2\sin(k_{zm}\frac{L}{2})}{k_{zm}} \qquad \text{if} \qquad m \neq 0$$

where $I_1(k\overline{r}_0) = \int_{-W/2}^{W/2} H_0\left(k\overline{r}_0\right)dx$

$I_1(k\overline{r}_0)$ is calculated analytically, following the expressions in Tadeu *et al.* ([31],[32]),

$$\int_{0}^{W/2} H_0\left(k\,\overline{r}_0\right)dx = \frac{W}{2}H_0\left(k\frac{W}{2}\right) + \pi\frac{L}{4}\left[H_1\left(k\frac{W}{2}\right)S_0\left(k\frac{W}{2}\right) - H_0\left(k\frac{W}{2}\right)S_1\left(k\frac{W}{2}\right)\right], \tag{5.21}$$

where $S_{ns}\left(\dots\right)$ are Struve functions of order ns .

5.2.4.1 Verification of the analytical integration

The above analytical expression is next implemented and compared with the numerical integration by means of a standard Gaussian quadrature, using a large amount of sampling points.

The integrations $\int_{-L/2}^{L/2}\int_{-W/2}^{W/2} G(\mathbf{x},\mathbf{x}_0,\omega)\,dx\,dz$ are computed along a planar quadrangular boundary element 0.2 m long (see Figure 5.4 where $L = 0.2$ m and $W = 0.2$ m). Computations are performed with a frequency increment of 0.5×10^{-7} Hz in the frequency range [0.0, 1×10^{-5} Hz]. The thermal properties assigned to the medium are those of the mortar: specific heat $c = 780$ J.kg^{-1}.ºC^{-1}, density 1860 kg.m^{-3} and thermal conductivity 0.72 W.m^{-1}.ºC^{-1} (thermal diffusivity of 4.96278×10^{-7} m$^2 s^{-1}$). L_{vs} is assumed to be 60.0 m.

To illustrate the convergence of Equation (5.20), Figure 5.5 presents the imaginary and real parts of the result obtained as the number of terms is successively taken into account in the integration ($k_{zm}=\dfrac{\sqrt{2\pi}}{L_{vs}}m,\ m=1,\ldots,M$), that is, as k_z increases, when the integration is performed for a frequency of 0.5×10^{-7} Hz. It can be observed that the integration converges very fast as k_z increases. Similar behaviour was found throughout the frequency range.

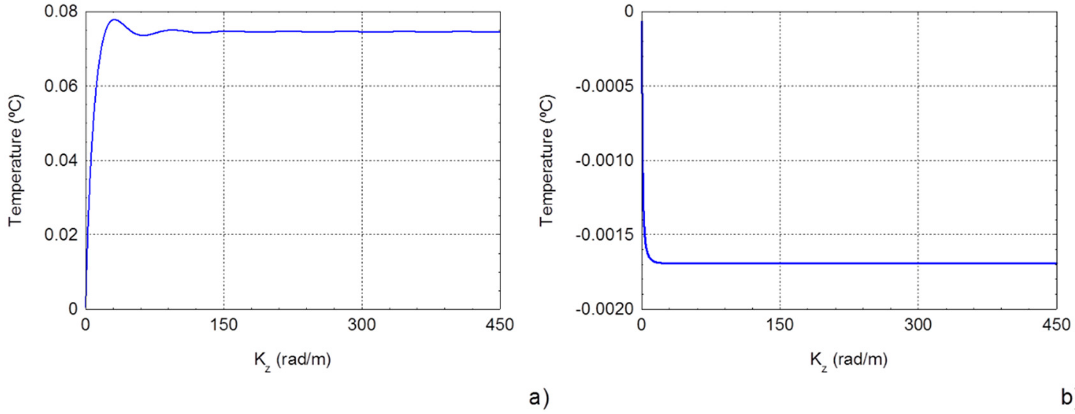

Figure 5.5: Convergence of the proposed analytical integration of the singular integrals: a) real part; b) imaginary part.

For the purpose of verification, the analytical results for the frequency range $\left[0.0,\,1\times10^{-5}\right]$ Hz are illustrated in Figure 5.6 by solid lines. The numerical integration results, given by a standard Gaussian quadrature with 2000×2000 points, are plotted by marked lines in the figure. The two solutions exhibit similar results. Even so, the accuracy of the result of the numerical integration depends on the number of sampling points. The variation of the error, as the number of Gauss points increases from 500×500 to 2000×2000 sampling points, is given in Figure 5.7. As expected, the accuracy of the numerical integration improves as the number of sampling points increases.

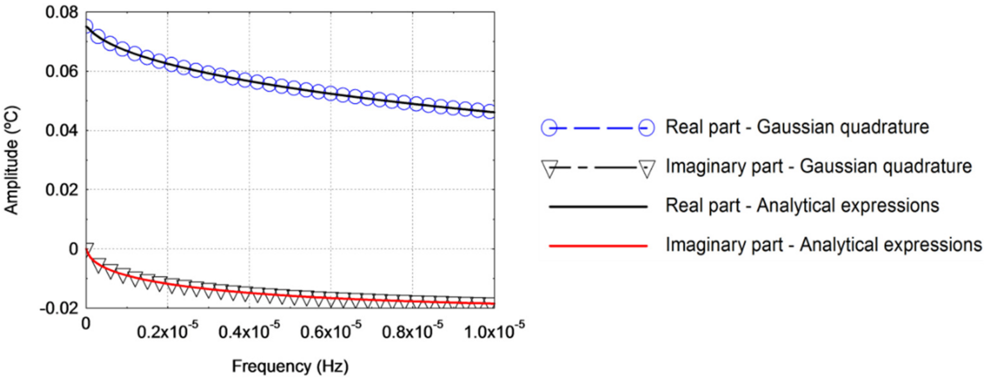

Figure 5.6: Comparison between analytical and numerical integration: - analytical results (as continuous lines) and numerical results using a standard Gaussian quadrature with 2000x2000 sampling points.

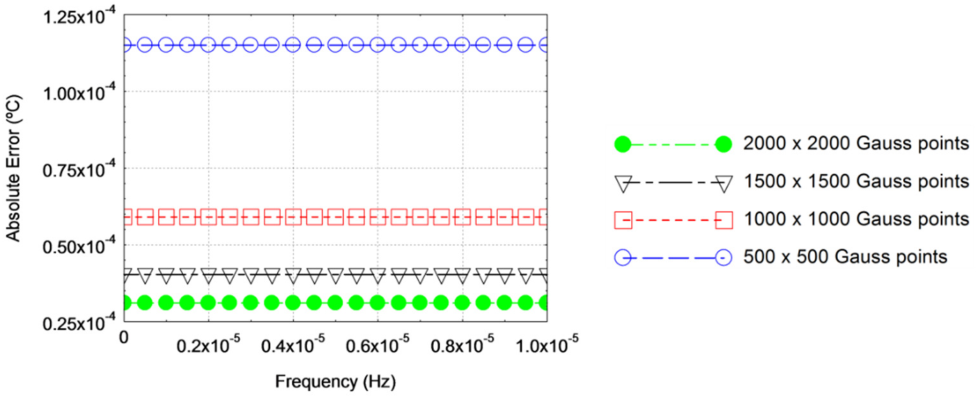

Figure 5.7: Numerical integration: variation of the error for different numbers of Gauss sampling points.

5.3 Verification of the 3D BEM formulation

In this section, the 3D BEM algorithms, incorporating the analytical solutions, are verified against analytical solutions derived for cylindrical circular inclusions limited by two perpendicular sections, where null heat fluxes were imposed.

5.3.1 Null heat fluxes or null temperatures along the boundary

The BEM formulation for the transient heat diffusion through a cylindrical inclusion with null heat fluxes or null temperatures along the boundary are validated using a circular cylindrical inclusion, with radius a , aligned along the z axis (see Figure 5.8), for which analytical solutions can be derived. A point heat source placed at (x_s, y_s, z_s) is assumed to excite the medium.

Two different conditions are prescribed on the boundary, i.e. null heat fluxes or null temperatures. To enable comparison with the 3D BEM model, the length of the inclusion is limited by imposing null heat fluxes on sections $z = 0.0$ m and $z = L_t$.

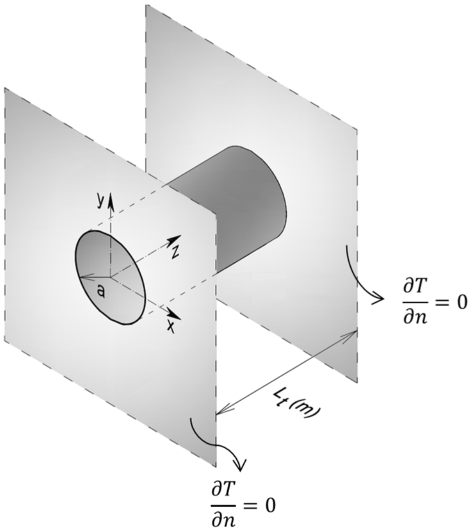

Figure 5.8: Unbounded medium with an embedded cylindrical inclusion.

The analytical solution for this problem is obtained by first applying a spatial Fourier transformation in the z direction, which allows the solution to be obtained as the sum of 2D solutions with a varying spatial wavenumber in that direction. The null normal heat fluxes at sections $z = 0.0$ m and $z = L_t$ are accomplished by adding the temperature field generated by the real source to that produced by virtual sources (image sources), which are placed in the z direction and act as mirrors of the real source, so as to ensure the required boundary conditions.

$$T(\boldsymbol{x}, \boldsymbol{x}_s, \omega) = \frac{2\pi}{L_{vs}} \sum_{m=-\infty}^{\infty} \hat{T}'(x, y, x_s, y_s, k_{zm}, \omega)\, \mathrm{e}^{-\mathrm{i} k_{zm} z}, \tag{5.22}$$

with $k_{zm} = \dfrac{\sqrt{2\pi}}{L_{vs}} m \ \left(m = 1,\ldots,NS \right)$ and $\hat{T}'(x,y,x_s,y_s,k_{zm},\omega) = \hat{T}(x,y,x_s,y_s,k_{zm},\omega)\left[\mathrm{e}^{-\mathrm{i}k_{zm}z_{m0}} + \sum_{m=1}^{NS_z}\sum_{j=1}^{4} \mathrm{e}^{-\mathrm{i}k_{zm}z_{mj}} \right]$

where $z_{m0} = z - z_s$, $z_{m1} = z + z_0 - 2L_t m$, $z_{m2} = z + z_0 + 2L_t\left(m-1\right)$, $z_{m3} = z - z_0 - 2L_t m$ and $z_{m4} = z - z_0 + 2L_t m$.

The number of virtual sources NS_z to be used in the calculations is defined so that the signal responses can be correctly computed in the time frame, which is determined by the frequency increment $1/\Delta f$. This procedure does not introduce any type of error into the computed time impulse response within the time window defined. Notice that L_{vs} should be at least twice the distance between the real source and the farthest virtual source. Each two-dimensional problem is solved using the separation of variables procedure with the Helmholtz equation and enforcing the boundary conditions throughout the boundary surface, using the Bessel series form. The following equations can be derived if the origin of the coordinate system coincides with the centre of the circle, cross section of the cylinder, and the source lies on the x axis.

Null temperatures along its boundary

$$\hat{T}(x,y,x_s,y_s,k_z,\omega) = -\frac{\mathrm{i}}{4\lambda} H_0(k\overline{r}_0) + \sum_{n=0}^{\infty} A_n H_n(k\overline{r})\cos(n\theta)\,, \tag{5.23}$$

with $A_n = \dfrac{\frac{\mathrm{i}}{4\lambda}\left(-1\right)^n \varepsilon_n H_n(k\overline{r}_{00}) J_n(ka)}{H_n(ka)}$, $\overline{r} = \sqrt{x^2 + y^2}$, $J_n\,(\ldots)$ are Bessel functions of order n, $\varepsilon_n = \begin{cases} 1 & if \quad n = 0 \\ 2 & if \quad n \neq 0 \end{cases}$, $\overline{r}_{00} = |x_s|$ and $\theta = \arctan\left(\dfrac{y}{x}\right)$.

Null heat fluxes along its boundary

$$\hat{T}(x,y,x_s,y_s,k_z,\omega) = -\frac{\mathrm{i}}{4\lambda} H_0(k\overline{r}_0) + \sum_{n=0}^{\infty} B_n H_n(k\overline{r})\cos(n\theta)\,, \tag{5.24}$$

with $B_n = \dfrac{\frac{\mathrm{i}}{4\lambda}\left(-1\right)^n \varepsilon_n H_n(k\overline{r}_{00})\left[\frac{n}{a} J_n(ka) - kJ_{n+1}(ka)\right]}{\left[\frac{n}{a} H_n(ka) - kH_{n+1}(ka)\right]}$.

Equations (5.23) and (5.24) converge very fast [33]. The number of terms is defined using a small criterion of convergence applied to the difference between successive values. In the present formulation, the convergence is verified by calculating the difference between the amplitude of the response for $n = N + 20$ and for $n = N$, using the response at the receiver placed closest to the boundary as reference.

The temperature responses are computed at two grids of receivers placed as illustrated in Figure 5.9 [Grid 1 ($y = 0.0$ m), Grid 2 ($z = 1.0$ m)], in the vicinity of a cylinder inclusion with a radius of $a = 0.5$ m and 2.0 m in length. The thermal properties are that of the mortar given in section 5.2.4.1. The 3D point source is placed at (-1.5 m, 0.0 m, 1.0 m). The responses were computed for complex frequencies $\omega_c = \omega - \mathrm{i}\eta$ (with $\eta = 0.7\Delta\omega$, $\Delta\omega = 2\pi \times \Delta f$ and $\Delta f = 0.5 \times 10^{-7}$ Hz). The constant η cannot be made arbitrarily large, since this leads either to a severe loss of numerical accuracy or to underflows and overflows in the evaluation of the exponential windows. Temperature computations were performed at frequency 0.5×10^{-7} Hz.

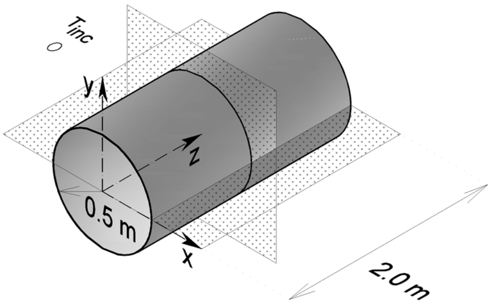

Figure 5.9: Scheme of the receiver grids placed in the vicinity of the cylindrical inclusion subjected to a heat source located at O. Grid 1 ($y = 0.0$ m) and Grid 2 ($z = 1.0$ m).

The responses have been computed both analytically and using the BEM formulations. The behaviour of the formulations was verified by using two different numbers of boundary elements to discretize the inclusion: 30x20 (20 in the z direction) and 50x32 (32 in the z direction).

Figure 5.10 and Figure 5.11 illustrate the responses (real and imaginary parts) obtained when null temperatures are imposed on the boundary surface of the cylinder, on receiver Grids 1 and 2, respectively. Each figure shows the real and imaginary parts of the analytical response and the error obtained when the system is solved using the BEM. As expected, the BEM accuracy improves as the receiver is placed further away from the inclusion. In both cases, it can be seen that the magnitude of the error increases as the receivers approach the inclusion's boundary. It can further be seen that the solution improves as the number of boundary elements increases, which illustrates the good accuracy of the BEM response. When 30x20 boundary elements are used, the highest value of the error is about -3x10^{-3} ºC in the two grids of receivers.

Figure 5.12 and Figure 5.13 give the response (real and imaginary parts) obtained when null heat fluxes are prescribed along the boundary surface of the cylinder, on receiver grids 1 and 2, respectively. Again, the figures illustrate the analytical response and the numerical error when the problem is solved using the BEM. As in the previous case, the receivers placed further away from boundary exhibit lower amplitude errors. Once more, the solution is seen to improve for higher numbers of boundary elements, which illustrates the good accuracy of the BEM model. When 30x20 boundary elements are used, the highest value of the error is about 4x10^{-3} ºC in Grid 1 and 2x10^{-3} in Grid 2.

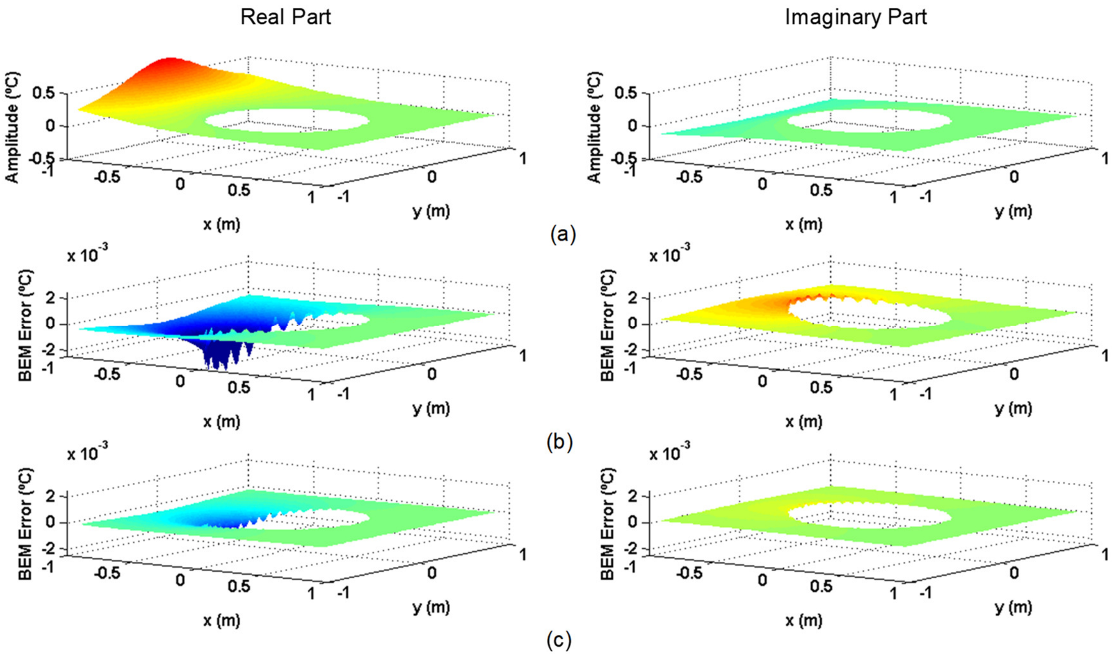

Figure 5.10: Comparative analysis of analytical and BEM responses (real and imaginary parts) at Grid 1, when null temperatures are prescribed, considering different numbers of boundary elements: a) analytical response; b) error using BEM (with 30x20 boundary elements); c) error using BEM (with 50x32 boundary elements).

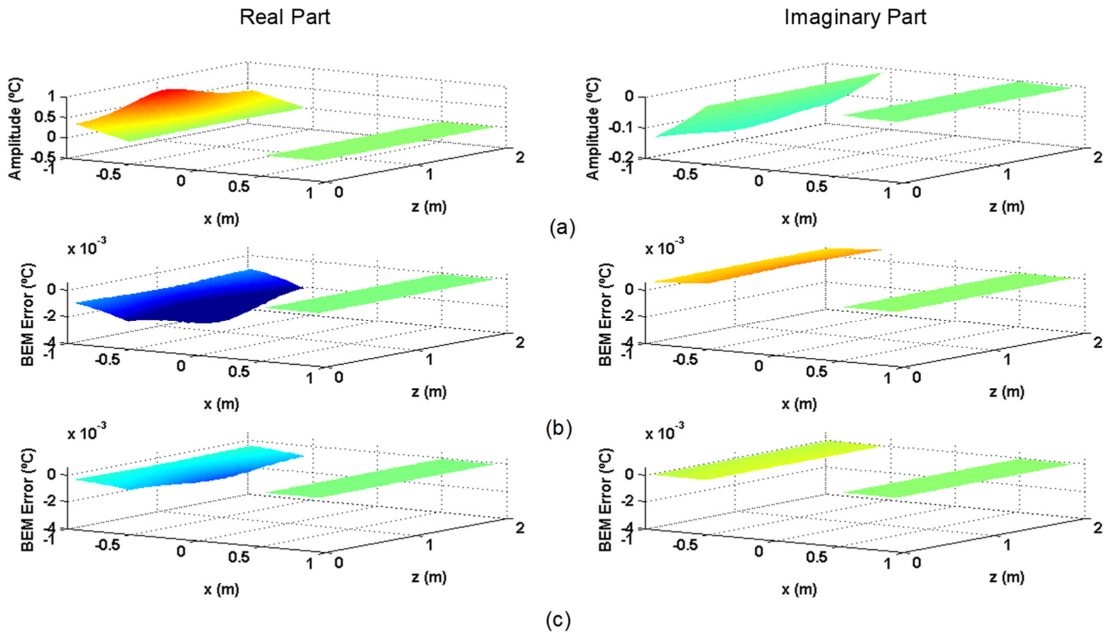

Figure 5.11: Comparative analysis of analytical and BEM responses (real and imaginary parts) at Grid 2, when null temperatures are prescribed, considering different numbers of boundary elements: a) analytical response; b) error using BEM (with 30x20 boundary elements); c) absolute error using BEM (with 50x32 boundary elements).

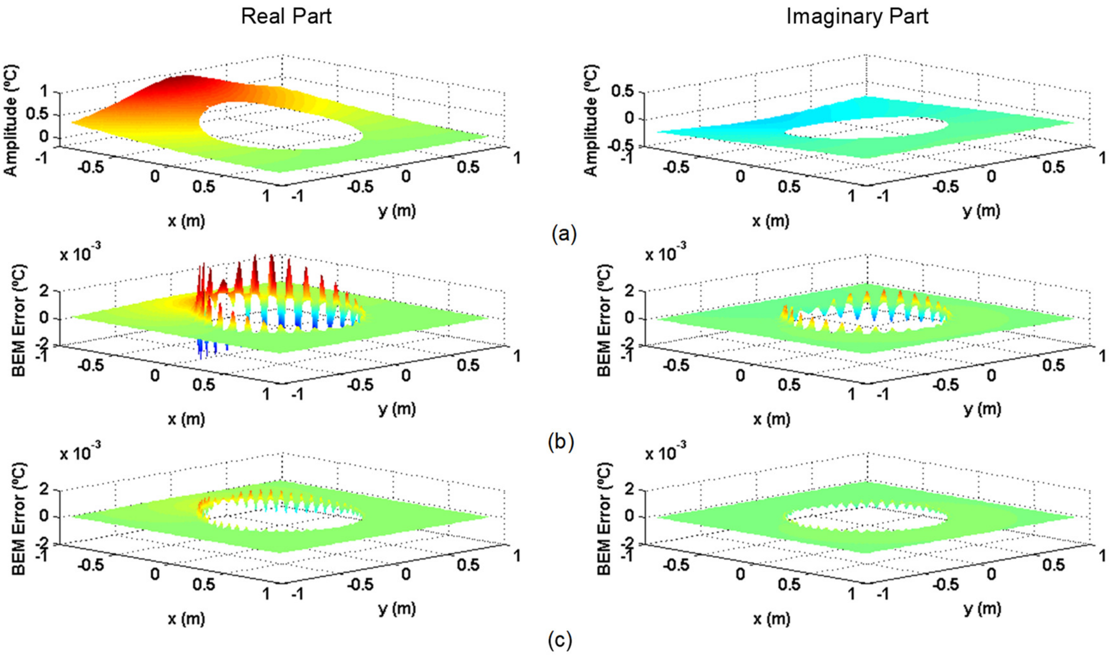

Figure 5.12: Comparative analysis of analytical and BEM responses (real and imaginary parts) at Grid 1, when null heat fluxes are prescribed, considering different numbers of boundary elements: a) analytical response; b) error using BEM (with 30x20 boundary elements); c) error using BEM (with 50x32 boundary elements).

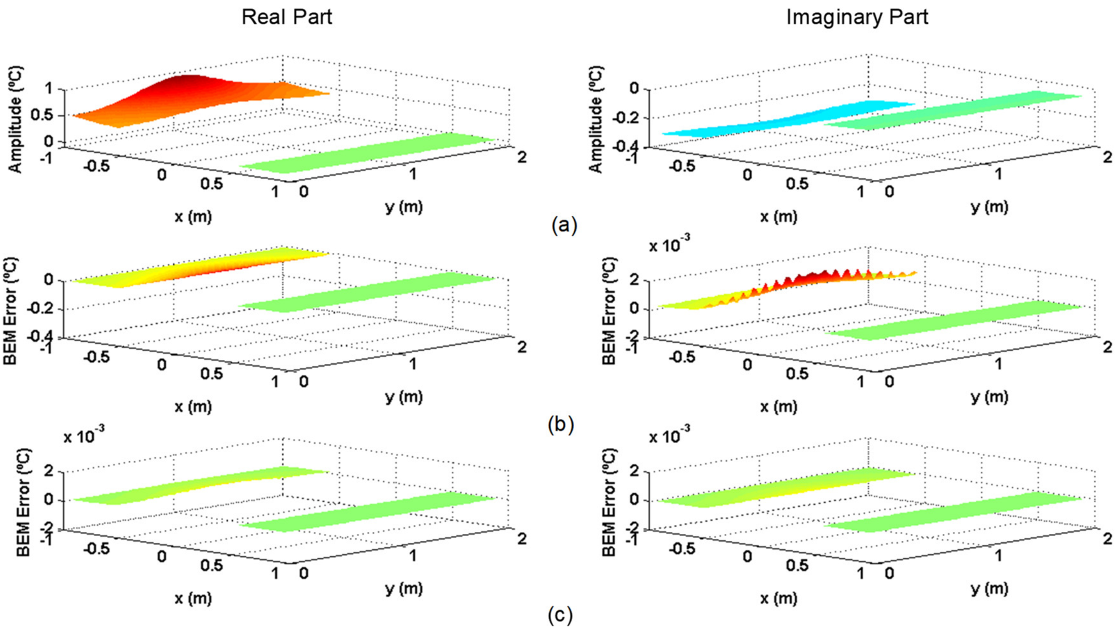

Figure 5.13: Comparative analysis of analytical and BEM responses (real and imaginary parts) at Grid 2, when null heat fluxes are prescribed, considering different numbers of boundary elements: a) Analytical response; b) error using BEM (with 30x20 boundary elements); c) error using BEM (with 50x32 boundary elements).

5.3.2 Continuity of temperatures and heat fluxes along the boundary

The BEM formulation for the transient heat diffusion through cylindrical inclusions with continuity of heat fluxes and temperatures along the interfaces is verified using two circular cylindrical concentric inclusions, embedded in an unbounded space, aligned along the z axis (see Figure 5.14), for which an analytical solution can be derived.

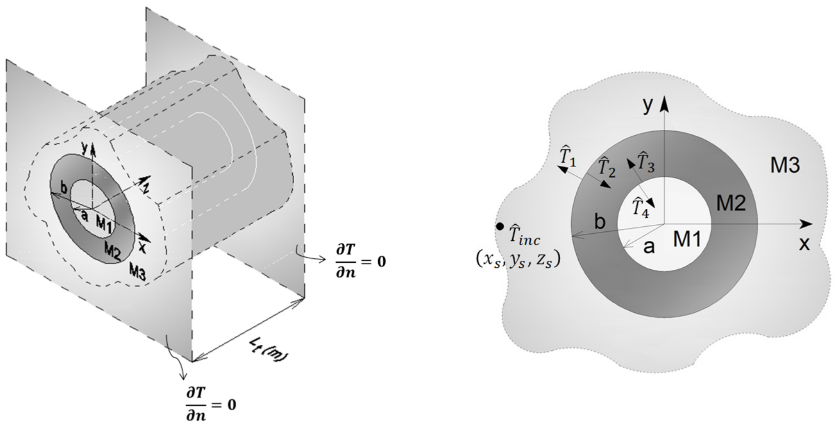

Figure 5.14: Two circular cylindrical concentric inclusions embedded in an unbounded space, with length limited by adiabatic sections.

Continuity of temperatures and heat fluxes are prescribed at the interfaces between inclusions and on the exterior boundary. Following the procedure described before, the length of the inclusion is limited by imposing null heat fluxes on sections $z = 0.0\text{ m}$ and $z = L_t$.

The analytical solution for this problem is obtained by applying the mirror image source technique described in section 5.3.1. The heat source is assumed to be placed in medium M3 at $\left(x_s, y_s, z_s\right)$ as illustrated in Figure 5.14. $\hat{T}_{inc}$ is the heat field incident generated by the heat source. As before, a spatial Fourier transform is applied in the z direction.

The heat field propagating in the outer medium (M3) depends on the amount of energy that diffuses from the external boundary of the cylindrical inclusion M2, at $r = b$, given by the following expression:

$$\hat{T}_1\left(\omega, r, \theta, k_{zm}\right) = \sum_{n=0}^{\infty} A_n H_n\left(k_3 r\right)\cos\left(n\theta\right), \tag{5.25}$$

where $k_3 = \sqrt{\frac{-i\omega}{K_3} - \left(k_{zm}\right)}$ and A_n is the unknown amplitude for each n value.

The heat field generated in the middle of M2 depends on two distinct terms. One is the heat field $\hat{T}_2$, produced at the external boundary, at $r = b$, and transmitted into the medium M2. The other one is the heat field $\hat{T}_3$, generated at the interface between M2 and M1, at $r = a$, due to the energy that is transmitted into M2. $\hat{T}_2$ and $\hat{T}_3$ can be obtained through the following equations:

$$\hat{T}_2\left(\omega, r, \theta, k_{zm}\right) = \sum_{n=0}^{\infty} B_n J_n\left(k_2 r\right)\cos\left(n\theta\right), \tag{5.26}$$

$$\hat{T}_3\left(\omega, r, \theta, k_{zm}\right) = \sum_{n=0}^{\infty} C_n H_n\left(k_2 r\right)\cos\left(n\theta\right), \tag{5.27}$$

where $k_2 = \sqrt{\frac{-i\omega}{K_2} - \left(k_{zm}\right)}$, K_2 is the thermal diffusivity of medium M2 and B_n and C_n are the unknown amplitudes for each n value.

The heat field in the medium M1 only depends on the energy transmitted through the inner surface of the interface between M2 and M1, at $r = a$. Therefore, only a single term ($\hat{T}_4$) is necessary to obtain the heat field generated in this medium. The term $\hat{T}_4$ can be written as:

$$\hat{T}_4\left(\omega,r,\theta,k_{zm}\right) = \sum_{n=0}^{\infty} D_n J_n\left(k_1 r\right)\cos\left(n\theta\right), \qquad (5.28)$$

where $k_1 = \sqrt{\frac{-i\omega}{K_1} - \left(k_{zm}\right)}$, K_1 is the thermal diffusivity of medium M1 and D_n is the unknown amplitude for each n value.

For each n value, a system of four equations with four unknown factors is derived, ensuring the continuity of temperatures and heat fluxes along the interfaces, at $r = a$ and $r = b$:

$$\hat{T}_{inc}\left(\omega,r,\theta,k_{zm}\right) + \hat{T}_1\left(\omega,r,\theta,k_{zm}\right) = \hat{T}_2\left(\omega,r,\theta,k_{zm}\right), \text{ at } r = b, \qquad (5.29)$$

$$\lambda_3 \frac{\partial\left[\hat{T}_{inc}\left(\omega,r,\theta,k_{zm}\right)\right]}{\partial r} + \lambda_3 \frac{\partial\left[\hat{T}_1\left(\omega,r,\theta,k_{zm}\right)\right]}{\partial r} = \lambda_2 \frac{\partial\left[\hat{T}_2\left(\omega,r,\theta,k_{zm}\right)\right]}{\partial r}, \text{ at } r = b, \qquad (5.30)$$

$$\hat{T}_2\left(\omega,r,\theta,k_{zm}\right) + \hat{T}_3\left(\omega,r,\theta,k_{zm}\right) = \hat{T}_4\left(\omega,r,\theta,k_{zm}\right), \text{ at } r = a, \qquad (5.31)$$

$$\lambda_2 \frac{\partial\left[\hat{T}_2\left(\omega,r,\theta,k_{zm}\right)\right]}{\partial r} + \lambda_2 \frac{\partial\left[\hat{T}_3\left(\omega,r,\theta,k_{zm}\right)\right]}{\partial r} = \lambda_1 \frac{\partial\left[\hat{T}_4\left(\omega,r,\theta,k_{zm}\right)\right]}{\partial r}, \text{ at } r = a, \qquad (5.32)$$

The resolution of the system gives the amplitude terms A_n, B_n, C_n and D_n:

$$\begin{bmatrix} a_{11} & a_{12} & a_{13} & a_{14} \\ a_{21} & a_{22} & a_{23} & a_{24} \\ a_{31} & a_{32} & a_{33} & a_{34} \\ a_{41} & a_{42} & a_{43} & a_{44} \end{bmatrix} \begin{bmatrix} A_n \\ B_n \\ C_n \\ D_n \end{bmatrix} = \left(-1\right)^n \varepsilon_n \begin{bmatrix} b_1 \\ b_2 \\ c_3 \\ d_4 \end{bmatrix}, \qquad (5.33)$$

with $a_{11} = H_n\left(k_3 b\right)$; $a_{12} = -J_n\left(k_2 b\right)$; $a_{13} = -H_n\left(k_2 b\right)$; $a_{14} = 0$;

$a_{21} = 0$; $a_{22} = J_n\left(k_2 a\right)$; $a_{23} = H_n\left(k_2 a\right)$; $a_{24} = J_n\left(k_1 a\right)$;

$a_{31} = \lambda_3\left[nH_n\left(k_3 b\right) - \left(k_3 b\right)H_{n+1}\left(k_3 b\right)\right]$; $a_{32} = -\lambda_2\left[nJ_n\left(k_2 b\right) - \left(k_2 b\right)J_{n+1}\left(k_2 b\right)\right]$;

$$a_{33} = -\lambda_2 \left[nH_n(k_2 a) - (k_2 a) H_{n+1}(k_2 b) \right]; \; a_{34} = 0 ;$$

$$a_{41} = 0 ; \; a_{42} = \lambda_2 \left[nJ_n(k_2 a) - (k_2 a) J_{n+1}(k_2 a) \right];$$

$$a_{43} = \lambda_2 \left[nH_n(k_2 a) - (k_2 a) H_{n+1}(k_2 a) \right]; \; a_{44} = -\lambda_1 \left[nJ_n(k_1 a) - (k_1 a) J_{n+1}(k_1 a) \right];$$

$$b_1 = \frac{iA}{4\lambda_3} H_n(k_3 r_0) J_n(k_3 b); \; b_2 = 0 ; \; b_3 = \frac{iA}{4} H_n(k_3 r_0) \left[nJ_n(k_3 b) - (k_3 b) J_{n+1}(k_3 b) \right]; \; b_4 = 0 .$$

The accuracy of the BEM solution has been studied by computing the response at two receivers located in the system, as illustrated in Figure 5.15 [rec1 (-0.05, 0.0, 1.0) m, rec2 (-0.4, 0.0, 0.9) m].

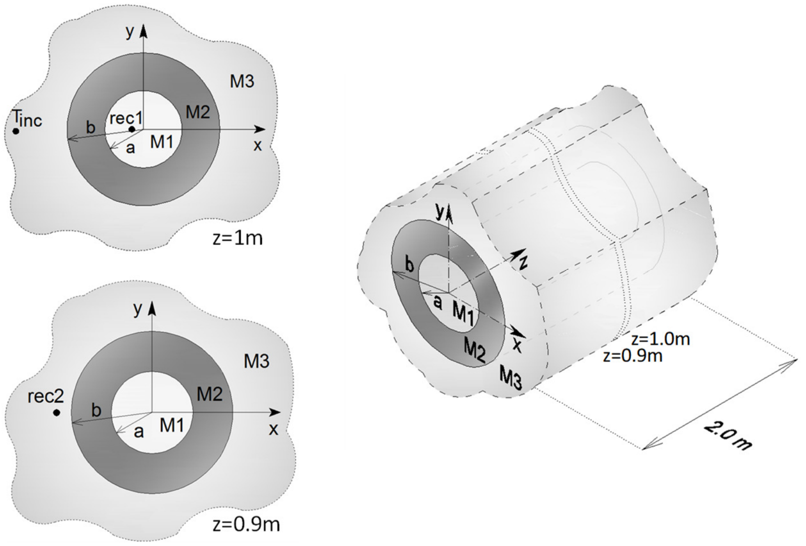

Figure 5.15: Scheme of the two receivers placed on two concentric cylindrical inclusions embedded in an unbounded space [rec1 $(-0.05,\ 0.0,\ 1.0)$ m , rec2 $(-0.4,\ 0.0,\ 0.9)$ m], subjected to a 3D point heat source, T_{inc}.

The material thermal properties of the cylindrical inclusion (medium M2) with radius $b = 0.30$ m composed of an inner body (medium M1) with radius $a = 0.15$ m and of the host uniform solid medium (medium M3) are listed in Table 5.1. L_{vs} is assumed to be 60.0 m . The system is 2 m in length and limited by adiabatic surfaces.

Table 5.1: Material thermal properties of the two circular cylindrical concentric inclusions embedded in an unbounded space.

Medium	Conductivity λ $\mathrm{W.m^{-1}.^{o}C^{-1}}$	Density ρ $\mathrm{kg.m^{-3}}$	Specific heat c $\mathrm{J.kg^{-1}.^{o}C^{-1}}$
M1	0.12	712.00	1550.00
M2	63.90	7832.00	434.00
M3	1.40	2300.00	880.00

The system was subjected to a point heat source, $\hat{T}_{inc}$, placed at (-1.0 m, 0.0 m, 1.0 m). Temperature computations were performed in the frequency range $[0.0\ ,1\times10^{-5}]$ Hz. The responses were computed for complex frequencies $\omega_c=\omega-\mathrm{i}\eta$ (with $\eta=0.7\Delta\omega$, $\Delta\omega=2\pi\times\Delta f$ and $\Delta f=0.5\times10^{-7}\ \text{Hz}$).

The responses were computed both analytically and using the 3D BEM formulation, considering different numbers of boundary elements. Figure 5.16 a) and c) show the analytical response (real and imaginary parts) at the two receivers. Figure 5.16 b) and d) illustrate the absolute value of the error at receivers 1 and 2 when the problem is solved with the proposed BEM algorithm, using two numbers of boundary elements to discretize the inclusions: 800(20×40) and 1800(30×60). It can be observed that the solution improves as the number of boundary elements increases. As expected, the BEM error is higher at receiver 2 since this is nearest to the heat source.

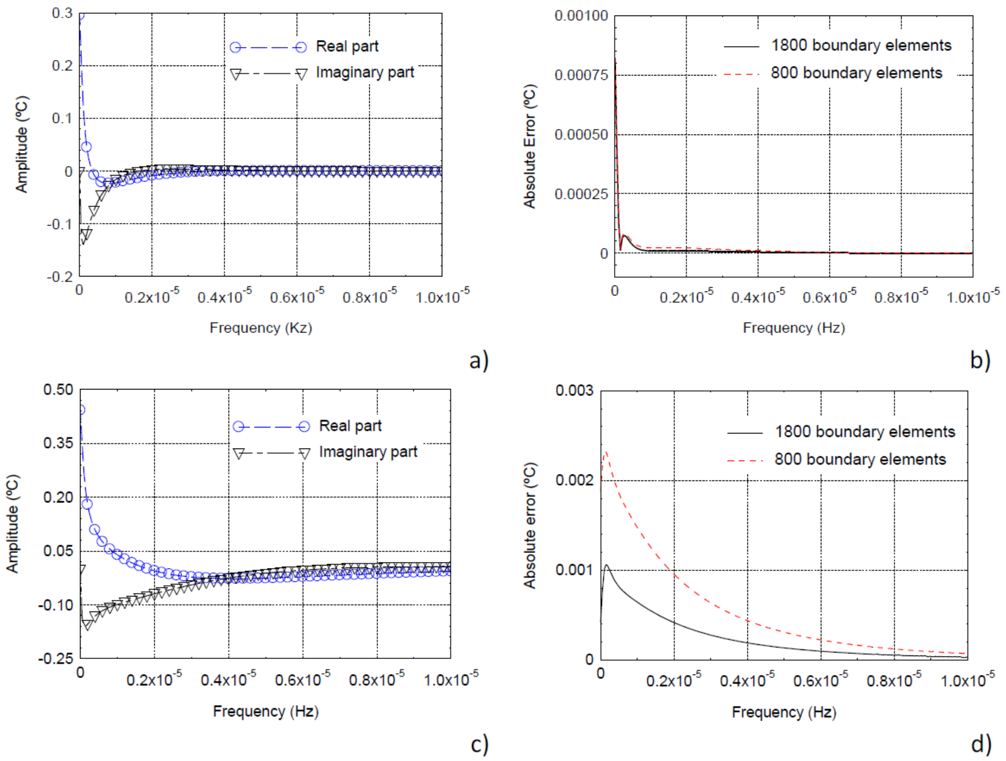

Figure 5.16: Analytical solutions and BEM error at two receivers: a) rec1 – analytical results; b) rec1 - variation of the BEM error with the frequency; c) rec2 – analytical results; d) rec2 - variation of the BEM error with the frequency.

Figure 5.17 illustrates the temperature responses, at frequency 0.5×10^{-7} Hz, computed at a grid of receivers (Grid 1) placed at $z=1.0$ m, crossing the system. This figure shows the real and imaginary parts of the analytical response and the error obtained when the system is solved using the BEM. It can be seen that the magnitude of the error increases as the receivers approach the inclusion's boundary. On the other hand, as expected, the BEM accuracy improves as the receivers are placed further away from the heat source. It can further be observed that the solution improves as the number of boundary elements increases, which illustrates the good accuracy of the BEM response.

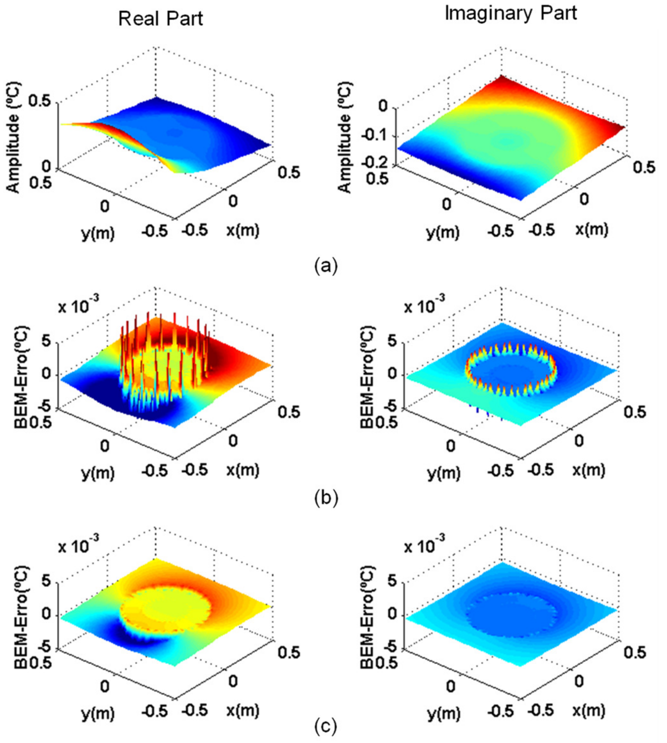

Figure 5.17: Comparative analysis of analytical and BEM responses (real and imaginary parts), at frequency 0.5×10^{-7} Hz, at the Grid 1 of receivers, for different numbers of boundary elements: a) analytical response; b) BEM error for 800 boundary elements; c) BEM error for 1800 boundary elements.

5.4 Numerical applications

In order to illustrate the applicability of the proposed 3D BEM model, two different problems are analysed. The BEM algorithm is first used to simulate the heat conduction through a concrete column embedding a concentric, non-concentric or sloped cylindrical inclusion, subjected to an external 3D point heat source. The effect of the inclination, as well as the thermal properties of the cylindrical inclusion, on the temperature distribution inside the column and on its surface, is analysed.

Finally, the BEM formulation is used to simulate the dynamic heat transfer by conduction through a geometrical point thermal bridge in a 3D building corner. A sinusoidal variation of the external temperature is assumed. The dynamic thermal bridging effect near the corner is evaluated.

5.4.1 3D cylindrical inclusions

The proposed model was used to simulate the heat conduction through a concrete column (medium M2) with a radius of 0.125 m, containing a cylindrical inclusion (medium M1) with a radius of 0.05 m (Figure 5.18). The model was subjected to a 3D external heat point source, located at (-0.7 m, 0.0 m, 0.375 m).

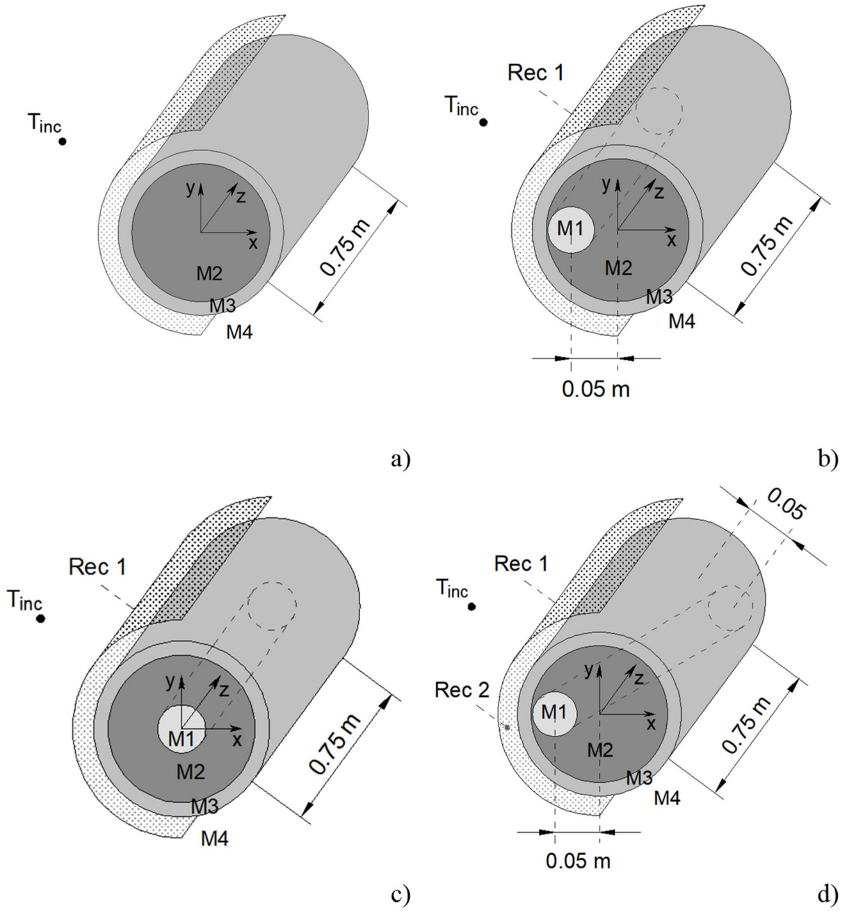

Figure 5.18: Geometrical models used in the first numerical applications. a) Case 0 – without inclusion (reference case); b) Case 1 – non-concentric inclusion; c) Case 2 - concentric inclusion; d) Case 3 - inclusion inclined along the z axis.

Medium M3 is a thin air layer, with a thickness of 0.005 m, representing the convection and radiation effect on the external surface of the concrete column.

Continuity of temperatures and heat fluxes was prescribed at the interfaces between inclusions and on the exterior boundary. The length of the inclusion was limited by imposing null heat fluxes on sections $z = 0.0\text{ m}$ and $z = 0.75\text{ m}$.

Four cases were simulated: Case 0 – Concrete column without inclusion (Figure 5.18 a)); Case 1 – Concrete column with a parallel cylindrical inclusion positioned at $x = -0.05\text{ m}$ and $y = 0.0\text{ m}$ (Figure 5.18 b)); Case 2 – Concrete column with a concentric cylindrical inclusion centred at $x = 0.0\text{ m}$ and $y = 0.0\text{ m}$ (Figure 5.18 c)); Case 3 – Concrete column with a cylindrical inclusion inclined 13.3% along the z axis, with an offset of 0.05 m in x from the column's centre, as illustrated in Figure 5.18 d).

In all cases two different materials were considered for the inclusions (steel and a thermal insulation material). The material thermal properties assumed for the different mediums of the model, are listed in Table 5.2.

Table 5.2: Materials' thermal properties of the concrete columns.

Medium	Material	Thermal conductivity $\lambda\ (\text{W.m}^{-1}.^{\circ}\text{C}^{-1})$	Density $\rho\ (\text{kg.m}^{-3})$	Specific heat $c\ (\text{J.kg}^{-1}.^{\circ}\text{C}^{-1})$
M1	Steel	63.90	7832.00	434.00
	Thermal insulation	0.046	130.00	1638.00
M2	Concrete	1.40	2300.00	880.00
M3	Surface air layer	0.125	1.29	1000.00
M4	External environment (air)	0.026	1.29	1000.00

Temperature in time domain

The heat responses in the spatial–temporal domain are obtained by means of an inverse Fourier transform in the frequency domain. In order to prevent the aliasing phenomena, complex frequencies, with a small imaginary part of the form $\omega_c = \omega - \mathrm{i}\eta$ (with $\eta = 0.7\Delta\omega$ and $\Delta\omega$ being the frequency step), are used in the computation procedure.

The time evolution of the heat source amplitude can be diversified. The time Fourier transform of the incident heat field defines the frequency domain where the BEM solution needs to be computed $\hat{T}_0(x,y,\omega)=\int_0^{\infty} T_0(x,y,t)e^{-i\omega t}dt$. The response needs to be computed from 0.0 Hz up to high frequencies. An intrinsic characteristic of this problem is that the heat responses decay very fast as the frequency increases, which allows us to limit the upper frequency for the solution.

The final equation is given by

$$T(x,y,t)=\frac{1}{2\pi}\int_0^{\infty}\hat{T}_0(x,y,\omega)\hat{T}(x,y,\omega)e^{i\omega t}d\omega\,, \tag{5.34}$$

which is computed as a discrete inverse fast Fourier transform.

The calculations were performed in the frequency range $\left[0.0,\ 1.024\times10^{-3}\right]\text{ Hz}$ with a frequency increment of $\Delta f=0.5\times10^{-6}\text{ Hz}$, which results in a time window of $1/\left(0.5\times10^{-6}\right)\text{ s}$. The source starts emitting energy at instant $t=4\text{ h}$ and continues for 10 h. The heat source time dependence is assumed to be rectangular.

The temperature field distribution was computed at two grids of receivers placed at $y=0.0\text{ m}$ and $z=0.75\text{ m}$, crossing the system, for Case 1 and Case 3, this time considering a cylindrical inclusion with a length of 1.5 m. Figure 5.19 shows the temperature responses at the receivers 9 h after the source begins heating. The effect of the inclusion properties and inclination on the temperature distribution inside the column and on its surface, was analysed.

It can be observed that due to its low thermal resistance, the steel inclusion is responsible for greater heat distribution across the concrete column. Thus, the surface temperatures will be lower than in the case with the insulation inclusion, especially for the receivers furthest from the source (in z direction). The thermal insulation, however, acts as a barrier to the heat flux, thereby maintaining higher temperatures at the external surface of the concrete column on the heat source side. The further away the steel inclusion is from the surface, the slower is the process of heat dissipation. Therefore, the temperatures on the surface of the concrete column with the inclined inclusion are higher than those on the concrete column with the parallel inclusion.

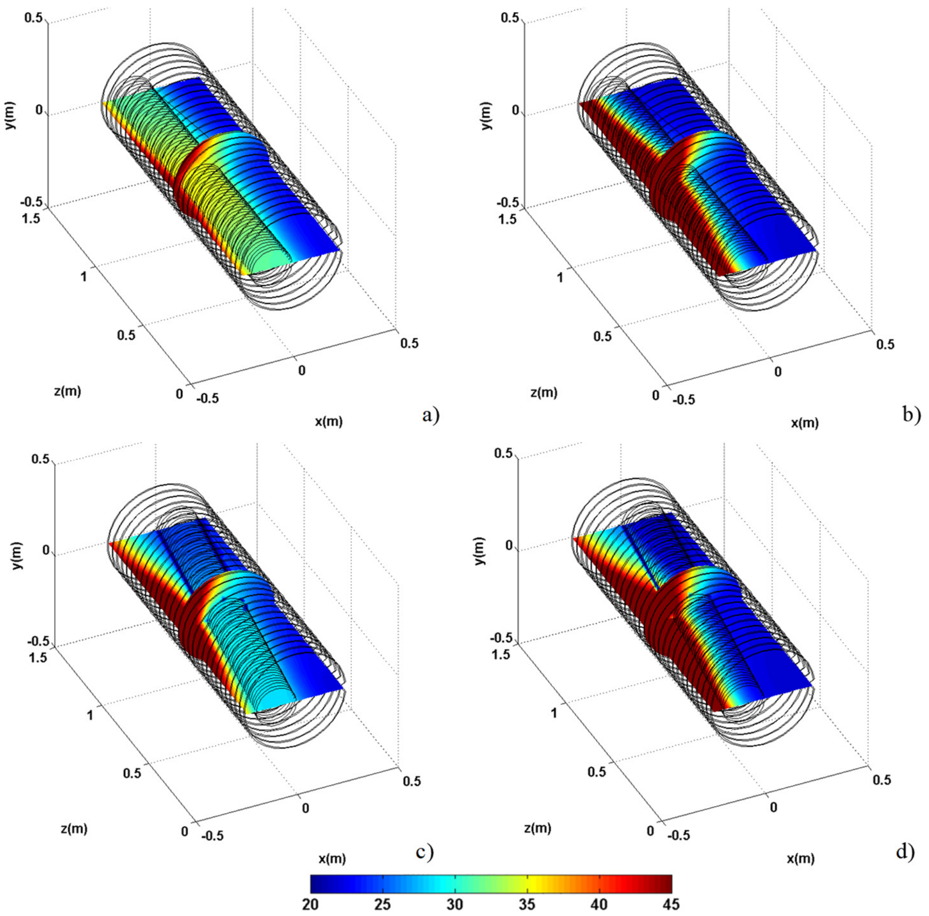

Figure 5.19: Temperature (in ºC) distribution recorded at two grids of receivers across and along the model. a) Case 1 - Concrete column with a non-concentric steel cylindrical inclusion; b) Case 1 - Concrete column with a non-concentric insulation cylindrical inclusion; c) Case 3 - Concrete column with an inclined steel cylindrical inclusion; d) Case 3 - Concrete column with an inclined insulation cylindrical inclusion.

5.4.2 3D building corner

The BEM formulation proposed in section 5.2.3 was use to simulate the dynamic heat diffusion through a geometrical PTB corresponding to a 3D concrete building corner.

Figure 5.20 illustrates the type of problem to be solved: a 3D building corner representing a junction between two vertical walls and the roof of a building. The external surfaces of the walls and roof are subjected to a temperature variation $\left(T = T\left(x, y, z, t\right)\right)$, while the indoor temperature is assumed to be constant $\left(T = T_0\right)$.

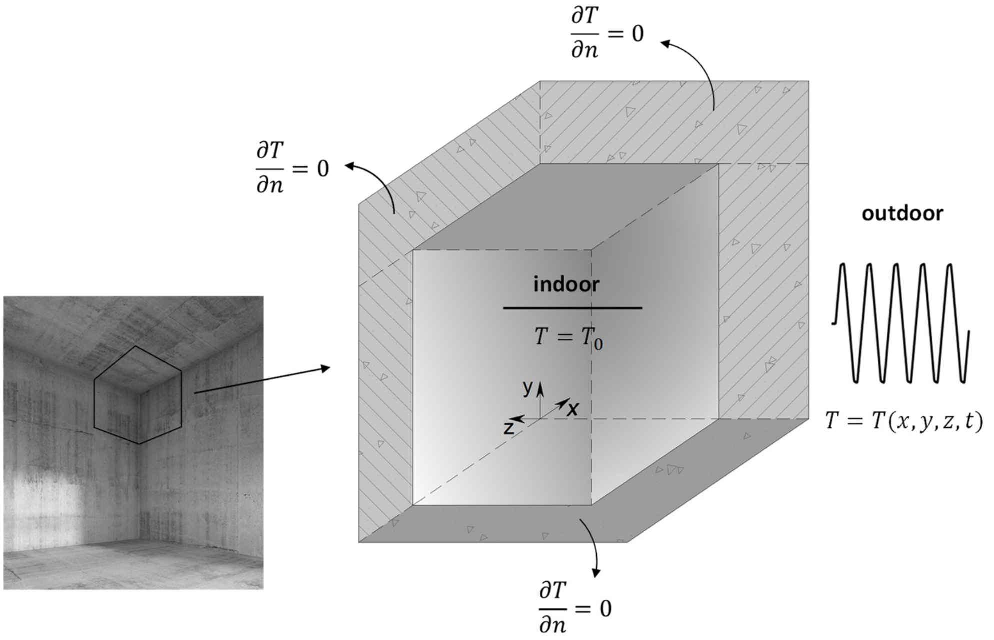

Figure 5.20: Three-dimensional building corner scheme and boundary conditions of the problem.

The point thermal bridge (PTB) in the 3D corner is characterized by a 3D heat flux. At a certain distance from the 3D corner, along the wall to wall junction and along the two wall to roof junctions, the thermal bridge becomes linear (2D heat flux) and the heat flux in the middle of each building element becomes one-directional (1D). Therefore, null heat fluxes can be prescribed along the 2D cut-off planes of the problem. The internal dimension of each building component was taken to be $1.0 \text{ m} \times 1.0 \text{ m}$, as recommended in ISO 10211:2007 [34].

The external and internal surface thermal resistances (R_{se} and R_{si}, respectively) are modelled considering a thin air layer (0.003 m thick) along the outer and the inner surfaces to take into account convection and radiation phenomena. The R_{si} value depends on the direction of the heat flow. However, in this research work, the R_{si} was assumed to be 0.13 m^2.ºC/W for all inner surfaces. The R_{se} used for the outer surface was 0.04 m^2.ºC/W, in accordance with ISO 6946:2007 [35].

The R_{si} and R_{se} result in equivalent thermal conductivity values of 0.0231 W/(m.ºC) and 0.075 W/(m.ºC) for the internal and the external air layers, respectively. The density and the specific heat of the two thin air layers as well as the thermal properties of the concrete are the same listed in Table 5.2.

The 3D building corner detail was assumed to have a constant temperature of 20 ºC throughout the full domain at $t = 0.0$ h. At that time, it was all subjected to an exterior temperature (θ_e) change. The temperature time dependence was assumed to be sinusoidal, with a period of 24 h, and with amplitude oscillations of 15 ºC, as illustrated in Figure 5.21. The indoor temperature (θ_i) was kept at 20 ºC. The analysis simulates 6 cycles in order to allow the system response to start behaving almost in a 24 h cycle.

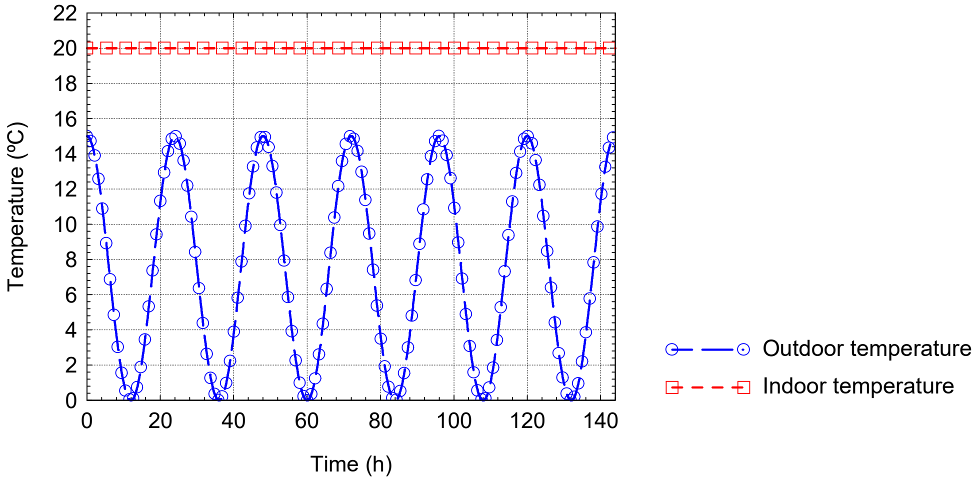

Figure 5.21: Imposed temperature over time: sinusoidal variation of the external temperature (θ_e) (6 cycles with a period of 24 h); constant indoor temperature (θ_i) of 20 ºC.

The frequency domain of computation ranged from 0.0 Hz to 4096/(144×3600) Hz, with a frequency increment of 1.0/(144×3600) Hz, which determined a total time window of 144 h for the analysis. Each interface between materials was discretised using 4563 boundary, while 1872 constant boundary elements were used to model the lateral interfaces at the cut off planes.

The temperature distribution was obtained using two very fine grids of receivers, placed as illustrated in Figure 5.22. The grid 1 is a longitudinal square grid along the internal surface of the concrete roof and the plane sections between roof and walls. The grid 2 contains three different planes of grid receivers lying in the same planes of the two walls and roof internal surfaces of the 3D building corner detail.

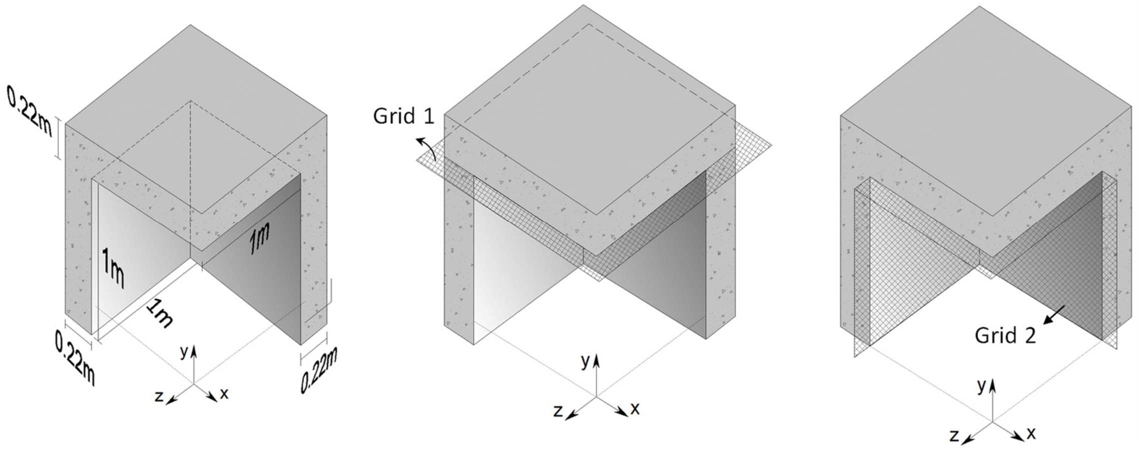

Figure 5.22: 3D concrete building corner dimensions and scheme of the receivers' grids.

A set of snapshots of the time domain simulations is presented to illustrate the resulting heat diffusion across the point thermal bridge. Figure 5.23 shows the temperature field distribution at different time instants. A colour scale is used in the plots, with the red and blue shades corresponding, respectively, to higher and lower temperature amplitudes.

In the first plot, at t ≈ 102 h (Figure 5.23 a), the exterior temperature had already started the second cycle of 24 h and dropped from 15 °C to 7.5 °C. However, high temperature values are still registered along the internal surfaces of the building corner and the linear and point thermal bridging effect is barely perceptible in this plot.

At t ≈ 108 h (Figure 5.23 b), the exterior temperature had fallen to 0 °C and the surface temperatures are now decreasing through the full domain. The thermal bridging effect is now visible near the 2D junctions and the 3D corner.

At t ≈ 114 h (Figure 5.23 c) the exterior temperature had increased to 7.5 °C, however, the temperature is still decreasing along the two grids of receivers and reaches the lowest values, showing the existence of a thermal delay. The point thermal bridging effect is now very pronounced leading to significantly lower temperatures in the vicinity of the 3D corner.

At t ≈ 120 h (Figure 5.23 d) the exterior temperature had reached again 15 °C, completing the second cycle of 24 h. The temperature is increasing through the full domain. However, at this instant, lower temperatures are registered by the receivers placed in the middle of the junctions between building components than close to the internal and the external surfaces. This difference is more pronounced near the 3D corner where the thermal phase lag is higher.

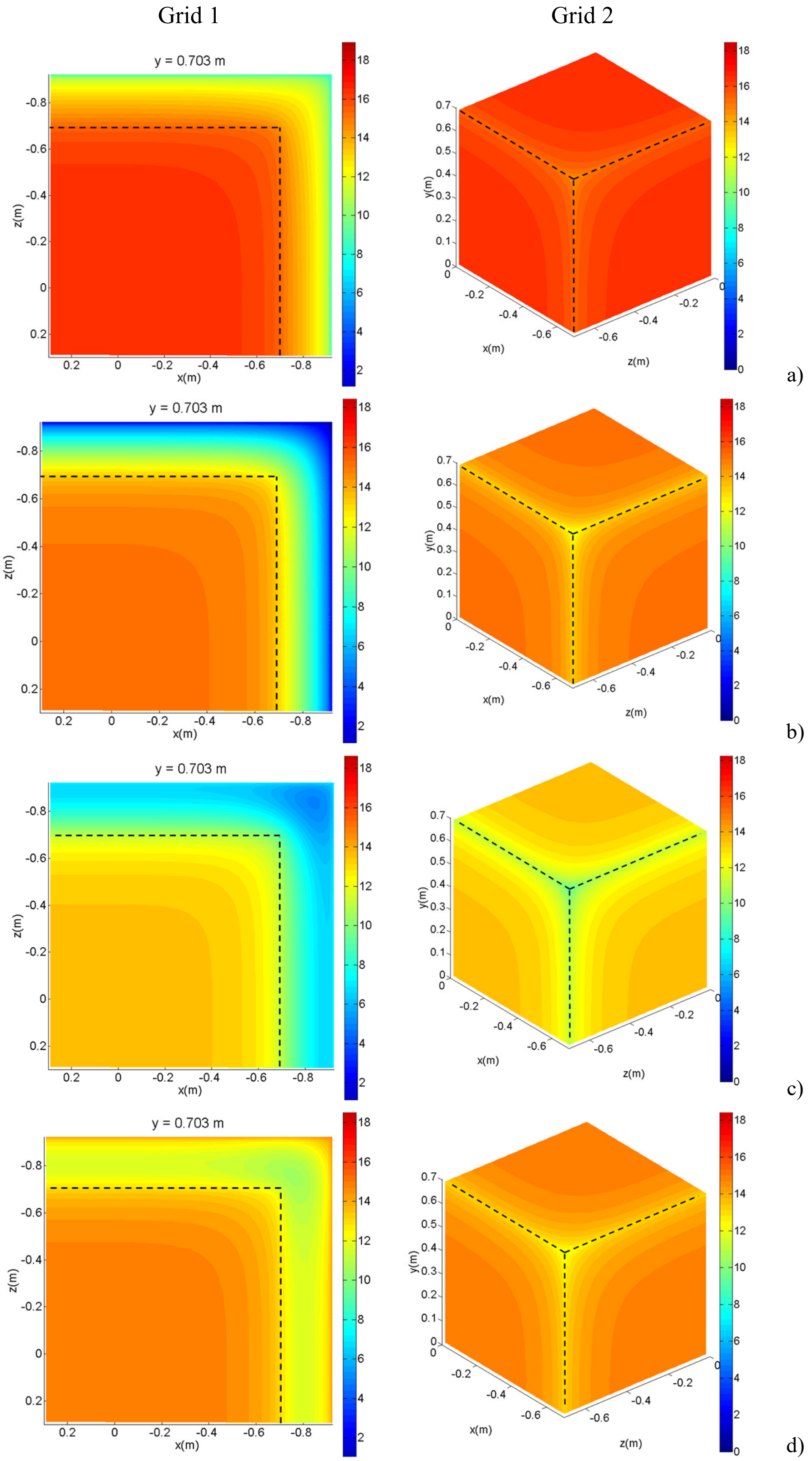

Figure 5.23: Temperature distribution (in ºC) recorded at the two grids of receivers. Time responses at: a) t ≈ 102 h; b) t ≈ 108 h; c) t ≈ 114 h; d) t ≈ 120 h.

As the time passed, the system behaves periodically and exhibit similar temperature distribution along the domain for equivalent phases of the time window.

5.5 Conclusions

This chapter has first described the 3D Boundary Element Method (BEM) formulations, in the frequency domain, for the simulation of the heat diffusion inside 3D inclusions containing an inner 3D body/defect. Different boundary conditions were considered: null heat fluxes, null temperatures and continuity of temperatures and heat fluxes. The BEM formulation for a more general model, with the same boundary conditions of a typical PTB problem, was also described.

An analytical solution was proposed for the integration of the singular integrals, that appear when the element to be integrated is the loaded one (singular element). The analytical integrations were first compared with numerical solutions using a standard Gaussian quadrature scheme. Then the three-dimensional BEM models, incorporating the analytical solutions, were verified against analytical formulations derived for a cylindrical circular inclusion limited by two perpendicular sections, where null heat fluxes where imposed. The responses showed very good accuracy.

Two different numerical applications were performed to demonstrate the applicability of the BEM models. The proposed model was first used to simulate the heat conduction through a concrete column containing a cylindrical inclusion, subjected to an external 3D point heat source. The effect of both the inclination and the thermal properties of the cylindrical inclusion on the temperature distribution inside the column and on its surface, was analysed. Finally, the 3D BEM model was used to simulate the dynamic heat transfer by conduction through a geometrical point thermal bridge (PTB) corresponding to a 3D concrete building corner. A sinusoidal variation of the external temperature was assumed in the simulations. Time solutions were obtained by applying inverse Fourier transformations. The variation of the temperature distribution over time, in the vicinity of the PTB, was computed. The BEM algorithm was found to be suitable for simulating the dynamic heat transfer through the PTB.

References

[1] P. Iodice, N. Massarotti, A. Mauro, Effects of inhomogeneities on heat and mass transport phenomena in thermal bridges, energies 9 (3) (2016) 126.

[2] E. Kossecka, J. Kosny, Equivalent wall as a dynamic model of a complex thermal structure, Journal of Thermal Insulation and Building Envelopes 20 (1997) 249-268.

[3] K. Martin, C. Escudero, A. Erkoreka, I. Flores, J.M. Sala, Equivalent wall method for dynamic characterisation of thermal bridges, Energy and Buildings 55 (2012) 704–714.

[4] F. Aguilar, J.P. Solano, P.G. Vicente, Transient modeling of high-inertial thermal bridges in buildings using the equivalent thermal wall method, Applied Thermal Engineering 67 (1-2) (2014) 370-377.

[5] Y. Gao, J.J. Roux, L.H. Zhao, Y. Jiang, Dynamical building simulation: A low order model for thermal bridges losses, Energy and Buildings 40 (2008) 2236-2243.

[6] A. Tadeu, I. Simões, N. Simões, J. Prata, Simulation of dynamic linear thermal bridges using a BEM model in frequency domain, Energy and Buildings, 43 (2011) 3685–3695.

[7] G. Mao, G. Johannesson, Dynamic calculation of thermal bridges, Energy and Buildings 26 (1997) 233-240.

[8] K. Dikarev, A. Berezyuk, O. Kuzmenko, A. Skokova, Experimental and numerical thermal analysis of joint connection «floor slab – balcony slabe» with integrated thermal break, Energy Procedia 85 (2016) 184–192.

[9] J. Šadauskiene, J. Ramanauskas, L. Šeduikyte, M. Daukšys, A. Vasylius, A Simplified methodology for evaluating the impact of point thermal bridges on the high-energy performance of a passive house, sustainability 7 (2015) 16687-16702.

[10] T. Theodosioua, K. Tsikaloudakia, D. Bikasa, Analysis of the thermal bridging effect on ventilated facades, Procedia Environmental Sciences 38 (2017) 397 – 404.

[11] T. Theodosiou, A. Tsikaloudaki, K. Kontoleon, D. Bikas, Thermal bridging analysis on cladding systems for building facades, Energy and Buildings 109 (2015) 377–384.

[12] K.J. Bathe. Numerical methods in finite element analysis. Prentice-Hall, New Jersey, 1976.

[13] M.N. Ozisik, Finite difference methods in heat transfer. CRC Press Inc, USA, 1994.

[14] Gh. Juncu, Unsteady conjugate forced convection heat/mass transfer from a finite flat plate, International Journal of Thermal Sciences 47 (2008) 972–984.

[15] C.A. Brebbia, J.C. Telles, L.C. Wrobel, Boundary elements techniques: theory and applications in engineering, Springer-Verlag, Berlin-New York, 1984.

[16] Y. Ochiai, Steady heat conduction analysis in orthotropic bodies by triple-reciprocity BEM, Computer Modeling in Engineering and Sciences 2 (4) (2001) 435-446.

[17] B. Šarler, Towards a mesh-free computation of transport phenomena, Engineering Analysis with Boundary Elements 26(9) (2002) 731-738.

[18] F. Ma, J. Chatterjee, D.P. Henry, P.K. Banerjee, Transient heat conduction analysis of 3D solids with fibre inclusions using the boundary element method, International Journal for Numerical Methods in Engineering 73 (2008) 1113-1136.

[19] P. Jablonski, Integral and geometrical means in the analytical evaluation of the BEM integrals for a 3D Laplace equation. Engineering Analysis with Boundary Elements 34 (2010) 264-273.

[20] Q. Xianyun, J. Zhang, G. Xie, F. Zhou, G. Li, A general algorithm for the numerical evaluation of nearly singular integrals on 3D boundary element, Journal of Computational and Applied Mathematics 235(14) (2011) 4174-4186.

[21] H. Zhou, Z. Niu, C. Cheng, Z. Guan, Analytical integral algorithm applied to boundary layer effect and thin body effect in BEM for anisotropic potential problems, Computers & Structures 86 (2008) 1656–1671.

[22] J.C.F. Telles, A self-adaptive co-ordinates transformation for efficient numerical evaluation of general boundary element integrals, International Journal for Numerical Methods in Engineering 24 (1987) 959-973.

[23] X.L. Chen, Y.J. Liu, An advanced 3-D boundary element method for characterizations of composite materials, Engineering Analysis with Boundary Elements 29 (2005) 513–523.

[24] K. Hayami, Variable transformations for nearly singular integrals in the boundary element method, Publications of the Research Institute for Mathematical Sciences 41 (2005) 821–842.

[25] H. Ma, N. Kamiya, Distance transformation for the numerical evaluation of near singular boundary integrals with various kernels in boundary element method, Engineering Analysis with Boundary Elements 26 (2002) 329-339.

[26] H. Ma, N. Kamiya, A general algorithm for the numerical evaluation of nearly singular boundary integrals of various orders for two- and three-dimensional elasticity, Computational Mechanics 29 (2002) 277-88.

[27] D.N. Srivastava, Contractor, Efficient evaluation of integrals in 3-D Boundary Element Method using linear shape functions over plane triangular elements, Applied Mathematical Modelling 16 (6) (1992) 282-290.

[28] Z. Niu, W.L. Wendland, X.X. Wang, H.L. Zhou, A semi-analytical algorithm for the evaluation of the nearly singular integrals in three-dimensional boundary element methods. Computer Methods in Applied Mechanics and Engineering, 194 (2005) 1057-74.

[29] A. Tadeu, J. António, 3D Acoustic wave simulation using BEM formulations: closed form integration of singular and hypersingular integrals, Engineering Analysis with Boundary Elements 36 (2012) 1389–1396.

[30] L.C. Wrobel, CA. Brebbia, A formulation of the Boundary Element Method for axisymmetric transient heat conduction, International Journal of Heat and Mass Transfer 24 (1981) 843-850.

[31] A. Tadeu, P.F.A. Santos, E. Kausel, Closed-form integration of singular terms for constant, linear and quadratic boundary elements. Part I. SH wave propagation, Engineering Analysis with Boundary Elements 23 (1999) 671-681.

[32] A. Tadeu, J. António, I. Castro, Coupling the BEM/TBEM and the MFS for the numerical simulation of acoustic wave propagation, Engineering Analysis with Boundary Elements 34 (2010) 405-416.

[33] H.S. Carslaw, J.C. Jaeger, Conduction of heat in solids. Oxford University Press, Vivian Ridler, Walton Street, Oxford, second edition, 1959.

[34] International Standard Organization, ISO 10211, Thermal bridges in building construction - Heat flows and surface temperatures - Detailed calculations, 2007.

[35] International Standard Organization, ISO 6946, Building components and building elements - Thermal resistance and thermal transmittance - Calculation method, 2007.

CHAPTER 6

EXPERIMENTAL VALIDATION OF THE FREQUENCY DOMAIN BEM MODEL FOR THE 3D DYNAMIC SIMULATION OF POINT THERMAL BRIDGES OF BUILDINGS

6 EXPERIMENTAL VALIDATION OF THE FREQUENCY DOMAIN BEM MODEL FOR THE 3D DYNAMIC SIMULATION OF POINT THERMAL BRIDGES OF BUILDINGS

6.1 Introduction

The thermal behaviour of point thermal bridges (PTBs) is still barely explored in the literature. Due to the three-dimensional (3D) modelling complexity and high computer run time required for the simulations, most of the studies are performed in steady-state conditions ([1],[2]). However, in spite of being more complex the dynamic simulation models lead to reliable estimation results and a better knowledge of the point thermal bridging effect in the building envelope. Furthermore, dynamic models also offer more versatile applicability [3].

The accuracy of the 3D dynamic numerical modelling tools used to simulate the thermal performance of building details depends on many factors ([4],[5]) and it can be compromised for different reasons, such as errors in the model inputs or the neglecting of some physical model aspects. Therefore, experimental measurements can be very useful, not only to evaluate the real behaviour of the physical model but also to validate the numerical model and to improve the model's predictions. These measurements are normally performed, in situ or in the laboratory, using temperature and heat flux sensors. Despite this, very few studies are found in the literature in which the 3D numerical models' results are compared with experimental measurements.

Corvacho [6] performed measurements of the dynamic thermal behaviour of linear and point thermal bridges in the 2D and 3D corners of a test cell with known constructive details. The experimental results were used to evaluate the dynamic thermal behaviour of each thermal bridge and also to validate a numerical modelling tool. Simões *et al.* [7] has experimentally validated a 3D semi-analytical solution in the frequency domain for transient heat conduction in a multilayer system subjected to a spherical heat source. The experimental measurements were performed in laboratory using a Single-specimen Lambda-meter EP-500 apparatus and T-type thermocouples. The results showed a good agreement between the two methods. Zalewski *et al.* [8] performed an experimental campaign to quantify the surface and linear heat losses in a prefabricated building wall with vertical steel frameworks, using tangential-gradient heat flux-meters and thermocouples. The experimental results were compared with the numerical responses obtained with a commercial software for the steady-state 3D heat transfer simulation (TRISCO) [9]. Ascione *et al.* [10] used experimental in situ data to evaluate the thermal behaviour of a building corner. The results were used to validate a dynamic simplified methodology proposed by the authors, based on the conduction transfer function methods. Asdrubali *et al.* [11] presented a quantitative infrared technique to evaluate in situ the thermal bridging effect. The methodology proposed by the authors only requires the thermograms analysis and simple measurement of the air temperature to estimate the thermal bridging effect as a percentage increment of the one-dimensional (1D) homogenous wall thermal transmittance. The authors have concluded that the proposed methodology can also be used to analyze, improve and validate 3D simulation tools especially designed for the evaluation of building energy performance.

Contrary to the in situ measurements, the laboratory tests are normally performed under controlled environment conditions which allow us to measure each variable effect and also to control or even eliminate some of the undesirable factors that may influence the experimental results.

Furthermore, the laboratory apparatus allows the exactly replication of the experiments, enabling therefore the evaluation of the equipment precision and the confidence level of the laboratory tests.

The hot box [12] has been one of the most common items of laboratory apparatus used for the thermal characterization of building components containing heterogeneities. This test can follow two different methods: the calibrated hot box and the guarded hot box. On both hot box methods, the thermal behaviour of the specimen can be evaluated under steady-state ([13],[14]) or dynamic conditions ([15]-[17]), depending if the temperatures imposed inside the boxes are constants or variable in time. In generally, the dynamic analysis using a hot box requires the use of sensors to measure the heat flux and the surface and/or interfaces temperatures over time.

Several studies can be found in the literature describing the use of calibrated or guarded hot box facilities for the evaluation of the dynamic behaviour of building systems. However, all of them are applied to building details with a plane geometry, such as walls ([15]-[18]) and windows ([19],[20]), and none of them includes the analysis of non-regular geometries, such as 2D and 3D building corners, representing geometrical linear and point thermal bridges, respectively.

In this research work, a calibrated hot box is used to evaluate the dynamic thermal behaviour of a 3D wooden building corner representing a PTB. To the best of my knowledge, this type of equipment has never been used for the evaluation of non-planar building components. The main purpose is to get dynamic results of the heat flux and surface temperatures for use in the validation of the 3D BEM formulation presented in Chapter 5. In the calibrated hot box, the area of the specimen to be measured is significantly higher than in the guarded hot box which turns the first method more suitable for the analysis of the 3D building corner geometry. This chapter first gives a detail about the calibrated hot box apparatus and the test procedures. The experimental measurements are then analysed and compared with the dynamic numerical responses obtained with BEM.

6.2 Description of the calibrated hot box apparatus and measurement devices

The present section describes the hot box apparatus and the measurement equipment used to evaluate the dynamic heat transfer through a 3D wooden building corner.

The calibrated hot box was designed and built according to the requirements specified in ISO 8990:1994 [12]. The 3D corner specimen was placed in an EPS surround panel between two thermally insulated chambers, one hot and the other cold, in order to incite heat transfer through the specimen. Both the hot and cold chambers have one opening at the end to be coupled, respectively, to a heating system and to a climatic chamber (Fitoclima 1000 from Aralab), which provides the desired test temperature inside the boxes. The climatic chamber can work for a wide range of temperatures [-80; 180] °C. One baffle panel was placed in each chamber, in front of the internal and the external surface of the specimen, to reduce the radiative effects. A set of fans was used to control the air flux velocity during the experimental tests and also to avoid the stratification of the temperature inside the chambers. The apparatus was installed in a controlled room environment (set point of 20 °C). Figure 6.1 illustrates the calibrated hot box apparatus layout.

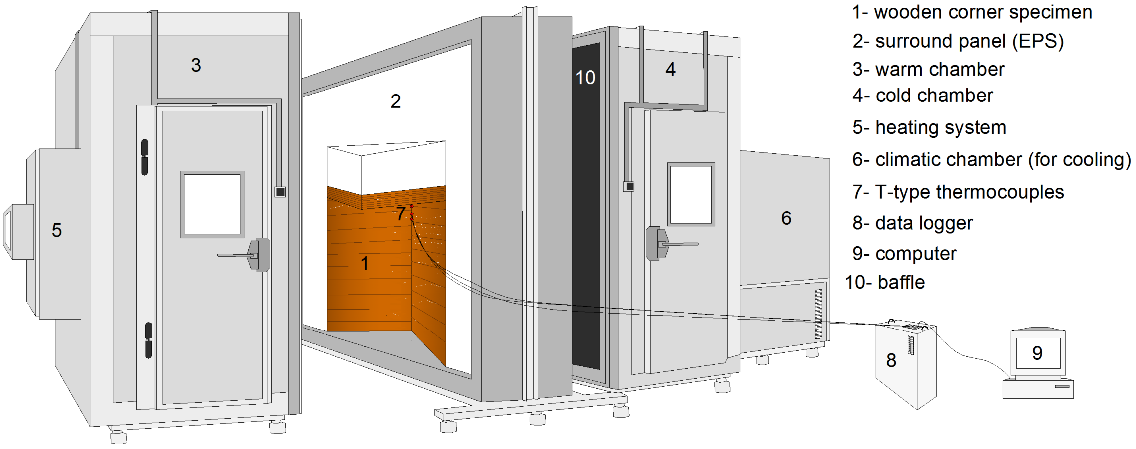

Figure 6.1: Calibrated hot box – Apparatus layout.

Measuring equipment specifications

Three ultrathin flat plate heat flux sensors, consisted of thermoelectric laminated panels sandwiched between flexible heterogeneous plastic layers and two HFP01 heat flux sensors [21] of a high-accuracy thermal resistance measuring system (TRSYS01) [22] were used to measure the heat fluxes occurring through the specimen.

The TRSYS01 is a measurement system normally used to determine, in situ, the thermal transmittance of building elements. The system includes two pairs of thermocouples and two HFP01 heat flux plates. The HFP01 sensor measures the differential temperature across the ceramic-plastic composite body of HFP01. This sensor generates a small output voltage proportional to the local heat flux, which enables the heat flux to be calculated by dividing the voltage by the sensitivity of the instrument. The HFP01 accuracy is about ± 5 %. The TRSYS01 data were recorded by a GL820 Midi DataLogger at 10-min intervals during the test. The two pairs of thermocouples from the TRSYS01 system are used to register the surface temperatures on the cold side of the specimen. The accuracy of each TRSYS01 thermocouple is ± 0.1 °C and they can be used for measurements in the -30 to 70 °C range [22].

33 wire T-type thermocouples, with a diameter less than 0.25 mm, were used to measure the internal surface temperatures of the specimen, near the 2D and the 3D junctions. The uncertainty of each T-type thermocouple was ± 0.16 ºC. They are suitable for measurements in the −200 to 350 °C range. The thermocouples were fixed to the surface by adhesive tape with an outer surface of high emissivity (> 0.8), so as not to influence the measurement of surface temperatures. The thermocouples were connected to a data logger system (Agilent 34980A). During the test, the temperatures were recorded at 1-minute intervals.

Before the experimental test of the 3D wooden building corner some preliminary tests were carried out to determine the errors associated with the experimental measurements and evaluate the measuring equipment in terms of reliability and reproducibility. The description and main results of these tests were already presented in Chapter 3.

6.3 Description of the specimen and the laboratory procedure

The building corner specimen used in this research work was made from three cross laminated timber (CLT) panels, normally used for the walls, floors and roofs in timber buildings. They were bolted together to represent a geometrical PTB, corresponding to a junction between two walls and a roof of a building (3D building corner). The CLT panels used are composed of seven layers of structural lumber boards, stacked crosswise and glued together [23]. The dimensions of each panel are: 0.18 m thick, 1 m wide and 1.5 m long.

The thermal conductivity, the mass density and the specific heat of the CLT material were experimentally determined. The thermal conductivity was evaluated by the guarded hot plate method (ISO 8302:1991[24]) using a single-specimen Lambda-meter, EP-500 model, from Lambda-Meβtechnik GmbH Dresden, following the test procedure defined in EN 12667:2001

[25]. The mass density was determined using the procedure described in EN 1602:1996 [26]. The specific heat was obtained using a Netzsch (DSC200F3) apparatus, following the ratio method. These tests were carried out at ITeCons - Institute for Research and Technological Development in Construction, Energy, Environment and Sustainability.

Five tests specimens were used for each test procedure. Table 6.1 gives the average value and standard deviation obtained for each CLT thermal property.

Table 6.1: CLT panels' thermal properties.

Material	Thermal conductivity λ $\left(\mathrm{W.m^{-1}.^{o}C^{-1}}\right)$		Density ρ $\left(\mathrm{kg.m^{3}}\right)$		Specific heat c $\left(\mathrm{J.kg^{-1}.^{o}C^{-1}}\right)$	
CLT	average	standard deviation	average	standard deviation	average	standard deviation
	0.13	0.00	574.69	35.63	1406.60	114.43

Figure 6.2 illustrates the 3D wooden corner specimen placed between the two hot box chambers.

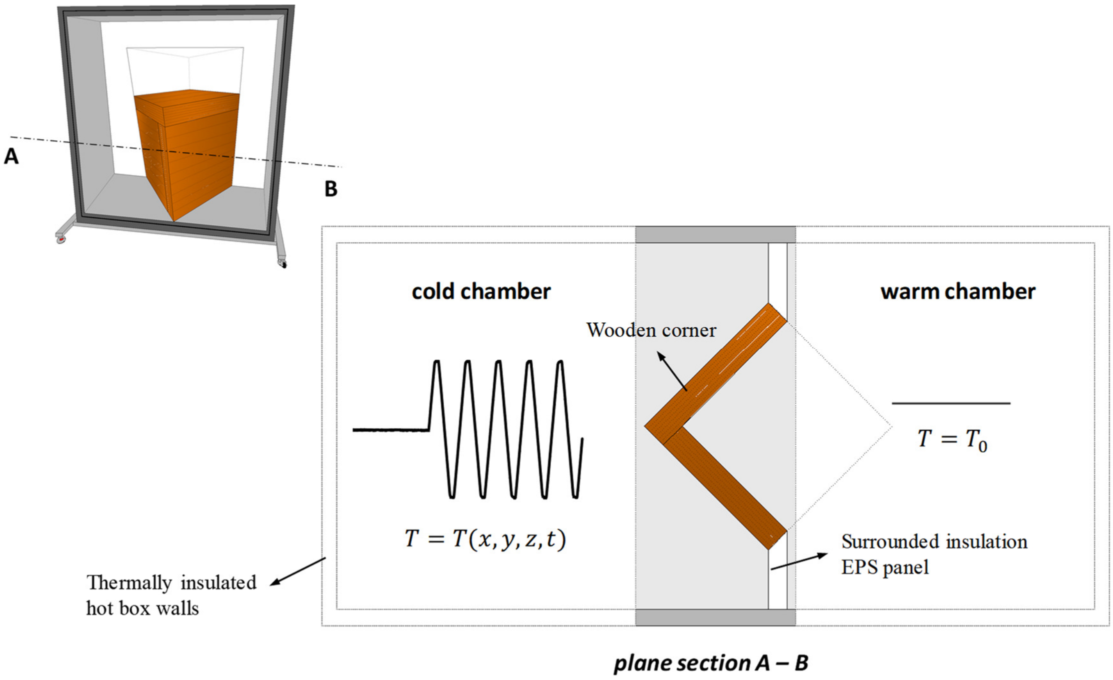

Figure 6.2: Wood building corner scheme and boundary conditions of the problem.

The cold chamber of the hot box represents the external environment and the warm chamber represents the indoor environment. A variation of temperature $(T = T(x, y, z, t))$ was imposed inside the cold chamber, while the set point temperature inside the warm chamber was kept constant $(T = T_0)$.

At the start of the tests, over a period between $t = 0.0$ h and $t = 48.0$ h, the set point temperatures inside the hot and the cold chambers was kept constant (20 ºC and 0 ºC, respectively) to reach steady-state conditions up to the first time step of the dynamic simulations. At $t = 48.0$ h the imposed temperature inside the cold chamber started to vary. The temperature time dependence followed a sinusoidal evolution for a period of 24 h, and with amplitude oscillations of 20 ºC, ranged between -10 ºC and 10 ºC, as shown in Figure 6.3. The temperature set point inside the warm chamber was kept at 20 ºC. Since the heating system used in the warm chamber does not allow cooling, the temperature inside it ranged between 18.2 °C and 19.7 °C, without ever stabilizing at 20.0 °C. The real temperature registered inside the warm chamber is given in Figure 6.3. Five cycles were used for the experimental simulations.

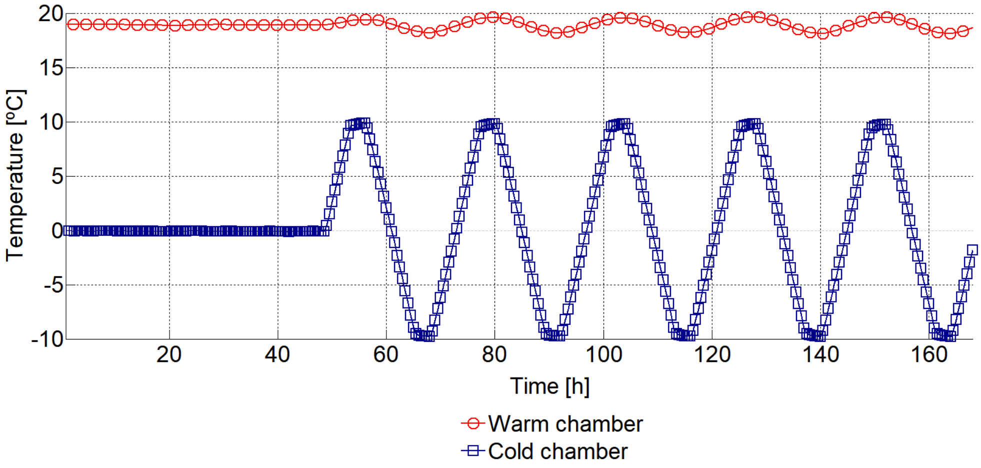

Figure 6.3: Temperatures over time: sinusoidal change in the cold chamber temperatures (5 cycles of 24 h); imposed temperature inside the warm chamber.

Two ultrathin flat plate heat flux sensors were used to measure the heat fluxes though the wall (centre of the panel) on both sides of the specimen and the other one was used to register the heat fluxes occurring through the roof on the warm side of the specimen. The heat fluxes across the PTB (near the 3D corner), on both sides of the wooden corner, were measured using the two HFP01 heat flux sensors from the TRSYS01 system. The internal surface temperatures at the point and linear thermal bridges, on the warm side of the specimen, were measured using the 33

T-type thermocouples, placed 0.01 m away from the wall-to-wall junction along a 0.32 m long line starting at the 3D corner. The internal surface temperatures at the centre of the wood panels (wall and roof), on the warm side of the specimen, were registered using one pair of TRSYS01 thermocouples (TC11 and TC12, respectively). The other pair of TRSYS01 thermocouples (TC21 and TC22) were used to measure the surface temperatures at the PTB and at the centre of the panel, on the cold side of the 3D wooden corner. Figure 6.4 shows the sensors layout.

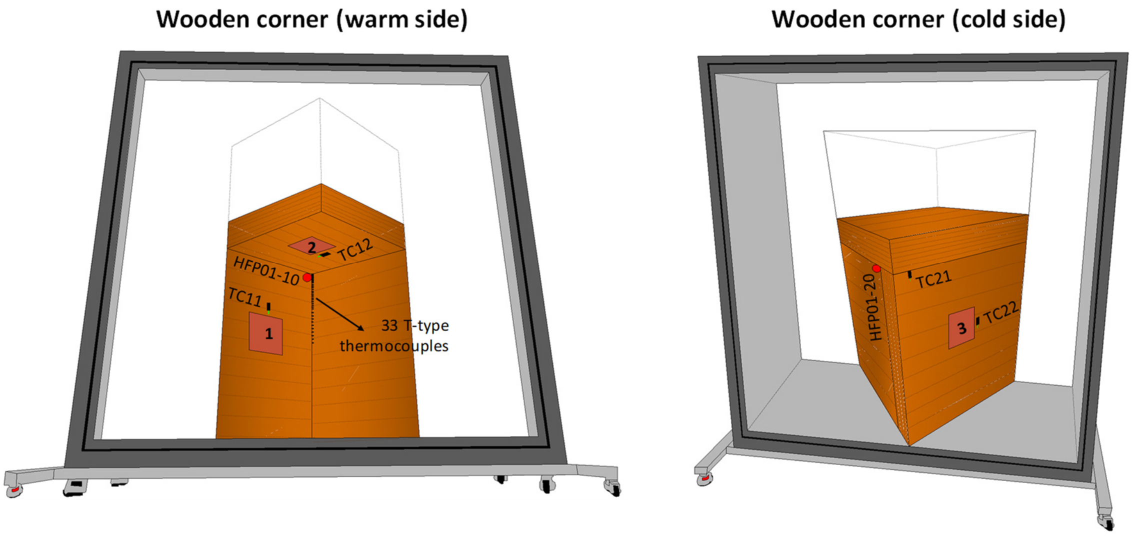
Wooden corner (warm side)

Wooden corner (cold side)

Figure 6.4: Scheme of the sensors layout (1, 2 and 3 -ultrathin plate heat flux sensors; HFP01-10 and HFP01-20 – TRSY01 heat flux sensors; TC11, TC12, TC21 and TC22 – TRSY01 thermocouples).

6.4 Laboratory measurements

This section presents the measurements of the laboratory test described above. The thermal behaviour of the wooden corner is evaluated under steady-state (t=48 h) and dynamic conditions (between t=48 h and t=168 h). In both cases, the dynamic point thermal bridging effect is evaluated by comparing the heat responses near the 3D corner with the ones occurring near the 2D junctions and at the centre of the wooden panels (walls and roof).

Figure 6.5 presents the temperature responses measured by the line of 33 T-type thermocouples when steady-state conditions are attained. It can be seen that the lowest surface temperature ($T_{sur,min}$=12.6 ºC) is registered near the 3D corner, where the thermal bridging effect is more pronounced. At a distance of 0.06 m from the corner, the effect of the point thermal bridge is no longer perceptible and the surface temperature in the 2D junction tends to be constant (T_{sur}=15.5 ºC).

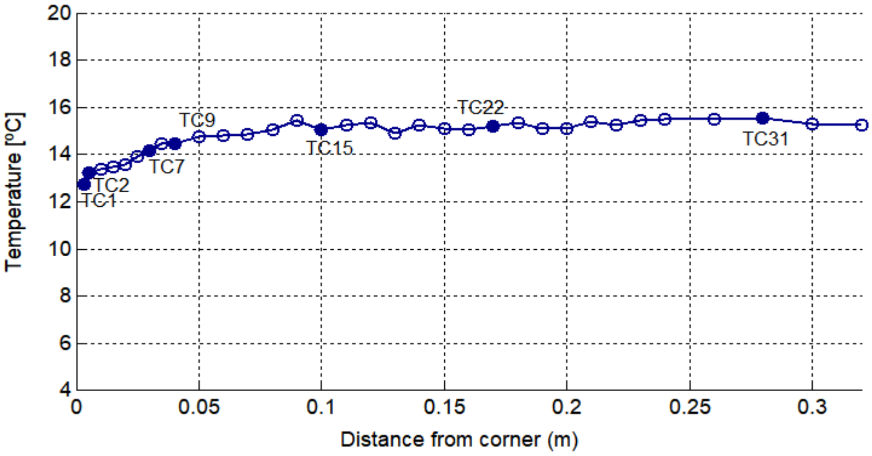

Figure 6.5: Internal surface temperature registered along the T-type thermocouples line, on the warm side of the wood corner, under steady-state conditions.

A set of seven thermocouples identified in Figure 6.5 (filled markers) were used to illustrate the thermal behaviour of the PTB under the dynamic conditions given in Figure 6.3. Of these seven thermocouples, number 1 is the nearest to the 3D corner (0.003m) and number 31 is the farthest from the 3D corner (0.28m). Figure 6.6 gives the variation of the surface temperature over time, registered by these thermocouples. The figure also gives the surface temperature change over time, registered by thermocouples TC11 and T12 of the TRSYS01 system, placed at the centre of the wall and roof panels, according to the scheme presented in Figure 6.4.

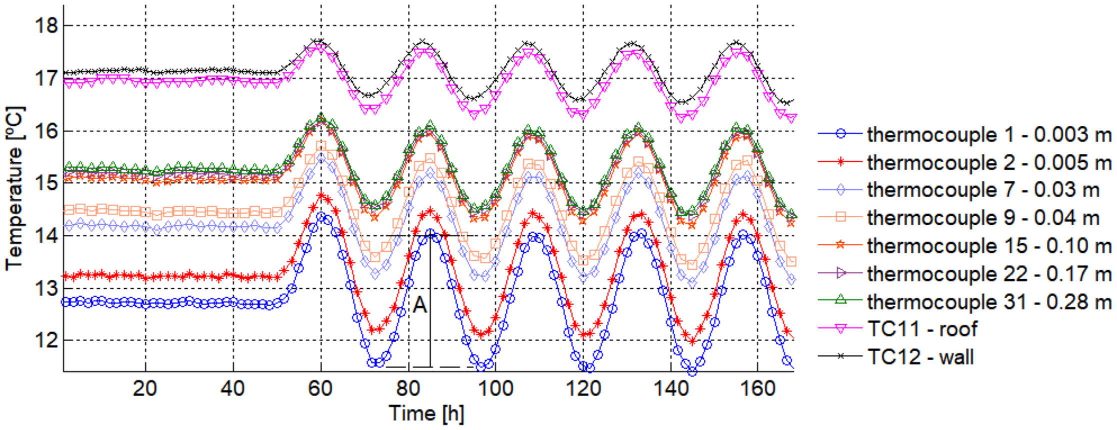

Figure 6.6: Variation of the surface temperature over time, registered by several T-type thermocouples placed on the warm side of the 3D wooden corner. Key gives the distance of each thermocouple to the corner.

The results show that the surface temperature curves have a cyclic behaviour. In steady-state, the surface temperature near the 3D corner is about 2.6 ºC lower than in the LTB (0.28 m from the 3D corner) and 4.4 ºC lower than in the wall. These differences are higher under dynamic conditions, in the low temperature limits (around 3 ºC and 5 ºC, respectively). It can also be seen that the thermal amplitude (A) is higher in the close vicinity of the 3D corner, due to the point thermal bridging effect. This is evidenced in Figure 6.7, which gives the thermal amplitude (A) variation along the thermocouples line for the second period of the curves.

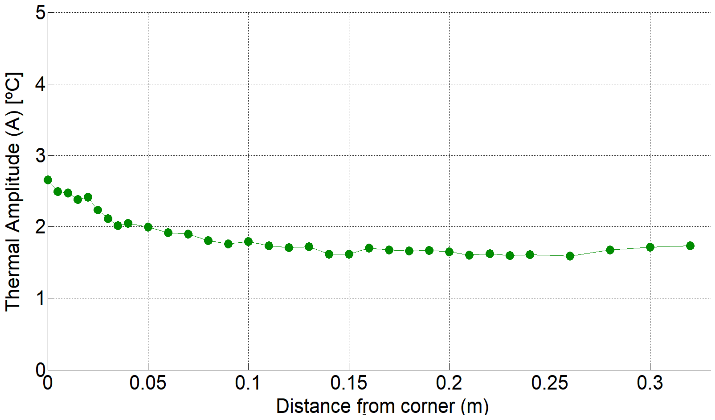

Figure 6.7: Thermal amplitude variation along the T-type thermocouples line for the second period of the temperature curves.

Figure 6.8 gives the variation of the surface temperature over time, registered by the TC21 and TC22 thermocouples of the TRSYS01 system, placed on the cold side of the wooden corner, according to the scheme presented in Figure 6.4.

It can be observed that, under steady-state conditions, the external surface temperature registered at the wall by thermocouple TC22 is 1.15 ºC, higher than the external surface temperature registered near the 3D corner by thermocouple TC21, which is 0.64 ºC. Under dynamic conditions, the minimum surface temperature registered by thermocouple TC22 is -6.8 ºC, higher than the minimum surface temperature in the 3D corner, which is -7.9 ºC. However, the maximum temperatures recorded on both surfaces by TC21 and TC22 over time are similar (≈ 9.3 ºC).

The thermal phase lag in the PTB was determined based on the maximum surface temperatures registered near the 3D corner on both surfaces of the building corner. The results are presented in Table 6.2. It can be seen that the average thermal phase lag in the PTB (4.9 h) is higher than the thermal phase lag in the wall (1.8 h) and in the LTB (4.1 h) (see Chapter 3, section 3.5).

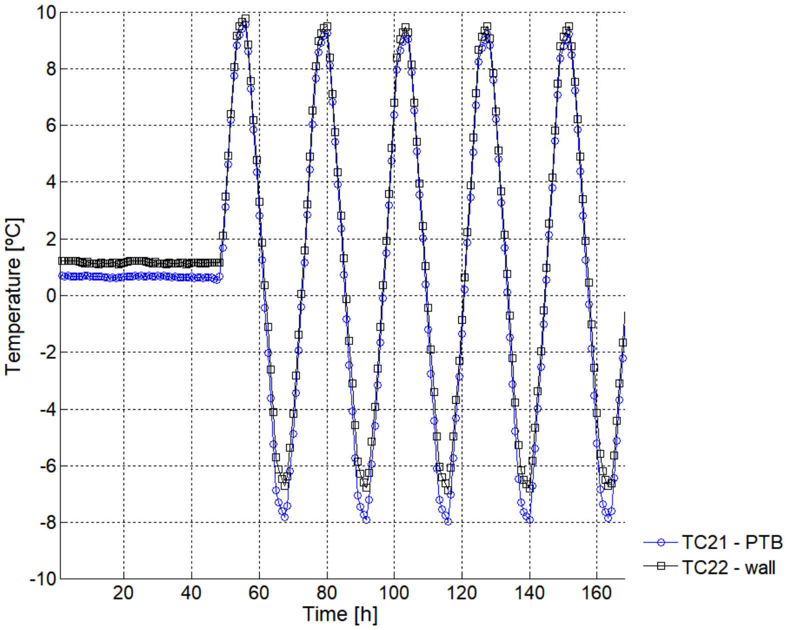

Figure 6.8: Variation of the surface temperature over time, registered by the TRSYS01 thermocouples placed on the cold side of the 3D wooden corner.

Table 6.2: Thermal phase lag in the LTB and the wall, based on the dynamic experimental results.

Cycle	1	2	3	4	5	average
Thermal Phase Lag – PTB (h)	4.6	5.1	4.8	5.1	5.0	4.9

Figure 6.9 gives the variation of the heat flux over time, registered by the heat flux plate HFP01-10 and by the two flat plate heat flux sensors (1 and 2), placed on the warm side of the wood corner, as shown in Figure 6.4. The heat fluxes registered at the centre of the wood panels (wall and roof) are significantly lower than the heat fluxes registered near the 3D corner (PTB). The heat flux amplitude is significantly higher near the 3D corner. Under steady-state conditions, the heat flux in the PTB is about 18 W/m^2 and the heat flux through the wall is about 11.3 W/m^2, which is similar to the heat flux through the roof (≈11.5 W/m^2). Under dynamic conditions, the heat flux amplitude is about 5.5 W/m^2 through the wall and roof and 9 W/m^2 in the PTB, ranging between 8.5 W/m^2 and 14.0 W/m^2 and between 13.5 W/m^2 and 22.5 W/m^2, respectively.

Figure 6.10 gives the variation of the heat flux over time, registered by the heat flux plate HFP01-20 and by the Flat plate heat flux sensor 3, placed on the cold side of the wooden corner, according to the scheme presented in Figure 6.4.

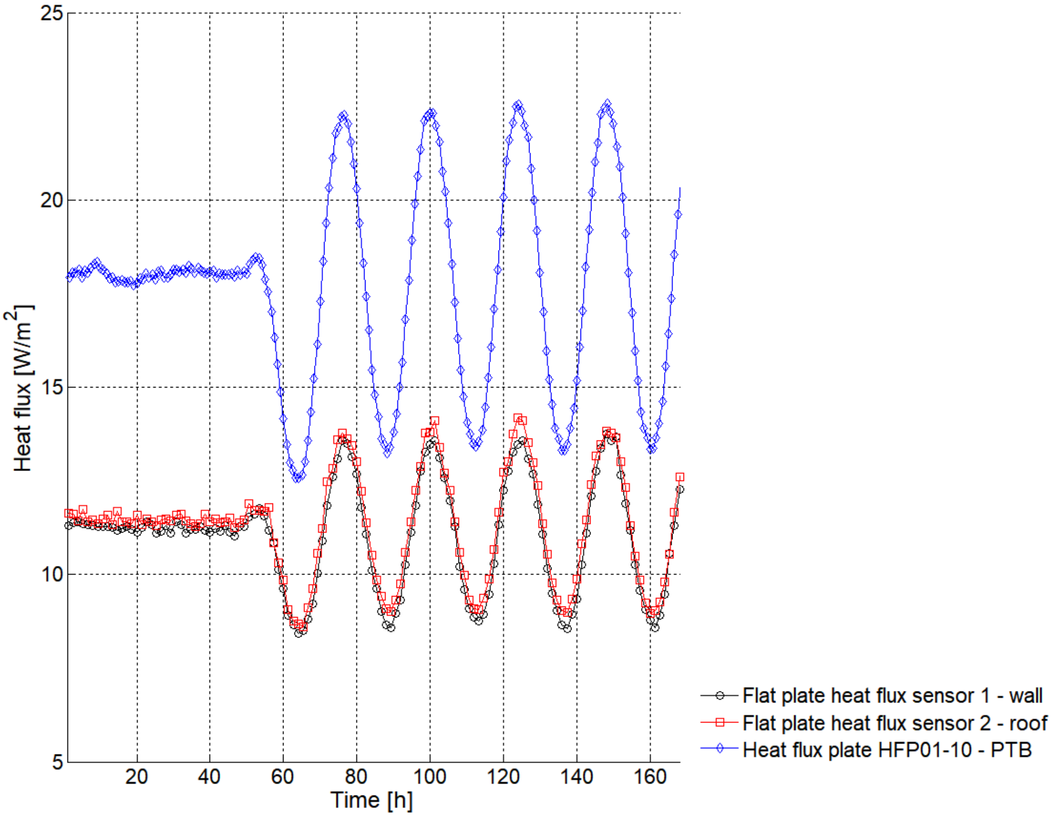

Figure 6.9: Variation of the heat flux over time, registered by the heat flux plate HFP01-10 and by the two flat plate heat flux sensors (1 and 2), placed on the hot side of the 3D wood corner.

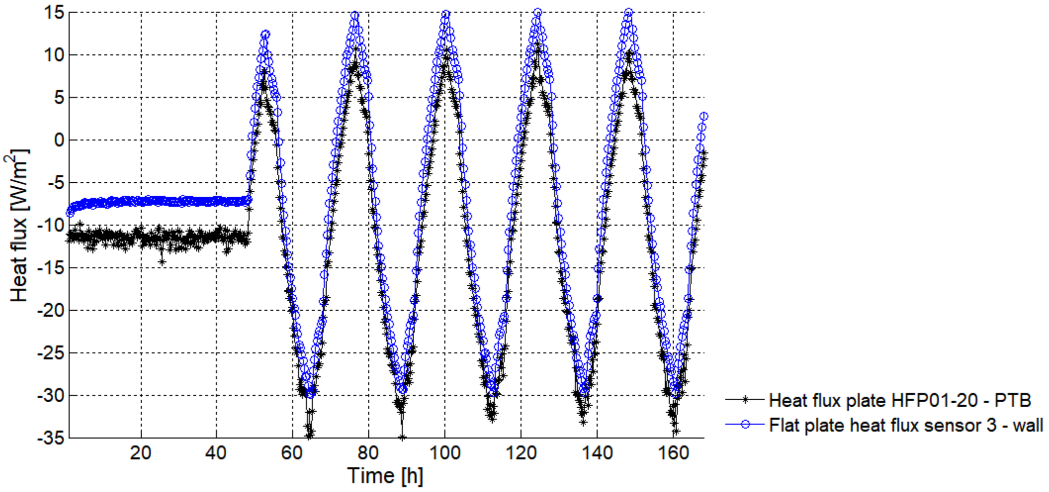

Figure 6.10: Variation of the heat flux over time, registered by heat flux plate HFP01-20 and by the flat plate heat flux sensor 3, placed on the cold side of the 3D wood corner.

The heat flux absolute values registered in the wall by the flat plate heat flux sensor 3 are higher than the heat flux absolute values registered in the PTB by the HFP01-20 sensor. Under steady-state conditions, the heat flux through the PTB is about -7 W/m^2 and the average heat flux through the wall is about -11 W/m^2. Under dynamic conditions, the heat flux amplitude is about 46 W/m^2 through the PTB and 45 W/m^2 through the wall, ranging between -33 W/m^2 and 13 W/m^2 and between -30 W/m^2 and 15 W/m^2, respectively.

6.5 Experimental vs numerical results

This section presents the experimental validation of the 3D BEM model presented in Chapter 5, for the simulation of the transient heat diffusion through a geometrical PTB in a 3D building corner. For that purpose, the BEM formulation was used to simulate the dynamic heat conduction through the 3D wooden corner. The heat transfer measurements of the 3D wooden building corner, under steady-state and dynamic conditions, obtained using the calibrated hot box are compared with the numerical results of the 3D BEM simulations.

Figure 6.11 illustrates the 3D physical model of the problem. Medium M2 is the wood used for the corner, while medium M1 and medium M3 represent two thin air layers that, respectively, account for the convection and radiation phenomena on the outer and inner surfaces of the corner.

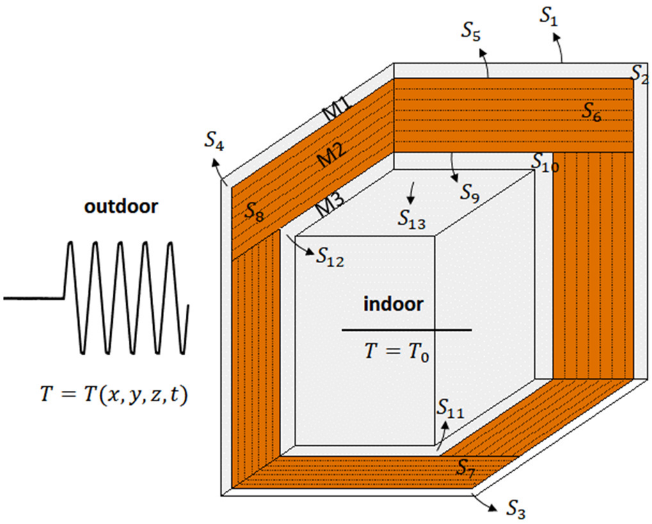

Figure 6.11: 3D wooden building corner scheme and boundary conditions of the problem.

Medium M1 is bounded by surfaces S_1, S_2, S_3, S_4 and S_5. Medium M2 is bounded by surfaces S_5, S_6, S_7, S_8 and S_9. Medium M3 is bounded by surfaces S_9, S_{10}, S_{11}, S_{12} and

S_{13}. Null heat fluxes $(\partial T/\partial n = 0)$ are prescribed along the boundary cut-off surfaces S_2, S_3, S_4, S_6 S_7, S_8, S_{10}, S_{11} and S_{12} and temperatures $(T = T_0)$ and $(T = T(x,y,z,t))$ are prescribed along the exterior boundary of the fictitious thin air layers (surfaces S_1 and S_{13}). Continuity of heat fluxes and temperatures are imposed along the interfaces S_5 and S_9.

The interfaces between materials as well as the internal and the external boundary surfaces were discretised using 4563 constant boundary elements, while 1872 constant boundary elements were used to model the lateral surfaces at the cut off planes of the building corner detail.

The heat transfer through the 3D wooden corner was simulated numerically under the same dynamic conditions used for the experimental simulations (see section 6.3). At $t = 0.0$ h the systems were assumed to have a uniform temperature of 0.0 ºC throughout the full domain. Note that non-uniform initial conditions could be imposed throughout the domain, but this would make the BEM model more elaborate. The frequency domain of computation ranged from 0.0 Hz to $4096/(168 \times 3600)$ Hz, with a frequency increment of $1/(168 \times 3600)$ Hz, which determined a total time window of 168.0 h for the analysis.

The R_{si} and R_{se} values used in the numerical simulations were 0.16 m^2.ºC/W and 0.14 m^2.ºC/W, at the wall surface. These values were calculated based on the experimental measurements. The radiation/convection effect is lower near the 2D and 3D corners, leading to higher surface thermal resistances. Therefore, the mean value 0.18 m^2.ºC/W was estimated for the R_{si} near the LTB and the PTB.

The following figures present the surface temperatures and the heat fluxes obtained with the BEM under steady-state and dynamic conditions for different points of the internal and external surfaces of the wooden corner. The numerical results are compared with the experimental measurements.

<u>Steady-state conditions:</u>

Figure 6.12 presents both the surface temperatures measured by the line of 33 T-type thermocouples and the surface temperatures obtained with BEM at the same points on the wooden corner and under the same steady-state conditions (19 ºC inside the hot chamber and 0 ºC inside the cold chamber). The error bar represents the uncertainty of each thermocouple $(\pm 0.16\ ^{\circ}\mathrm{C})$. As

can be seen, there is a good agreement between experimental measurements and numerical responses.

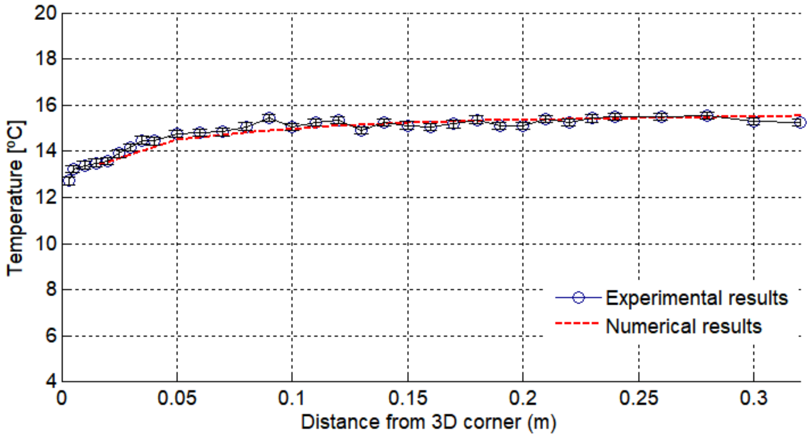

Figure 6.12: Internal surface temperature registered along the T-type thermocouples line, under steady-state conditions: numerical and experimental results.

<u>*Steady-state and unsteady-state conditions:*</u>

Figure 6.13 presents the internal surface temperature change over time, registered by two T-type thermocouples and the thermocouple TC12 from the TRSY01 system. Thermocouple number 7 is nearest to the 3D corner (0.03 m), thermocouple number 31 is in the 2D wall-to-wall junction, 0.28 m from the 3D corner and the TC12 thermocouple is in the centre of the wall panel. The figure also shows the internal surface temperature obtained with BEM for three receivers placed at the same coordinates as the three thermocouples. The experimental and numerical results were obtained under the dynamic conditions given in Figure 6.3.

The numerical responses need a period of time to reach the steady-state because the initial conditions prescribed at $t = 0.0$ h were at a uniform temperature of 0.0 ºC in the full physical domain. Good agreement is then seen between the experimental measurements and the numerical responses in both steady-state and transient conditions.

Note that, other measuring points of the physical model could have been used in this analysis since the numerical responses obtained for the remaining points were also found to be in agreement with the experimental results.

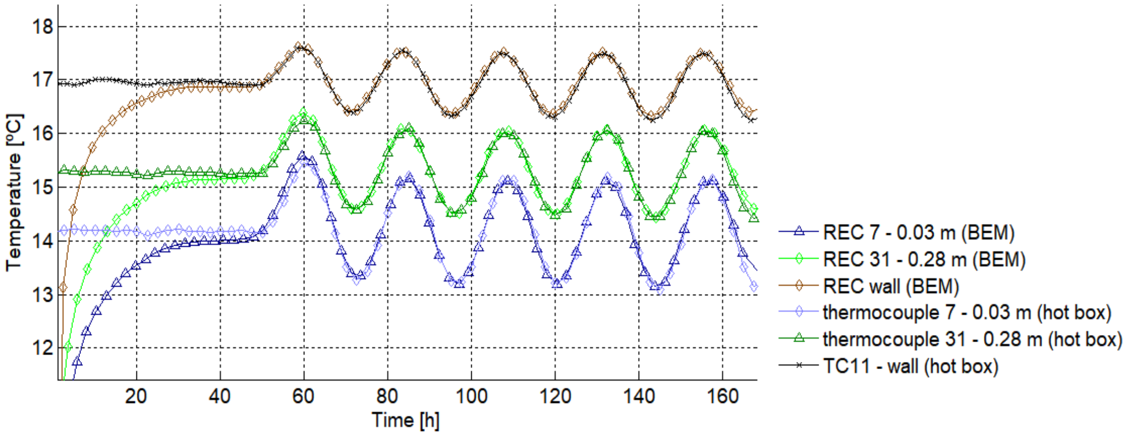

Figure 6.13: Variation of the internal surface temperatures over time at three different points of the wooden corner (PTB, LTB and wall): experimental and numerical results. The key gives the distance of each thermocouple/receiver from the 3D corner.

Figure 6.14 gives the variation of the surface temperature over time on the cold side of the wooden corner (external surface), obtained near the 3D corner (PTB) and in the centre of the wooden panel (wall) through the numerical simulation and with the experimental measurements.

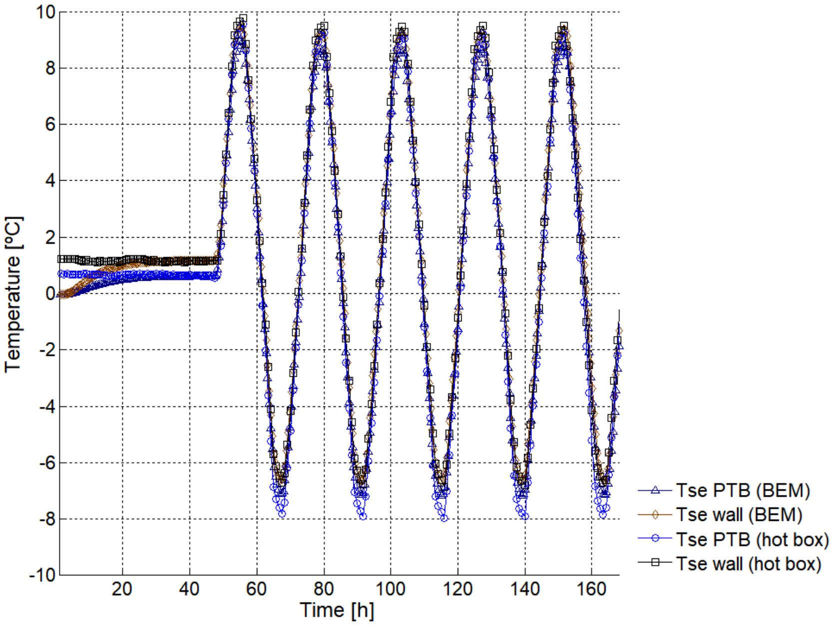

Figure 6.14: Variation of the external surface temperature over time: experimental and numerical results.

It can be seen that the experimental and numerical curves of the external surface temperature on the wall are very close over the full time window. On the other hand, near the PTB, the amplitude of the external surface temperature curve obtained with BEM is lower than that obtained experimentally. However, this difference is less than 1 ºC.

Figure 6.15 gives the heat flux change over time, on the warm surface of the wooden corner, obtained near the 3D corner (PTB) and in the centre of the wooden panel (wall) through numerical simulation and with the experimental measurements.

It can be observed that the heat flux curves obtained with the experimental measurements are in agreement with the heat flux curves obtained with the numerical simulation. The main differences between the BEM and the experimental results are observed in the local minimums and maximums of the heat flux curves, both in the PTB and in the centre of the wall. These differences are, however, less than 0.5 W/m^2, which is within the uncertainty range of the sensors (± 5 %).

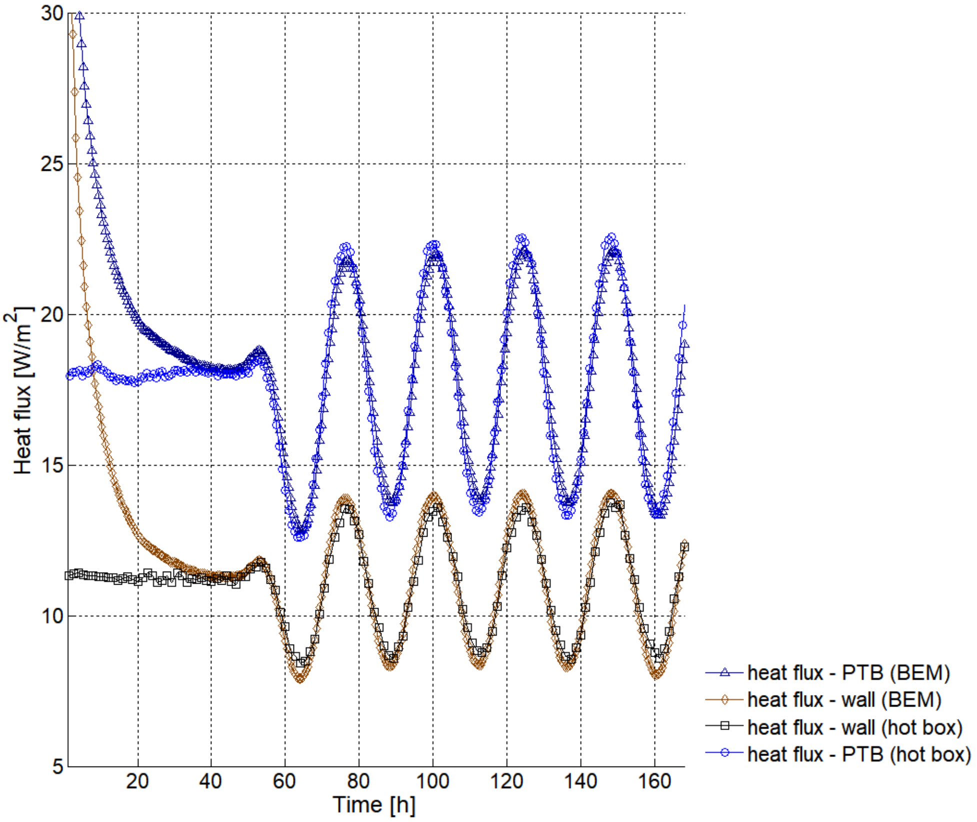

Figure 6.15: Variation of the heat flux over time on the internal surface: experimental and numerical results.

Figure 6.16 presents the variation of the heat flux over time near the 3D corner and in the centre of the wall, on the cold surface of the wooden corner, obtained by the numerical and experimental simulations. It can be observed that the heat fluxes measured experimentally are similar to the heat fluxes obtained with the numerical simulation, for both steady-state and dynamic conditions.

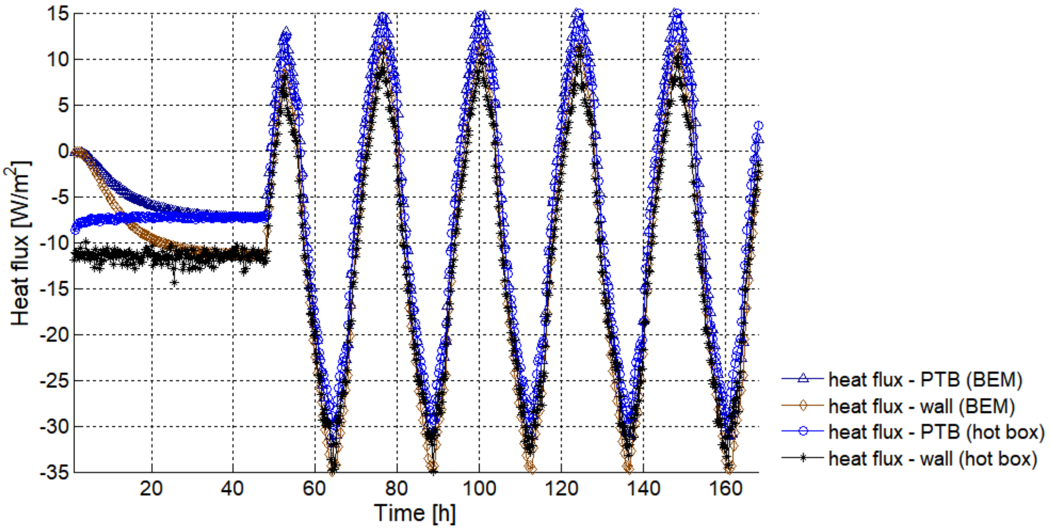

Figure 6.16: Variation of the external heat flux over time: experimental and numerical results.

The comparison between the experimental and numerical results confirms the reliability of the 3D BEM simulations and, therefore, validates the proposed BEM model.

6.6 Conclusions

This chapter conducted an experimental campaign to evaluate the dynamic thermal behaviour of a 3D wooden building corner, representing a point thermal bridge (PTB). The tests were performed with a calibrated hot box. The variation of the surface temperatures and the heat fluxes over time was registered at different distances from the 3D corner using thermocouples and heat flux sensors. The dynamic point thermal bridging effect was evaluated. The results clearly showed that the heat flux and the thermal amplitude are higher near the 3D corner.

The experimental validation of the 3D BEM formulation proposed in Chapter 5 was then presented. For this, the heat transfer through the 3D wooden corner was numerically simulated using the proposed BEM model, assuming the same dynamic boundary conditions as those used in the experimental work. The surface temperatures and the heat fluxes obtained with BEM for different points of the internal and external surfaces of the wooden corner were compared with the experimental results. The experimental and numerical results showed good agreement, which validates the proposed frequency domain BEM model.

References

[1] K. Dikarev, A. Berezyuk, O. Kuzmenko, A. Skokova, Experimental and numerical thermal analysis of joint connection «floor slab – balcony slabe» with integrated thermal break, energy procedia 85 (2016) 184–192.

[2] J. Šadauskiene, J. Ramanauskas, L. Šeduikyte, M. Daukšys, A. Vasylius, A simplified methodology for evaluating the impact of point thermal bridges on the high-energy performance of a passive house, sustainability 7 (2015) 16687-16702.

[3] A. Deconinck, S. Roels, Comparison of characterisation methods determining the thermal resistance of building components from onsite measurements, Energy and Buildings 130 (2016) 309–320.

[4] G. Mao, Thermal bridges: from research to applications. Tekn. Lic. thesis, Arbetsrapport 1995:1, KTH, Avd. för Byggnadsteknik, Stockholm, Sweden.

[5] T. Kalema, T. Haapala, Effect of interior heat transfer coefficients on thermal dynamics and energy consumption, Energy and Buildings 22 (1995) 101-113.

[6] M.H. Corvacho, Pontes térmicas, análise do fenómeno e proposta de soluções, PhD thesis, Faculdade de Engenharia da Universidade do Porto, Portugal, 1996 (in portuguese).

[7] N. Simões, I. Simões, A. Tadeu, C.A.B. Vasconcellos, W.J. Mansur, 3D transient heat conduction in multilayer systems - Experimental validation of semi-analytical solution, International Journal of Thermal Sciences 57 (2012) 192-203

[8] L. Zalewski, S. Lassue, D. Rousse, K. Boukhalfa, Experimental and numerical characterization of thermal bridges in prefabricated building walls, Energy Conversion Manage 51 (2010) 2869–2877.

[9] P. Standaert, Computer program to calculate 3D & 2D steady state heat transfer in objects described in a rectangular grid using the energy balance technique, Physibel document TRISCO V10.0 w Manual, 2002.

[10] F. Ascione, N. Branco, R.F. Masi, G.M. Mauro, M. Musto, G.P. Vanoli, Experimental validation of a numerical code by thin film heat flux sensors for the resolution of thermal bridges in dynamic conditions, Applied Energy 124 (2014) 213-222.

[11] F. Asdrubali, G. Baldinelli, F. Bianchi, A quantitative methodology to evaluate thermal bridges in buildings, Applied Energy 97 (2012) 365–373.

[12] International Organization for Standardization, ISO 8990: Thermal insulation - Determination of steady-state thermal transmission properties - Calibrated and guarded hot box, 1994.

[13] F. Asdrubali, G. Baldinelli, Thermal transmittance measurements with the hot box method: Calibration, experimental procedures, and uncertainty analysis of three different approaches, Energy and Buildings 43 (2011) 1618-1626.

[14] Y. Fang, P.C. Eames, B. Norton, T.J. Hyde, Experimental validation of a numerical model for heat transfer in vaccum glazing, Solar Energy 80 (2006) 564-577.

[15] K. Martín, I. Flores, C. Escudero, A. Apaolaza, J.M. Sala, Methodology for the calculation of response factors through experimental tests and validation with simulation, Energy and Buildings 42 (2010) 461-467.

[16] K. Martin, C. Escudero, I. Gómez, J. M. Sala, Analysis of a thermal bridge in a guarded hot box testing facility, Energy and Buildings 50 (2012) 139-149.

[17] G. Mao, Laboratory Measurements and Modelling of the Dynamic Thermal Performance of a Thermal Bridge, Nordic Journal of Building Physics, 11 (1997-1998).

[18] H. Kus, E. Özkan, Ö. Göcer, E. Edis, Hot box measurements of pumice aggregate concrete hollow block walls, Construction and Building Materials 38 (2013) 837–845.

[19] A. Gustavsen, H. Goudey, D. Arasteh, S. Uvsløkk, G. Talev, B.P. Jelle, C. Kohler, Experimental and Numerical Examination of the Thermal Transmittance of High Performance Window Frames, Thermal Performance of the Exterior Envelopes of Whole Buildings, XI International Conference, Florida, December 2010.

[20] F. Asdrubali, G. Baldinelli, F. Bianchi, Influence of cavities geometric and emissivity properties on the overall thermal performance of aluminium frames for windows, Energy and Buildings 60 (2013) 298 – 309.

[21] Hukseflux Thermal Sensors, User Manual HFP01/ HFP03, manual version 0612, June 2016.

[22] Hukseflux Thermal Sensors, User Manual TRSYS01 - High-accuracy building thermal resistance measuring system with two measurement locations, TRSYS01 manual v1620, 2016.

[23] APA - The engineered wood association. (c2016). Cross-Laminated Timber (CLT) - Retrieved 5 Abril, 2016, from http://www.apawood.org/cross-laminated-timber.

[24] International Organization for Standardization, ISO 8302: Thermal insulation - Determination of steady-state thermal resistance and related properties - Guarded hot plate apparatus, 1991.

[25] European Standard, EN 12667: Thermal performance of building materials and products. Determination of thermal resistance by means of guarded hot plate and heat flow meter methods. Products of high and medium thermal resistance, 2001.

[26] European Standard, EN 1602: Thermal insulating products for building applications. Determination of the apparent density, 1997.

CHAPTER 7

DYNAMIC BEHAVIOUR OF POINT THERMAL BRIDGES IN 3D BUILDING CORNERS

7 DYNAMIC BEHAVIOUR OF POINT THERMAL BRIDGES IN 3D BUILDING CORNERS

7.1 Introduction

The Energy Performance of Buildings Directive 2010/31/EU [1] requires all new buildings to be nearly zero-energy by the end of 2020. One way to achieve this is to improve the thermal resistance of the buildings envelope by adding more insulation. However, special care must be taken with thermal bridges, since their relative effect tends to increase when the thermal resistance of the building envelope is improved [2].

It is well known that thermal bridging can have a significant influence on a building's energy consumption [3]. Therefore, taking into account all the thermal bridges details can be essential when dealing with very-low energy houses. Furthermore, thermal bridges increase the risk of surface condensation and building pathologies ([4]-[6]). Thus, the accurate simulation of linear and point thermal bridges can be very useful to quantify the additional heat loss at these junctions and identify weak points in order to ensure that the details are free of mould and surface condensation.

A point thermal bridge (PTB) is characterized by a localized concentration of three-dimensional (3D) heat fluxes [7] and can generally be classified as repeating or geometrical [3]. A repeating PTB occurs where there is a point penetration of the insulation layer that is normally repeated in a specific pattern (for example wall ties and ETICS fasteners). This type of point thermal bridges (PTBs) is normally included in the overall thermal transmittance value (U) of the plane element, calculated under steady-state conditions. A geometrical PTB, however, normally occurs at a specific intersection between three or more building elements (such as a 3D building corner) and it is not normally included in the national energy performance calculation procedures.

Some studies have been performed to analyse the impact of repeating PTBs in building components. However, due to the complexity of 3D dynamic simulations, most studies assumed simplified approaches and steady-state conditions. Šadauskiene *et al.* [2] presented a simplified methodology for the evaluation of PTBs caused by aluminium fasteners used on ventilated facades systems. This methodology uses an empirical relationship to calculate the static point thermal transmittance values of the PTBs according to the thermal and geometrical properties of the external walls. The results show that PTBs may increase the U-value of the entire wall by 30 %. Theodosiou *et al*. [8] have also analysed the point thermal bridging effect in metal cladding systems on ventilated facades. The problem was solved assuming steady-state conditions, using a computational model based on the finite element method. The results show that neglecting the influence of PTBs can significantly worsen the thermal insulation quality of the facade, leading to a considerable underestimation of the heat flows which can range from 5 % up to 20 % [9].

Regarding geometrical PTBs, there is still a lack of research focussing on the analysis of this type of 3D junctions and their impact on the thermal performance of buildings envelopes. The influence of geometrical PTBs is currently neglected, since their effect on the heat flows through the building envelope is considered to be small, when compared with LTBs and extremely difficult to estimate, especially if dynamic conditions are assumed. However, no scientific evidence has been found to conclude that the dynamic effect of geometrical PTBs on the hygrothermal performance of the building envelope can in fact be negligible.

Iodice *et al*. [10] used a finite element method (FEM) model to simulate the steady-state and dynamic 3D heat conduction and vapor diffusion in a 3D thermal bridge detail (junction between two walls and an intermediate floor), with a concrete pillar and slab containing inhomogeneities (steel-stud). The study shows that the heat flow through the 3D building detail increases more than 16% when the inhomogeneities are considered in the simulations. However, Iodice *et al.* only analysed the impact of the steel studs on the thermal performance of the 3D detail, while the additional heat losses caused by the geometrical PTB (3D corner) were not evaluated.

In addition to the thermal effect, high values of relative humidity are normally observed in the vicinity of geometrical PTBs [11] due to a reduction of the convection effect near the corners. This phenomenon, when associated with low surface temperatures, increases the risk of mould growth caused by moisture condensation, which often results in the deterioration of building materials. You *et al*. [12] studied the phenomenon of moisture condensation on the interior surfaces of a building caused by air infiltration in a high humidity climate. The influence of the temperature, relative humidity and wind speed of outdoor air on the moisture condensation on the interior surface of the room was analysed by a CFD simulation. The authors concluded that the places where moisture condensation is most likely to occur are the corners, that is, the junctions between two vertical walls and the junction between two vertical walls and the ceiling.

One way to prevent surface condensation in this type of thermal bridges is to promote the ventilation of these areas, which is not always easy, especially when there is furniture near the corners. Another way is to increase the surface temperatures near the corners by choosing constructive solutions with lower thermal transmittance. For this, a better understanding of the surface temperatures distribution in the vicinity of the PTB is required to be able to choose the most appropriate solutions. So that the analysis can be as realistic as possible, dynamic conditions should be considered in the simulations.

In this chapter, the dynamic effect of a geometrical PTB in a 3D building corner (junction between two walls and roof) is analysed. The main purpose of this work is to evaluate the effect of the geometry in the dynamic thermal performance of the 3D building corner detail. The problem is solved using the frequency domain boundary element method (BEM) formulation ([13],[14]) proposed in Chapter 5 (section 5.2.3) and validated in Chapter 6 of this thesis. Three different cases are analysed in terms of different scenarios for the thermal insulation layer. The numerical simulations are performed considering a sinusoidal variation of the external temperature over time, while the internal temperature is assumed to be constant. The dynamic heat flow rate through the PTB is compared with the dynamic heat flow rate through the LTBs and through the plane building elements (walls and roof). Furthermore, for each case study, the point thermal transmittance determined under steady-state conditions is compared with the dynamic point thermal transmittance. The variation of the temperature distributions over time, in different planes of the building corner domain, is also analysed. The internal surface temperature in the PTB is compared with the internal surface temperatures in the wall and in the LTB junction.

7.2 Problem definition

Figure 7.1 illustrates the type of problem to be solved: a 3D building corner representing a junction between two vertical walls and the roof of a building. The external surfaces of the walls and roof are subjected to a temperature variation ($T = T(x, y, z, t)$), while the indoor temperature is assumed to be constant ($T = T_0$). The PTB in the 3D corner is characterized by a 3D heat flux. At a certain distance from the 3D corner, along the wall-to-wall junction and along the two wall-to-roof junctions, the thermal bridge becomes linear (2D heat flux) and the heat flux in the middle of each building plane element becomes one-directional (1D). Therefore, null heat fluxes can be prescribed along the 2D cut-off planes, as shown in Figure 7.1.

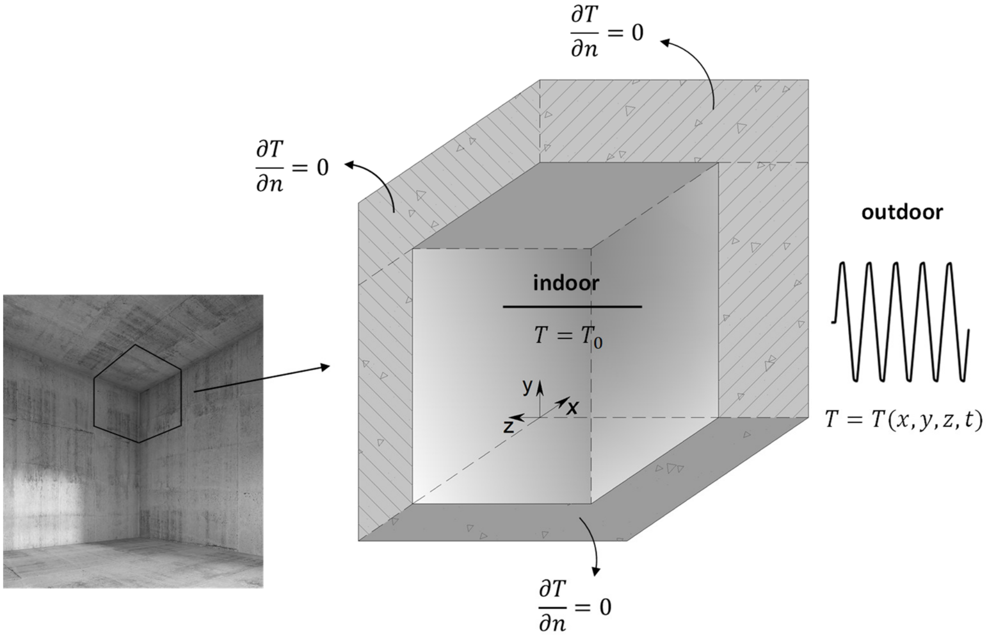

Figure 7.1: Three-dimensional building corner scheme and boundary conditions of the problem.

7.3 Case studies

The 3D BEM formulation proposed in Chapter 5 was used to simulate the heat conduction through a PTB formed at the 3D corner of a building. Three cases were simulated, as illustrated in Figure 7.2: walls and roof without thermal insulation (Case 1); walls and roof with an external thermal insulation layer (Case 2); walls and roof with an internal thermal insulation layer (Case 3).

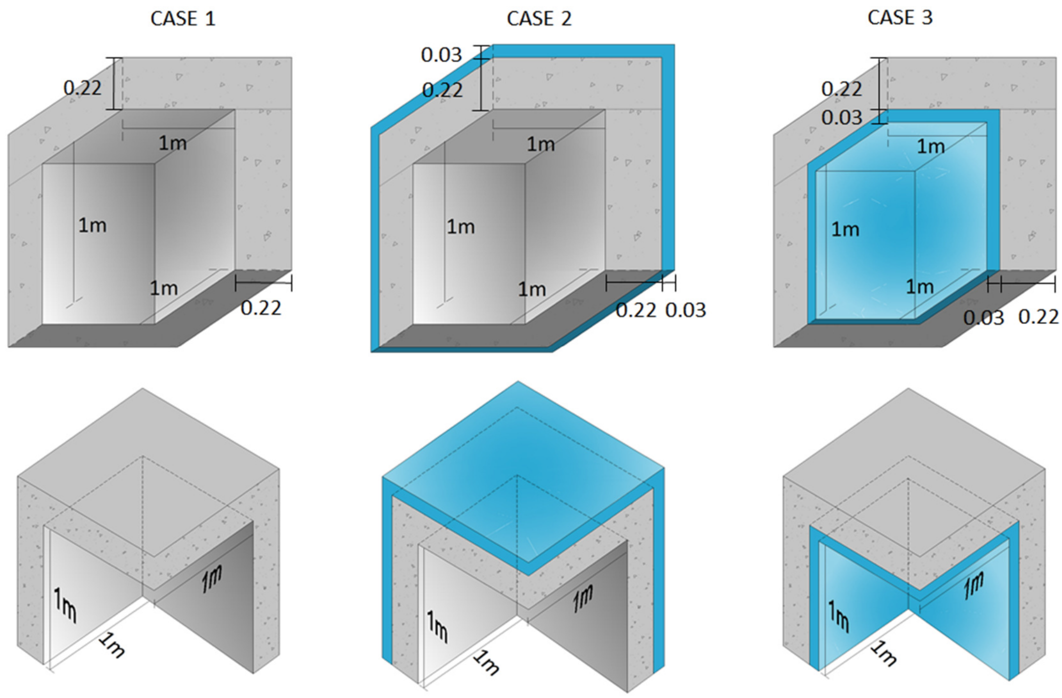

Figure 7.2: 3D Building corner geometry used in the numerical applications: Case 1 – walls and roof without thermal insulation; Case 2 – walls and roof with an external thermal insulation layer; Case 3 – walls and roof with an internal thermal insulation layer (dimensions in m).

The surface thermal resistance was modelled as a thin air layer on the inner and outer surfaces to take into account both convection and radiation phenomena. The internal surface thermal resistance $\left(R_{si}\right)$ depends on the direction of the heat flow [15] which, under dynamic conditions, is liable to vary in time. However, in this study, the value $R_{si}=0.13$ m^2.ºC/W [15] was used for all the internal surfaces, as indicated in ISO 10211:2007 [7]. The external surface thermal resistance $\left(R_{se}\right)$ was assumed to be 0.04 m^2.ºC/W for the outer surfaces, according to ISO 6946:2007 [15].

As mentioned before, the 3D geometrical model of the building corner is delimited by cut-off planes. The cut-off planes are positioned far away enough from the corner to ensure that the heat transfer is no longer affected by the presence of the point thermal bridge formed at the junction of the three building elements. In the examples, the length of the walls and roof followed ISO 10211:2007 [7], enabling a length of 1 m to be applied.

The thermal conductivity, the mass density and the specific heat of each material were characterized experimentally. The thermal conductivity was evaluated by the Guarded Hot-Plate Method (ISO 8302:1991 [16]) using a Lambda-Meßtechnik GmbH Dresden apparatus, single-specimen Lambda-meter EP-500 model, following the test procedure defined in EN 12667:2001 [17]. The mass density was determined using the procedure described in EN 1602:1996 [18]. The specific heat was obtained using a Netzsch apparatus, model DSC200F3, following the ratio method. The thermal properties of the materials are listed in Table 7.1.

Table 7.1: Thermal properties of the materials.

Material	Thermal conductivity $\lambda\ \left(\text{W.m}^{-1}.^{\circ}\text{C}^{-1}\right)$	Density $\rho\ \left(\text{kg.m}^{-3}\right)$	Specific heat $c\ \left(\text{J.kg}^{-1}.^{\circ}\text{C}^{-1}\right)$
Thermal insulation	0.046	130.00	1638.00
Concrete	1.40	2300.00	880.00
External surface air layer 3 mm thick	0.075	1.29	1000.00
Internal surface air layer 3 mm thick	0.0231	1.29	1000.00

7.3.1 Steady-state conditions

To confirm the importance of computing the PTB dynamically, the problem was first solved assuming a steady-state condition, corresponding to the static response. The quantity describing the influence of the PTB on the total heat flow, in W/ºC, known as point thermal transmittance (χ), was computed by imposing distinct outdoor and indoor temperatures, θ_e and θ_i, respectively, that were assumed to be time independent. The following equation was used, in accordance with ISO 10211:2007 [7]:

$$\chi = L_{3D} - \sum_{j=1}^{N_j} U_j A_j - \sum_{m=1}^{N_m} \psi_m l_m \text{ , with } N_j = 3 \text{ and } N_m = 3 \text{ ,} \tag{7.1}$$

where N_j is the number of plane building elements, N_m is the number of 2D junctions between plane elements, $L_{3D} = \phi_{3D}/(\theta_i - \theta_e)$ is the thermal coupling coefficient from the three-dimensional calculation, in W/ºC, computed for the total system (see Figure 7.3 a)), ϕ_{3D} is the total heat flow rate in W, computed with the proposed BEM model, $U_j = q/(\theta_i - \theta_e)$ is the thermal transmittance (in W/(m^2.ºC) of the plane element j separating the internal and the external environment, q is the heat flow rate, in W/m^2, for the 1D component j, and A_j is the area (in m^2) over which the U_j applies, ψ_m is the linear thermal transmittance (in W/(m.ºC)) of the junction m between two building components, representing a linear thermal bridge (LTB), and l_m is the length over which the value ψ_m applies.

The linear thermal transmittance ψ of each LTB was computed as

$$\psi_m = L_{2D,m} - \sum_{j=1}^{N_j} U_j l_j \text{ , with } N_j = 2 \tag{7.2}$$

where $L_{2D,m} = \phi_{2D,m}/(\theta_i - \theta_e)$ is the thermal coupling coefficient obtained from a 2D calculation of the LTB detailed m, in W/(mºC) and $\phi_{2D,m}$ is the heat flow rate per metre length, occurring through the LTB detail m, computed with the proposed BEM model.

Figure 7.3 b), c) and d) gives the different details of LTB considered in the application of equations (7.1) and (7.2).

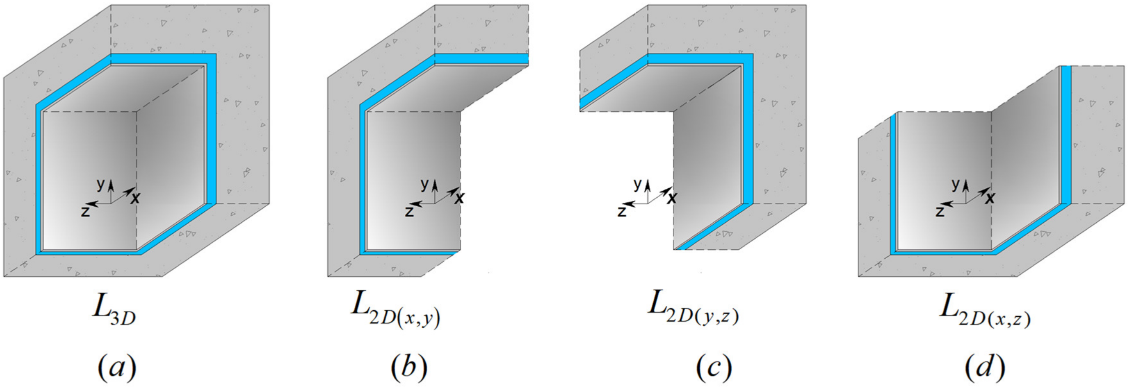

Figure 7.3: Three-dimensional building corner scheme separated into its two-dimensional components: a) 3D building corner; b) LTB – left wall to roof junction; c) LTB – right wall to roof junction; d) LTB – right wall to left wall junction.

The thermal coupling coefficients L_{3D} and $L_{2D,m}$ were determined by integrating the heat fluxes along the inner components' surfaces. However, any other integration line through the systems would give the same result, since the systems were being simulated for steady-state conditions.

In the three case studies $L_{2D(y,z)} = L_{2D(x,y)} = L_{2D(x,z)}$ and $U_{(x,y)} = U_{(y,z)} = U_{(x,z)}$, since the constructive details and the surface thermal resistances were assumed to be the same for the three 1D components of the building corner.

The steady-state computations were performed using the BEM model proposed above, imposing a null frequency with a small imaginary part, $\omega_c = -i\eta$ (η=0.7$\Delta\omega$, with $\Delta\omega$ being nearly zero, $\Delta\omega = 1.0 \times 10^{-40}$ Hz).

Each interface between materials was discretised using 4563 constant boundary elements, while 1872 constant boundary elements were used to model the lateral interfaces at the cut off planes.

The temperature distribution was obtained along 6 very fine grids of receivers, placed as illustrated in Figure 7.4.

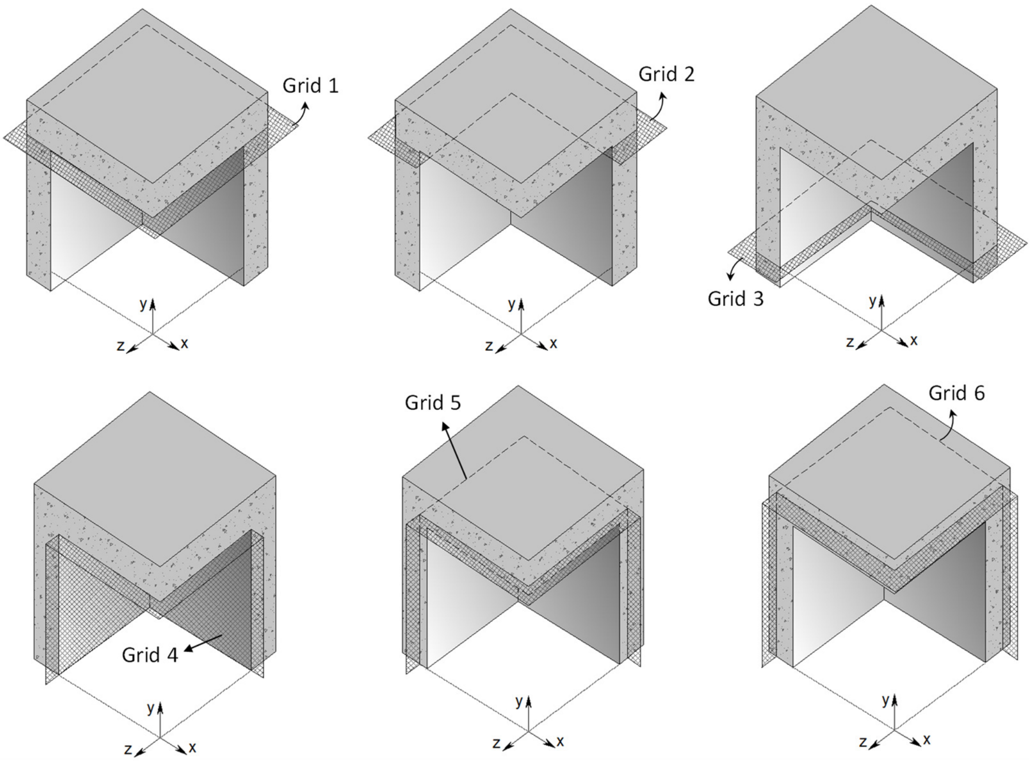

Figure 7.4: Scheme of the receivers' grids in Case 1.

Grid 1 is a longitudinal square grid along the internal surface of the concrete roof and the plane sections between roof and walls. Grid 2 is a longitudinal grid crossing the 2D corner corresponding to the wall-to-wall junction, 0.01 m from the 3D corner. Grid 3 is similar to the grid 2 but placed 0.7 m from the 3D corner. Grid 4 contains three different planes of grid receivers lying in the planes of the two walls and roof internal surfaces of the 3D building corner detail. Grids 5 and 6 are similar to Grid 4 but placed in different locations depending on the case study: in Case 1, Grid 5 and Grid 6 are placed inside the concrete, 0.06 m and 0.17 m from the internal surface, respectively; in Case 2, Grid 5 is placed in the middle of the insulation layer and Grid 6 in the middle of the concrete layer; in Case 3, Grid 5 is placed in the middle of the concrete layer and Grid 6 in the middle of the insulation layer.

Figures 7.5, 7.6 and 7.7 show the temperature distribution recorded at each grid of receivers in the case studies 1, 2 and 3, respectively, under steady-state conditions when the exterior and interior temperatures were 15 °C and 20 °C. A colour scale is used in the plots, with the red and blue shades corresponding, respectively, to higher and lower temperatures. As expected, the analysis of the results revealed that lower surface temperatures occurred in Case 1. Case 3 had the lowest temperatures inside the wall, in the middle of the concrete layer. The PTB effect on the temperature distribution is clearly visible in the three cases.

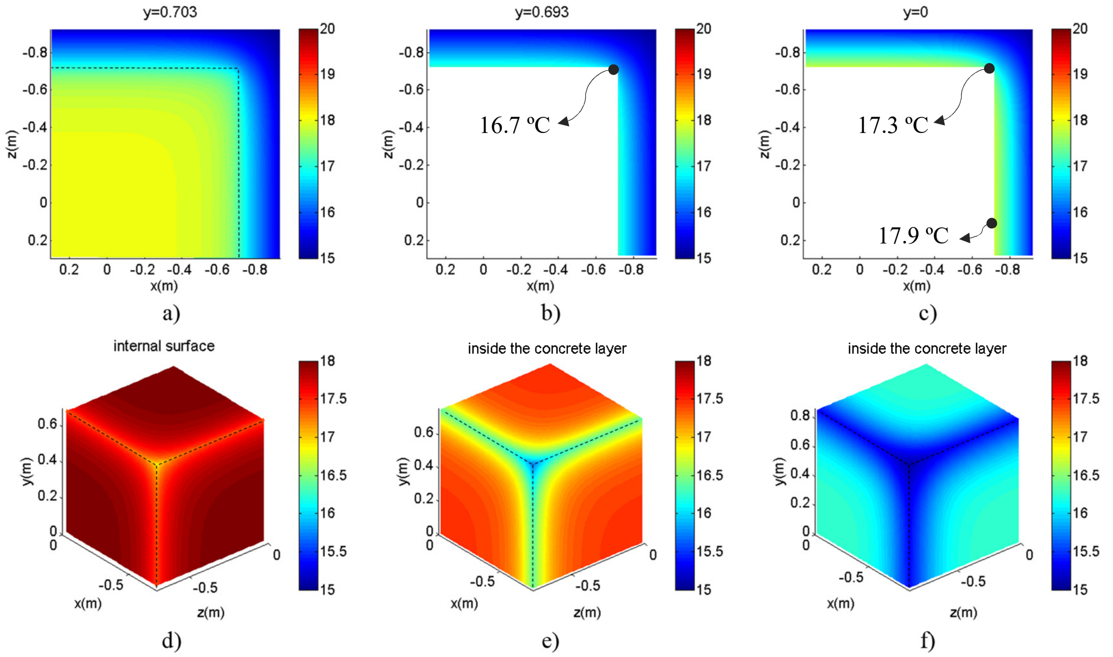

a)

b)

c)

d)

e)

f)

Figure 7.5: Temperature distribution (in °C) across the 3D concrete building corner under steady-state conditions ($\theta_e = 15$ °C and $\theta_i = 20$ °C) – Case 1: a) Grid 1; b) Grid 2; c) Grid 3; d) Grid 4; e) Grid 5; f) Grid 6.

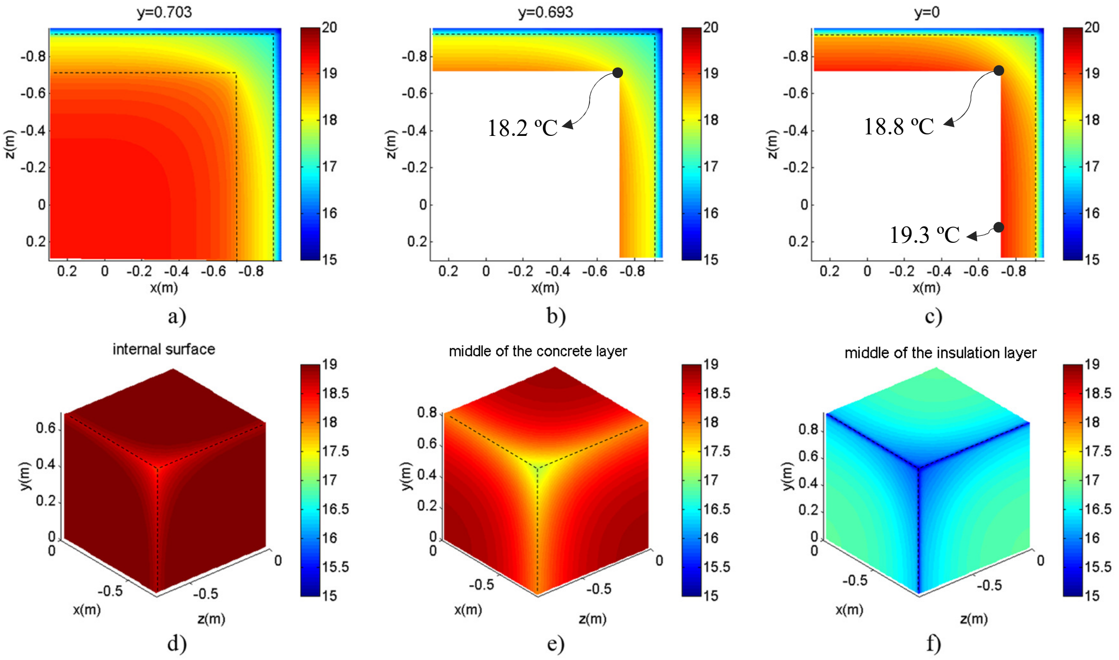

Figure 7.6: Temperature distribution (in °C) across the 3D concrete building corner under steady-state conditions ($\theta_e = 15$ °C and $\theta_i = 20$ °C) – Case 2: a) Grid 1; b) Grid 2; c) Grid 3; d) Grid 4; e) Grid 5; f) Grid 6.

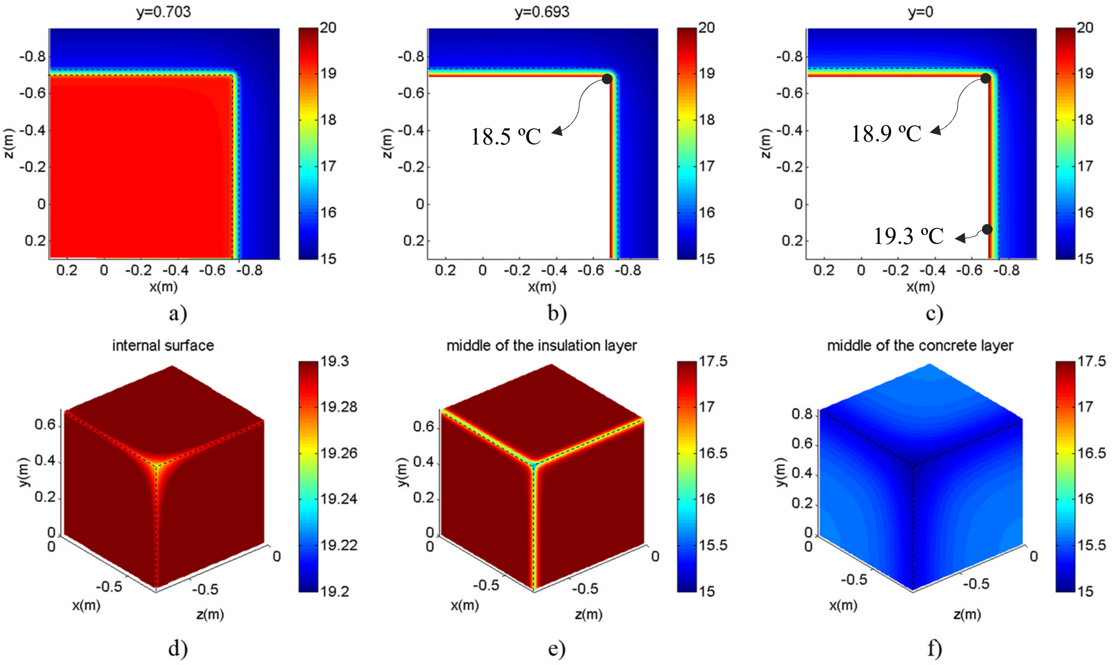

Figure 7.7: Temperature distribution (in °C) across the 3D concrete building corner under steady-state conditions ($\theta_e = 15$ °C and $\theta_i = 20$ °C) – Case 3: a) Grid 1; b) Grid 2; c) Grid 3; d) Grid 4; e) Grid 5; f) Grid 6.

Figure 7.8 gives the variation of the internal surface temperature along two different sections of the building corner, when steady-state conditions are assumed. The dashed lines with marks illustrate the internal surface temperature along the LTB junction, starting in the 3D corner. The straight lines present the internal surface temperature along the wall, starting in the 2D corner. Different colours identify each case study results (Case 1 – black lines; Case 2 – blue lines; Case 3 – red lines).

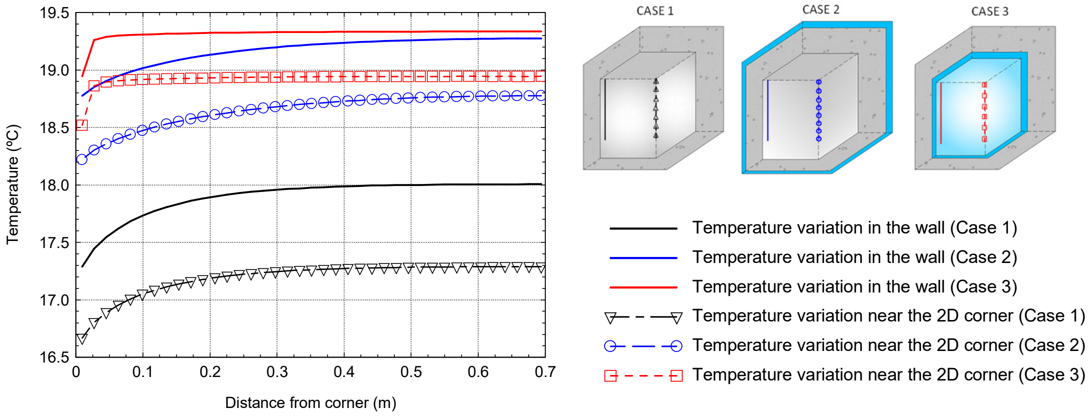

Figure 7.8: Variation of the internal surface temperature along the LTB junction starting in the 3D corner (dashed line with mark) and along the wall starting in the 2D corner (straight lines), under steady-state conditions ($\theta_e = 15$ °C and $\theta_i = 20$ °C).

It can be seen that, in the three case studies the lowest surface temperatures are registered near the 3D corner, where the thermal bridging effect is more pronounced. The difference between the surface temperature in the 3D corner and the surface temperature in the middle of the wall is higher in Case 1 (0.7 ºC) and lower in Case 2 (0.4 ºC). Note that these results were obtained for a temperature gradient of 5 ºC, between the internal and the external environment, and therefore these values will tend to increase for the highest temperature gradients that typically occur in the winter.

Table 7.2 gives the temperature factors at the internal surfaces (f_{Rsi}) of the wall, LTB and PTB of the 3D building corner, obtained by the following equation:

$$f_{Rsi}(x,y,z) = \frac{\theta_{si}(x,y,z) - \theta_e}{\theta_i - \theta_e}, \tag{7.3}$$

This factor is very useful to characterize the thermal quality of building details and to prevent the adverse effects of surface condensation such as mould growth and damage to building materials.

Lower f_{Rsi} values are associated with lower surface temperatures and the consequently higher risk of surface condensation.

Moreover, the f_{Rsi} allows to determine the temperature on the inner surface θ_{si} for any temperature gradient between the indoor and outdoor environments $(\theta_i - \theta_e)$ [7]. Table 7.2 shows that the f_{Rsi} values are significantly lower near the 3D corner (in the PTB) than on the wall surface, even when thermal insulation is applied. These values are lower than the minimum acceptable f_{Rsi} for preventing of mould growth in dwellings determined for different climate data [19] (for example, in the United Kingdom f_{Rsi} should be greater than 0.75 [20] and for some climate zones of the Switzerland f_{Rsi} should be greater than 0.78 [21]).

Table 7.2: Temperature factor at the internal surfaces of the 3D building corner (wall, LTB and PTB)

Case	f_{Rsi}		
	wall	LTB	PTB
1	0.58	0.46	0.34
2	0.85	0.76	0.65
3	0.87	0.79	0.70

Table 7.3 gives the results of computing the point thermal transmittance of the three case studies. Case 2 shows the greatest point thermal bridge contribution with $\chi = 0.016$ W/ºC. The static point thermal transmittance is lower in Case 3 ($\chi = 0.007$ W/ºC).

Table 7.3: Determination of the point thermal transmittance, χ: steady-state BEM results.

Case	L_{3D} W/ºC	L_{2D} W/(mºC)	U W/(m^{2}ºC)	ψ W/(mºC)	χ W/ºC
1	9.886	6.349	3.057	0.235	0.010
2	3.919	2.322	1.021	0.280	0.016
3	3.193	2.083	1.021	0.041	0.007

It can be concluded that, for all the case studies, under steady-state conditions, the point thermal bridge can be neglected in terms of heat losses. However, the risk of moisture condensation should be assessed, since the surface temperature near the 3D corner is clearly reduced, comparing with the surface temperature in the middle of the 1D building element and also in the LTB junctions, as shown in Figure 7.8.

7.3.2 Unsteady-state conditions

The 3D BEM model developed under this research was then used to simulate the dynamic heat transfer by conduction through the three building corner details presented in Figure 7.2. For this, at $t = 0.0$ h, the three physical models were assumed to have a uniform temperature of 20 ºC throughout the full domain. Note that, non-uniform initial conditions could be imposed throughout all the domain, however, this would make the BEM model more complex. At $t = 0.0$ h they were all subjected to an exterior temperature change. The temperature time dependence was assumed to be sinusoidal, with a period of 24 h, and with amplitude oscillations of 15 ºC, as illustrated in Figure 7.9. Six cycles were simulated to allow the system response to achieve a cyclic behaviour over time.

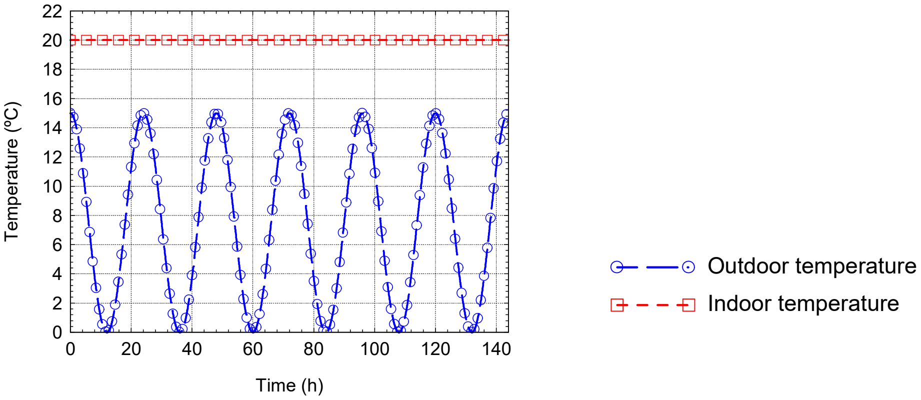

Figure 7.9: Imposed temperature time evolution: sinusoidal type variation in the exterior environment (6 cycles with a period of 24h); constant indoor temperature.

The frequency domain of computation ranged from 0.0 Hz to $4096/(144 \times 3600)$ Hz, with a frequency increment of $1.0/(144 \times 3600)$ Hz, which determined a total time window of 144 h for the analysis. The BEM model was implemented using the same boundary discretization as described before. The temperature distribution was computed in the same grids of receivers used to compute the steady-state response. A series of snapshots of the time domain simulations is presented to illustrate the resulting heat diffusion across the point thermal bridge.

Figures 7.10 to 7.15 show the temperature field distribution at the 6 receivers' grids, respectively, for the three cases, at different time instants with intervals of 6 h: (b) t ≈ 102 h; c) t ≈ 108 h; d) t ≈ 114 h and e) t ≈ 120 h). A colour scale is used in the plots, with the red and blue shades corresponding, as before, to higher and lower temperatures.

In the first plot, at t ≈ 102 h (Figures 7.10 b) to 7.15 b), the exterior temperature had already started the penultimate cycle of 24 h and dropped from 15 °C to 7.5 °C. However, higher temperature values are still registered along the internal domain of the three cases. At this instant, the linear thermal bridging effect is noticeable in the middle of the insulation layers of Case 2 and Case 3 (Grid 6 and Grid 5, respectively) and in the middle of the concrete layer in case 1 (Grid 5 and Grid 6). On the other hand, the point thermal bridging effect is barely perceptible, being visible in Figure 7.13 b, with smaller range scale of temperatures. As expected, the surface temperature near the PTB is significantly lower in Case 1 (14.7 ºC) than in Case 2 (16.1 ºC) and Case 3 (17.9 ºC). The thermal gradient between the internal surface near the 3D corner and the internal surface in the wall is about 1.8 ºC in Case 1, 2.3 ºC in Case 2 and 0.9 ºC in Case 3.

At t ≈ 108 h (Figures 7.10 to 7.15 c), the exterior temperature had fallen to 0 °C and the surface temperatures are now decreasing through the full domain of case 1 (without thermal insulation). In case 2, the internal insulation acts as a barrier to the heat transfer and the temperatures in the concrete layer and in the internal surface of the roof practically did not vary. The point thermal bridging effect in the temperature distribution is now clearly visible near the 3D corner. In case 1 the surface temperature decreased almost 3.0 ºC in the PTB, 2.0 ºC in the LTB and 1.4 ºC in the wall, when compared with the first plot. In Cases 2 and 3, the decrease was less marked because of the effect of the thermal insulation.

At t ≈ 114 h (Figures 7.10 d) to 7.15 d) the exterior temperature had increased to 7.5 °C. However, the temperature is still decreasing along the grid of receivers and reaches the lowest values at the internal surfaces on the three cases. The point thermal bridging effect is now very pronounced, thus leading to significantly lower temperatures in the vicinity of the 3D corner. In Cases 1 and 2 these plots also show the effect of the thermal inertia of the material in the interior domain of the PTB. In case 1, the lack of thermal insulation leads to significantly lower surface temperatures than in the other two cases. This difference is 7 ºC near the PTB and 6 ºC in the vicinity of the LTB.

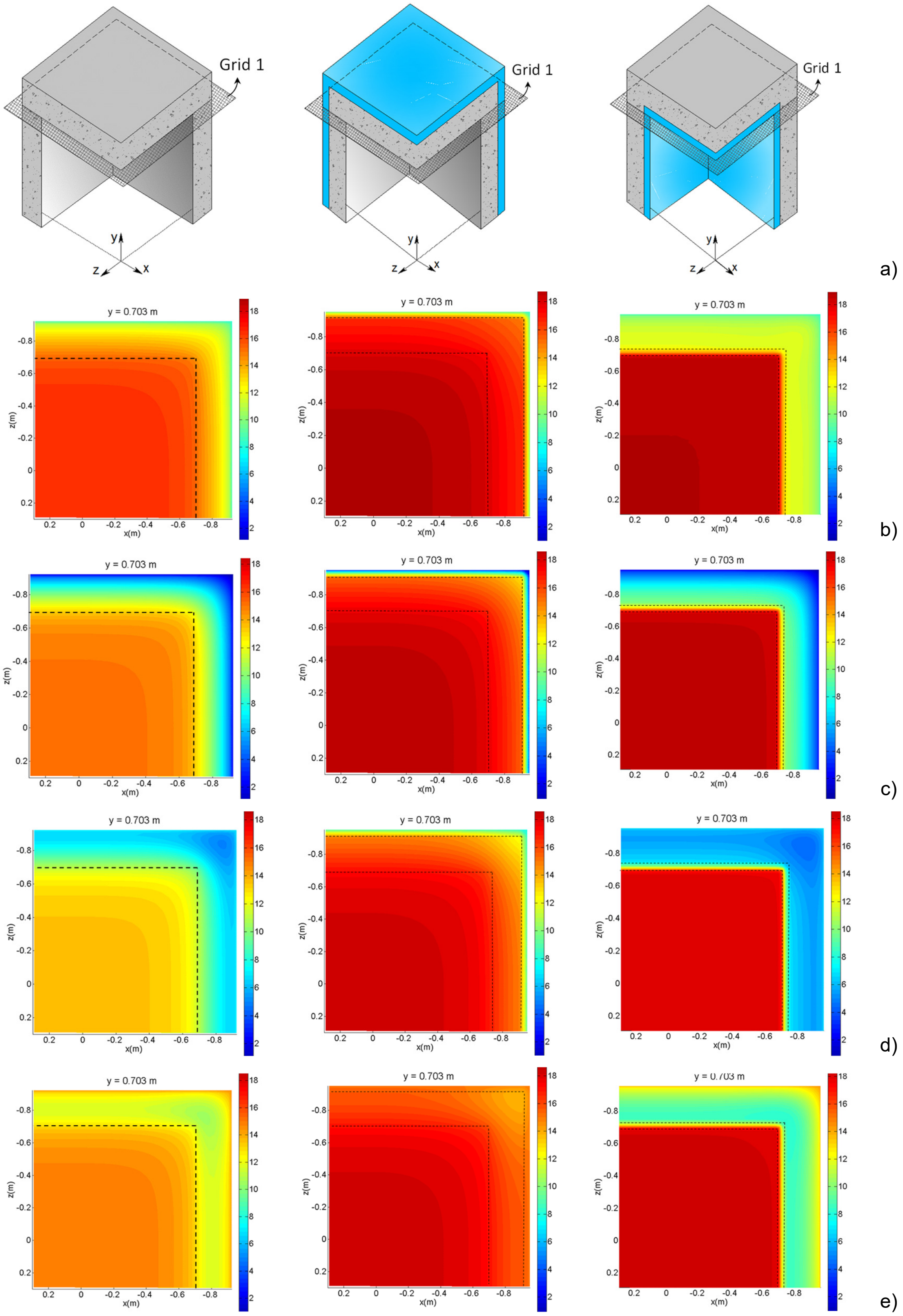

Figure 7.10: Temperature distribution (in ◦C) under dynamic conditions in cases 1, 2 and 3 (Grid 1): a) scheme of the case study and grid of receivers; b) t ≈ 102 h; c) t ≈ 108 h; d) t ≈ 114 h; e) t ≈ 120 h.

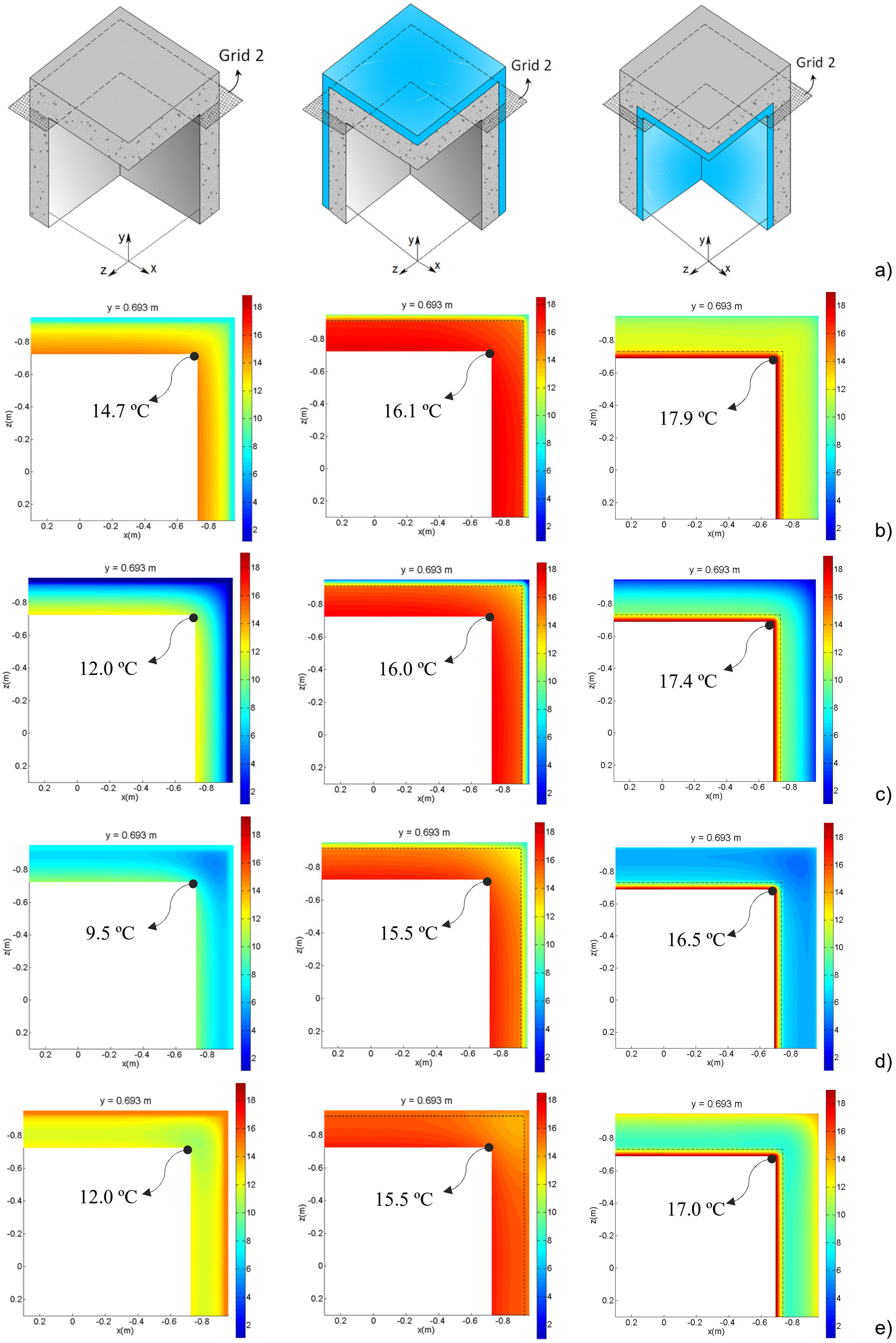

Figure 7.11: Temperature distribution (in ◦C) under dynamic conditions in cases 1, 2 and 3 (Grid 2): a) scheme of the case study and grid of receivers; b) t ≈ 102 h; c) t ≈ 108 h; d) t ≈ 114 h; e) t ≈ 120 h.

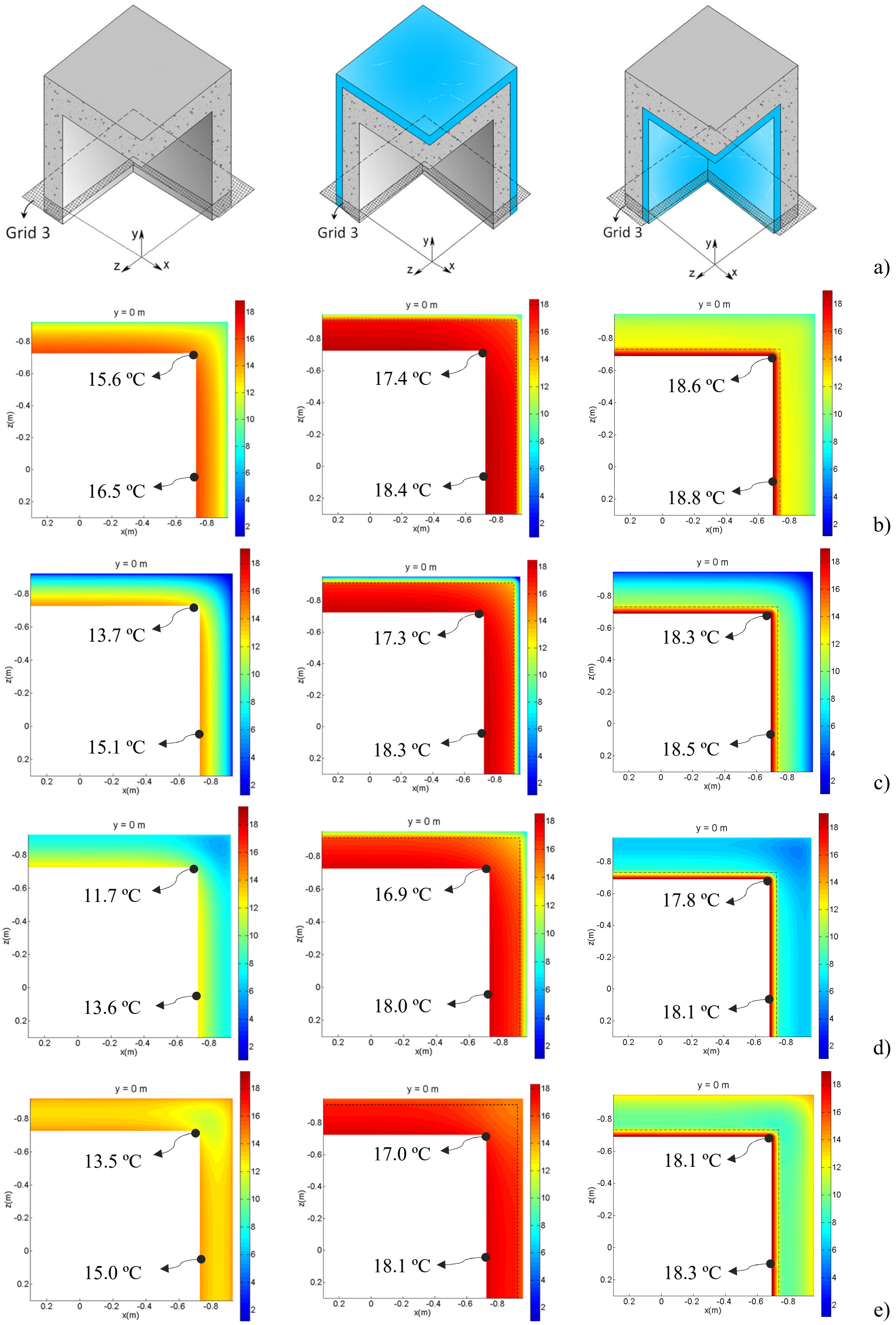

Figure 7.12: Temperature distribution (in ◦C) under dynamic conditions in cases 1, 2 and 3 (Grid 3): a) scheme of the case study and grid of receivers; b) t ≈ 102 h; c) t ≈ 108 h; d) t ≈ 114 h; e) t ≈ 120 h.

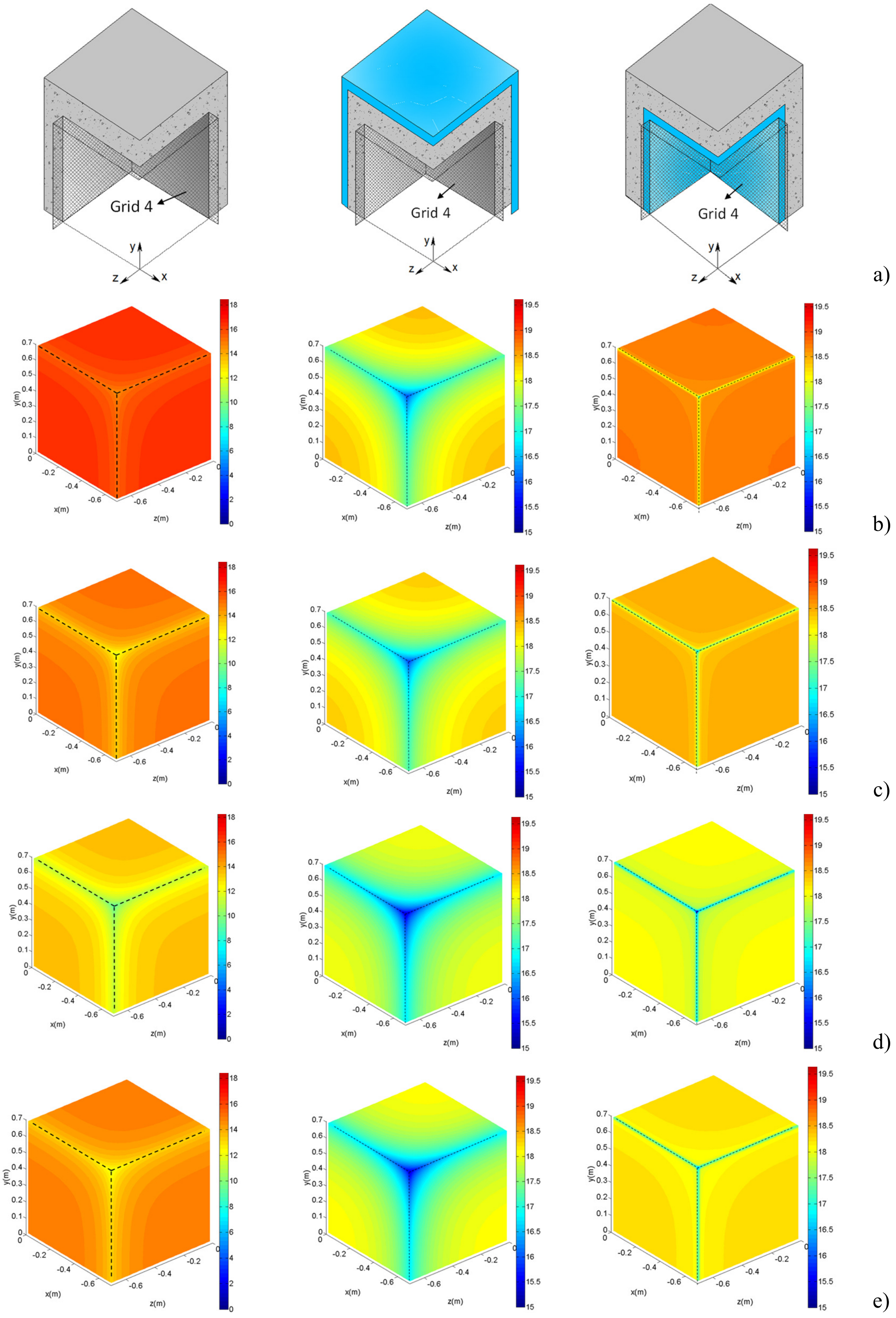

Figure 7.13: Temperature distribution (in ◦C) under dynamic conditions in cases 1, 2 and 3 (Grid 4): a) scheme of the case study and grid of receivers; b) t ≈ 102 h; c) t ≈ 108 h; d) t ≈ 114 h; e) t ≈ 120 h.

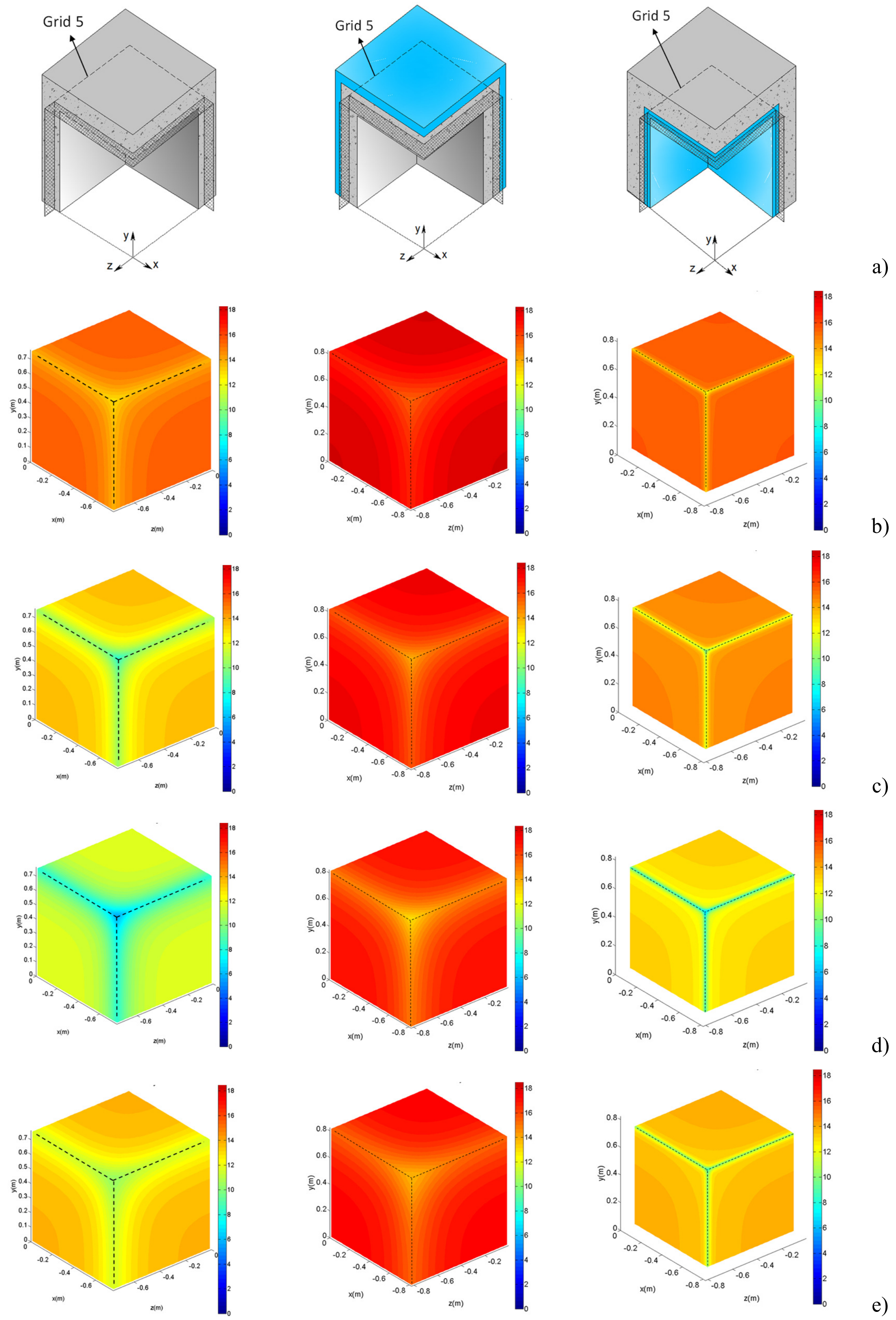

Figure 7.14: Temperature distribution (in ◦C) under dynamic conditions in cases 1, 2 and 3 (Grid 5): a) scheme of the case study and grid of receivers; b) t ≈ 102 h; c) t ≈ 108 h; d) t ≈ 114 h; e) t ≈ 120 h.

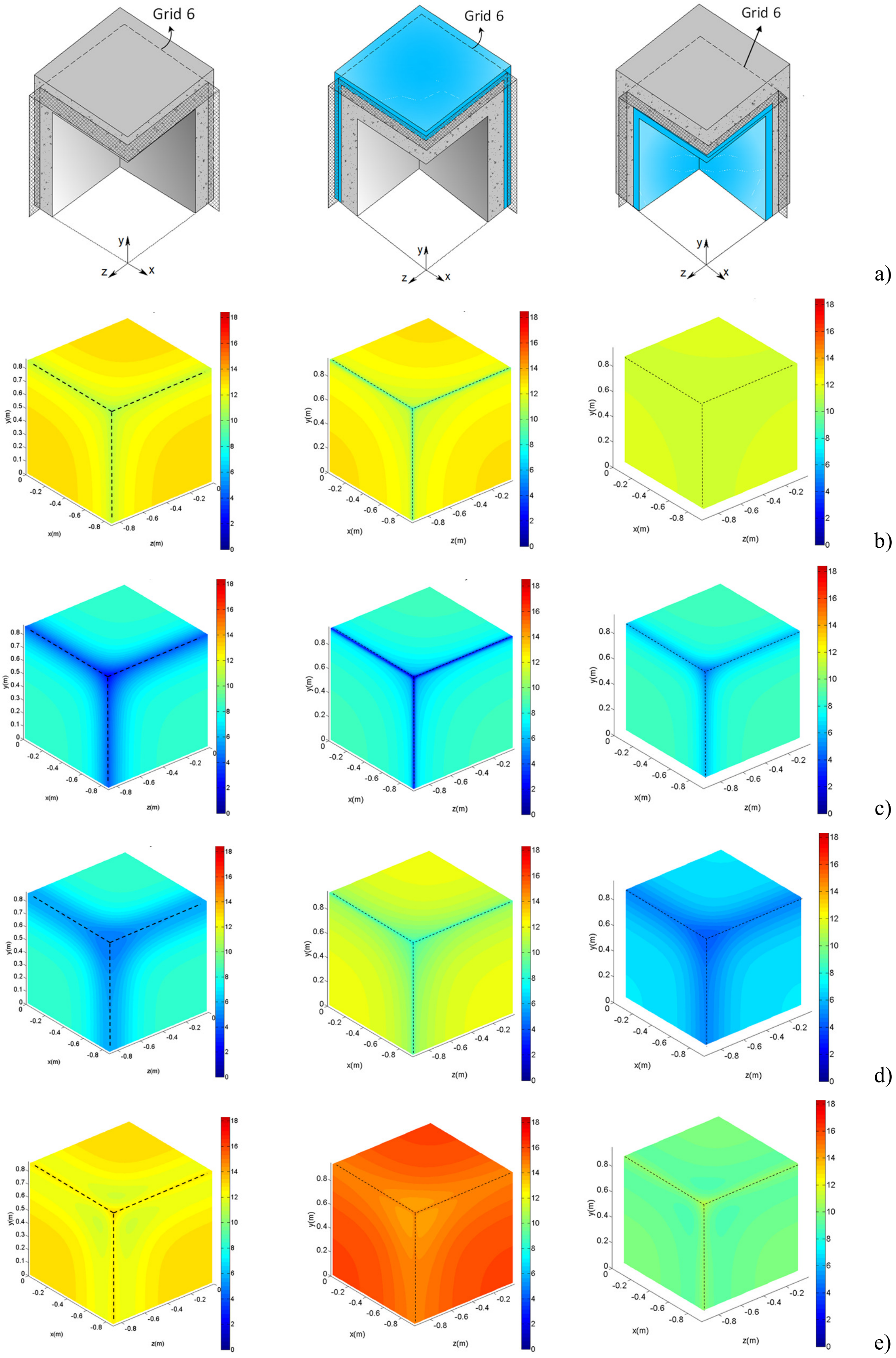

Figure 7.15: Temperature distribution (in ◦C) under dynamic conditions in cases 1, 2 and 3 (Grid 6): a) scheme of the case study and grid of receivers; b) t ≈ 102 h; c) t ≈ 108 h; d) t ≈ 114 h; e) t ≈ 120 h.

At t ≈ 120 h (Figures 7.10 e)-7.15 e) the exterior temperature had reached again 15 °C, completing the penultimate cycle of 24 h. The temperature is increasing through the full domain of the three case studies. However, at this instant, the temperatures registered by the receivers placed in the middle of the junctions between building components are lower than the temperatures registered close to the internal and the external surfaces. This difference is more pronounced near the 3D corner, where the thermal phase lag is higher, especially in Case 1 and Case 2.

It can also be seen that, in the four instants analysed, the surface temperatures in the PTB and the LTB are higher in Case 3 (with an internal thermal insulation layer).

Figure 7.16 presents the internal surface temperature variation over time in the PTB (black curve), the LTB (red curve) and in the plane wall (blue curve), obtained for each case study (Case 1 - a); Case 2 – b); Case 3 – c)). It can be seen that the surface temperatures are significantly lower near the 3D corner (in the PTB) and highest at the plane wall, in all three case studies. The thermal amplitude of the surface temperature over time is higher in the PTB, especially in Case 1, without thermal insulation (Figure 7.16 a)).

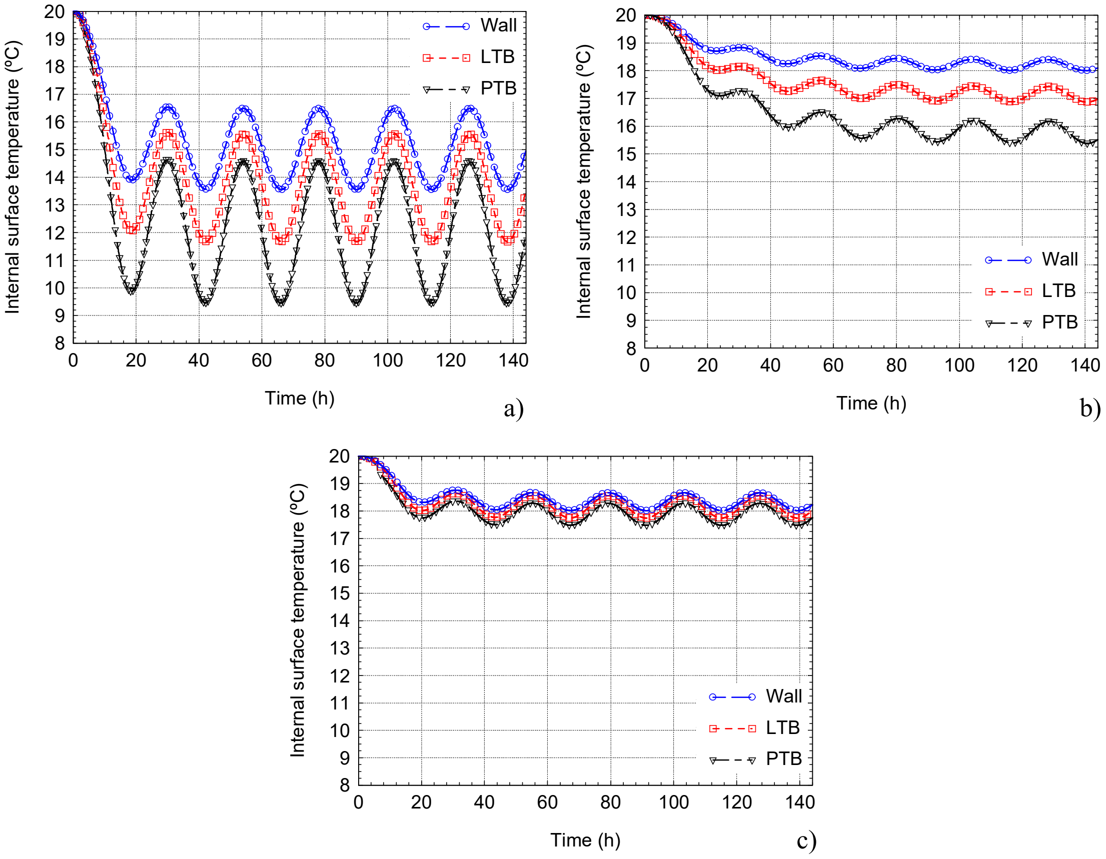

Figure 7.16: Variation of the internal surface temperatures over time – a) Case 1; b) Case 2; c) Case 3.

The plots in Figure 7.17 present the variation of the heat flow rate per metre length through the LTB ($\phi_{l,LTB}$) and the heat flow rate through the PTB (ϕ_{PTB}), as well as the variation of the dynamic linear and point thermal transmittances ($\phi_{l,LTB}/(\theta_i - \theta_e)$ and $\phi_{PTB}/(\theta_i - \theta_e)$, respectively), over time, obtained for the three case studies (Case 1, Case 2 and Case 3).

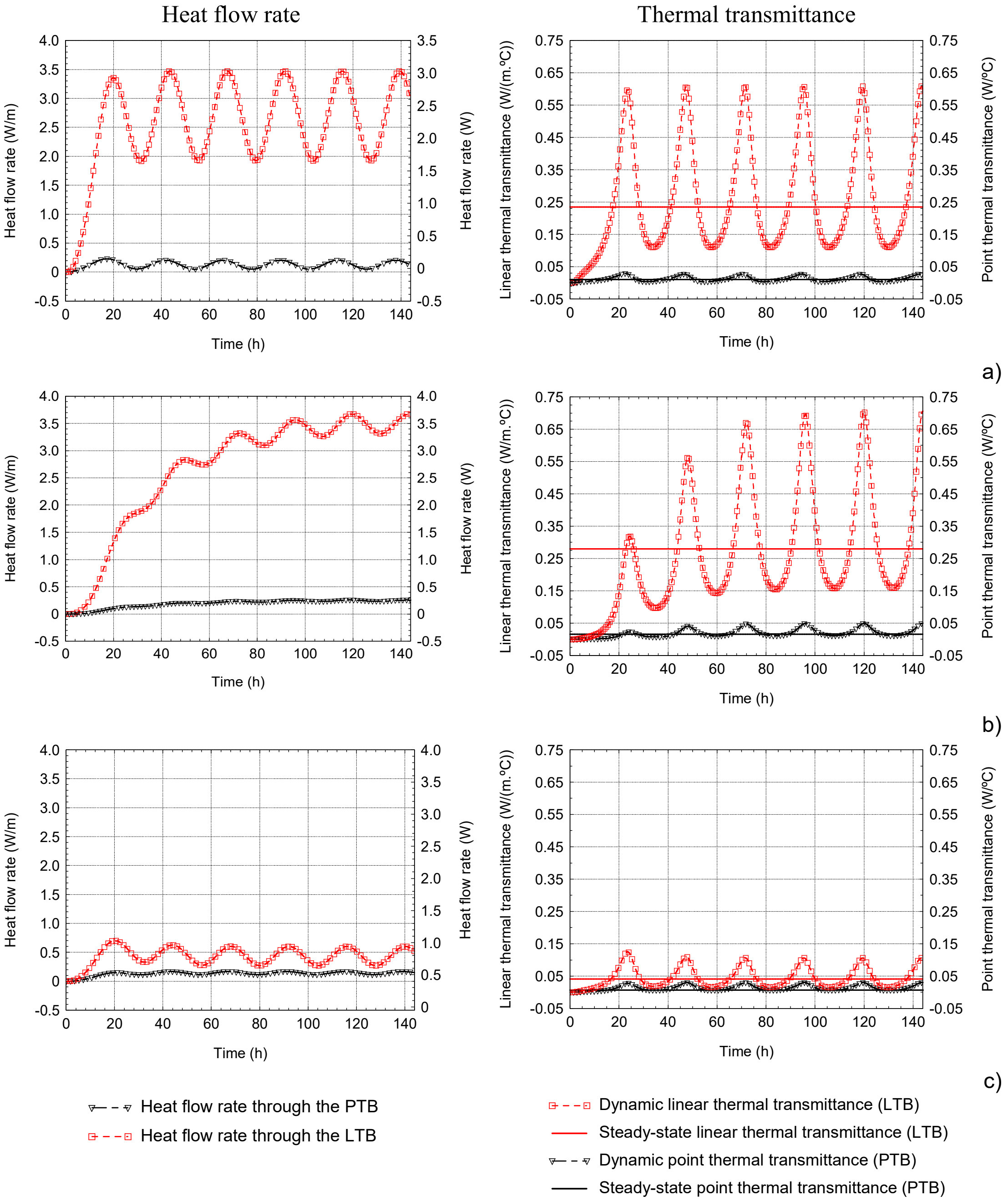

Figure 7.17: Variation of the heat flow rate and the thermal transmittance of the LTB and PTB in the 3D building corner: a) Case 1; b) Case 2; c) Case 3.

The method adopted for computing $\phi_{l,LTB}$ and ϕ_{PTB} was similar to that used for steady-state conditions. However, as the problem is dynamic, the position of the planes over which the global heat flux is computed is crucial, since it leads to distinct values because of the dynamic effects. In this work, the inner surfaces were selected because these are where moisture condensation and pathologies often occur, and they are the surfaces that are relevant to evaluating the dynamic heat flow.

It can be concluded that, for the three case studies, the heat flow rates through the PTB are significantly lower than those through the LTB. It can also be seen that the difference between the point thermal transmittances obtained under dynamic and steady-state conditions is not very significant, since both steady-state and dynamic heat fluxes are very low. Furthermore, the heat loss through the PTB occurs only at a point, whereas the linear heat loss occurs throughout the whole length of the LTBs. Therefore, it can be concluded that in the three cases analysed here, the PTB can be neglected in terms of heat loss. However, the evaluation of the dynamic behaviour of PTB details can be very important to prevent moisture condensation problems, since it enables the evaluation of minimum surface temperatures over time, and therefore, higher performance solutions can be studied and proposed.

7.4 Conclusions

In this chapter, the simulation of the transient heat diffusion through a point thermal bridge (PTB) in a 3D concrete building corner corresponding to a junction between two walls and roof has been presented. The heat transfer simulations were performed using the 3D BEM model proposed in Chapter 5 and experimentally validated in Chapter 6. Three examples were simulated considering different thermal insulation scenarios: corner without thermal insulation; corner with an external insulation layer; corner with an internal insulation layer.

In each case study, the point thermal transmittance was computed for both steady-state and transient analysis. The heat flow through the PTBs analysed under this research was found to be significantly lower than the heat flow through the adjacent building elements and through the LTB junctions. Therefore, it was concluded that in the three cases analysed here the PTB can be neglected in terms of heat losses. However, the evaluation of the dynamic point thermal bridging effect in the 3D building envelope details can be very important when it comes to overcoming moisture condensation problems, since lower surface temperatures are registered in the vicinity of the PTBs. Moreover, the dynamic behaviour of the point thermal bridges clearly depends on where the insulation layer is applied.

References

[1] Directive 2010/31/EU of the European Parliament and of the Council of 19 May 2010 on the energy performance of buildings.

[2] J. Šadauskiene, J. Ramanauskas, L. Šeduikyte, M. Daukšys, A. Vasylius, A simplified methodology for evaluating the impact of point thermal bridges on the high-energy performance of a passive house, Sustainability 2 (7) (2015) 16687-16702.

[3] H. Erhorn, H. Erhorn-Klutting, M. Citterio, M. Cocco, D. Orshoven, A. Tilmans, P. Schild, P. Bloem, K.E. Thomsen, J. Rose, An effective handling of thermal bridges in the EPBD context, final report of the IEE ASIEPI work on thermal bridges, March 2010.

[4] G. Santos, N. Mendes, Hygrothermal bridge effects on the performance of buildings, International Communications in Heat and Mass Transfer 53 (2014) 133–138.

[5] G. Santos, N. Mendes, P. Philippi, A building corner model for hygrothermal performance and mould growth risk analyses, International Journal of Heat and Mass Transfer 52 (2009) 4862–4872.

[6] R. Freire, L. Coelho, G. Santos, V. Mariani, Predicting building's corners hygrothermal behavior by using a Fuzzy inference system combined with clustering and Kalman filter, International Communications in Heat and Mass Transfer 71 (2016) 225–233.

[7] International Organization for Standardization, ISO 10211, Thermal bridges in building construction - Heat flows and surface temperatures - Detailed calculations, 2007.

[8] T. Theodosiou, K. Tsikaloudaki, D. Bikas, Analysis of the thermal bridging effect on ventilated facades, Procedia Environmental Sciences 38 (2017) 397 – 404.

[9] T. Theodosiou, A. Tsikaloudaki, K. Kontoleon, D. Bikas, Thermal bridging analysis on cladding systems for building facades, Energy and Buildings 109 (2015) 377–384.

[10] P. Iodice, N. Massarotti, A. Mauro, Effects of inhomogeneities on heat and mass transport phenomena in thermal bridges, Energies 9 (3) (2016) 126.

[11] G.H. Santos, N. Mendes, Hygrothermal bridge effects on the performance of buildings, International Communications in Heat and Mass Transfer 53 (2014) 133–138.

[12] S. You, W. Li, T. Ye, F. Hu, W. Zheng, Study on moisture condensation on the interior surface of buildings in high humidity climate, Building and Environment 125 (2017) 39-48.

[13] A. Tadeu, J. Prata, N. Simões, Closed form integration of singular and hypersingular integrals in 3D BEM formulations for heat conduction, Mathematical Problems in Engineering, Volume 2012, Article ID 647038, 21 pages.

[14] A. Tadeu, J. Prata, N. Simões, Dynamic simulation of three-dimensional heat conduction through cylindrical inclusions using a BEM model formulated in the frequency domain, Applied Mathematics and Computation 261 (2015) 397–407.

[15] International Organization for Standardization, ISO 6946: Building components and building elements - Thermal resistance and thermal transmittance - Calculation method, 2007.

[16] International Organization for Standardization, ISO 8302: Thermal insulation – Determination of steady-state thermal resistance and related properties – Guarded hot plate apparatus, 1991.

[17] European Standards, EN 12667: Thermal performance of building materials and products. Determination of thermal resistance by means of guarded hot plate and heat flow meter methods. Products of high and medium thermal resistance, 2001.

[18] European Standards. EN 1602: Thermal insulating materials, Thermal insulation, Construction materials, Density measurement, Bulk density, Test specimens, Testing conditions, Buildings, 1996.

[19] International Organization for Standardization, ISO 13788: Hygrothermal performance of building components and building elements - Internal surface temperature to avoid critical surface humidity and interstitial condensation - Calculation methods, 2012.

[20] BRE IP 17/01, Assessing the effects of thermal bridging at junctions and around openings. BRE, Building Research Establishment Ltd, Garston, 2001.

[21] SIA 180-C1:2015 Bauwesen, Wärmeschutz, Feuchteschutz und Raumklima in Gebäuden – Korrigenda C1 zur Norm SIA 180:2014 , Zürich, 2015.

CHAPTER 8

FINAL CONSIDERATIONS

8 FINAL CONSIDERATIONS

8.1 Overview and main conclusions

Despite growing concerns about the impact of thermal bridges on the energy performance of buildings, most studies on dynamic thermal bridging analysis use very simplified approaches and therefore there is still a shortage of information on the effective behaviour of linear and point thermal bridges under dynamic conditions. The aim of this research work was to fill this gap by accurately evaluating the dynamic effect of linear and point thermal bridges of buildings, using multidimensional heat transfer models based on the boundary element method (BEM) and formulated in the frequency domain. The work involved the development, verification and validation of the BEM models and applying them to specific problems involving linear and point thermal bridges in building corners. This section sets out the main research contributions and conclusions of the thesis.

An alternative method for computing the dynamic heat fluxes through linear thermal bridges (LTB) is presented in Chapter 2. This method combines a two-dimensional (2D) BEM formulation in the frequency domain for modelling 2D building corners with an analytical solution to compute the response of the flat walls, when the problem is one-dimensional (1D). The good agreement between the two models was demonstrated by comparing the numerical and the analytical results obtained for a multilayer system wall. The applicability of the proposed methodology was demonstrated for a 2D concrete wall corner.

The BEM model was experimentally validated using hot box measurements (Chapter 3). For this, a wooden corner representing an LTB was placed between the two chambers of a calibrated hot box. A sinusoidal temperature variation was imposed in the cold chamber, while the temperature inside the warm chamber was kept constant. The surface temperature and the heat flux near the corner and at the centre of the wooden panels were registered on the both sides of the specimen, using thermocouples and heat flux sensors. The experimental results were then compared with the BEM responses obtained for the same physical model and assuming the same boundary conditions. This comparison showed that the proposed BEM model can be used in the dynamic analysis of linear thermal bridges (LTBs).

The experimental results also made it possible to evaluate the real thermal behaviour of the thermal bridge, taking into account all the factors that affected its performance. It is clear from the results that, even in homogeneous materials with high thermal performance, such as wood, the dynamic thermal bridging effect is relevant in that it leads to a significant increase of the heat flow, higher thermal and heat flux amplitudes and an important fall in the surface temperature. It was also possible to ascertain that there is in fact an increase in the surface thermal resistance in the vicinity of the thermal bridge, due to the convection effect near the corner.

A sensitivity analysis was then performed to assess the influence of the constructive solution and the external temperature variation on the dynamic thermal behaviour of LTBs in building corners (Chapter 4). For that purpose, several numerical applications were performed for two wall materials (concrete and wood) and with the insulation layer having different placements. After calculations in the frequency domain, time solutions were obtained using inverse Fourier transformations, thus enabling the simulation of different external temperature variations. The analyses included evaluating the heat fluxes and the surface temperature variation over time in the constructive details, assuming a sinusoidal variation of the external temperature. Subsequently, the same case studies were modelled but now using real climate data from four European cities and considering different thicknesses for the thermal insulation layer.

The study results evidenced that the variation of the heat flow rate in the LTB strongly depends on the building materials and on the constructive system. The importance of modelling thermal bridges dynamically was also demonstrated, since significantly higher linear thermal transmittance values were found under transient conditions than under steady-state conditions. This behaviour leads to lower surface temperatures and so increases the risk of surface condensation. Besides this, the study showed that the ratio between the total heat loss through 1 m of LTB and the total heat loss through 1 m^2 of wall surface are similar to those found for steady-state conditions. Therefore, the effective percentage contribution of the LTB to the thermal performance of a building envelope in the dynamic simulation of buildings may be at least as important as in a steady-state analysis.

The development of the 3D numerical tool to model the dynamic point thermal bridging effect in 3D building corners involved a sequence of BEM formulations for the simulation of the 3D heat transfer by conduction through inclusions, taking into account adequate boundary conditions. These formulations are presented in Chapter 5. Analytical solutions were calculated and verified for the integration of the singular integrals that are found in the classical 3D BEM formulations, when the element to be integrated is the loaded one (singular element). The good accuracy of the 3D BEM formulations with the analytical solutions incorporated was demonstrated by comparing the BEM responses with the analytical results obtained for cylindrical circular inclusions. The simulation of dynamic heat conduction through a PTB in a 3D concrete corner clearly showed the applicability of the developed BEM model.

A series of experiments, again using the calibrated hot box apparatus, were performed to validate the 3D BEM formulation. A 3D wooden corner that represented a junction between two walls and a roof was used in the simulations (Chapter 6). The experimental results showed that the thermal bridging effect is more pronounced near the 3D corner, where the heat fluxes and thermal amplitudes are significantly higher and the surface temperatures considerably lower than at the LTB junctions. The comparison between the experimental and numerical results confirmed the reliability of the 3D BEM simulations.

The applicability of the proposed 3D BEM model was then illustrated (Chapter 7) for a 3D concrete building corner and the dynamic thermal bridging effect in its vicinity was evaluated. The influence of an insulating material and its position on the thermal behaviour of the point thermal bridge was also analysed. The study showed that the evaluation of the dynamic point thermal bridging effect in the 3D building envelope details can be very important to avoid moisture condensation problems. However, it was concluded that, in the three cases analysed under this research, the PTB can be neglected in terms of heat losses.

This research work has shown the importance of modelling linear and point thermal bridges dynamically. The study found that thermal bridges effectively change the dynamic nature of the building envelope and significantly influence its dynamic thermal performance. The evaluation of the dynamic thermal bridging effect on building envelope details can be very important when it comes to tackling building pathologies caused by surface condensation. It is also concluded that the accurate simulation of linear and point thermal bridges should not be neglected during the dynamic energy simulation of buildings.

8.2 Future work

Although we consider that the main objectives proposed for this research have been achieved, we are aware that there is still a long way to go to improve understanding of the dynamic thermal bridging effect on the building envelope. Therefore, we feel it is extremely important to continue this study by performing the following tasks:

- To carry out the numerical and experimental simulation of the dynamic effect of linear and point thermal bridges in building corners, incorporating other materials used in common buildings solutions.

- To generalize the developed numerical tools to solve other types of linear and point thermal bridges of buildings.

- To include the developed modelling tools in the energy simulation of compartments and buildings. It will then be possible to evaluate the influence of linear and point thermal bridges on the energy performance of a reference building in order to estimate the effective contribution of these thermal bridges in terms of heat loads.

- To describe the convection and radiation phenomena in the numerical simulations in greater detail. Note that, in this research work, those phenomena were taken into account in a simplified way by adding a very thin air layer with an additional thermal resistance to the external and the internal surfaces of the physical models.